A novel faulted section location technique for future active distribution networks

Panagiotis Bountouris

A thesis submitted for the degree of Doctor of Philosophy to

Department of Electronic and Electrical Engineering

University of Strathclyde

September 2022

Dedicated to my wife Pinelopi

and my son Nikos

This thesis is the result of the author's original research. It has been composed by the author and has not been previously submitted for examination which has led to the award of a degree.

Signature: 

Abstract

Distribution Network Operators (DNOs) face increasingly higher challenges to preserve quality and continuity of supply due to the widespread penetration of Distributed Energy Resources (DER) [1–8]. In parallel, more advanced technologies are being introduced into secondary substations for better observability and controllability. These features provided via instrumented substation assets and Information Communication Technologies (ICT) present opportunities for the development and implementation of new functions aiming to the effective operation and monitoring of active distribution networks [9–14].

This thesis focuses on one of these functionalities – that is, leveraging the ability of Low Voltage (LV) sensors to locate 11 kV unsymmetrical faults by monitoring and processing the network voltage profile during fault conditions. In particular, a novel technique has been developed which identifies the Faulted Section (FS) of the Medium Voltage (MV) feeder after a fault has occurred. The proposed algorithm, of which the successful operation depends solely on distributed LV voltage monitoring devices, represents the main contribution of the research work. A key characteristic is that, although the LV sensors connected at the secondary side of MV/LV step-down transformers require communication to transmit the data to a central point, they do not require time synchronisation. The technique facilitates the fault location procedure, which is of major importance as it accelerates restoration, reduces the system down-time, minimises repair cost, and hence, increases the overall availability and reliability of the distribution network.

Moreover, the thesis deals with the challenges related to the complexity of mod-

ern distribution networks, taking into account ring topologies, MV lateral connections, pre-fault load unbalance and the presence of DERs. In this sense, the empirical characterisation of grid connection stability and fault response of small scale commercially available LV PV inverters was realised. The purpose was twofold: 1) highlight the diversity among the inverters' responses as observed during the testing and indicate the risk of loss of PV generation during typical MV and HV level faults and 2) develop a dynamic model representing the behaviour of a real inverter under the applied physical testing conditions. The particular model was deployed in the power system studies conducted, aiding the evaluation of the FS location technique.

Laboratory investigation was also carried out at the facilities of the Power Networks Demonstration Centre (PNDC) to further examine the performance of the developed faulted section location algorithm. The tests were performed in both MV radial and ring PNDC network configurations and measurements were acquired from various LV test-bays. It was demonstrated that the scheme can reliably identify the faulted section of the line while consistently maintaining high accuracy across a wide range of fault scenarios. Further sensitivity analysis demonstrates that the proposed scheme is robust against partial loss of communications and noise interference.

The thesis concludes with an overview of future work that is required to further advance the concepts demonstrated.

References

[1] I. Oladeji, P. Makolo, M. Abdillah, J. Shi, and R. Zamora, "Security impacts assessment of active distribution network on the modern grid operation—A Review," *Electronics*, vol. 10, no. 16, 2021.

[2] H. Kelsey, Z. Peterson, M. Coddington, F. Ding, B. Sigrin, D. Saleem, and S. Baldwin, "An overview of Distributed Energy Resource (DER) interconnection: Current practices and emerging solutions.," *National Renewable Energy Laboratory. NREL/TP-6A20-72102.*, 2019.

[3] D. Infield and L. Freris, *Renewable Energy in Power Systems*. John Wiley & Sons Ltdl, 1 ed., 2008.

[4] K. Kauhaniemi and L. Kumpulainen, "Impact of distributed generation on the protection of distribution networks," in *2004 Eighth IEE International Conference on Developments in Power System Protection*, vol. 1, pp. 315–318 Vol.1, 2004.

[5] A. Dyśko, "UK distribution system protection issues," *IET Generation, Transmission & Distribution*, vol. 1, pp. 679–687(8), July 2007.

[6] K. Jennett, "Comprehensive and quantitative analysis of protection problems associated with increasing penetration of inverter-interfaced dg," *IET Conference Proceedings*, pp. 31–31(1), January 2012.

[7] F. Coffele, "Quantitative analysis of network protection blinding for systems incorporating distributed generation," *IET Generation, Transmission & Distribution*, vol. 6, pp. 1218–1224(6), December 2012.

[8] S. Borlase, *Smart Grids, Advanced Technologies and Solutions*. CRC Press, 2 ed., 2018.

[9] B. Panajotovic, M. Jankovic, and B. Odadzic, "Ict and smart grid," in *2011 10th International Conference on Telecommunication in Modern Satellite Cable and Broadcasting Services (TELSIKS)*, vol. 1, pp. 118–121, 2011.

[10] M. Mourshed, S. Robert, A. Ranalli, T. Messervey, D. Reforgiato, R. Contreau, A. Becue, K. Quinn, Y. Rezgui, and Z. Lennard, "Smart Grid Futures: Perspectives on the Integration of Energy and ICT Services," in *7th International Conference on Applied Energy (ICAE2015)*, vol. 75 of *Clean, Efficient and Affordable Energy for a Sustainable Future: The 7th International Conference on Applied Energy (ICAE2015)*, (Abu Dhabi, Saudi Arabia), pp. 1132 – 1137, Elsevier, Mar. 2015.

[11] J. I. Moreno, M. Martínez-Ramón, P. S. Moura, J. Matanza, and G. López, "Smart grid: ICT control for distributed energy resources," *International Journal of Distributed Sensor Networks*, vol. 12, no. 5, p. 1329421, 2016.

[12] G. J. Smit, "Efficient ICT for efficient smart grids," in *2012 IEEE PES Innovative Smart Grid Technologies (ISGT)*, pp. 1–3, 2012.

[13] T. Atasoy, H. E. Akınç, and O. Erçin, "An analysis on smart grid applications and grid integration of renewable energy systems in smart cities," in *2015 International Conference on Renewable Energy Research and Applications (ICRERA)*, pp. 547–550, 2015.

[14] K. Kuroda, T. Ichimura, Y. Matsufuji, and R. Yokoyama, "Key ICT solutions for realizing smart grid," in *2012 International Conference on Smart Grid (SGE)*, pp. 1–8, 2012.

Acknowledgements

First and foremost, I would like to express my gratitude to Dr Federico Coffele for his invaluable supervision, patience and time. He has been a great example and a source of inspiration for me, which motivated me all along the PhD journey.

My gratitude extends remarkably to my second supervisor Prof. Campbell Booth for his valuable guidance and thorough feedback on my thesis.

This endeavour would not have been possible without the voluntary and prompt support of Dr Dimitrios Tzelepis. His immense knowledge, hard-work and mentoring have encouraged me in all the time of my academic research.

I am also grateful to my former colleagues in PNDC and the PNDC members for their support over the duration of the projects related to this research.

Finally, I want to thank my beloved wife Pinelopi for her love and constant support, for all the late nights, early mornings and missed weekends. She has always been there waiting for me, while I was undertaking my research and writing my thesis. She is my muse, the mother of our son and my best friend.

Contents

List of Figures

List of Tables

List of Abbreviations

AC Alternating Current

ANN Artificial Neural Networks

CI Customer Interruptions

CML Customer Minutes Lost

DC Direct Current

DER Distributed Energy Resources

DG Distributed Generation

DNO Distribution Network Operator

DUT Device Under Test

DWT Discrete Wavelet Transform

EPRI Electric Power Research Institute

FFT Fast Fourier Transformation

FLISR Fault Location Isolation and Restoration

FPI Fault Passage Indicator

FRT Fault Ride Through

GC Grid Code

GE General Electric

GPS Global Positioning System

ICT Information Communication Technologies

IEC International Electrotechnical Commission

IM Impedance Measurements

KVL Kirchhoff's Voltage Law

LoM Loss of Mains

LV Low Voltage

MSR Master

MV Medium Voltage

PMU Phasor Measurement Unit

PNDC Power Networks Demonstration Centre

PoW Point on Wave

PV Photovoltaic

RES Renewable Energy Sources

RMU Ring Main Unit

RoCoF Rate of Change of Frequency

RTDS Real Time Digital Simulator

RTU Remote Terminal Unit

SAIDI System Average Interruption Duration Index

SAIFI System Average Interruption Frequency Index

SCADA Supervisory Control And Data Acquisition

SG Synchronous Generator

SL Slave

SLD Single Line Diagram

SVM Support Vector Machine

TDR Time Domain Reflectometry

THD Total Harmonic Distortion

TW Traveling Waves

URD Underground Residential Distribution

VS Vector Shift

WECC Western Electricity Coordinating Council

Chapter 1

Introduction

1.1 Introduction to the research

The increasing population growth and related economic development at industrial, commercial, and tertiary levels has resulted in continuously rising electricity demand. In parallel, power systems have been subjected to significant upgrades in terms of structure and capacity. Ensuring power systems reliability has been one of the major priorities for electricity DNOs throughout this evolution [1], [2].

System Average Interruption Frequency Index (SAIFI) and System Average Interruption Duration Index (SAIDI) are globally used reliability indices defining the average number of times that a customer's service is interrupted and the average interruption duration per customer served per year, respectively [3], [4]. Customer Minutes Lost (CML) corresponding to SAIDI and Customer Interruptions (CI) per 100 customers per year (SAIFI x 100) are the distribution reliability measures typically used by the government regulator, Ofgem, for gas and electricity markets of Great Britain (GB) [5]. Figure 1.1 provides information regarding the reliability performance of the DNOs in UK against their annual targets for the year 2018-2019 [6].

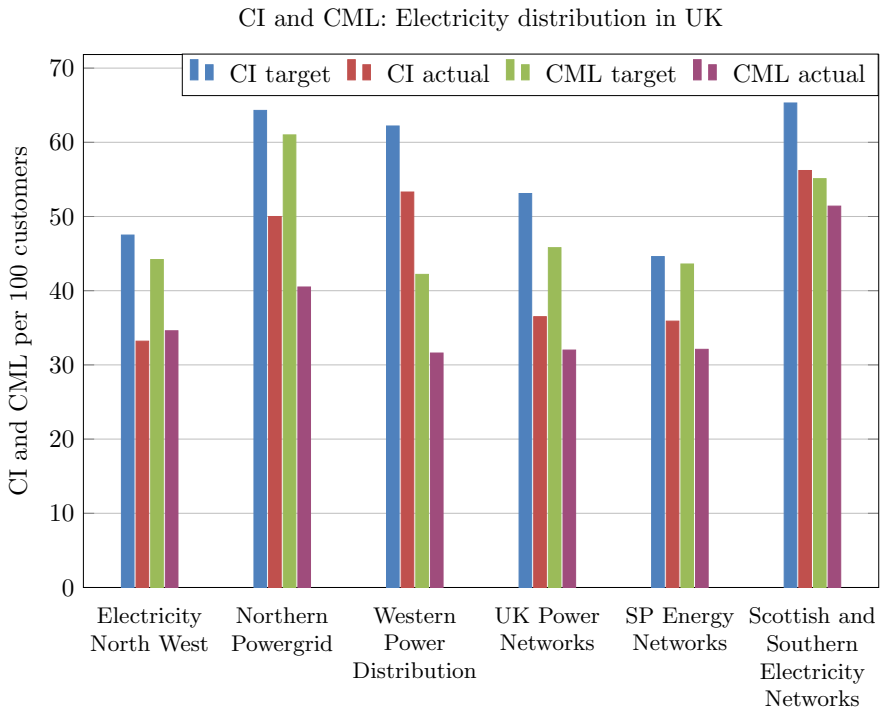

Figure 1.1: Annual Interruption Incentive Scheme performance per 100 customers by DNO group (Planned and Unplanned) [6].

Unplanned outages due to electrical faults are placed among the most typical causes of compromising reliability in electrical networks – other causes are intermittent power sources and uncertain load profile [2]. According to the statistics, 70-80% of the faults in European countries are encountered in the MV parts of distribution networks, with the most frequent ones to be transient in nature [5].

Transient faults are cleared when power is disconnected for a short period of time - normally via automatic re-close function - and then restored. Normally, up to three re-closures are attempted, after which the breaker is locked out. Possible causes of transient faults are lightning, animal or tree contact, clashing of two conductors due to wind blowing etc. [7].

Permanent faults require fault location, isolation and repair of the damaged equipment by the maintenance crew prior power supply restoration. This kind of faults are typically caused due to insulation breakdown. Insulation may fail because of its own

weakening or due to overvoltage. Weakening of the insulation can happen because of ageing, high temperature, adverse weather conditions (i.e. rain, hail, snow), chemical pollution, foreign objects etc. Overvoltage can be produced by several causes such as switching operation and lightning [7]. The disconnection times of permanent faults usually range from a few minutes to many hours resulting to sustained outages.

Depending on the circumstances, different type of faults may occur. From Table B.4, it can be seen that the the most severe and least probable electrical faults are the three-phase symmetrical faults. On the other hand, single phase to earth faults, while typically somewhat less severe, are the most common fault type and still require isolation in any earthed system [7].

Table 1.1: Statistics with regards to fault types [7]

Fault type	**Probability of occurrence**	**Severity**
ph-earth	85%	Least severe
ph-ph	8%	
ph-ph-earth	5%	
ph-ph-ph	2%	Most severe

Optimal service reliability can be attained when the design and operation of the distribution system strive to minimise the effect of any fault that may occur. Fault management including Fault Location Isolation and Restoration (FLISR) constitutes an important procedure for DNOs. In particular, accurate and fast localisation of the MV faulted section can have a significant impact on the power supply recovery time and thus the reliability of the distribution network.

Several MV faulted section location methods have been implemented throughout the years, however literature indicates a number of problems such as high implementation cost and time consuming procedures [8–10]. On the other hand, DNOs adopting modern practices like self-healing and auto-reconfiguring MV networks are capable to improve their reliability indices such as CML and CI.

An example of automated faulted section location architecture is the one deploying Fault Passage Indicators (FPIs) relying on a central Supervisory Control And Data Acquisition (SCADA) system. SCADA includes a topological display, power flow mon-

itoring and remote control of MV switches. The FPI status is provided to the operator remotely and thus the field crew focuses directly on the faulted section [11], [12]. The challenge with this method is the cost of FPIs and the required communication infrastructure which reduce the applicability of this solution from a cost benefit analysis perspective [12], [13], [14].

This kind of approach requires optimal grid monitoring and control which in this case can be reached when exploiting the maximum benefit from smart secondary (MV/LV) substations. The smart MV/LV concept is highly related to the presence of Ring Main Units (RMUs) equipped with Remote Terminal Units (RTUs) which can be operated remotely and effectively isolate the MV faulted section as well as restore the healthy part of the network [15].

During the last ten years, secondary substations have started to being upgraded with new functionalities, including LV measurement to monitor the power flow in LV networks which is changing due to the vast penetration of Renewable Energy Sources (RES) in the distribution networks [16].

Considering the present trend of growing penetration of RES, which is driven by the carbon reductions objectives and the net zero target by 2050 [17], it is expected that the instrumentation in secondary substations and in LV networks will continue to grow. This is confirmed by several studies conducted by DNOs, industry and academia in UK, which have demonstrated the applicability and cost benefits of LV instrumentation [18–24].

1.2 Research motivation

The future availability of LV monitoring data will create a number of opportunities for applications leveraging the extracted information, which are today not financially viable due to the high implementation cost of a complete system for measurement and collection of data [25].

Power systems reliability is dependent on the issues of service interruption and power supply loss, usually caused by electrical faults [26]. Independent regulatory au-

thorities set objectives regarding utilities' performance as well as deterrents to reduce the duration and frequency of outages. Consequently, among the various socioeconomic effects, power interruptions affect utilities' financial performance [27]. Figure 1.2 gives an overview of the financial rewards and penalties as derived from the Annual Interruption Incentive Scheme (IIS) for the year 2018/2019, based on the CI/CML performance of the DNOs group. Therefore, locating faults in an automatic and cost effective way is of major importance for electric utilities which aim to mitigate the long outages and thus achieve their reliability objectives.

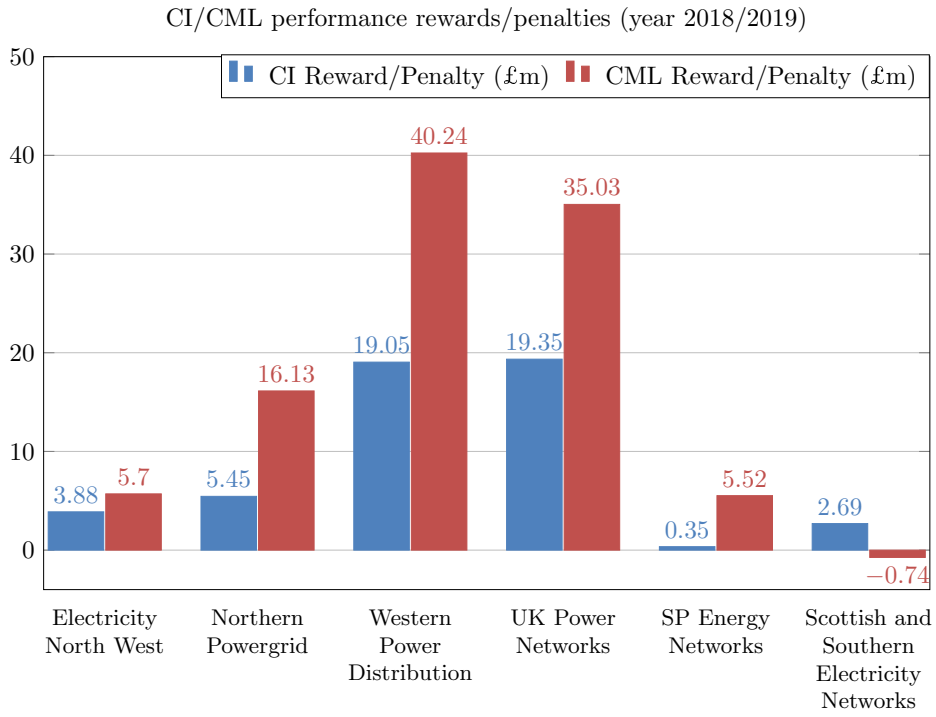

Figure 1.2: 2018/2019 penalties/rewards based on CI/CML performance by DNO group during unplanned interruptions [6].

Knowing that almost 90% of failures occur in the distribution systems [26] and more than half of them on the MV grid [5], special focus has been dedicated to this part of the network by both industry and academia. However, pre-locating the section of the faulted cable/line as well as pinpointing the fault has been proven a challenging exercise in MV distribution networks due to the broad topography of modern distribution

systems, the numerous laterals, the phase unbalance and the connected DGs [8], [9].

Traditional MV faulted section location methods include practices such as "sectionalizing" and DC thumping [9], [10]. Such techniques require switching surges on the faulted feeder often resulting to even further damage of the utilities' equipment (i.e. insulation degradation). According to [28] the investment cost of a pad mounted sectionalizing switch is 20,337 United States Dollars (USD) and this of a pole top gang operated switch is 4,700 USD. In addition to the high cost, sectionalizing is considered very time consuming, therefore leading to long outages [8].

Moreover, FPIs have been used for many years by utilities contributing to prelocating the section of the conductor with the fault. According to [29], the cost of FPIs ranges from 30 USD per phase for manual reset devices used in troubleshooting, to several hundred dollars for devices that communicate status and monitoring data via radio. The installation and maintenance cost is added to the required man-hours for the visual inspection of the devices [8].

Eventually, traditional methods demand investment for infrastructure which will be explicitly dedicated to FS location. Leveraging distributed LV monitoring technology can significantly drop the deployment cost of new FS location techniques which are based on data analysis and at the same time will enable the integration of various smart functions to the same infrastructure [9, 30, 31].

1.3 Research methodology

The research presented in this thesis has been undertaken in the following stages.

Firstly, a comprehensive literature review of existing and proposed fault location techniques in the field of traditional and modern distribution networks has been performed, to identify limitations, advantages and technical requirements of these techniques, and research gaps.

Based on the identified research gaps, the potential merits arising from the utilisation of LV monitoring and available signal processing methods a novel FS location solution has been investigated. The technique focuses on unbalanced faults which,

according to Table B.4, occur with a probability of 98% in electrical networks. In particular, a data driven study has been performed to characterise the voltage profile at the LV side of secondary substations during asymmetrical 11 kV faults and investigate potential LV trends aiming to the localisation of the MV FS.

The observations derived from the data driven study were used as an input for the development of an MV FS algorithm which involved signal analysis techniques belonging to Wavelet transform group and Fast Fourier Transformation (FFT). The algorithm was developed with the aid of MATLAB programming language and is completely novel.

The performance of the proposed solution has been initially validated by simulation based analysis where a wide range of network scenarios are investigated. This exercise was performed in DigSILENT PowerFactory which is a powerful power systems simulation package widely used by electric utilities industry.

Throughout this study, multiple configurations have been utilised including radial and ring topologies. Additionally, load unbalance during steady state conditions is examined due to the fact that the algorithm uses sequence components as the main input.

Finally, the study assesses the impact of inverter based and synchronous DGs on the effectiveness of the proposed algorithm. Special focus has been put to the behaviour of PV inverter based generation connected at the LV side of the network during faults. Testing realised in laboratory environment evaluated the performance of various small scale inverters under fault conditions.

Further testing observations enabled the detailed modelling of the Fault Ride Through (FRT) strategy of one of the inverters under test. The model was created in MATLAB Simulink and implemented in this study to achieve the representation of realistic DERs response and extend the evaluation of the faulted section technique.

The developed FS location technique is also validated via a hardware level study. This was achieved at the facilities of PNDC, a research and demonstration centre owned by the University of Strathclyde. The centre has interconnected 11 kV and 400 V networks and can be configured in both radial and ring topologies, with a capability of emulating 11 kV distribution lines of up to 60 km in length. Moreover, it comprises

of pole- and ground-mounted step-down transformers and substations with associated protection and control equipment. The LV network can be loaded using a variety of programmable load banks, and provides points for connections of devices under test. In addition, an industry-standard supervisory control and data acquisition (SCADA) system is available to effectively monitor and control the network and the MV fault thrower for applying resistive faults at various locations across the network [32].

Therefore, the PNDC MV/LV network provided the proper ground to apply real 11 kV faults and test the FS algorithm under realistic fault conditions. Distributed monitoring devices were installed at the LV side of several step-down transformers connected across the MV network. The captured voltage measurements were extracted from the measuring devices and the data were processed offline for the validation of the algorithm. Additional assessment was pursued to demonstrate the feasibility of the generated FS location scheme by considering the impact of noise interference, loss of communications and variation of the time window length.

1.4 Research contribution

The main research contributions of the research undertaken and presented in this thesis can be summarised as:

- Development of a novel MV faulted section location technique explicitly focusing on asymmetrical faults. The proposed method relies exclusively on voltage measurements captured by distributed monitoring devices, installed at the LV side of step-down transformers across the network. The implementation of LV monitoring technology allows reduction in deployment cost in comparison with this of associated MV infrastructure. Moreover, the algorithm is based on measurements obtained from secondary substations, which constitute a strategic point of the active distribution networks. This feature allows for integration of the algorithm in multi-function platforms, thus further enhancing their efficiency and value. This contrasts with existing techniques (i.e. FPIs), which require infrastructure exclusively dedicated to MV faulted section location. Furthermore, compared to

knowledge based methods, the developed technique does not require training. It can be applied in all type of distribution network topologies, such as radial and ring including the connection of MV laterals and DGs.

- As part of the algorithm, a methodology aiming the fault period discrimination for each of the distributed LV voltage measurements has also been developed. Discrete Wavelet Transform is implemented to capture the instance of fault initiation and a near-zero threshold of the voltage magnitude is used to identify the fault clearance. This is a powerful tool of the algorithm as it cancels the requirement of GPS implementation for monitoring synchronisation.

- Demonstration of algorithm feasibility in software simulations conducted in DigSILENT PowerFactory and MATLAB Simulink. The developed technique has been evaluated under a number of distribution network scenarios.

  In particular, the proposed method was able to delimit the MV faulted section with success rate of 99.07% under the following simulated conditions:

  - Injection of various asymmetrical fault types and fault resistances. Specifically, solid as well as resistive phase to earth and phase to phase faults, of 20 Ω and 60 Ω respectively, were implemented throughout simulations.
  - Application of selected fault conditions in radial, ring and multi-branch system configurations
  - Application of unbalanced load conditions at the LV side of the several MV/LV transformers
  - Connection of multiple DGs including PVs and synchronous generation connected at both MV and LV part of the network.
  - Representation of an active distribution network dominated by LV connected PV generation, with a percentage of 85.3% in relation to maximum load. This exercise deployed a dynamic model emulating a commercially available inverter, which was developed and validated against hardware testing observations.

- Demonstration of practical feasibility in both software and hardware level implementation via the use of the extracted simulation data as well as the real LV data from PNDC LV network.

  Specifically, the developed algorithm has been proven robust with 100% of success rate when assessed in the real 11 kV network of PNDC under:

  - Real asymmetrical resistive faults of different types (i.e. 20 Ω phase to earth and 60 Ω phase to phase faults).
  - Injection of selected fault conditions in the real 11 kV network of both ring and radial configurations.

  Same rate of success (100%) was reported when the technique processed the simulation data under the following conditions:

  - The algorithm operated accurately when processing data with random noise interference of ± 5%.
  - Assumption of loss of communications. The algorithm identified the correct faulted section even if the measurements from one monitoring point were missing.
  - Variation of discriminated fault period time window length. The algorithm remained accurate when the fault time window was reduced to 25%.

1.5 Thesis overview

An outline of the work contained within this thesis is presented below:

Chapter 2 presents the state of the art related to fault location in distribution networks. An overview has been provided in both conventional and modern techniques. These are based on fundamental frequency components (voltage, current), travelling waves theory, time domain reflectometry, fault passage indication, and knowledge-based approaches. Throughout this survey, the essential requirements, benefits and limitations of these techniques have been summarised.

Chapter 3 proposes a novel method which solves the problem of faulted section localization in MV distribution networks when an asymmetrical fault occurs. First it presents the results of a data driven study to explore potential trends when asymmetrical faults occur. Measurements such as voltage magnitude, angle, positive and negative sequence components are captured across a simplistic emulated distribution network while applying fault conditions. The outcome of this study in conjunction with the theoretical background provided demonstrates that the combination of LV positive and negative sequence components can effectively indicate the MV faulted section. Moreover, the architecture of the proposed algorithm is analytically explained including the fault period discrimination technique as well as the identification of the MV faulted section.

Chapter 4 presents the modelling methodology. Initially, 'base' models are utilised representing the PNDC network. Emulating the PNDC network will facilitate the validation of the technique throughout a hardware level study - described in Chapter 6. Furthermore, various distribution network concepts and conditions are implemented to extend the assessment of the faulted section location method. Radial and ring topologies, MV lateral connection, pre-fault unbalance conditions, and the presence of DGs are the simulation cases investigated. Special focus has been added on the effect of inverter connected DER, as for example PV generation.

Chapter 5 presents the analysis of the simulation results, discussing several scenarios in order to demonstrate the accuracy of the faulted section location algorithm. The chapter contains the outcome out of the study performed in both 'base' and 'expanded' models. The later were used to showcase the effect of MV laterals, the impact of unbalanced loads as well as the presence of DGs. In addition, the chapter demonstrates the performance of the realistic dynamic PV inverter model built for the purposes of this study as well as its influence on the proposed fault location technique.

Chapter 6 focuses on the validation and scrutiny of the algorithm's performance under a number of implementation challenges and realistic conditions. Physical testing is conducted in the MV/LV network of the PNDC enabling the injection of a number of faults in both radial and ring topologies. The testing procedure, setup and the

monitoring technology are described in detail. Moreover, data extracted from the simulations study are exploited to apply additional realistic conditions and stretch the algorithm's validation activity. Particularly, the effectiveness of the proposed faulted section location technique is evaluated under the effect of random noise interference, loss of communications and the impact of varying the measurements time window length.

Chapter 7 concludes the thesis by summarizing and highlighting the key outcomes and contributions resulting from this work. Potential avenues for future research in this area are also suggested.

1.6 Publications arising from this research

- P. Bountouris, H. Guo, I. Abdulhadi, F. Coffele, "Medium voltage fault location using distributed LV measurements", presented at 14th IET DPSP, Belfast 2018
- P. Bountouris, I. Abdulhadi, A. Dysko, F. Coffele, "Characterising grid connection stability of low voltage PV inverters through real-time hardware testing", presented at 25th IET CIRED, Madrid 2019
- P. Bountouris, H. Guo, D. Tzelepis, I. Abdulhadi, F. Coffele, C. Booth, "MV faulted section location in distribution systems based on unsynchronized LV measurements", *International Journal of Electrical Power & Energy Systems*, DOI: https://doi.org/10.1016/j.ijepes.2020.105882, March 2020
- P. Bountouris, I. Abdulhadi, F. Coffele, "Dynamic Model of Commercially Available Inverters with Validation Against Hardware Testing", *IEEE Transactions on Power Systems*, DOI: https://doi.org/10.1109/TPWRS.2022.3179667, 2022

1.7 References

[1] Yves Chollot, Jean-Marc Biasse, and Alain Malot, "Improving MV Network Efficiency with Feeder Automation," June 2011.

[2] H. Abunima, J. Teh, C.-M. Lai, and H. J. Jabir, "A systematic review of reliability studies on composite power systems: A coherent taxonomy motivations, open chal-

lenges, recommendations, and new research directions," *Energies*, vol. 11, no. 9, 2018.

[3] G. C. F. P. J. Taylor, S. Jupe, "Assessing the impact of ICT on the reliability of active distribution systems," pp. 1370–1370, 01 2013.

[4] C. P. SERIES, "Analysis of distribution system reliability and outage rates," *Reclosers Technical Data TD280026EN*, July 2017.

[5] Utility Regulator, "Annex M - Reliability incentive," June 2017.

[6] Utility Regulator, "RIIO-ED1 Annual Report 2018-19," Feb. 2020.

[7] Y. G. Paithankar and S. R. Bhide, "Fundamentals of Power System Protection," 2011.

[8] "IEEE Guide for fault locating techniques on shielded power cable systems," *IEEE Std 1234-2007*, pp. 1–34, 2007.

[9] "IEEE Guide for determining fault location on ac transmission and distribution lines," *IEEE Std C37.114-2014 (Revision of IEEE Std C37.114-2004)*, pp. 1–76, 2015.

[10] Megger, "Fault finding solutions." https://electrical-engineering-portal.com/res/Megger-Book-Fault-Finding-Solutions.pdf.

[11] E. Bjerkan, "Efficient fault management using remote fault indicators," in *CIRED 2009 - The 20th International Conference and Exhibition on Electricity Distribution - Part 2*, pp. 1–25, 2009.

[12] J. Duller, A. Halim, G. Paton, B. Traill, and S. Sparling, "Next-generation adaptive network restoration on distribution feeders," *CIRED - Open Access Proceedings Journal*, vol. 2017, no. 1, pp. 1334–1337, 2017.

[13] M. Kezunovic, "Smart fault location for smart grids," *IEEE Transactions on Smart Grid*, vol. 2, pp. 11–22, March 2011.

[14] E. Bjerkan, "Efficient fault management using remote fault indicators," pp. 1 – 4, 07 2009.

[15] R. Yves Chollot and Laurent Guise, "Transitioning to smart MV/LV substations as the cornerstone of your smart grid."

[16] T. Yang, "10 - ICT technologies standards and protocols for active distribution network," in *Smart Power Distribution Systems* (Q. Yang, T. Yang, and W. Li, eds.), pp. 205–230, Academic Press, 2019.

[17] C. on Climate Change, "Net Zero – the UK's contribution to stopping global warming."

[18] M. Lees, "Customer-led network revolution - Enhanced network monitoring report," Dec. 2014.

[19] M. Dale, "LV network templates for a low-carbon future: Close down report," June 2013.

[20] Gideon Evans and David MacLeman, "LCNF Tier 1 Close-down report - Demonstrating the benefits of monitoring LV networks with embedded PV panels and EV charging point," 2013.

[21] G. Murphy, "Ashton Hayes smart village - Close down report."

[22] "Low voltage network solutions - Closedown report," June 2014.

[23] "Networks for a low carbon community - LCN fund TIER 1 close down report," Dec. 2013.

[24] B. Godfrey, "Network management on the Isles of Scilly closedown report," Dec. 2016.

[25] E. D. S. O. for Smart Grids, "Minimum functional requirements for Smart Secondary Substations Lite."

[26] R. Medjoudj, H. Bediaf, and D. Aissani, "Power system reliability: Mathematical models and applications," in *System Reliability* (C. Volosencu, ed.), ch. 15, Rijeka: IntechOpen, 2017.

[27] D. Business, "Getting electricity: Factors affecting the reliability of electricity supply," 2017.

[28] R. Billinton and S. Jonnavithula, "Optimal switching device placement in radial distribution systems," *IEEE Transactions on Power Delivery*, vol. 11, no. 3, pp. 1646–1651, 1996.

[29] S. E. Laboratories, "Fault Indicators for the safe, reliable, and economical operation of modern power systems," 2010.

[30] P. Bountouris, H. Guo, D. Tzelepis, I. Abdulhadi, F. Coffele, and C. Booth, "MV faulted section location in distribution systems based on unsynchronized LV measurements," *International Journal of Electrical Power & Energy Systems*, vol. 119, p. 105882, 2020.

[31] A. Angioni, S. Lu, H. Hooshyar, I. Cairo, S. Repo, F. Ponci, D. Della Giustina, A. Kulmala, A. Dedè, A. Monti, G. Del Rosario, L. Vanfretti, and C. C. Garcia, "A distributed automation architecture for distribution networks, from design to implementation," *Sustainable Energy, Grids and Networks*, vol. 15, pp. 3–13, 2018. Technologies and Methodologies in Modern Distribution Grid Automation.

[32] C. D. Booth, F. Coffele, and G. M. Burt, "The power networks demonstration centre: An environment for accelerated testing, demonstration and validation of existing and novel protection and automation systems," in *12th IET International Conference on Developments in Power System Protection (DPSP 2014)*, pp. 1–6, 2014.

Chapter 2

A review of fault location methods in distribution networks

2.1 Chapter overview

This chapter presents a thorough literature review of conventional and modern fault location and faulted section location methods in distribution networks. Faulted section location methods identify a cable or overhead line section where a fault has occurred, while fault location techniques determine the precise location of a fault. Section 2.7 presents a comparison of the reviewed techniques with regards to the requirements, advantages and disadvantages. This chapter also summarises how the research reported in this thesis makes specific contributions to the identified disadvantages and shortcomings in the reviewed methods.

2.2 Background

Minimising the impact of faults on users, expressed by CML and CI indices, is a major objective for DNOs when designing and operating their distribution networks. Fig. 2.1 illustrates an example MV network with typical protection, such as breakers, fuses and re-closer, where a permanent fault has occurred. The re-closer has detected the fault and divided the network into two sections. The section upstream of the re-closer

remains connected so as to maintain power supply continuity to a part of the consumers. The rest of the customers will remain disconnected until the faulted section is located and isolated.

Therefore, post-detection fault management including FLISR constitutes an important procedure for DNOs. In particular, accurate and fast location of the MV faulted section can have a significant impact on the power supply recovery time and thus the reliability of the distribution network.

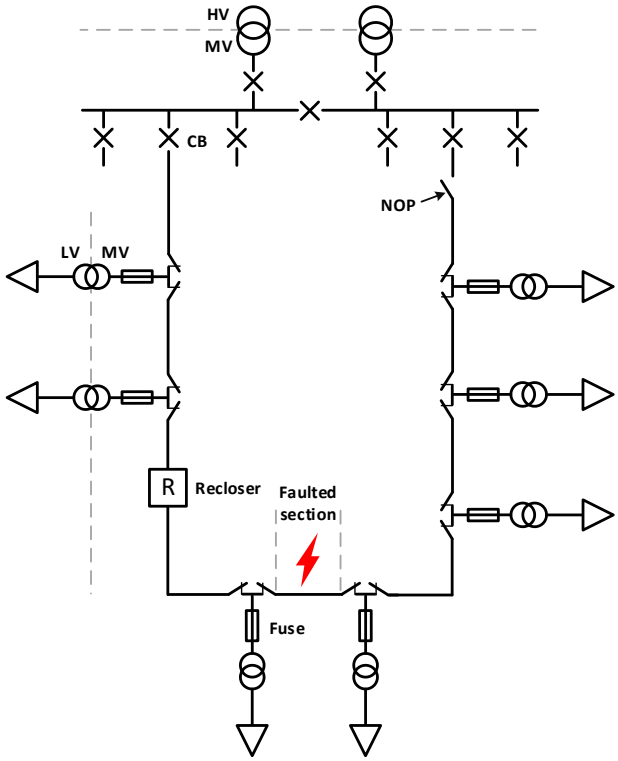

Figure 2.1: MV network with recloser for protection against transient and permanent faults.

Over the years, academia and industry have developed a number of fault location methods based on technologies such as Time Domain Reflectometry (TDR), Impedance Measurements (IM), FPI, Travelling Waves (TW), etc. to achieve the above goal. The different fault location techniques can be grouped in four main categories:

- Conventional methods

- Impedance-based methods
- Travelling wave-based methods
- Knowledge-based methods

2.3 Conventional methods

Prior to the development of automated fault location techniques, distribution network operators followed conventional practices to localise faults. Customers' complaints have been the most typical way of finding faults, leading the maintenance team to the associated area where the faults are identified via visual inspection. This approach is taken when the fault has occurred on overhead lines and the damage is visible.

Nowadays, equipment like FPIs are deployed in modern distribution networks (on both MV overhead lines and underground cables) to facilitate the aforementioned procedure by decreasing the search area and time. FPIs can be pole mounted or clipped on the MV overhead lines, installed at appropriate locations across the distribution network.

FPIs are distinguished in two major categories. The operation of the first type of FPIs depends on the detection of induced magnetic field and provides a visual indication when a predetermined magnetic flux threshold is exceeded [1]. The second category of FPIs is based on current measurements acquired with the aid of current sensors which are mounted on the phase and/or neutral conductors. They can detect phase fault and earth fault currents based on the set current threshold [2]. FPIs can provide local or remote readings in the event of a short circuit current passing through the conductors. Therefore, physical inspection is usually required by the maintenance personnel to check the alarm signal.

Alternatively, remote indication could be applied by transmitting a signal to the control centre although this could be an expensive solution since communication link should be deployed [3, 4]. Finally, in case of DGs are connected in the network, directional FPIs could be implemented, although this technology would also increase the cost as voltage and current measurements are required [3–5]. Fig. 2.2 shows an example

of MV faulted section location and restoration by combining FPIs and RMUs in a real distribution network [5].

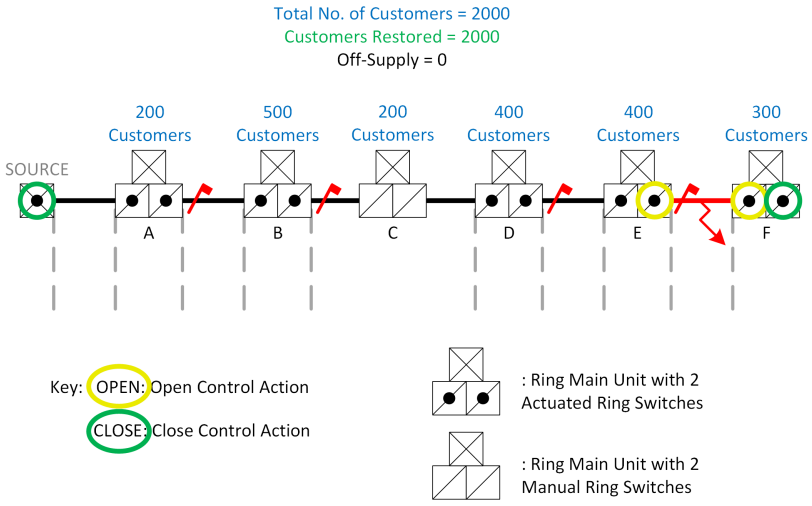

Figure 2.2: Automatic restoration example combining RMUs and FPIs - UKPN MV distribution network [6].

In contrast with faults on overhead lines, faults on underground cables are not visible. Therefore, a number of methods such as sectionalizing, TDR, cable thumping and others have been applied over the years to pinpoint the exact fault location [7].

A sectionalising method called "cut and try" has been used by utilities for fault localisation purposes. This approach involves actual cutting of cable sections and testing them separately with the aid of DC hipot. The latter is a DC high-potential test which assesses the dielectric withstand of the MV cable. This procedure is repeated until the faulted section is identified and replaced. This method has been proved very crude, costly and destructive, so it is rarely implemented nowadays [7–9]. Fig. 2.3 illustrates a "cut and try" case, indicating the cable sections which according to the technique need to be tested after a fault has occurred across the cable.

Another similar method named "sectionalising by re-fusing" has also been deployed by DNOs, mainly for fault location on Underground Residential Distribution (URD) loops. Sections of the cable loop are isolated and then the first section is energised by manually closing the corresponding primary fuse mechanism. If the fuse melts, the procedure is repeated with the next fuse until the faulted section is identified

and isolated. Throughout the application of this fault location method, a phase to earth voltage is applied on the isolated section of the cable loop, frequently resulting in damage to the utility's equipment (i.e. fuses, cables, bushings, splices) due to the imposed switching surges and fault currents [7].

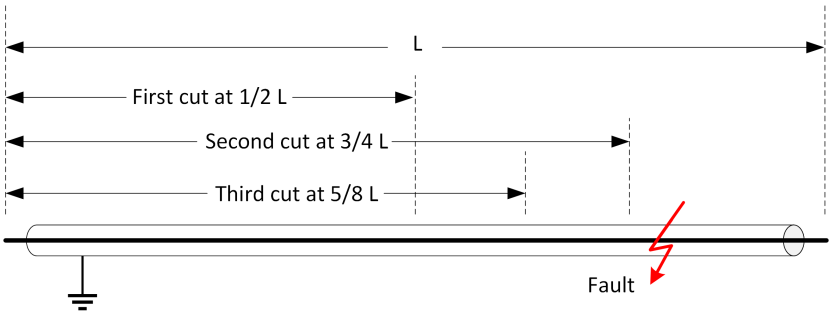

Figure 2.3: Fault location sectionalizing method: "cut and try".

TDR is an underground cable fault locating method, widely used in power distribution networks. The TDR is based on the propagation of a short time duration pulse into the cable under test. The pulse is injected between the phase conductor and shield (neutral) and then reflected back after it reached a point where the cable's impedance characteristic is changed [10]. The captured time (t) and propagation velocity (v) of the pulse can be effectively used to calculate the distance (l) aiding the user to quantify the impedance change or failure present in the cable [11]. The calculation of the exact distance of the pulse's reflection is given by equation 2.1:

$$l = \frac{v * t}{2} \tag{2.1}$$

The equivalent electrical circuit depicted in Fig. 2.4, describes how the TDR interprets each cable segment – i.e per one foot length. The arrangement of the illustrated passive components, including the combined inductance (L), series resistance (R_s), capacitance (C) and parallel resistance (R_p) as shown in Fig. 2.4, refer to the characteristic impedance (Z_0) of the cable. Therefore, the ideal cable, consisting of cable segments of equal passive components values, would generate reflections only at its terminal. Consequently, any damage to the cable would change its characteristic impedance in an intermediate point.

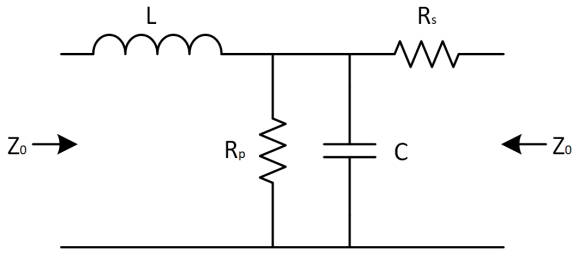

Figure 2.4: Cable Incremental Equivalent Circuit [12].

The calculation of the reflection coefficient showed in equation 2.2 provides the magnitudes of the pulse reflections, where r is the reflection coefficient, Z is the cable's impedance deviation value (caused by fault), and finally Z_0 is the cable's characteristic impedance:

$$r = \frac{Z - Z_0}{Z + Z_0} \tag{2.2}$$

Normally, the propagation time of the pulse is measured by the TDR instrument, so the length of the cable can be calculated when the pulse's velocity is known. The propagation velocity is affected by factors like the condition of the insulation between the two conductors or the cable condition (i.e. corrosion, water ingress), so default values (shown in Table 2.1) can be used, in case the velocity of the travelling pulse is not known [11].

Table 2.1: Typical propagation velocities

Type of Cable	**Typical Propagation Velocity**
XLPE	82 – 86 m/μs (269 – 282 ft/μs)
PILC	77 – 82 m/μs (253 – 269 ft/μs)
Hybrid	83 m/μs (272 ft/μs)
Overhead wire	148 m/μs (485 ft/μs)
Telecommunication	95 – 120 m/μs (312 – 394 ft/μs)

At a preliminary stage, fault classification, in terms of fault type and resistance needs to be done. This type of information determines the appropriate technique and thus equipment required to achieve accurate fault diagnosis. TDR would be ideal for fault resistances below 100 Ω and fault types such as open circuits and conductor-to-

conductor short circuits. However, faults on primary underground distribution cables are mainly highly resistive (kΩs – MΩs). In case of high fault resistance, above 200 Ω, an impulse/surge generator is required for accurate location [10, 13].

The technique involving a surge generator or "thumper" in parallel with the use of a TDR, is defined as arc reflection. The surge generator comprises of a dc power supply, a high voltage capacitor and a high voltage switch. The purpose of the power supply is to charge the capacitor at high voltage level and then the HV switch to close, discharging the capacitor into the connected cable. By this way, an arc appears at the fault location dropping the fault resistance to low levels (below 200 Ω). This phenomenon, creates suitable conditions for the pulse, which is injected by the TDR, to be reflected back (Fig. 2.5). The LV TDR can be connected to the cable under test along with the HV surge generator securely, due to the presence of an arc reflection filter. This piece of equipment protects the TDR from the surge generator HV pulses, so the former to be looking down the cable while "thumping" [10].

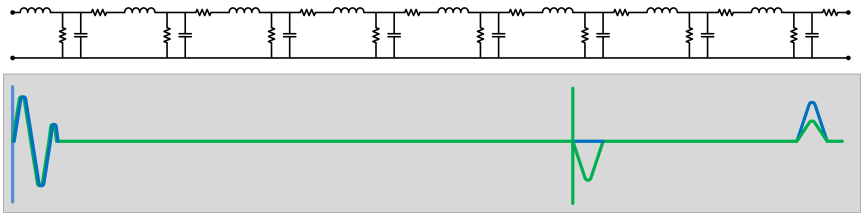

Figure 2.5: Equivalent circuit, TDR traces showing fault location [10].

It can be realised that, the conventional methods described in this section can be time consuming and frequently apply stress to the network equipment. Therefore, by eliminating re-closing, re-fusing, and unnecessary or excessive thumping, cost savings can be achieved due to reduced stress on service-aged cable insulation, cable accessories, transformers, and customer and utility equipment. In this sense, numerous automated techniques have been proposed to facilitate the fault location and faulted section location process in distribution systems.

2.4 Impedance-Based Fault Location Methods

The IM methods belong to the family of techniques using the fundamental harmonic voltage and current measurements. They are one of the most commonly assessed techniques as they have the least requirements for measurements. There are two broad impedance-based fault location methods categories; the one-ended [14–16] and the multi-ended methods [17, 18] depending on the number of nodes deployed for capturing measurements. One-ended measurements based techniques [19–22] are the most common, well-known as apparent impedance methods and require only a voltage and current measurement. On the contrary, two-end (or multi-end) techniques [23, 24] use multiple measurement points (nodes), processing the variances between them appropriately to locate the fault.

2.4.1 One-End Methods

One-end impedance based methods are dependent on voltage and current measurements captured at just one node.

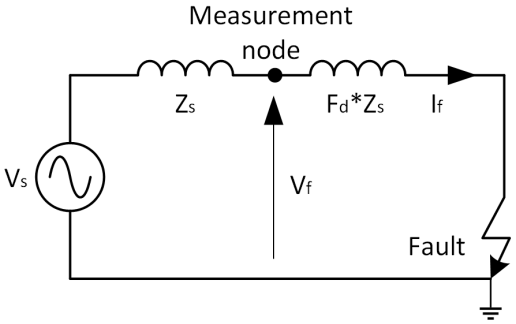

Figure 2.6: Simplified line model for general one-end methods.

Fig. 2.6 shows a simplified line model for a one-end method. V_f and I_f represent the voltage and current under fault conditions. The line impedance per unit length is defined as Z_l, while the fault distance from the measuring point is the f_d. Vs is the source voltage and Z_s is the source impedance. The fault distance can be found by using the following equation:

$$f_d = \frac{V_f}{I_f * Z_l} \tag{2.3}$$

Although a simplified measurement infrastructure is required, the technique presents a few major disadvantages. According to [25], one of the main drawbacks is the multiple fault location estimation problem. In this case, the calculated fault, (f_d corresponds to multiple network points found on different branches. The combination of this type of fault location methods with additional instrumentation [26, 27], or a complementary analysis of monitoring information (e.g., voltage sag, currents fluctuation, etc.) usually provides a solution for this problem. Also, the dependence of these techniques on the fault resistance (R_f) increases the possibility of a fault location error, especially when the resistance is not small. Moreover, one of the most significant weaknesses of the one-end approach comes up when DGs are connected in the network. This is explained by the fact that measurements recorded at only one node are not adequate to characterise a fault model based on impedance, while energy is injected from more than one network points. Under these circumstances, the estimation of the equivalent impedance at one point would probably be misleading.

Several approaches can be found in literature considering different parameters as fault types, fault resistances, network loading and configuration. An impedance based fault location technique is described in [16], using modal transformation of voltage and current values captured at one-end substation. Although network configuration modifications, non-homogenous network sections and unbalanced loading do not affect the proposed method, the latter applies only on radial distribution networks and does not take into account the presence of DGs and bi-directional power flow. The authors in [14] propose a technique which exploits the voltage and current measurements acquired at the primary substation and at substations where DG is connected to locate faults in a radial distribution network. The fact that only two DGs connected at specific nodes of the network have been considered makes the robustness of the method questionable, especially in active distribution networks dominated by DGs.

2.4.2 Multi-End Methods

The two or multi-end impedance based measurement methods implement voltage and current measurements captured at multiple points. The use of multiple monitoring points makes the multi-end fault location philosophy compatible with DG scenarios and bi-directional flows. This compatibility is accomplished by modelling the impedance of line segments, removing the potential power sources outside of it. Seemingly, the effective operation of the multi-end approach necessitates one measurement point at each generation or consumption spot. In contrast with the one-end philosophy, this method prevents the multiple position estimation, taking into account the input and output points affected.

However, the aforementioned characteristics make multi-end methods a better solution than one-end, the main drawback is the deployment cost. The implementation of such a technique requires the use of multiple voltage and current sensors strictly time synchronised to provide measurements with high level of consistency. Moreover, measurement errors and loss of synchronisation can make the accuracy of these techniques very poor, especially in short lines or cable sections [28]. In addition, the use of communication links for the transmission of measured voltage and current data to a control centre would inevitably increase the technique's implementation cost.

The technique presented in [17] involves the examination of three-phase fundamental frequency components in a two terminals network. Moreover, a procedure is proposed to process measurements from lines with more terminals, locating the faulted section. One of the technique's benefits is that it is not dependent on the type of fault. However, the required synchronisation of the measurements across the various terminals with the aid of GPS increases the deployment cost. The study conducted in [29] introduced another fault type independent technique comprising of two general fault location methods, using power system parameters acquired at the main power substation and at the end node. The technique uses a data mining associated method for faulted section identification and a model-based method to calculate the distance between the faulted point and the main substation. This fault location technique performs effectively providing errors lower than 0.15%, but its operation is limited only to radial networks. A

different impedance based method [18] estimates the fault distance implementing high frequency transients produced by the fault. The function depends on phasors rather than sequence components analysis to quantify the potential asymmetry in a distribution system. On the other hand, a double ended fault location method introduced in [30] analyses individually all positive, negative and zero sequence components (voltages and currents). The implementation of all the three components provided high level of accuracy and the author highlights that none of them should be ignored.

2.5 Travelling waves

The content of this section provides information with regards to the estimation of the distance of a fault from a particular measurement point with the aid of TW. This approach exploits the phenomenon of high frequency waves generated when a fault occurs on a power system network. The major characteristic of the TW based methods is the processing of the propagation time of fault effects [31]. These waves propagate at near speed of light velocities towards both directions from the fault location. After arriving at the line terminals they are reflected back to the fault point and repeatedly back to the line ends. The detection of these impulses as well as the estimation of the propagation time can lead to accurate fault location if the propagation velocity and the length of the line are known.

Based on the above principles, extensive research has been conducted with regards to the distribution level applicability of travelling waves for fault location applications. Similar to the transmission networks, one-end [32] and multi-end [33, 34] travelling waves techniques are developed processing the wave reflections and arriving time accordingly. In the single ended method [35], the travel time between the two first reflections is implemented to calculate the distance from the measuring point at the line end to the fault. Anticipated challenges on detection of the second reflection of the wave could lead to unreliable operation of the single-end technique, especially for distribution networks. The double ended method takes advantage of the transient wave reflected to each of the two line ends at different times. The distance of each line end

from the fault is estimated with the aid of the measured time difference. Although the high accuracy of the double ended method, the necessary expensive communication infrastructure and a very accurate GPS clock ensuring time synchronisation, make the single ended method a more applicable technique mainly due to economical reasons.

Travelling waves based fault location techniques can be accurate and fast when implemented in transmission system. However, successful implementation of TWs in distribution networks is not practical nor cost-effective. The technique requires very high sampling rates (MHz – GHz) in order to process fast transients. Also, the increased waves reflections and attenuation caused by loading taps and lateral connections as well as the very short time resolution required due to the short cable length in distribution networks will inevitably have adverse impact to the accuracy of the method. Therefore, the TW based fault location techniques in distribution systems can be very complex, inaccurate and cost intensive.

2.6 Knowledge-based methods

Knowledge-based techniques are used to overcome the uncertainty of unknown parameters (i.e. fault resistance) which challenge the precision levels of fault location methods using fundamental (impedance measurements) and high frequency (travelling waves) components. These methods can be based on neural networks, fuzzy logic or genetic algorithms.

2.6.1 Artificial Neural Network

Artificial Neural Network (ANN) is an intelligent technique that can be implemented for locating faults in distribution systems. The particular method is able to distinguish complex patterns of information leading to accurate fault location. The basic requirement of this technique in order to provide satisfactory results is a training process using a group of data as an input and the expected outcome. An example of a generic ANN concept is depicted in Fig. 2.7. In this case, the training input data comprises of the parameters V and ϕ, referring to a particular point's voltage magnitude and angle

measurements respectively. The target output is the identified fault location. An ANN method involving the standard back propagation approach [36] was developed by the authors in [37] aiming accurate fault location in a distribution network with DGs. The technique performs training with the aid of current samples acquired from the output of each DG during a fault event. The precision of the method is inevitably highly dependant on the amount of DGs connected in the system. A feed-forward ANN fault location and classification algorithm is presented in [38]. The latter uses both current and voltage measurements to locate the fault. The algorithm provided satisfactory results (maximum percentage error 3%) when assessed under several fault scenarios. The method requires off-line training with data reflecting any network alterations occurred, including local demographic data or daily basis demand and generation levels. It is therefore inferred that, ANN fault location methods cannot be generally applicable in distribution networks which dynamically change configurations and fault levels.

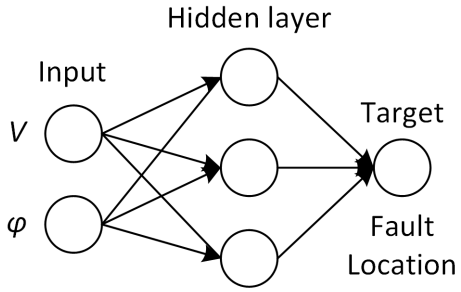

Figure 2.7: Example ANN.

2.6.2 Support Vector Machine

Support Vector Machine (SVM) is a knowledge-based method mainly used for regression and classification purposes [39]. In [40] authors use three-phase voltage and current measurements from all the DG connection points to perform fault diagnosis with the aid of SVM. The developed scheme can correctly provide information with regards to the fault type, faulted section location and fault impedance. As with [37] and the use of ANN, in [40] the accuracy of the suggested faulted section multi class classification SVM method is compromised from 100% to 92.06%, when the number of DGs taken

into account drops from 3 to 1. Finally, [41] combines both ANN and SVM methods for fault localization in distribution systems. Training of the two knowledge-based tools is accomplished by simulating various faults at each node of the configured network. The proposed method generates accurate fault location results although the ANN has to be retrained if the network topology is modified, which is a major disadvantage concerning the applicability of the technique in distribution networks.

2.6.3 Fuzzy logic

Fuzzy logic involves the concept of possibility - characterised by a number between one (possible) and zero (impossible) - instead of the concept of probability. With this method the uncertainty in decision making can be modelled and define the possibilities for a number of hypotheses based on experience. [42] presents a fault location technique based on fuzzy set theory, where the expert knowledge can be quantified by membership functions of fuzzy sets. The fault location is selected from the fuzzy set according to the grades of the membership of various hypotheses. The membership functions can be altered dynamically due to factors like weather conditions or different network topologies affecting eventually the decision making. Thus, fuzzy logic cannot be considered for implementation in distribution networks due to their dynamically varying parameters such as distributed generation and network topologies.

2.7 Technical benchmark

The aim of this section is to highlight the requirements, advantages and disadvantages of the reviewed faulted section location and fault location methods. Table 2.2 contains the mentioned characteristics of the existing techniques.

Table 2.2: Comparison of fault location methods in distribution systems

Method	Requirements	Advantages	Disadvantages
Faulted section location methods			

Continued on next page

Table 2.2 – *Continued from previous page*

Method	Requirements	Advantages	Disadvantages
FPIs	Detection of inducing magnetic field and/or overcurrent during faults. Visual inspection.	Relatively easy implementation.	Physical inspection. High cost if remote or directional indication needed.
Cable thumping	Portable high voltage surge generator. Personnel needs to track the thumping sound.	Relatively easy implementation. Reliable for open-circuits faults.	Time consuming. Not applicable for short-circuit faults. Only for underground cables. HV surges weaken the cables insulation.
Fault location methods			
TDR	A portable Time Domain Reflectometer.	No degradation to the cable insulation is caused due to the low energy signal. Reliable for open-circuit and conductor to conductor faults.	Approximate estimation of the fault location. Fault resistance and electrical noise compromise accuracy. Parallel implementation of cable thumping is often required.

Continued on next page

Table 2.2 – *Continued from previous page*

Method	Requirements	Advantages	Disadvantages
Impedance measurements	Voltage and current measurements at primary substation level. Network configuration, line and load data.	Relatively easy implementation.	***One-end***: Lower accuracy with multiple fault location estimations. Influenced by high DG connections. ***Multi-end***: High cost.
Travelling waves	Network topology. Communication infrastructure. HF-sampling rate.	Accurate operation and independent of network data. Immune to modelling errors.	Expensive high frequency measurement devices and equipment for pulse generation.
Knowledge based	Voltage and current measurements at secondary substation level. Network configuration, line and load data.	Limited online calculations. Fast execution. Ability to generalize.	Vulnerable to modelling errors. Extensive offline training and data are required.

Traditional methods can be time consuming or expose stress to utilities' equipment. Due to these limitations, various automated methods using SCADA and FPIs have been developed to address the problem of fault location.

As discussed in section 2.3, FPIs have been used for fault location in overhead lines and underground cables by many utilities around the world. Although they are fairly easy to install and implement, their main drawback is that they necessitate visual inspection and therefore patrolling by the maintenance crew. Smarter solutions such as

remote or directional fault passage indication would increase the implementation cost dramatically.

In underground network fault localisation techniques like sectionalizing by re-fusing and cable thumping often result in damage to the utility's equipment (i.e. fuses, cables) due to the imposed switching surges. Although cable thumping is a reliable and easy to apply method, it is only applicable for open circuit faults and not for those that do not arc-over (i.e. short circuit faults). On the other hand, TDR transmits a low energy signal to locate open-circuit faults as well as conductor to conductor shorts, avoiding degradation of the cable insulation. One disadvantage of the TDR is that it performs an approximate fault location estimation and cannot precisely pinpoint the exact fault location. Sometimes this is adequate and other times this can only enhance the precision of cable thumping. In addition TDR is unable to "see" high resistance ground faults (over 200 Ohms).

With regards to the automated fault location methods, the fundamental frequency measurements based techniques, discussed in section 2.4, necessitate complementary line, loads and network topology related information to the required voltage and current measurements. The main weakness of the one-end impedance-based algorithms is that they are prone to multiple estimations while the drawback of the multi-end ones is the high deployment cost. On the other hand, the TW-based fault location techniques provide higher fault localization accuracy compared to the fundamental frequency methods, however even more complex and expensive infrastructure is required.

Knowledge-based methods provide robust solutions in the domain of fault location in distribution networks, although their implementation demands a large amount of training data and a retraining subsequent when modification in power system topology is realised [3]. Consequently, knowledge-based methods are only applicable on the specific network configuration on which they have been set-up. More generic approaches, deploying signal analysis for fault locating methods, are thus more widely used in distribution networks.

2.8 Chapter summary

This chapter presents a comprehensive literature review of several fault location methods in distribution systems. Specifically, Sections 2.3 to 2.6 focus on the basic theory and associated assumptions of conventional techniques as well as travelling waves, impedance and knowledge based methods.

Section 2.7 summarises the advantages and limitations of all reviewed fault location methods. It is remarked that no single method is capable to overcome all the challenges since each of those is developed to suit specific problems and conditions depending on the complexity of network and the availability of dedicated infrastructure. Therefore, the development of a global solution addressing the various characteristics of distribution networks, such as the multilateral configurations or the continuous penetration of DGs in both MV and LV parts, in a cost effective manner is considered critical in this thesis.

The proposed technique belongs to the family of faulted section location methods and provides solution to the problem of localising asymmetrical faults at the MV part of the distribution networks while merely relying on LV sensing devices. Therefore, the deployment cost is kept in lower levels compared to the techniques requiring expensive MV monitoring equipment. In parallel, the fact that the algorithm depends on measurements acquired from a strategic point of the active distribution networks makes it possible to be integrated in multi-function platforms further enhancing their efficiency and value. This contrasts with the FPI technology which requires infrastructure exclusively dedicated to fault location. Moreover, in comparison with the knowledge based methods, the proposed technique does not require training and can be applied in all type of distribution network topologies, such as radial and ring including the connection of MV laterals and DGs.

2.9 References

[1] T. Instruments, "Fault Monitoring for Overhead Fault Indicators Using Ultra-Low-Power Reference Design." https://cutt.ly/v1JS024. Accessed: 3-Dec-2022.

[2] SIEMENS, "SICAM FPI." https://cutt.ly/V1JP5fE. Accessed: 3-Dec-2022.

[3] M. Kezunovic, "Smart fault location for smart grids," *IEEE Transactions on Smart Grid*, vol. 2, pp. 11–22, March 2011.

[4] E. Bjerkan, "Efficient fault management using remote fault indicators," in *CIRED 2009 - The 20th International Conference and Exhibition on Electricity Distribution - Part 2*, pp. 1–25, 2009.

[5] J. Duller, A. Halim, G. Paton, B. Traill, and S. Sparling, "Next-generation adaptive network restoration on distribution feeders," *CIRED - Open Access Proceedings Journal*, vol. 2017, no. 1, pp. 1334–1337, 2017.

[6] J. Duller, A. Halim, G. Paton, B. Traill, and S. Sparling, "Next-generation adaptive network restoration on distribution feeders," *CIRED - Open Access Proceedings Journal*, vol. 2017, no. 1, pp. 1334–1337, 2017.

[7] "IEEE guide for fault locating techniques on shielded power cable systems," *IEEE Std 1234-2007*, pp. 1–34, July 2007.

[8] R. Schuerger, R. Fleig, and O. Escobedo, "Ac vs. dc over-potential testing of ac equipment," in *2016 IEEE/IAS 52nd Industrial and Commercial Power Systems Technical Conference (I CPS)*, pp. 1–5, 2016.

[9] W. Thue, *Electrical Power Cable Engineering*. 2012.

[10] Megger, "Basic TDR Operation." shorturl.at/hmtzJ. Accessed: 30-Nov-2022.

[11] I. HV Technologies, "The basics of time domain reflectometry (TDR)." https://bit.ly/3K3hF46. Accessed: 19-Dec-2018.

[12] Megger, "Fault finding solutions."

[13] Megger, "Cable fault location — how to find step by step." https://goo.gl/Nm7imZ. Accessed: 19-Dec-2018.

[14] C. G. Espinal and J. M. Flórez and S. P. Londoño, "Advanced fault location strategy for modern power distribution systems based on phase and sequence components and the minimum fault reactance concept," *Electric Power Systems Research*, vol. 140, pp. 933 – 941, 2016.

[15] R. Krishnathevar and E. E. Ngu, "Generalized impedance-based fault location for distribution systems," *IEEE Transactions on Power Delivery*, vol. 27, pp. 449–451, Jan 2012.

[16] K. Ramar and E. E. Ngu, "A new impedance-based fault location method for radial distribution systems," in *IEEE PES General Meeting*, pp. 1–9, July 2010.

[17] A. A. Girgis, D. G. Hart, and W. L. Peterson, "A new fault location technique for two- and three-terminal lines," *IEEE Transactions on Power Delivery*, vol. 7, pp. 98–107, Jan 1992.

[18] F. M. Aboshady, M. Sumner, and D. W. P. Thomas, "A double end fault location technique for distribution systems based on fault-generated transients," in *2017 IEEE 26th International Symposium on Industrial Electronics (ISIE)*, pp. 32–36, June 2017.

[19] Y. H. J. M. Damir Novosel, David Hart, "System for locating faults and estimating fault resistance in distribution networks with tapped loads."

[20] S. J. Lee, M. S. Choi, S. H. Kang, B. G. Jin, D. S. Lee, B. S. Ahn, N. S. Yoon, H. Y. Kim, and S. B. Wee, "An intelligent and efficient fault location and diagnosis scheme for radial distribution systems," *IEEE Transactions on Power Delivery*, vol. 19, pp. 524–532, April 2004.

[21] M. S. Choi, S. J. Lee, D. S. Lee, and B. G. Jin, "A new fault location algorithm using direct circuit analysis for distribution systems," *IEEE Transactions on Power Delivery*, vol. 19, pp. 35–41, Jan 2004.

[22] R. H. Salim, M. Resener, A. D. Filomena, K. R. Caino de Oliveira, and A. S. Bre-

tas, "Extended fault-location formulation for power distribution systems," *IEEE Transactions on Power Delivery*, vol. 24, pp. 508–516, April 2009.

[23] C. Liu, T. Lin, C. Yu, and J. Yang, "A fault location technique for two-terminal multisection compound transmission lines using synchronized phasor measurements," *IEEE Transactions on Smart Grid*, vol. 3, pp. 113–121, March 2012.

[24] T. Lin, P. Lin, and C. Liu, "An algorithm for locating faults in three-terminal multisection nonhomogeneous transmission lines using synchrophasor measurements," *IEEE Transactions on Smart Grid*, vol. 5, pp. 38–50, Jan 2014.

[25] E. Personal, A. García, A. Parejo Matos, D. Larios, F. Biscarri, and C. León, "A comparison of impedance-based fault location methods for power underground distribution systems," *Energies*, vol. 9, pp. 1–30, 12 2016.

[26] M.C. de Almeida and F.F. Costa and S. Xavier-de-Souza and F. Santana, "Optimal placement of faulted circuit indicators in power distribution systems," *Electric Power Systems Research*, vol. 81, no. 2, pp. 699 – 706, 2011.

[27] S. Lotfifard, M. Kezunovic, and M. J. Mousavi, "A systematic approach for ranking distribution systems fault location algorithms and eliminating false estimates," *IEEE Transactions on Power Delivery*, vol. 28, pp. 285–293, Jan 2013.

[28] Z. Zhang, S. Gong, A. D. Dimitrovski, and H. Li, "Time synchronization attack in smart grid: Impact and analysis," *IEEE Transactions on Smart Grid*, vol. 4, pp. 87–98, March 2013.

[29] J. R. Ramírez, J. M. Florez, and C. G. Espinal, "Fault location method based on two end measurements at the power distribution system," in *2015 IEEE 6th Latin American Symposium on Circuits Systems (LASCAS)*, pp. 1–4, Feb 2015.

[30] "IEEE guide for Determining Fault Location on AC Transmission and Distribution Lines," *IEEE Std C37.114-2004*, pp. 1–44, June 2005.

[31] Z. Q. Bo, G. Weller, and M. A. Redfern, "Accurate fault location technique for distribution system using fault-generated high-frequency transient voltage signals,"

IEE Proceedings - Generation, Transmission and Distribution, vol. 146, pp. 73–79, Jan 1999.

[32] J. Cai, Y. Yang, X. Zeng, and S. Deng, "A novel travelling wave fault location method based on distance proportion and time difference for distribution network," in *2015 5th International Conference on Electric Utility Deregulation and Restructuring and Power Technologies (DRPT)*, pp. 1200–1205, Nov 2015.

[33] Z. Xiangjun, K. K. Li, L. Zhengyi, and Y. Xianggen, "Fault location using travelling wave for power networks," in *Conference Record of the 2004 IEEE Industry Applications Conference, 2004. 39th IAS Annual Meeting.*, vol. 4, pp. 2426–2429 vol.4, Oct 2004.

[34] H. Ye, K. Rui, Z. Zhu, X. Zeng, D. Yang, and Y. Cao, "A novel single-phase grounding fault location method with traveling wave for distribution networks," in *2015 5th International Conference on Electric Utility Deregulation and Restructuring and Power Technologies (DRPT)*, pp. 1175–1179, Nov 2015.

[35] H. Hizman, P. A. Crossley, P. F. Gale, and G. Bryson, "Fault section identification and location on a distribution feeder using travelling waves," in *IEEE Power Engineering Society Summer Meeting,*, vol. 3, pp. 1107–1112 vol.3, July 2002.

[36] I. Goodfellow, Y. Bengio, and A. Courville, *Deep Learning*. MIT Press, 2016. `http://www.deeplearningbook.org`.

[37] S. Javadian and M. Massaeli, "A fault location method in distribution networks including dg," *Indian Journal of Science and Technology*, vol. 4, pp. 1446–1451, 01 2011.

[38] Y. Aslan, "An alternative approach to fault location on power distribution feeders with embedded remote-end power generation using artificial neural networks," *Electrical Engineering*, vol. 94, 09 2011.

[39] P. Bouboulis, S. Theodoridis, C. Mavroforakis, and L. Evaggelatou-Dalla, "Complex support vector machines for regression and quaternary classification," *IEEE*

Transactions on Neural Networks and Learning Systems, vol. 26, pp. 1260–1274, June 2015.

[40] R. Agrawal and D. Thukaram, "Identification of fault location in power distribution system with distributed generation using support vector machines," in *2013 IEEE PES Innovative Smart Grid Technologies Conference (ISGT)*, pp. 1–6, Feb 2013.

[41] D. Thukaram, H. P. Khincha, and H. P. Vijaynarasimha, "Artificial neural network and support vector machine approach for locating faults in radial distribution systems," *IEEE Transactions on Power Delivery*, vol. 20, pp. 710–721, April 2005.

[42] P. Jarventausta, P. Verho, and J. Partanen, "Using fuzzy sets to model the uncertainty in the fault location process of distribution networks," *IEEE Transactions on Power Delivery*, vol. 9, pp. 954–960, April 1994.

Chapter 3

Description of the developed faulted section location technique

3.1 Chapter overview

The proposed technique relies on the deployment of monitoring infrastructure at the LV side of various step-down transformers across the distribution network. Such infrastructure is already being rolled out by DNOs through various innovation projects [1, 2]. In particular, the algorithm uses voltage measurements acquired from the referred LV points in order to process the sequence components derived when asymmetrical faults occur at the MV part of the network [3], [4]. Collection and manipulation of the voltage sequence component dataset enables the specific approach to define the Faulted Section (FS) residing among MV pieces of switchgear.

Section 3.2 justifies the selection of positive over negative sequence component ratio as the main parameter of the developed algorithm through a preliminary data driven study and theoretical analysis. Section 3.3 introduces the elements and describes the logic of the proposed technique.

3.2 Preliminary analysis

The particular analysis examines how the faults occurring on the 11 kV network impact the signatures (i.e. RMS voltage, voltage angle and sequence components) captured at the LV side of the step-down transformers. This is achieved through simulations where asymmetrical faults are injected in different locations across an example network. The latter replicates the real network of PNDC. Both solid and resistive faults were applied throughout this investigation. For resistive faults, fault resistances of 20 Ω and 60 Ω were examined, which are the lowest that can be achieved in the real PNDC network for phase to earth and phase to phase faults respectively. Fig. 3.1 depicts the implemented network configurations as well as the three different fault locations, F_1, F_2 and F_3, studied. Specifically, this preliminary data-driven study takes into account radial and ring topologies as well as the presence of Distributed Generation (DG) at both LV and MV side of the network.

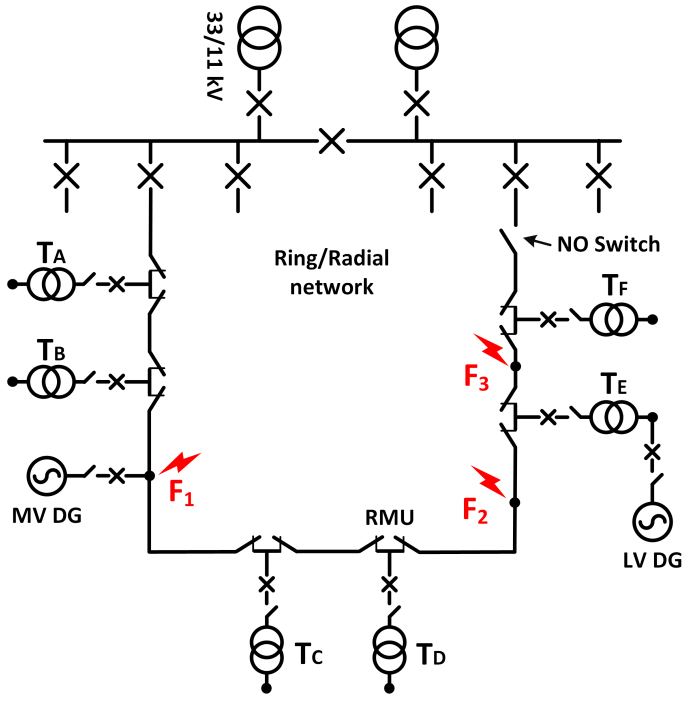

Figure 3.1: Radial/ring topology of a simulated distribution network section.

Firstly, the RMS voltage and phase angle profiles across the LV circuits are con-

structed with data acquired from the multiple measurement points, A to F. Fig. 3.2 shows the voltage and angle - in relation to the slack bus angle of the model - profiles when a fault occurs at location F_2, between transformers T_D and T_E, in radial topology without DG. It is obvious that looking only at RMS voltage or phase angle it is not adequate, since there is no consistency among the various fault types in terms of values deviation. For instance the RMS voltage measured at T_E is lower than this at T_D during a solid phase to earth fault which contradicts with the case of a solid phase to phase fault. Similarly, the angle of phase B measured at T_E is higher than this at T_D during a solid phase to phase fault in contrast to the case of a resistive (20 Ω) phase to earth fault, as can be seen at Fig. 3.2.

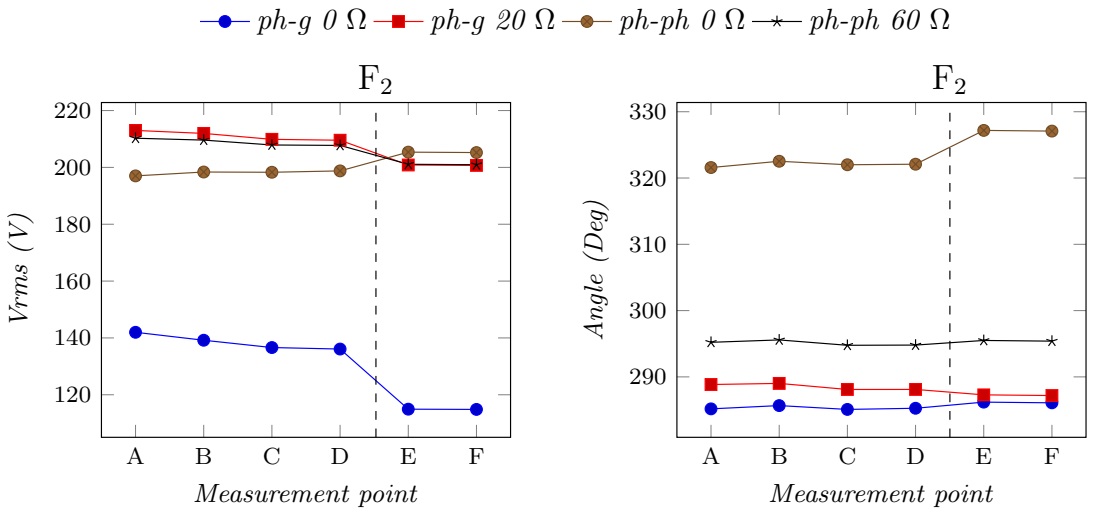

Figure 3.2: Phase B, voltage RMS and angle profile for fault at location F_2, in radial network without DG.

Furthermore, the perspective of assessing the deviation (%) from pre-fault to fault conditions of the phase angle and RMS voltage values to identify the FS was evaluated. Fig. 3.3 illustrates an example fault case by plotting the mentioned deviations for all measurement points, A to F. It is observed that the particular graphs do not provide a clear vision with regards to the fault location.

Specifically, while a solid phase to earth fault resides between transformers T_D and T_E the greatest voltage RMS change in terms of % is evident in transformer T_D (47.7%),

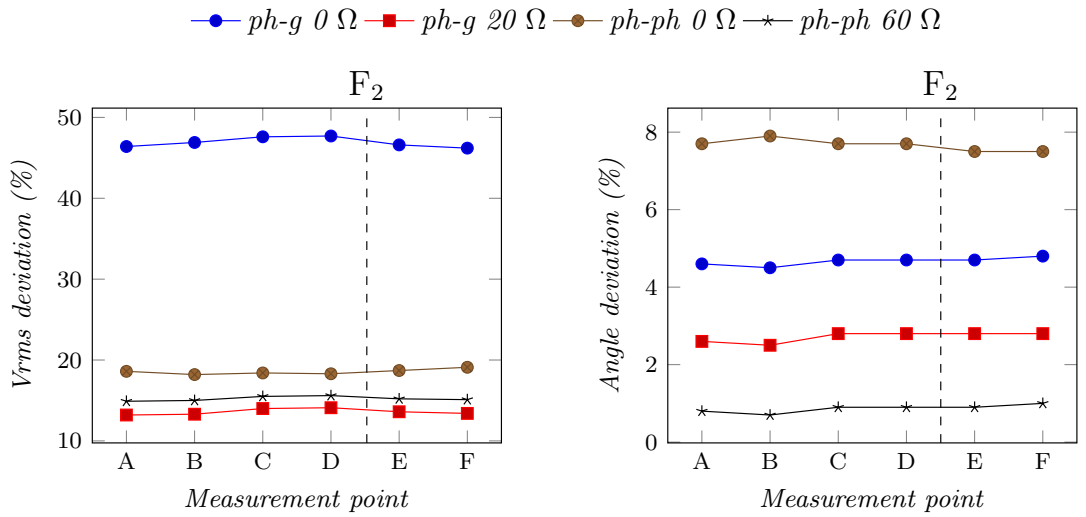

Figure 3.3: Phase B, voltage RMS and angle deviation (%) from pre-fault conditions when a fault occurs at location F_2, of ring network without DG.

which could be a correct indication of the FS. However, in the case of a solid phase to phase fault at the same location, the highest deviation is observed at transformer T_F (19.1%) which could be misleading.

Similarly, looking at the deviation of phase angle to locate the FS can be a challenging exercise. For a solid phase to phase fault the most significant effect is observed at transformer T_B, whereas for the other cases at largest change is found at transformer T_F, as depicted at Fig. 3.3.

From the initial observations, voltage and angle profiles consisting of multiple point measurements could provide hints to locate the faults. However, the fault indication cannot always be straightforward and accurate as it will depend on the monitored phase and fault types. This increases the complexity of deriving a generic rule or approach to locate the fault using the voltage and angle profile.

On the other hand, sequence components are considered a parameter significantly affected by the presence of asymmetrical faults. Sequence components replace a three-phase unbalanced system by three groups of balanced phasors [5]. The latter are designated as:

1. Positive-sequence components, comprising of three phasors of equal magnitude,

spaced 120° apart, and rotating in the same direction as the phasors under examination, i.e. positive direction.

2. Negative-sequence components, comprising of three phasors of equal magnitude, spaced 120° apart, rotating in the same direction as the positive sequence phasors but in the reverse sequence.

3. Zero-sequence components, which consist of three phasors equal in magnitude and in phase with each other.

Fig. 3.4 illustrates a three-phase unbalanced system along with the associated symmetrical components [5].

Based on the above, the voltage values of phases a, b and c are represented by equations (3.1) [5]:

$$\begin{aligned} V_a &= V_{a0} + V_{a1} + V_{a2} \\ V_b &= V_{b0} + V_{b1} + V_{b2} \\ V_c &= V_{c0} + V_{c1} + V_{c2} \end{aligned} \tag{3.1}$$

Also,

$$\begin{aligned} V_b &= V_{a0} + \alpha^2 V_{a1} + \alpha V_{a2} \\ V_c &= V_{a0} + \alpha V_{a1} + \alpha^2 V_{a2} \end{aligned} \tag{3.2}$$

where α is the operator giving the phase shift of 120° and a multiplication of unit magnitude, i.e. $\alpha = 1\angle 120°$ or $\alpha = e^{j120°}$. Similarly, $\alpha^2 = 1\angle 240°$ and $\alpha = e^{j240°}$. Using the operator α the phase quantities are expressed by the matrix in equation (3.3):

$$\begin{bmatrix} V_a \\ V_b \\ V_c \end{bmatrix} = \begin{bmatrix} 1 & 1 & 1 \\ 1 & \alpha & \alpha^2 \\ 1 & \alpha^2 & \alpha \end{bmatrix} \times \begin{bmatrix} V_{a0} \\ V_{a1} \\ V_{a2} \end{bmatrix} \tag{3.3}$$

Inverting the matrix of equation (3.3), we get zero, positive and negative voltage sequence components of phase a:

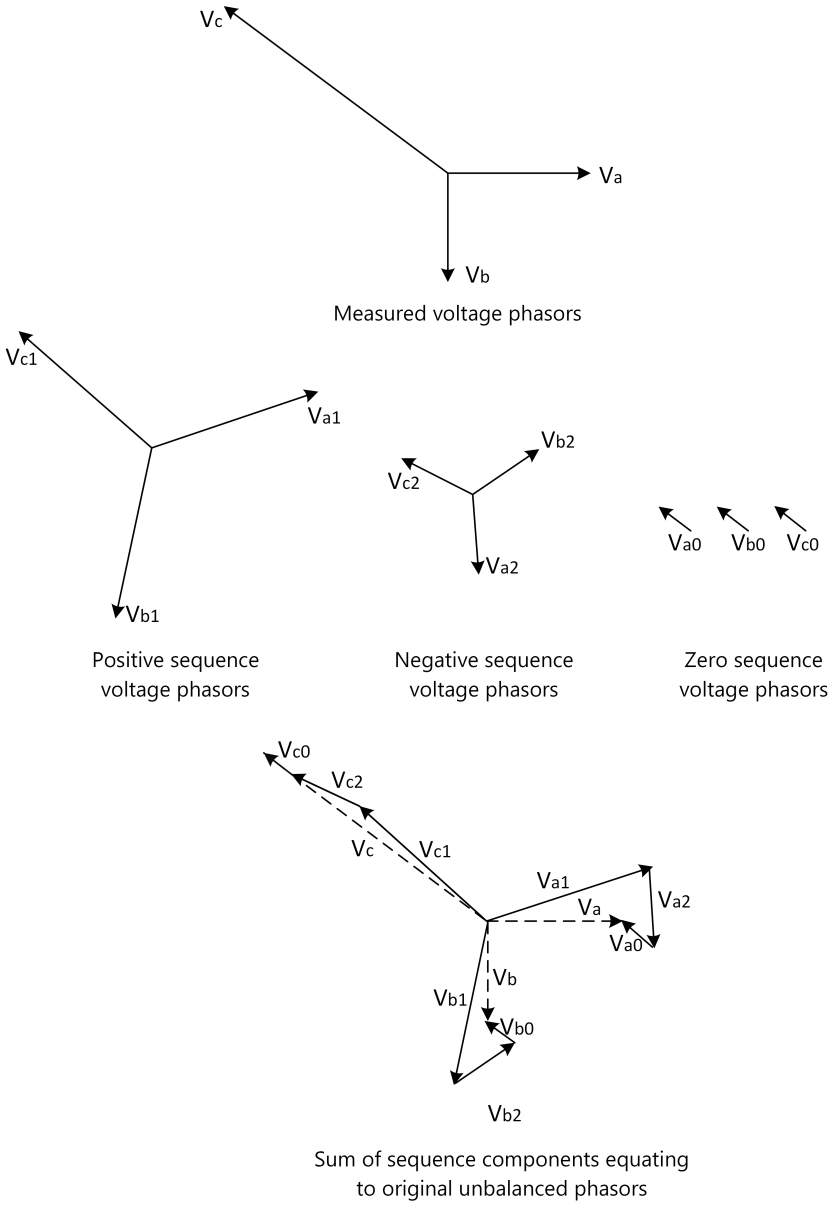

Figure 3.4: Symmetrical components of example unbalanced three-phase system [5].

$$\begin{bmatrix} V_{a0} \\ V_{a1} \\ V_{a2} \end{bmatrix} = \begin{bmatrix} 1 & 1 & 1 \\ 1 & \alpha^2 & \alpha \\ 1 & \alpha & \alpha^2 \end{bmatrix} \times \begin{bmatrix} V_a \\ V_b \\ V_c \end{bmatrix} \tag{3.4}$$

Zero sequence components are not observed at the LV network during 11 kV faults

due to the delta/star connection of the MV/LV transformers [6]. Therefore, only positive and negative sequence components can be examined.

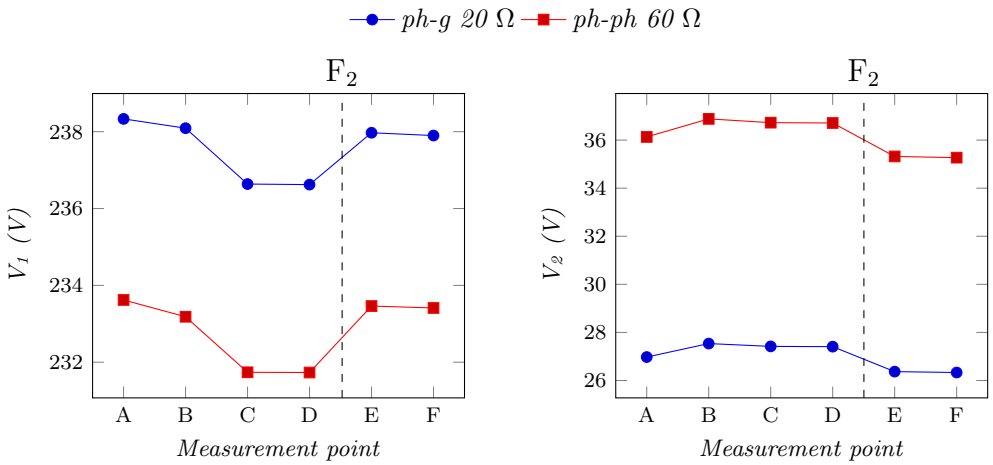

Figure 3.5: Positive and negative sequence voltage profile when resistive faults occur at location F_2 of ring network without DG.

Fig. 3.5 shows the profiles of positive and negative sequence components of voltage when resistive phase to earth and phase to phase faults occur in a ring network. Both profiles illustrated at Fig. 3.5, demonstrate consistency among the different scenarios. Specifically, positive sequence voltage drops towards the section containing the fault, B - C, whereas the negative sequence voltage rises towards the same area (maximum V_2 captured at T_B).

Similarly, the positive and negative symmetrical components profiles, captured during solid faults, are illustrated at Fig. 3.6. Both Fig. 3.5 and Fig. 3.6 indicate that sequence components can generally provide a more distinct trend during asymmetrical faults, in comparison to LV voltage RMS and angle profiles.

The impact of MV faults on the LV voltage sequence components is also highlighted with the analysis of an example unbalanced phase-to-phase solid fault. As shown in Fig. 3.7, a phase-to-phase fault is represented by a parallel connection of the positive and negative sequence networks at the point of the fault. This circuit is based on first principles of sequence components theory and circuit analysis [6]. In the depicted equivalent sequence network the MV bus can be seen, where a step-down (MV/LV)

transformer of impedance Z_T is connected. At the same circuit, Z_{LD} is the impedance of the load and Z (Z_1=Z_2) is the impedance between the MV connection of the step-down transformer and the fault location. At the LV side of the transformer, the monitoring point m_1 and m_2 measure the positive, V_{LV_1}, and negative, V_{LV_2}, voltage sequence component respectively.

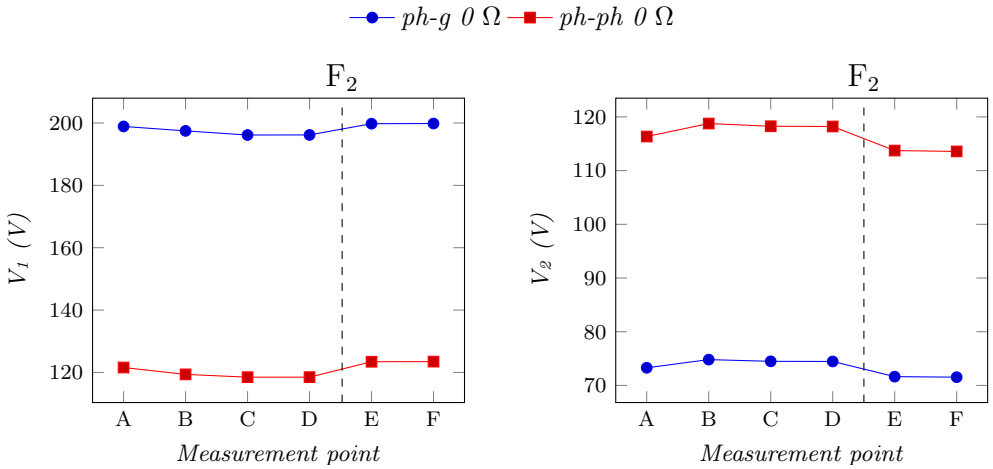

Figure 3.6: Positive and negative sequence voltage profile when solid faults occur at location F_2 of ring network without DG.

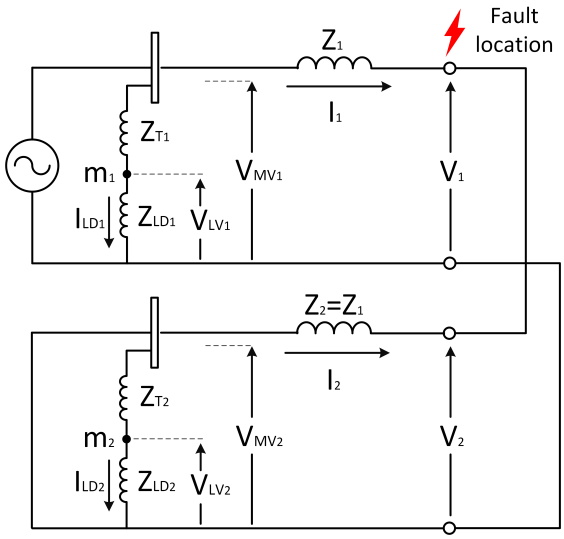

Figure 3.7: Equivalent sequence network during a phase to phase fault.

Equations (3.5a) and (3.5b) are used to apply Kirchhoff's Voltage Law (KVL) at

the equivalent circuit, depicted in Fig. 3.7. The rearranged equation (3.5b) to equations (3.6a) and (3.6b) highlights the transformer's MV side positive over negative sequence component ratio's dependency on the line impedance between the MV connection point and the fault location. It is considered that the currents I_1 and I_2 are expected to be unchanged regardless the point of the transformer's connection across the MV conductor.

Applying KVL at the equivalent sequence network in Fig.3.7, we have:

$$V_1 = V_2 \tag{3.5a}$$

$$V_{MV_1} + I_1 Z_1 = V_{MV_2} + I_2 Z_2 \tag{3.5b}$$

Given that I_1=-I_2 and Z_1=Z_2, equation (3.5b) is rearranged to (3.6a). Equation (3.6b) indicates that the MV positive over negative sequence component ratio is highly dependent on the line impedance Z_1.

$$V_{MV_1} = V_{MV_2} + 2I_2 Z_1 \tag{3.6a}$$

$$\frac{V_{MV_1}}{V_{MV_2}} = Z_1 \frac{2I_2}{V_{MV_2}} + 1 \tag{3.6b}$$

The equations (3.7a) and (3.7b) represent the positive and negative voltage sequence components at the LV side of the transformer.

$$V_{LV_1} = V_{MV_1} - I_{T_1} Z_{T_1} \tag{3.7a}$$

$$V_{LV_2} = V_{MV_2} - I_{T_2} Z_{T_2} \tag{3.7b}$$

The values V_{LV_1} and V_{LV_2} are mainly affected by the ratio of the transformer's windings rather than the load current I_{LD}, which is considered negligible during solid fault conditions, and the transformer's impedance, Z_T, which is normally ranged within 4-5%. Consequently, the ratio of positive over negative voltage sequence components captured at the secondary (LV) side of the step-down transformer can potentially have

a significant impact to the MV fault localisation exercise. The ratio k_s, is given by equation (3.8):

$$k_s = \frac{|V_{LV_1}|}{|V_{LV_2}|} \tag{3.8}$$

Fig. 3.8 illustrates the comparison among the positive, negative sequence components and k_s sensitivity during various asymmetrical faults, expressed by the percentage difference between adjacent LV measurement points. From Fig. 3.8.a) to Fig. 3.8.d) it can be seen that the ratio k_s presents higher sensitivity at sections related to the fault location compared to the positive and negative sequence components.

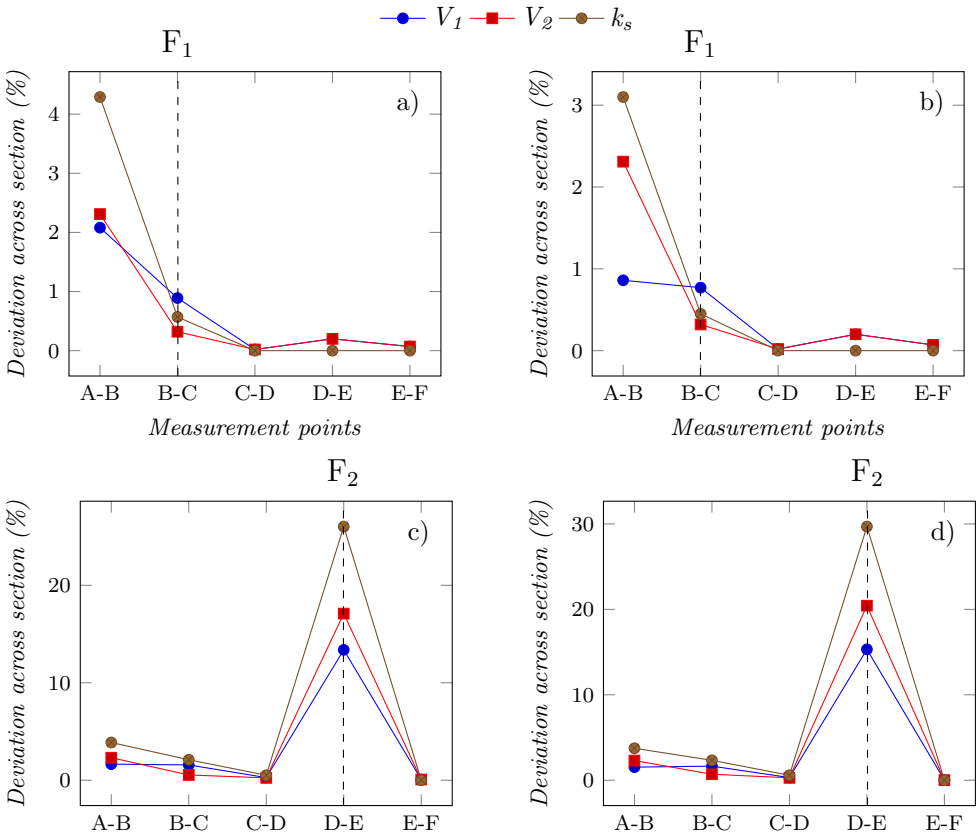

Figure 3.8: Deviation (%) of positive, negative voltage sequence components and k_s across adjacent measurement points under: a) solid phase to phase fault at location F_1 of radial network without DG, b) solid phase to earth fault at location F_1 of radial network without DG, c) solid phase to phase fault at location F_2 of radial network without DG, d) solid phase to phase fault at location F_2 of radial network with DG connected at MV side among T_B and T_C.

In particular, Fig. 3.8.a) and Fig. 3.8.b) relate to a solid phase to phase and phase to earth fault respectively, both at location F_1 of radial network without DG. It is observed that the deviation between k_s measurements captured from transformers T_A and T_B is clearly greater than the corresponding values of positive and negative sequence components. The particular observation is of major importance, as section A-B is placed just upstream of the faulted section.

Moreover, Fig. 3.8.c) and Fig. 3.8.d) refer to solid phase to phase fault conditions at location F_2 of radial network. The latter involves an MV connected DG between transformers T_B and T_C. It can be seen that k_s demonstrates high sensitivity during the particular faults, taking into account that the fault location F_2 resides within the section D-E.

Thus, taking into consideration the observations acquired from the data-driven study and the theoretical analysis presented in this section, it is concluded that the positive over negative voltage sequence components ratio, k_s, measured at the LV side of multiple transformers, constitute a strong indicator for unbalanced fault localisation across the MV part of the network. The same parameter is also used and assessed throughout this study for phase-to-earth faults as the zero sequence components are not present at the LV side of the step-down transformers due to their primary delta connected windings. The ratio k_s is characterized as a 'balance factor' because the greater the number of the ratio the less asymmetrical the system is at the particular point on the network.

3.3 Proposed algorithm

The proposed FS location algorithm is based on the implementation of sparse measurements acquired at the LV side of numerous step-down transformers connected across the MV network. The technical requirements of the associated LV monitoring system are determined by the need to conduct sequence component calculations. Three-phase voltage angle and magnitude data have to be used to derive the sequence components. For this purpose, processing elements called "slaves" perform the required calculations

for each measurement point. These elements could be either part of the software performing the algorithm or pieces of hardware distributed at the LV side of the step-down transformers. The slaves record the voltage waveforms and are able to extract only the part during the fault period (i.e. 0.1 s). Then, these waveform data are used to derive the magnitude and angle of the voltage so the sequence components can be calculated. Meanwhile, a "master" unit keeps collecting the calculated results from the "slaves" to implement the algorithm.

The sensing devices could be installed at two possible points of the LV side of a network; the LV side of the step down (MV/LV) transformers or a measuring point downstream on the LV feeder. Although, the latter could not be a realistic scenario for this case, as the intervening impedance of the conductor between the LV side of the transformer and the monitoring location would adversely affect the performance of the algorithm.

3.3.1 Principal elements of the method

Two parameters play a key role in this process: the balance factor, k_s, (refer to equation (3.8)) and the percentage difference of the ratios among various measurement points $\Delta k_{s_{ij}}\%$ (refer to equation (3.9)).

$$\Delta k_{s_{ij}}\% = \frac{\Delta k_{s_{ij}}}{\overline{k_{s_n}}} \times 100\% \tag{3.9}$$

The parameter $\Delta k_{s_{ij}}\%$, given by equation (3.9), indicates the percentage difference among the factors k_s estimated at various measuring points, such as k_{s_i} at point i and k_{s_j} at point j, within a measurement window, whilst $\overline{k_{s_n}}$ (equation (3.10)) is the average value of all the balance factors captured from the total, n_m, of the LV metering points within the particular window.

$$\overline{k_{s_n}} = \frac{1}{n_m} \sum_{i=1}^{n} k_{s_i} \tag{3.10}$$

The implementation of the above parameters is explained in sections 3.3.2 and 3.3.3, where the "slaves" and "master" unit operation is described thoroughly.

3.3.2 "Slave" units operation: fault period discrimination and calculation of k_s

As explained in the previous section, the proposed algorithm depends on the value of balance factor k_s. This factor, indicated by equation (3.8), utilizes the ratio of positive over negative voltage sequence components. However, for the correct operation of the algorithm it is important to ensure that the balance factor k_s is calculated only for the fault duration. Thus, a positive voltage-based function has been developed to extract the voltage traces during the fault.

An example scenario of a ph-ph resistive fault applied in the ring network depicted in Fig. 3.9, is used to better interpret this function. As illustrated in Fig. 3.10(a) the fault is triggered at t_F and the Circuit Breaker (CB) is opened at t_{CB}. Since the period of interest is between t_F and t_{CB}, the indexes of voltage traces corresponding to the fault and the subsequent opening of the CB have to be identified.

Initially, the opening of the CB t_{CB} is identified by comparing the voltage magnitudes with a near-zero threshold V_{TH}. The point of the time when the voltage magnitude values are below V_{TH}, will be marked as $t_{(V\approx 0)}$. As indicated by equation (3.11), the actual point of t_{CB} is found by 'shifting' backwards the value $t_{(V\approx 0)}$ by an amount of t_{sfb}. This time shift will ensure that the 'falling' period of voltage caused by CB tripping (and any other time delays arising from window-based signal processing) will not be included in the calculation of balance factor k_s.

$$t_{CB} = t_{(V\approx 0)} - t_{sfb} \tag{3.11}$$

The time of fault occurrence t_F, is derived by applying Discrete Wavelet Transform (DWT) to positive voltage traces (separately for each phase). DWT is a powerful tool which can be used for detection of singularities in signals (e.g. faults) [7, 8]. The reason for not using voltage magnitudes (like in the previous occasion), is due to the challenges imposed by highly-resistive faults in conjunction with the expected maximum voltage drop.

The DWT method used is Haar, due to its simple and convenient nature [9]. Con-

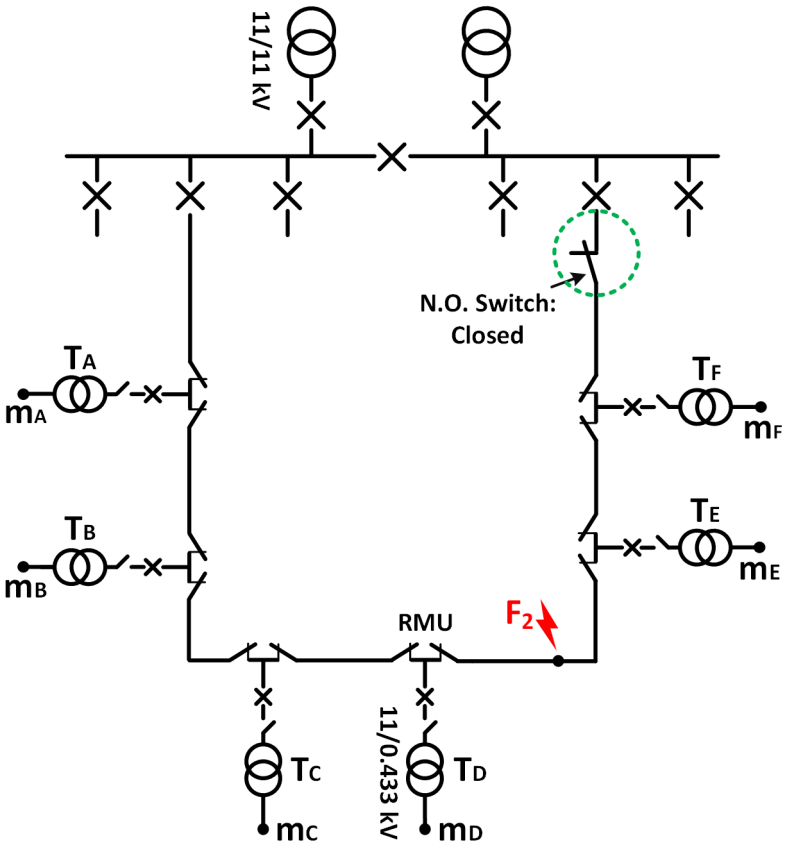

Figure 3.9: Phase-to-phase, 60 Ω fault occurring on a ring network.

sidering the sampling time implemented in both simulations and hardware testing is 100 μs, which means 10 kHz of sampling rate, the frequency band, on which the DWT is applied, is the [0.625-1.25] kHz. This corresponds to the third wavelet decomposition level, which has been selected for noise immunity, distinguishable wavelet coefficients (magnitude) and because the frequency band is still high enough to distinguish the transient events [10]. The third wavelet decomposition level was also successfully applied with a frequency band of [0.235-0.47] kHz at physical testing measurements with sampling frequency of 3.75 kHz.

In Fig. 3.10(b) the DWT of positive voltage traces is illustrated. The resulting signal $DWT(V_{abc})$ is compared with a near-zero threshold DWT_{TH}. The first occurrence (for any of the three phases) exceeding $DWT(V_{abc})$ is marked as t_{DWT}. Like in the previous occasion, the actual point of t_F is found by shifting forward the value t_{DWT}

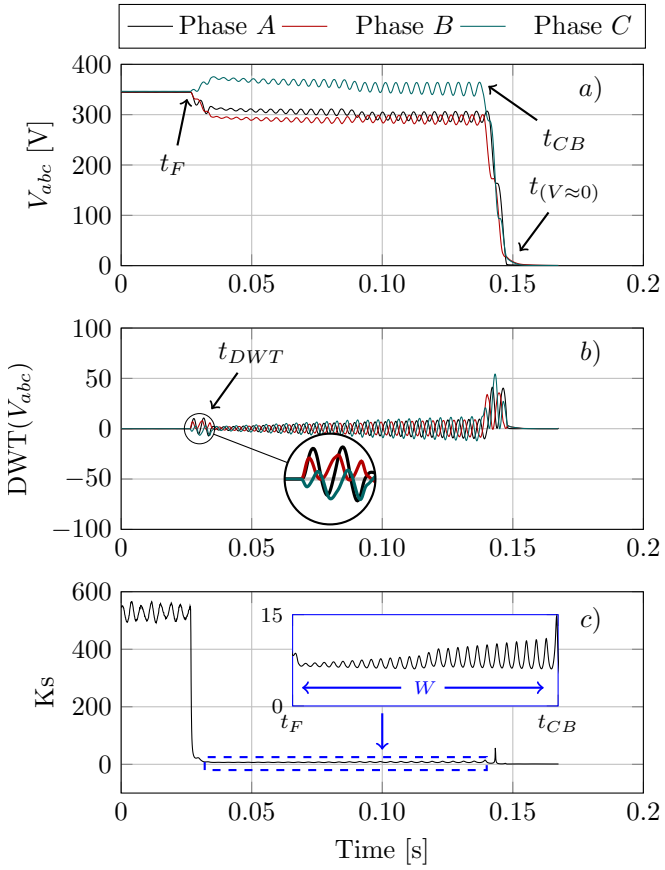

Figure 3.10: Phase-to-phase, 60 Ω fault occurring on a ring network: a) Voltage magnitudes, b) DWT of Voltage magnitudes, c) k_s.

by a predefined amount of t_{sff} (see equation (3.12)). It should be noted that in order to avoid any maloperation of the DWT, the data around t_{CB} could be omitted from the comparison.

$$t_F = t_{DWT} + t_{sff} \tag{3.12}$$

The time indexes t_F and t_{CB} are used to create a stationary time window W with n_W number of samples. It should be noted that balance factor k_s is initially formed as a time series object (see Fig. 3.10(c)). As such, in order to capture a single value which can be used in the proposed algorithm, the average value of k_s (i.e. $\overline{k_s}$) is calculated over the whole duration of the fault (indicated by window W), as presented in equation (3.13).

$$\overline{k_s} = \frac{1}{n_W} \sum_{t_F}^{t_{CB}} \frac{|V_1(t)|}{|V_2(t)|} \tag{3.13}$$

It should be highlighted that the procedure described above is an efficient approach to identify the fault occurrence and CB opening, ensuring no need of time-synchronized measurements.

3.3.3 "Master" unit operation: faulted section identification

The "master" unit function is based on the deployment of a tool called "3-points window". This term defines a group of data retrieved from three adjacent LV monitoring points. In Fig. 3.11, the "3-points windows" are represented by the dashed rectangular shapes. For instance, the window *A-B-C* contains data acquired from the slaves SL_A, SL_B and SL_C, which in turn retrieve measurements from monitoring units m_A, m_B and m_C.

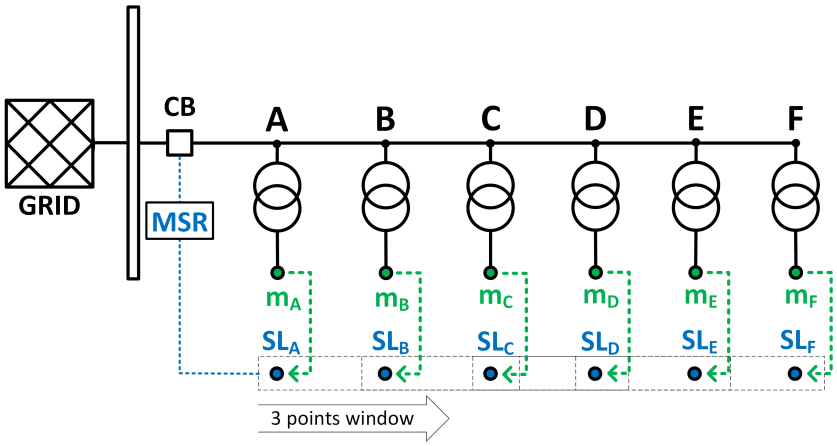

Figure 3.11: The "moving" 3-points window after a 20 Ω phase-to-earth fault introduced at location F_1 of a radial network.

When a fault event occurs the "master" unit, *MSR*, requests the "slaves" SL_A, SL_B and SL_C to perform the required data collection and calculations, as discussed in section 3.3.2. After the balance factors k_{s_A}, k_{s_B}, k_{s_C} are collected, the $\Delta k_{s_{A-C}}\%$ is calculated and a comparative analysis of the ratios k_s is applied. The latter results to the indicator *'1'* when $k_{s_A} > k_{s_B}$ and '0' when $k_{s_A} \leq k_{s_B}$. The same principle

applies for comparison between k_{s_B} and k_{s_C}. Thus, a comparison indication pair, i.e. *'1'-'0'*, is created by the window *A-B-C*. After the mentioned information is acquired - k_{s_A}, k_{s_B}, k_{s_C}, $\Delta k_{s_{A-B}}\%$ and comparison indicators pair of $k_{s_A} > k_{s_B}$ and $k_{s_B} > k_{s_C}$ - the 3-points window "moves" downstream by one monitoring point (i.e. m_B, m_C and m_D) and repeats the same calculation process. This procedure is repeated until the 3-points window includes data from the last monitoring unit of the network (i.e. m_F in Fig. 3.11).

3.3.4 Algorithmic logic in radial networks

Depending on the network configuration, by means of radial, ring or even considering the presence of MV laterals, different algorithmic paths are followed. In radial networks, the first criterion to identify the MV FS is the detection of the 3-points window with the greatest percentage difference $\Delta k_{s_{13}}\%$. When the mentioned window is found, it is used as a starting point and the algorithm searches downstream for the first window containing a comparison indication pair *'1'-'0'*. In this window, the FS is revealed by the indicator *'1'*. The pair *'1'-'1'* indicates the FS only when this is located between the last two step-down transformers.

The example fault scenario of Fig. 3.12 and the corresponding data contained in Table 3.1, are used to better explain the algorithm when applied in radial networks. The measured k_{s_1}, k_{s_2} and k_{s_3} of the window *A-B-C* refer to the k_{s_A}, k_{s_B} and k_{s_C} respectively. The last two columns of Table 3.1 provide the results of the comparative analysis between k_{s_1} - k_{s_2} and k_{s_2} - k_{s_3}.

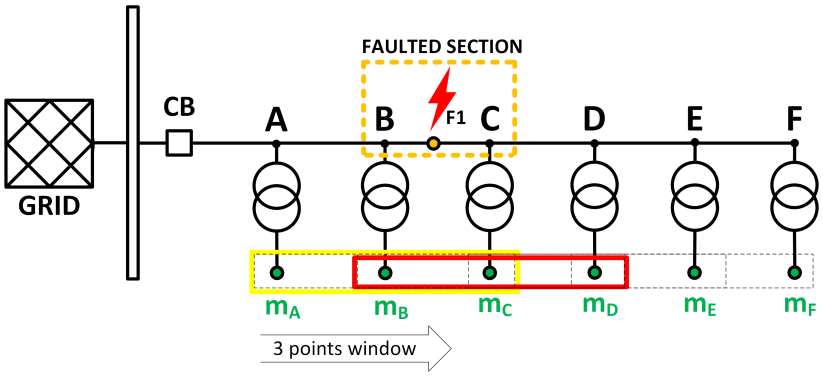

Figure 3.12: The "moving" 3-points window after a 20 Ω phase-to-earth fault introduced at location F_1 of a radial network.

Table 3.1: Phase to earth (20 Ω) fault / F_1.

3-points window	k_{s_1}	k_{s_2}	k_{s_3}	$\Delta k_{s_{13}}\%$	FS search	$k_{s_1} > k_{s_2}$	$k_{s_2} > k_{s_3}$
A-B-C	8.83	8.63	8.61	2.57%	↓	'1'	'1'
B-C-D	8.63	8.61	8.61	0.23%	→	'1'	'0'
C-D-E	8.61	8.61	8.61	0%		'0'	'0'
D-E-F	8.61	8.61	8.61	0%		'0'	'0'

The cell of Table 3.1 highlighted in yellow indicates the highest $\Delta k_{s_{13}}\%$ among the total of the collected 3-points-windows. The window associated to this $\Delta k_{s_{13}}\%$ value is the *A-B-C*, also highlighted in yellow at the diagram of Fig. 3.12, "carrying" the k_s comparison indicators pair *'1'-'1'*. Therefore, the 3-points window "moves" downstream the radial network searching for the first *'1'-'0'* comparison indicators pair, as the green arrows of Table 3.1 and this of Fig. 3.12 denote. Eventually, the window *B-C-D* is the one recorded a *'1'-'0'* pair. The referred window is enclosed by the red frame in Fig. 3.12. The indicator *'1'* (cell of Table 3.1 highlighted in red) of the noted pair reveals the FS. Therefore, *B-C* is the identified MV section where the asymmetrical fault occurred.

The procedure of the FS identification alters slightly when an MV lateral is connected within or downstream the MV zone referred by the window with the largest $\Delta k_{s_{13}}\%$. In this case, the 3-points window follows two separate "routes" towards the end of the two radial MV circuits. In both circuits, the first windows with the com-

parison indication pairs *'1'-'0'* or *'1'-'1'* (if this is found at the last 3-points window) have to be located, as described previously. When this is done, the 3-points-window with the largest $\Delta k_{s_{13}}\%$ - among the ones identified within each separate radial circuit - is the one referring to the FS.

A fault scenario, where a 20 Ω phase-to-earth fault is introduced at location F_4 of a radial network with an MV lateral, is presented with the aid of Table 3.2 and Fig. 3.13. Table 3.2 highlights the window *A-B-G*, with the largest $\Delta k_{s_{13}}\%$, which encompasses the connection of an MV lateral (Fig. 3.13). In this case, the approach implemented in radial networks is applied in two separate radial circuits, the *A-F* and *A-I*. It is clarified that the orange and green arrow, in Table 3.2, represent the FS search within circuits *A-I* and *A-F*, respectively.

Table 3.2: Radial topology / Phase to earth (20 Ω) fault / F_4.

Circuit	3-points window	k_{s_1}	k_{s_2}	k_{s_3}	$\Delta k_{s_{13}}\%$	FS search	$k_{s_1} > k_{s_2}$	$k_{s_2} > k_{s_3}$
Radial A-I	A-B-G	8.92	8.71	8.67	3.06%	↓↓	'1'	'1'
	B-G-H	8.71	8.66	8.66	0.58%	→	'1'	'0'
	G-H-I	8.66	8.66	8.66	0%		'0'	'0'
Radial A-F	A-B-C	8.92	8.71	8.68	2.83%		'1'	'1'
	B-C-D	8.71	8.68	8.68	0.35%	→	'1'	'0'
	C-D-E	8.68	8.68	8.68	0%		'0'	'0'
	D-E-F	8.68	8.68	8.68	0%		'0'	'0'

The 3-points window *A-B-G* is the starting point of the FS search in the two circuits, *A-I* and *A-F* (orange and green arrows). Throughout the search, two windows with pair *'1'-'0'*, *B-G-H* and *B-C-D*, have been found in circuits *A-I* and *A-F* correspondingly. The percentage difference $\Delta k_{s_{13}}\%$ of the former (cell coloured in dark blue) is higher than this of the latter (cell coloured in light blue), as it is remarked in Table 3.2. Therefore, the FS is located between the transformers T_B and T_G, where F_4 is actually introduced.

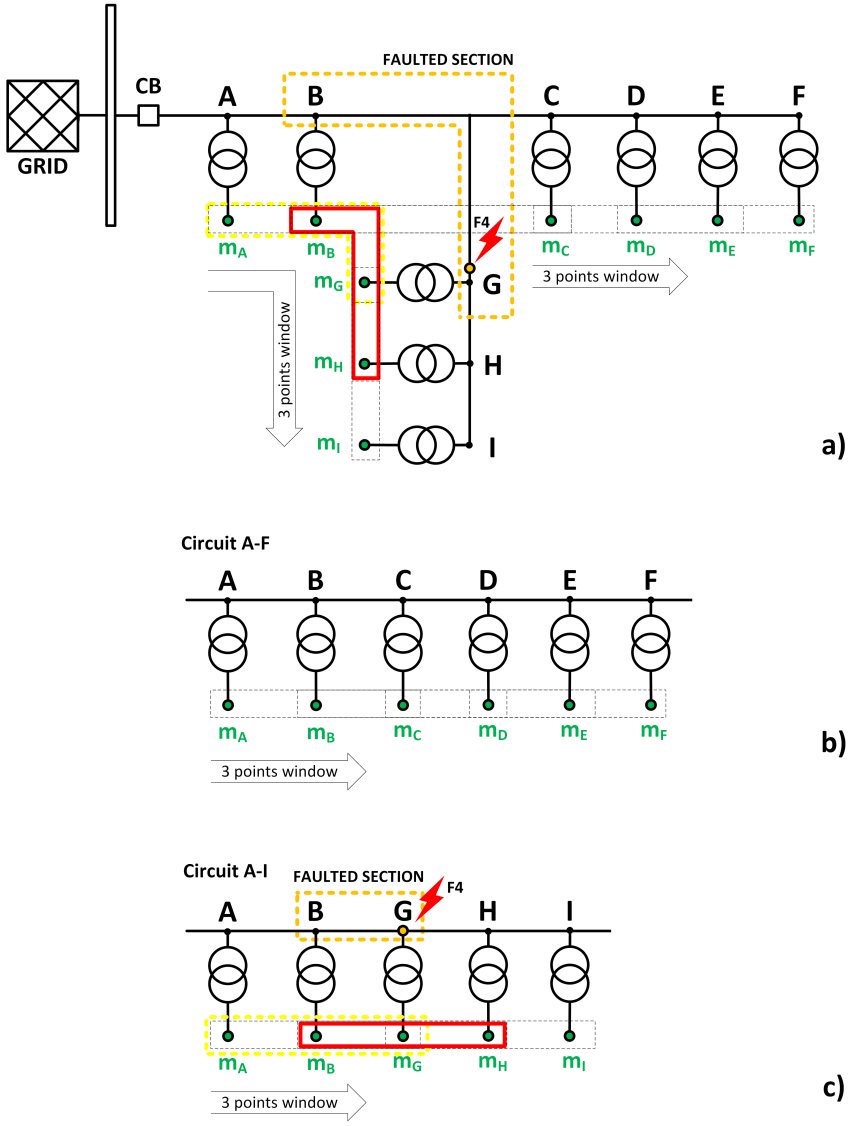

Figure 3.13: The "moving" 3-points window after a 20 Ω phase-to-earth fault is simulated in the radial topology of model B.

3.3.5 Algorithmic logic in ring networks

In ring networks, when an asymmetrical fault occurs the developed technique starts directly with the comparative analysis on the derived ratios, k_s. Therefore, the window containing the indicators pair *'1'-'0'* needs to be identified. If only one such window exists, the FS is located within the corresponding MV zone. It is highlighted that, in ring networks the capability of the algorithm is limited to the identification of the

MV section among three step-down transformers, instead between two when applied in radial topologies.

Fig. 3.14 depicts an example 20 Ω phase to earth fault scenario happened at location F_1. The captured data are reported in Table 3.3. Throughout this fault case, the highlighted three-points window *B-C-D* carries the pair *'1'-'0'* indicating the MV FS among transformers T_B, T_C and T_D. This can be seen in Fig. 3.14 with the aid of the red frame. Also, the FS is highlighted via the dashed orange frame.

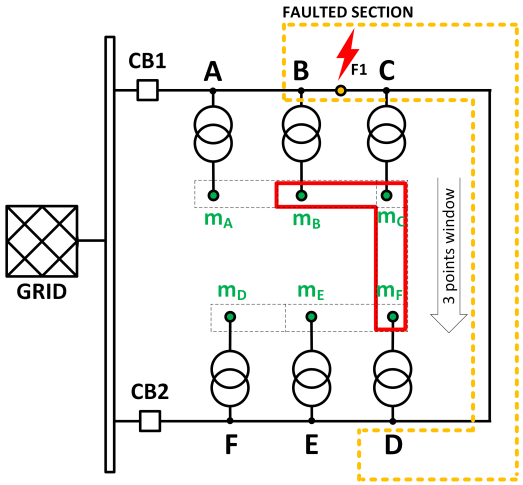

Figure 3.14: The "moving" 3-points window after a 20 Ω phase-to-earth fault is simulated in the ring topology of model A.

Table 3.3: Ring topology / Phase to earth (20 Ω) fault / F_1.

3-points window	k_{s_1}	k_{s_2}	k_{s_3}	$\lvert\Delta k_{s_{13}}\%\rvert$	FS search	$k_{s_1} > k_{s_2}$	$k_{s_2} > k_{s_3}$
A-B-C	8.83	8.65	8.64	2.18%		'1'	'1'
B-C-D	8.65	8.64	8.64	0.08%	→	'1'	'0'
C-D-E	8.64	8.64	9.01	4.13%		'0'	'0'
D-E-F	8.64	9.01	9.014	4.15%		'0'	'0'

In case there are more than one of such windows, the one with the maximum absolute value of percentage difference, $\lvert\Delta k_{s_{13}}\%\rvert$ is picked denoting the MV FS. However, if the 3-points-window containing the pair *'1'-'0'*, refers to an MV zone where an MV lateral is connected then additional steps need to be followed. Under this condition,

the radial topologies logic - explained previously - will be applied in two separate radial circuits. The two upstream ends of these circuits will be the two edge points of the previously identified 3-points window. The downstream end is common for both, as it is the last measurement point of the MV lateral. As discussed in section 3.3.4, the windows with *'1'-'0'* or *'1'-'1'* in both resulted radial circuits have to be identified. The one with the highest percentage difference, $|\Delta k_{s_{13}}\%|$ contains the FS. In this case (fault location on MV lateral), the algorithm is capable to locate the FS between two transformers as happens in normal radial networks.

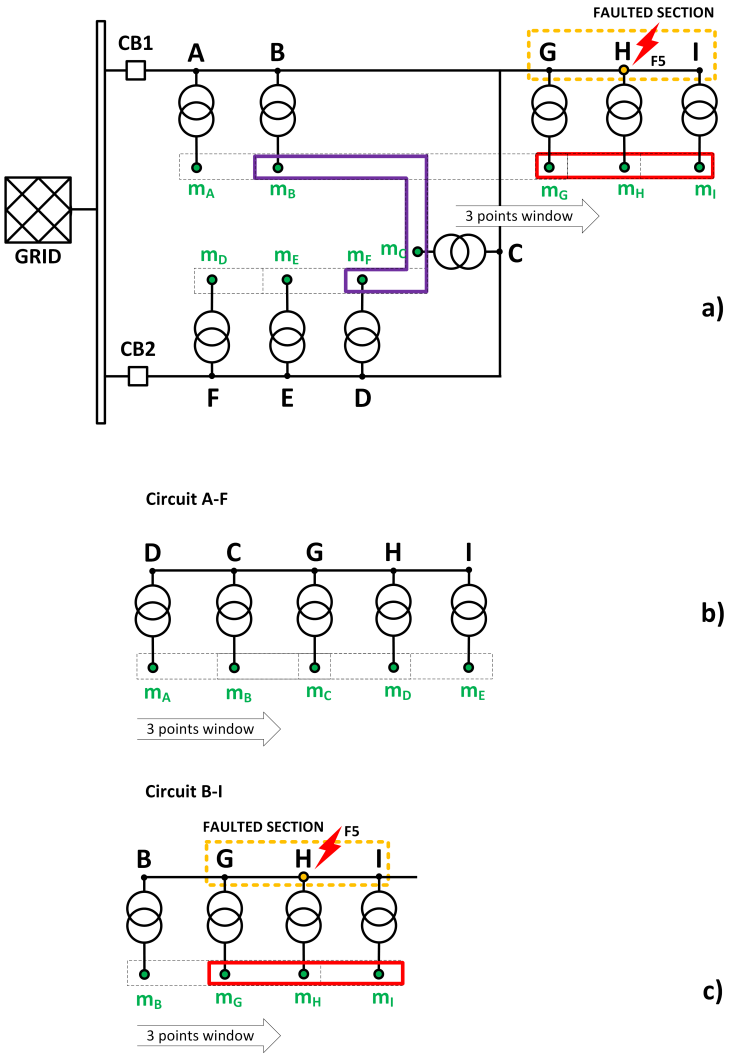

Figure 3.15: The "moving" 3-points window after a 20 Ω phase-to-earth fault is simulated in the radial topology of model B.

Fig. 3.15 shows an example network configured in ring topology with a fault at location F_5. According to Table 3.4, the window with the indicators pair *'1'-'0'*, identified within the ring circuit *A-B-C-D-E-F*, is the *B-C-D*. The corresponding MV zone (*B-C-D*) includes the connection of an MV lateral. The window *B-C-D*, in Fig. 3.15, indicating the pair *'1'-'0'* is marked with a purple frame. Also, the corresponding cell in Table 3.4, is coloured in purple.

Table 3.4: Ring topology / Phase to earth (20 Ω) fault / F_5.

Circuit	3-points window	k_{s_1}	k_{s_2}	k_{s_3}	$\lvert\Delta k_{s_{13}}\%\rvert$	FS search	$k_{s_1} > k_{s_2}$	$k_{s_2} > k_{s_3}$
Ring A-F	A-B-C	9.328	9.126	9.109	2.38%		'1'	'1'
	B-C-D	9.126	9.109	9.112	0.15%	↓↓	'1'	'0'
	C-D-E	9.109	9.112	9.53	4.55%		'0'	'0'
	D-E-F	9.112	9.53	9.541	4.57%		'0'	'0'
Radial B-I	B-G-H	9.126	9.078	7.626	17.42%	↓	'1'	'1'
Radial D-I	D-C-G	9.112	9.109	9.078	0.374%	↓	'1'	'1'
	C-G-H	9.109	9.078	7.626	17.236%	↓	'1'	'1'
B-I & D-I	G-H-I	9.078	7.626	7.626	17.9%	→ →	'1'	'0'

Subsequently, two radial circuits are examined starting from the two edge points of the highlighted window towards the end of the lateral i.e. *D-I* and *B-I*. Table 3.4 shows that the window *G-H-I*, which is common for both radial circuits *B-I* and *D-I*, contains the pair *'1'-'0'* and also the largest $\Delta k_{s_{13}}\%$ among the rest. Therefore, the FS is located between the transformers T_G and T_H, as it can be remarked in both Table 3.4 (cell highlighted in red) and Fig. 3.15.

3.4 Chapter summary

This chapter presented a novel MV FS location technique based on LV measurements acquired from secondary substations. The first part of this chapter justifies the use of the key algorithm parameter, k_s, through a data-driven study and theoretical analysis. The selected results from the preliminary study illustrate the voltage magnitude and angle profiles during fault conditions, their deviation in respect to the pre-fault values, the profiles of positive and negative sequence components during faults as well as the

impact of the faults on the sequence components values and the parameter k_s. The mentioned observations along with the fault analysis indicated that the positive over negative sequence component ratio constitute a strong factor for the localisation of the FS at the MV part of the network when asymmetrical faults occur.

Moreover, the section 3.3 describes thoroughly the principal elements and the architecture of the FS algorithm. One important feature of the technique is the capability to discriminate the fault period within the LV data-sets acquired from each monitoring point. This capability enables the alignment of the distributed measurements without the need of dedicated synchronisation technology such as GPS. Finally, the logic of the algorithm for both radial and ring topologies is explained through example simulated fault cases.

3.5 References

[1] SPEN, "LV Network Monitoring - ED2 Engineering Justification Paper." `https://bit.ly/3sA7KNX`, 2021.

[2] ESBN, "Local network visibility multiyear plan." `https://bit.ly/35ynzvg`, 2021.

[3] P. Bountouris, H. Guo, I. Abdulhadi, and F. Coffele, "Medium voltage fault location using distributed LV measurements," in *14th International Conference on Developments in Power System Protection (DPSP)*, pp. 1–6, March 2018.

[4] P. Bountouris, H. Guo, D. Tzelepis, I. Abdulhadi, F. Coffele, and C. Booth, "MV faulted section location in distribution systems based on unsynchronized LV measurements," *International Journal of Electrical Power and Energy Systems*, vol. 119, 2020.

[5] J. M. Gers and E. J. Holmes, *Protection of electricity distribution networks*. IET, 2011.

[6] A. Amberg and A. Rangel, *Tutorial on Symmetrical Components Part 2: Answer Key*. Schweitzer Engineering Laboratories, 2020. `https://selinc.com/api/download/100688`.

[7] S. Mallat and W. L. Hwang, "Singularity detection and processing with wavelets," *IEEE Transactions on Information Theory*, vol. 38, pp. 617–643, March 1992.

[8] D. Tzelepis, G. Fusiek, A. Dysko, P. Niewczas, C. Booth, and X. Dong, "Novel fault location in MTDC grids with non-homogeneous transmission lines utilizing distributed current sensing technology," *IEEE Transactions on Smart Grid*, 2017.

[9] T. Guo, T. Zhang, E. Lim, M. López-Benítez, F. Ma, and L. Yu, "A review of wavelet analysis and its applications: Challenges and opportunities," *IEEE Access*, vol. 10, pp. 58869–58903, 2022.

[10] V. Psaras, D. Tzelepis, D. Vozikis, G. P. Adam, and G. Burt, "Non-Unit Protection for HVDC Grids: An Analytical Approach for Wavelet Transform-Based Schemes," *IEEE Transactions on Power Delivery*, vol. 36, no. 5, pp. 2634–2645, 2021.

Chapter 4

Description of modelling and simulation approach and assumptions

4.1 Chapter overview

This chapter first presents the modelling of a distribution system in a software simulation environment. The developed model represents the existing distribution network of PNDC. It is built in DigSILENT Powerfactory to enable transient analysis, including asymmetrical, solid and resistive MV faults. It is noted that the protection functions are not modelled but circuit-breakers are pre-set to operate within a defined duration (100 ms) after the fault occurs. The model is configured in different ways in order to take into account realistic network conditions i.e. the presence of MV laterals. Furthermore, this chapter outlines the modelling methodology and simulations scenarios which involve the connection of DGs at both MV and LV parts of the grid. For this purpose, a model to represent inverter-interfaced DG built in MATLAB Simulink is introduced, emulating the behaviour of a real PV inverter during fault conditions.

4.2 Developed models

The simulation studies as well as the hardware based experiments, which supported the modelling work of this thesis, were funded by the industrial partners of PNDC via the following projects:

- "LV sensing for the location of 11 kV faults"
- "Testing LV PV Inverters Stability during Voltage Magnitude and Vector Shift Disturbances"
- "Generic Inverter Dynamic Model Development and Validation through Hardware Testing"

Throughout the PNDC project with title "LV sensing for the location of 11 kV faults", the DIgSILENT Powerfactory software was required for the conduction of the fault location study. Moreover, the project with title "Generic Inverter Dynamic Model Development and Validation through Hardware Testing" involved the modelling of a commercially available PV inverter in Matlab Simulink. For the purpose of this thesis, additional experimentation was conducted in two ways. First, the model of the project "LV sensing for the location of 11 kV faults" was updated by adding MV laterals, unbalanced loads and connected DGs to the distribution network. Secondly, the same distribution network was re-modelled in Matlab Simulink, in order to deploy the PV inverter model developed throughout the project with title "Generic Inverter Dynamic Model Development and Validation through Hardware Testing". By this way, an active distribution network was represented, which constitutes the research area of this thesis. As a result, three models have been built; the Model A and Model B in DigSILENT Powerfactory and the Model C in Matlab Simulink.

4.2.1 Model A

In this section, model A represents the 11 kV distribution network of PNDC. The single line diagram shown in Fig. 4.1 depicts the network configuration which has been modelled in DigSILENT Powerfactory [1]. The fault level of the system is 26.5 MVA.

The indicated normally open (NO) switch provides the option of emulating radial or ring topologies, similar to the real PNDC network. The CBs located at the 11 kV busbar will isolate the network when a fault occurs within 100 ms. The black dots m_A to m_F represent the monitoring points retrieving the required measurements at the LV side of the transformers during fault conditions. The loading level is defined at approximately 80% of the maximum load (600 kVA), that can be achieved with the aid of the available load-banks in PNDC.

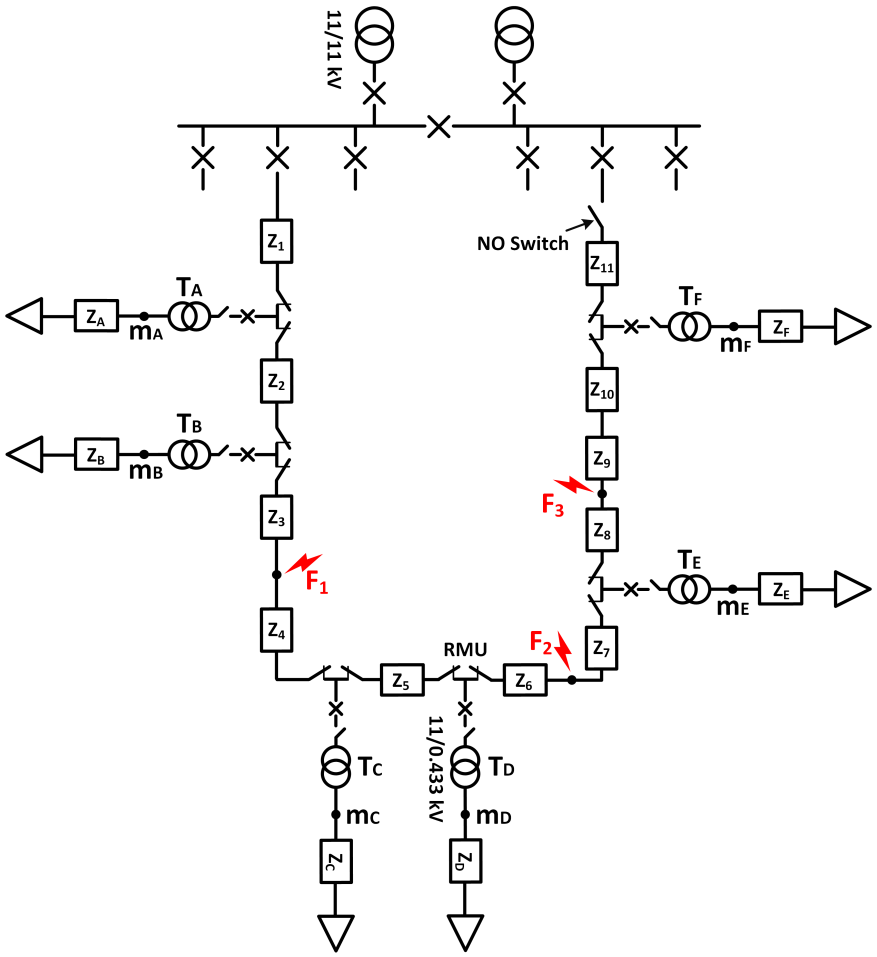

Figure 4.1: Simulated ring/radial PNDC network.

Appendix A contains all associated parameters of the various PNDC network elements used for model tuning purposes, based on the relevant datasheets and documentation. Tables B.3-A.3 of Appendix A include the following information:

- Table B.3: Impedance values Z_1-Z_{11} and Z_A-Z_F of MV and LV side respectively, of the underground cables, overhead lines and mock impedances.
- Table A.2: Impedance values of the delta-wye configured step-down (11/0.433 kV) transformers, T_A to T_F.
- Table A.3: LV loads connected to the transformers T_A to T_F.

4.2.2 Model B

This section presents a second network model as a variation of model A. The configuration of the simulated system, naming model B, is depicted in Fig. 4.2. It is an expanded version of model A, focusing on the presence of an MV lateral, unbalanced loads and DG connections in order to better reflect the complexity of real distribution systems. The new MV conductor is located between the T_B and T_C carrying three additional step-down transformers, T_G, T_H and T_I, with connected LV loads. The details of the MV lateral elements are included in Tables A.4, A.5 and A.6 of Appendix A:

- Table A.4: Impedance values Z_{12}-Z_{41} and Z_G-Z_I of MV and LV side respectively, of the underground cables, overhead lines and mock impedances.
- Table A.5: Impedance values of the delta-wye configured step-down (11/0.433 kV) transformers, T_G to T_I.
- Table A.6: LV loads connected to the transformers T_G to T_I.

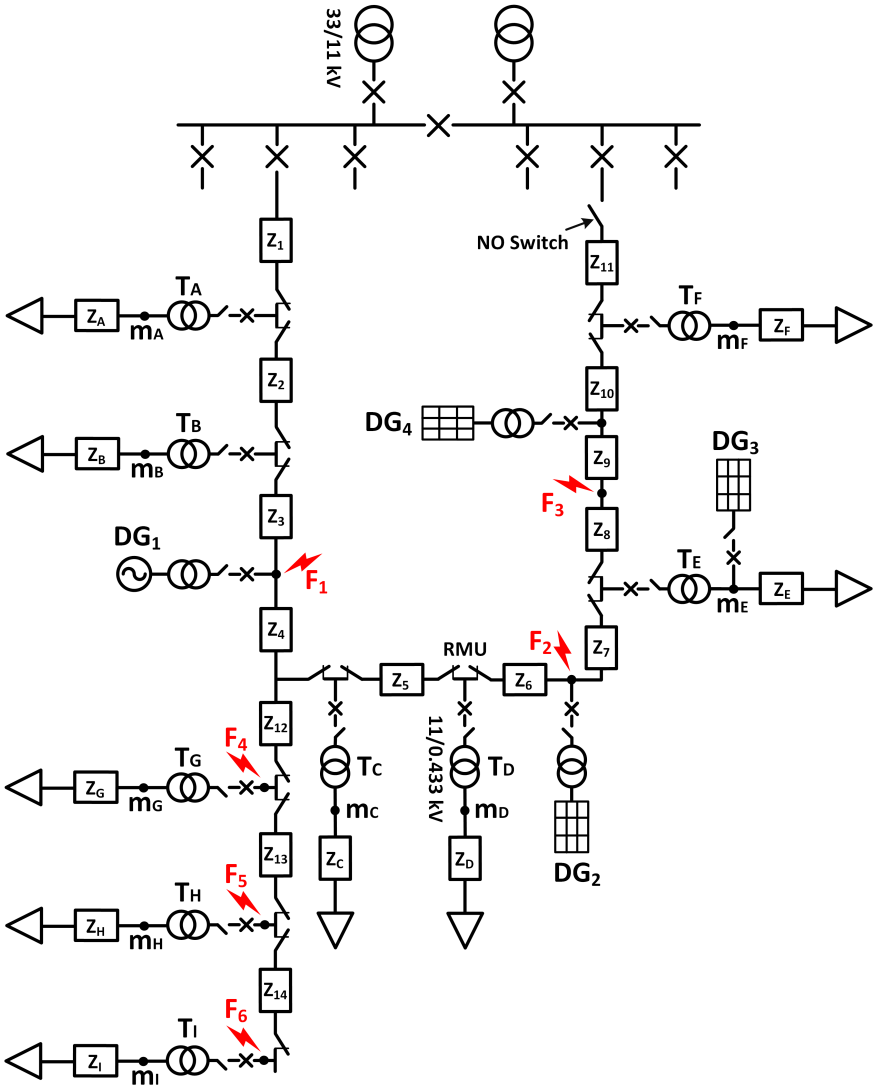

Figure 4.2: Simulated network with MV lateral.

4.2.3 Model C

Model C represents an active distribution network dominated by small scale LV connected PV systems, with a combined capacity of 495 kVA against a total overall system load of 580 kVA (85.3%). The network configuration based on this of model B and the PV connection points are depicted in Fig. 4.3. The inverter model interfacing the integrated PVs with the developed network, emulates the behaviour of an existing grid-tied off-the-shelf PV inverter during faults. The particular model is developed in MATLAB

Simulink [2].

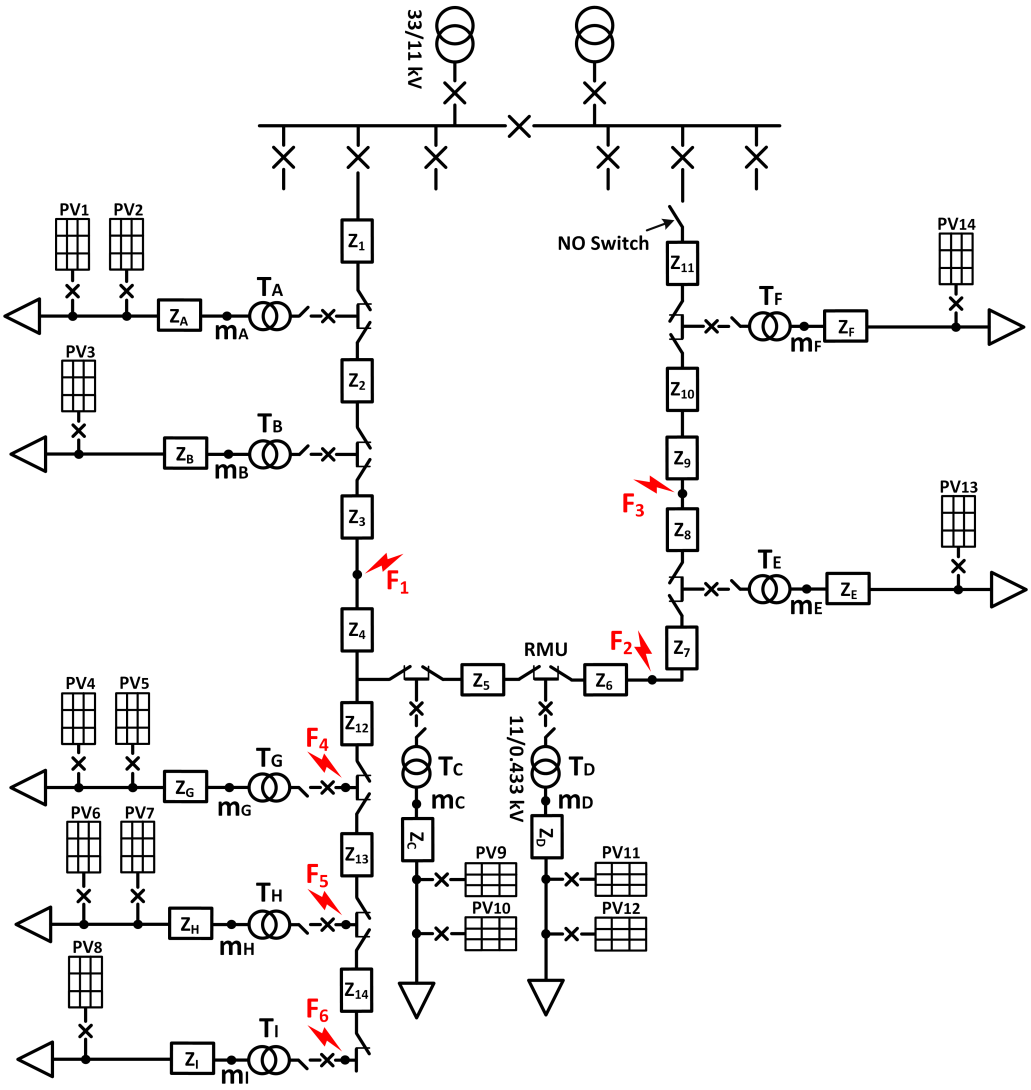

Figure 4.3: Simulated network with multiple PVs.

4.3 Simulation scenarios

Numerous simulation scenarios have been implemented with the aid of models A-C, to assess the performance of the proposed faulted section location algorithm. Table 4.1 lists different conditions and network configurations where asymmetrical faults of various types and locations have been introduced. The implemented fault resistances align

with the minimum fault resistances of 20 Ω and 60 Ω that can be achieved in the PNDC network for phase-earth and phase-phase faults respectively.

Table 4.1: Simulation scenarios.

Scenarios	**Model**	**Topology**	**Fault type**	**Fault resistance**	**Fault locations**
Distribution network of PNDC					
1.1-1.3	A	radial	phase-earth	0 Ω	F_1-F_3
1.4-1.6	A	radial	phase-earth	20 Ω	F_1-F_3
1.7-1.9	A	radial	phase-phase	0 Ω	F_1-F_3
1.10-1.12	A	radial	phase-phase	60 Ω	F_1-F_3
1.13-1.15	A	ring	phase-earth	0 Ω	F_1-F_3
1.16-1.18	A	ring	phase-earth	20 Ω	F_1-F_3
1.19-1.21	A	ring	phase-phase	0 Ω	F_1-F_3
1.22-1.24	A	ring	phase-phase	60 Ω	F_1-F_3
Distribution network with MV lateral					
2.1-2.6	B	radial	phase-earth	0 Ω	F_1-F_6
2.7-2.12	B	radial	phase-earth	20 Ω	F_1-F_6
2.13-2.18	B	radial	phase-phase	0 Ω	F_1-F_6
2.19-2.24	B	radial	phase-phase	60 Ω	F_1-F_6
2.25-2.30	B	ring	phase-earth	0 Ω	F_1-F_6
2.31-2.36	B	ring	phase-earth	20 Ω	F_1-F_6
2.37-2.42	B	ring	phase-phase	0 Ω	F_1-F_6
2.43-2.48	B	ring	phase-phase	60 Ω	F_1-F_6
Distribution network with 1% load unbalance					
3.1-3.6	B	radial	phase-earth	0 Ω	F_1-F_6
3.7-3.12	B	radial	phase-earth	20 Ω	F_1-F_6
3.13-3.18	B	radial	phase-phase	0 Ω	F_1-F_6
3.19-3.24	B	radial	phase-phase	60 Ω	F_1-F_6

Continued on next page

Table 4.1 – *Continued from previous page*

Scenarios	**Model**	**Topology**	**Fault type**	**Fault resistance**	**Fault locations**
Distribution network with 2% load unbalance					
3.25-3.30	B	radial	phase-earth	0 Ω	F_1-F_6
3.31-3.36	B	radial	phase-earth	20 Ω	F_1-F_6
3.37-3.42	B	radial	phase-phase	0 Ω	F_1-F_6
3.43-3.48	B	radial	phase-phase	60 Ω	F_1-F_6
Distribution network with 3% load unbalance					
3.49-3.54	B	radial	phase-earth	0 Ω	F_1-F_6
3.55-3.60	B	radial	phase-earth	20 Ω	F_1-F_6
3.61-3.66	B	radial	phase-phase	0 Ω	F_1-F_6
3.67-3.72	B	radial	phase-phase	60 Ω	F_1-F_6
Distribution network with 4% load unbalance					
3.73-3.78	B	radial	phase-earth	0 Ω	F_1-F_6
3.79-3.84	B	radial	phase-earth	20 Ω	F_1-F_6
3.85-3.90	B	radial	phase-phase	0 Ω	F_1-F_6
3.91-3.96	B	radial	phase-phase	60 Ω	F_1-F_6
Distribution network with connected DGs (synchronous and inverter based)					
4.1-4.6	B	radial	phase-earth	0 Ω	F_1-F_6
4.7-4.12	B	radial	phase-earth	20 Ω	F_1-F_6
4.13-4.18	B	radial	phase-phase	0 Ω	F_1-F_6
4.19-4.24	B	radial	phase-phase	60 Ω	F_1-F_6
Active distribution network dominated by LV connected PV systems					
4.25-4.30	C	radial	phase-earth	0 Ω	F_1-F_6
4.31-4.36	C	radial	phase-earth	20 Ω	F_1-F_6
4.37-4.42	C	radial	phase-phase	0 Ω	F_1-F_6
4.43-4.48	C	radial	phase-phase	60 Ω	F_1-F_6

All simulations have been performed using a time-step of 100 us, which corresponds

to a sampling frequency of 10 kHz. The selected sampling rate provides much higher resolution than the minimum required for monitoring faults in real networks. According to [3], the minimum consideration for the utilities when deciding the sampling rate for transient records should be 960 samples per second, which is approximately 20 samples/cycle for a 50 Hz system and 16 samples/cycle for a 60 Hz system. The former corresponds to a time-step of 1 ms, which is ten times longer than the time-step implemented in this study.

4.3.1 Distribution network of PNDC

Simulation scenarios 1.1 - 1.24 have been performed using the emulated radial and ring topologies of the PNDC network represented via model A [4], [5]. Specifically, both solid and resistive phase-to-earth and phase-to-phase faults at three different locations, F_1, F_2 and F_3, - depicted at Fig. 4.1 - were applied at the MV part of the network. The LV voltage measurements were extracted to evaluate the proposed algorithm.

4.3.2 Distribution network with MV lateral

Simulation cases 2.1 - 2.48 were performed with the aid of model B to examine the FS location technique in a faulted distribution network with a connected MV lateral [5]. In addition to the faults applied in model A, three new fault locations, F_4, F_5 and F_6 were introduced to the added MV part, as illustrated in Fig. 4.2. It is underlined that the DGs shown in Fig. 4.2, were not connected during the specific scenarios and the focus was put on the different topologies (radial, ring) of the particular network.

4.3.3 Distribution network with load unbalance

In real distribution networks, three and single phase loads are normally present resulting in load unbalance. TNEI, a UK consultancy company, analysed a total of 89 LV substations with 233 feeders within the business area of the Scottish Power Energy Networks (SPEN) in the UK [6]. They found that 165 out of these 233 LV feeders suffer from significant phase unbalance, where the mean ratio of the phase current to the average current for all three phases is greater than 1.3 [6]. Phase unbalance reflects

on voltage at the LV part of the network, causing negative sequence components to rise in steady-state conditions. This effect will be magnified during faults with large fault impedances resulting in relatively smaller fault currents with value similar to the load currents [7].

The dependence of the proposed algorithm on the LV voltage symmetrical components increases the significance of considering pre-fault load unbalance during simulations. To illustrate this phenomenon, simulation scenarios 3.1 - 3.96 deployed four levels of apparent power unbalance, 1%, 2%, 3% and 4%, by parametrising the loads of model B [5]. 4% is the minimum level of load unbalance which led the developed FS location technique to produce false results under resistive faults. Therefore, 4% of load unbalance was the maximum percentage applied during simulations. Equation (4.1) is implemented for the calculation of load unbalance [8].

$$S_{unb}(\%) = \frac{\max\{|S_a - \overline{Sabc}|, |S_b - \overline{Sabc}|, |S_c - \overline{Sabc}|\}}{\overline{Sabc}} \tag{4.1}$$

The mentioned levels of unbalance were applied on the loads *G*, *C*, *D*, *E* and *F*. Tables 4.2-4.4 include the active and reactive power measurements captured from each phase of the asymmetrical loads.

Table 4.2: Maximum load unbalance 1%: Active & reactive power per phase.

Load	P_A (kW)	Q_A (kVAr)	P_B (kW)	Q_B (kVAr)	P_C (kW)	Q_C (kVAr)
A	50.66	16.65	50.66	16.65	50.66	16.65
B	25.33	8.33	25.33	8.33	25.33	8.33
C	15.83	5.2	15.67	5.15	15.99	5.26
D	12.54	4.12	12.67	4.16	12.79	4.2
E	12.79	4.2	12.67	4.16	12.54	4.12
F	12.41	4.08	12.67	4.16	12.67	4.16
G	15.67	5.15	15.83	5.2	15.99	5.26
H	31.67	10.4	31.67	10.4	31.67	10.4

Continued on next page

Table 4.2 – *Continued from previous page*

Load	P_A (kW)	Q_A (kVAr)	P_B (kW)	Q_B (kVAr)	P_C (kW)	Q_C (kVAr)
I	12.67	4.16	12.67	4.16	12.67	4.16

Table 4.3: Maximum load unbalance 2%: Active & reactive power per phase.

Load	P_A (kW)	Q_A (kVAr)	P_B (kW)	Q_B (kVAr)	P_C (kW)	Q_C (kVAr)
A	50.66	16.65	50.66	16.65	50.66	16.65
B	25.33	8.33	25.33	8.33	25.33	8.33
C	15.83	5.2	15.52	5.1	16.15	5.31
D	12.41	4.1	12.67	4.16	12.92	4.24
E	12.92	4.24	12.67	4.16	12.41	4.1
F	12.41	4.08	12.67	4.16	12.92	4.24
G	15.52	5.1	15.83	5.2	16.15	5.31
H	31.67	10.4	31.67	10.4	31.67	10.4
I	12.67	4.16	12.67	4.16	12.67	4.16

Table 4.4: Maximum load unbalance 3%: Active & reactive power per phase.

Load	P_A (kW)	Q_A (kVAr)	P_B (kW)	Q_B (kVAr)	P_C (kW)	Q_C (kVAr)
A	50.66	16.65	50.66	16.65	50.66	16.65
B	25.33	8.33	25.33	8.33	25.33	8.33
C	16.32	5.36	15.36	5	15.83	5.2
D	12.29	4.04	12.67	4.16	13.05	4.29
E	13.05	4.29	12.67	4.16	12.29	4.04
F	12.29	4.04	12.67	4.16	13.05	4.29

Continued on next page

Table 4.4 – *Continued from previous page*

Load	P_A (kW)	Q_A (kVAr)	P_B (kW)	Q_B (kVAr)	P_C (kW)	Q_C (kVAr)
G	15.36	5	15.83	5.2	16.32	5.36
H	31.67	10.4	31.67	10.4	31.67	10.4
I	12.67	4.16	12.67	4.16	12.67	4.16

Table 4.5: Maximum load unbalance 4%: Active & reactive power per phase.

Load	P_A (kW)	Q_A (kVAr)	P_B (kW)	Q_B (kVAr)	P_C (kW)	Q_C (kVAr)
A	50.66	16.65	50.66	16.65	50.66	16.65
B	25.33	8.33	25.33	8.33	25.33	8.33
C	15.83	5.2	15.67	5.15	15.99	5.26
D	12.54	4.12	12.67	4.16	12.79	4.2
E	12.79	4.2	12.67	4.16	12.54	4.12
F	12.16	3.99	13.17	4.33	12.67	4.16
G	15.67	5.15	15.83	5.2	15.99	5.26
H	31.67	10.4	31.67	10.4	31.67	10.4
I	12.67	4.16	12.67	4.16	12.67	4.16

Fig. 4.4-4.7 illustrate the pre-fault active and reactive power profile of each phase when unbalances of 1%, 2%, 3% and 4%. The magnified parts of the plots highlight the deviation among the three phases of randomly selected loads.

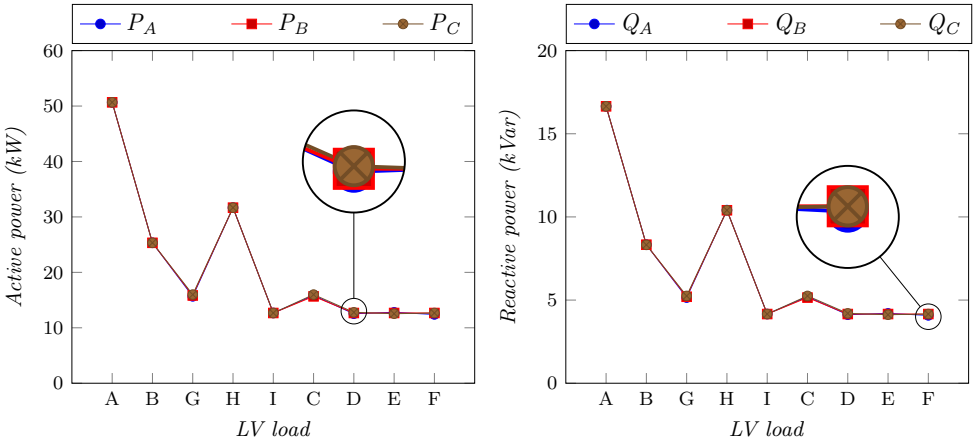

Figure 4.4: Per-phase load profile with maximum load unbalance of 1%.

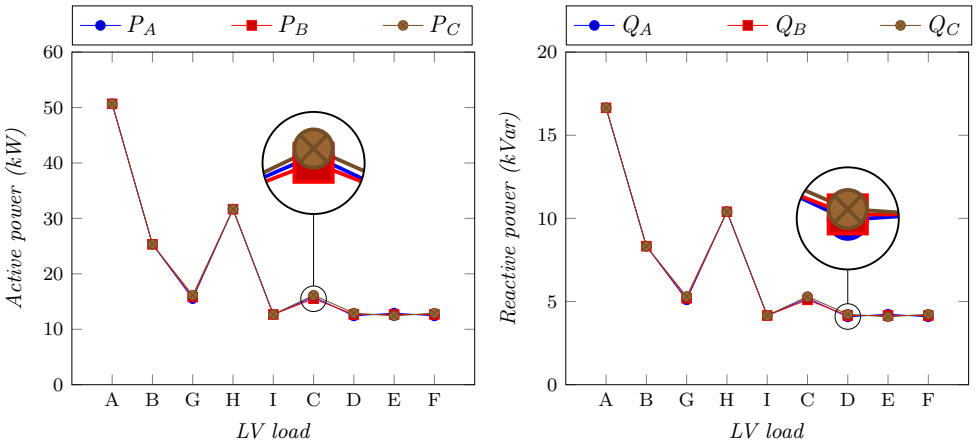

Figure 4.5: Per-phase load profile with maximum load unbalance of 2%.

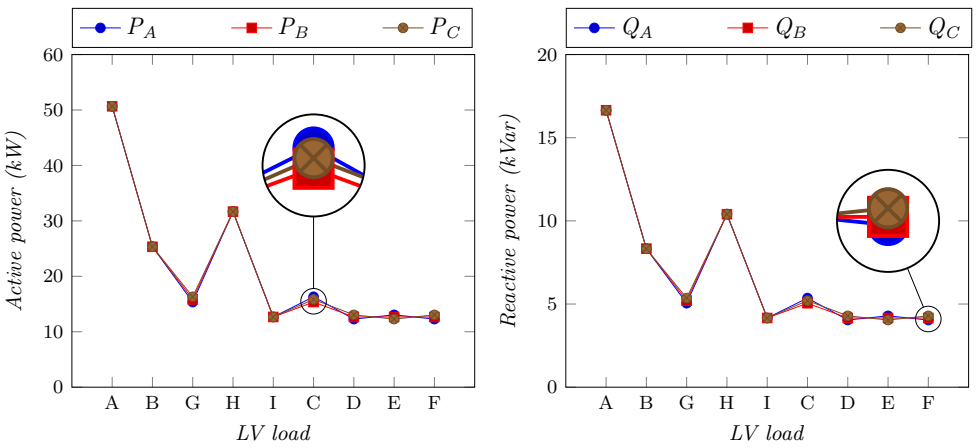

Figure 4.6: Per-phase load profile with maximum load unbalance of 3%.

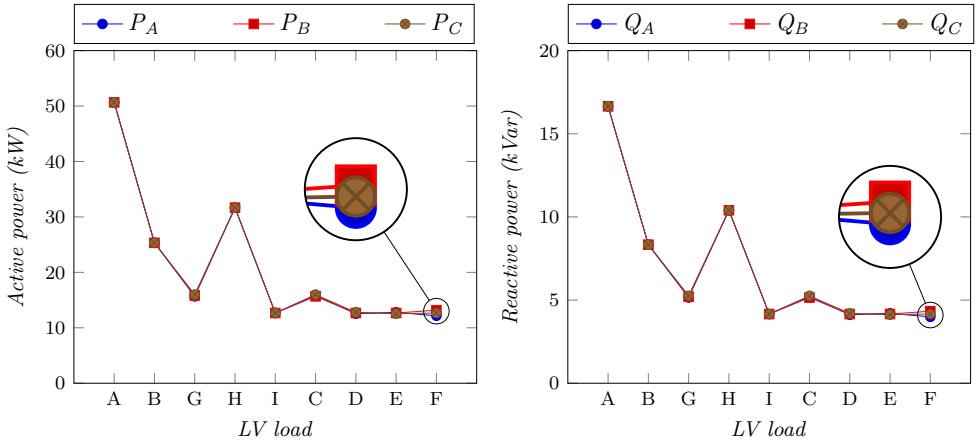

Figure 4.7: Per-phase load profile with maximum load unbalance of 4%.

4.3.4 Network topologies with distributed generation

The work introduced in this section aims to examine the performance of the algorithm in distribution networks with DGs with the aid of simulation scenarios 4.1 - 4.48. The first part, in Section 4.3.4.1, focuses on the presence of synchronous DG and PV plants from 50 to 500 kVA [4, 5]. The second part, in Section 4.3.4.2, examines the 85.3% penetration - in terms of total capacity versus maximum demand - of small scale LV connected photovoltaic systems. The latter is achieved with the aid of a dynamic model developed for the purpose of this study, which reflects the behaviour of a commercially available inverter. The model is validated against hardware testing [9].

4.3.4.1 Synchronous generation and PV plants

Scenarios 4.1 - 4.24 were performed with the aid of model B, where a Synchronous Generator (SG) and three PV systems are connected at both 11 kV and LV parts of the network. These are implemented with the default configuration and parameters provided by DIgSILENT Powerfactory. The connection points of the DGs listed in Table 4.6, are illustrated in Fig. 4.2.

The SG deployed in this study, is a DIgSILENT Powerfactory synchronous machine model. The Technical Reference Document for Synchronous Machine [10] is part of the software documentation, providing a detailed description of load flow and short

Table 4.6: Distributed generation

DG	Generation type	Network part	Capacity (kVA)
DG_1	SG	MV (11 kV)	50
DG_2	PV plant	MV (11 kV)	500
DG_3	PV plant	LV (0.433 kV)	50
DG_4	PV plant	MV (11 kV)	300

circuit analysis as well as all the associated model equations. For short-circuit analysis, synchronous machines are represented by the following equivalent circuits depending on the considered time phase throughout a grid fault:

- Subtransient equivalent
- Transient equivalent
- Synchronous equivalent

The distinction of the time dependence is due to the effect of increased stator currents on the induced currents in the damper windings, rotor mass and field winding. In the case of a fault near to a generator the stator current can increase so that the resulting magnetic field weakens the rotor field considerably. In steady state short circuit analysis, this field-weakening effect is represented by the corresponding equivalent source voltage and reactance. The associated positive sequence model of a synchronous machine is shown in Fig. 4.8. The delayed effect of the stator field on the excitation and damping field is modelled by using different reactances depending on the time frame of the calculation [10].

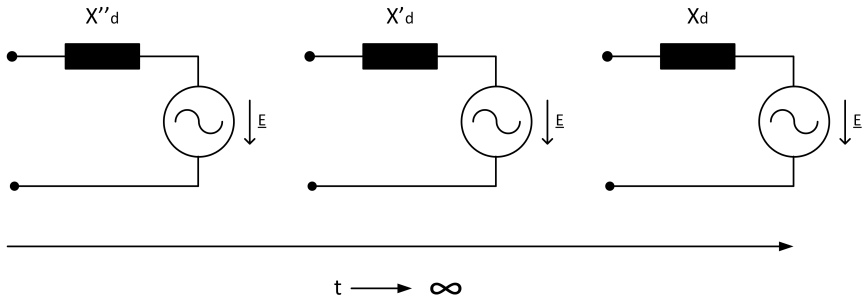

Figure 4.8: Powerfactory single-phase equivalent circuit diagrams of a generator for short-circuit current calculations which include the modelling of the field attenuation [10].

The Powerfactory short-circuit calculations are based on the IEC 60909 standard [11]. IEC 60909 only calculates the subtransient time phase. According to the Powerfactory documentation [10], short-circuit currents of longer time phases are assessed based on empirical methods by multiplying the subtransient fault current with corresponding factors. Fig. 4.9 depicts the basic IEC 60909 short circuit model of a synchronous machine.

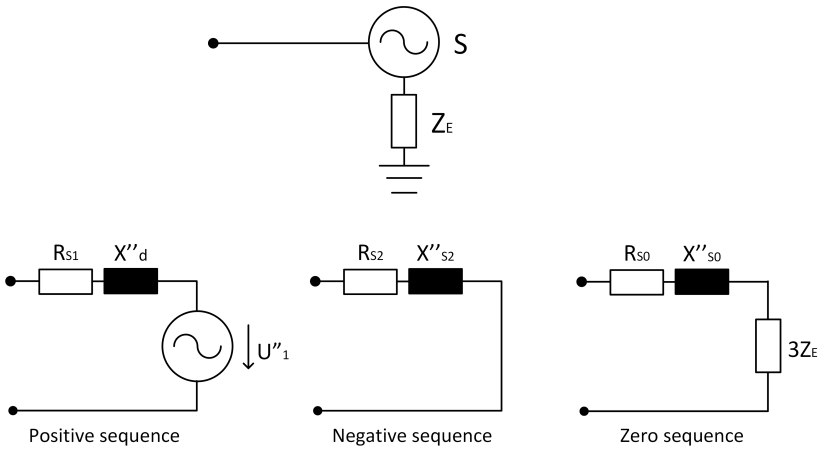

Figure 4.9: Powerfactory short-circuit model for a synchronous machine [10].

When calculating initial symmetrical short-circuit currents in systems fed directly from generators without unit transformers, for example in industrial networks or in low-voltage networks, the following impedances have to be used [10]:

Positive sequence system:

$$Z_{S1} = R_S + jX_d" \tag{4.2}$$

Negative sequence system:

$$Z_{S2} = R_S + jX_2" = R_S + jX_2 \tag{4.3}$$

Normally it is assumed that $X_2 = X_d"$. If $X_d"$ and $X_q"$ differ significantly the following can be used:

$$Z_{S2}" = X_2 = \frac{1}{2}(X_d" + X_q") \tag{4.4}$$

Zero sequence system:

$$Z_{S0}" = R_{S0} + jX_{S0}" \tag{4.5}$$

All other short circuit indices are also calculated according to the IEC 60909 (VDE 102/103) standard [10, 11].

Moreover, the PV plants listed in Table 4.6, are represented by the DIgSILENT Powerfactory modelling component "static generator". This consists of an array of photovoltaic panels, connected to the grid through a single inverter. In static generators, the negative sequence is only considered for technologies 3Ph (3-wire) and 3Ph-E (4-wire) [12]. The zero sequence is only considered for the technology 3Ph-E. In this case, the selected connection technology is 3Ph. The negative sequence model of the static generator is depicted in Fig. 4.10. Details with regards to the load flow and short circuit analysis of the particular component are provided in the Technical Reference Document [12].

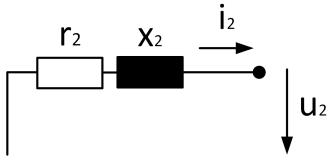

Figure 4.10: Negative-Sequence Model for 3Ph and 3Ph-E technology [12].

PV inverters connected in distribution networks do not normally have the capability of injecting negative sequence output current, i_2, during asymmetrical faults [13–15]. The controls of this type of inverters maintain a pre-established angular relationship between phase voltage and current during normal and fault conditions. The inverter phase locked loop (PLL) typically provides a balanced phase angle value to each of the three individual phase currents. As such, while the PV inverters may be able to generate currents of unbalanced magnitude they cannot provide an unbalanced phase relationship between individual phases. Therefore, the inverter controls are configured to produce only positive sequence currents [14].

Furthermore, FRT is the capability of the DGs to be able to remain connected to the system and operate through periods of voltage dips caused by network faults. To ensure that, the grid codes of the various countries prescribe FRT requirements [16]. The DGs implemented in this section belong to the category Type A (800W – 1MW) Power Generating Modules (PGM), as defined by the GB Grid Code [17]. In particular, the synchronous generator and the PV system are referred with the term Synchronous PGM and Power Park Module (PPM) respectively. According to [17], there are no specific FRT requirements for Type A PGM, either Synchronous or PPM.

Fig. 4.11 depicts a generic FRT or Low Voltage Ride Through (LVRT) characteristic. Whenever a generation unit operates in steady state conditions the output voltage (i.e. V_n) is maintained within the area A of the curve. During a fault at time t_0, the generating unit encounters a voltage sag i.e. V_0. Typically, the shortest time for which the PV generation is required to remain grid-connected for maximum depression down to 0% of rated voltage is 150 ms i.e. t_1 - t_0 in Area B of the curve [16]. If the fault is removed within the mentioned period i.e. at time t_1, then the voltage is requested to recover and reach the nominal value i.e. V_{n0}. However if the voltage drop remains, exceeding Area C of the curve, the generating unit can be disconnected from the grid.

Since there is no specific GB Grid Code requirement for LVRT/FRT considering Type A PGM and the fault period of the implemented simulation scenarios is 100 ms, the DGs presented in this section remained connected to the grid under any voltage depression caused by the applied faults.

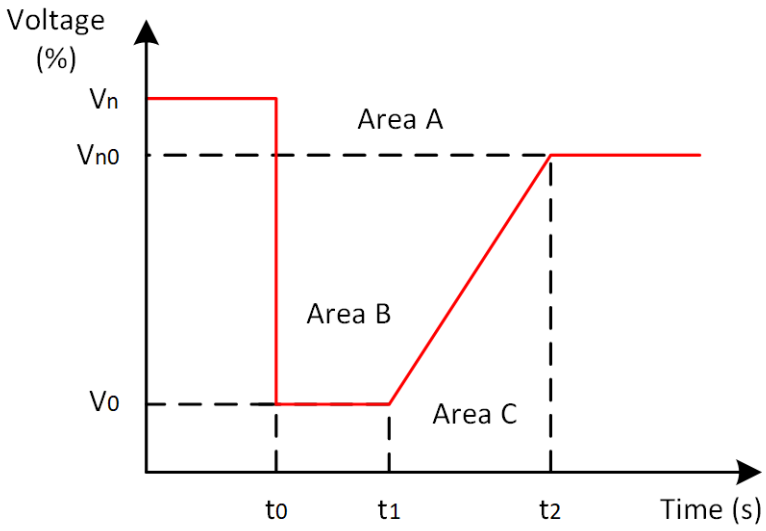

Figure 4.11: Typical FRT/LVRT curve.

Fig. 4.12 illustrates the reactive power capability of the PV systems modelled in Powerfactory in relation to the produced active power. According to Engineering Recommendation G99, the PGM shall be capable of operating at a power factor (pf) within the range 0.95 lagging to 0.95 leading relative to the voltage waveform [18].

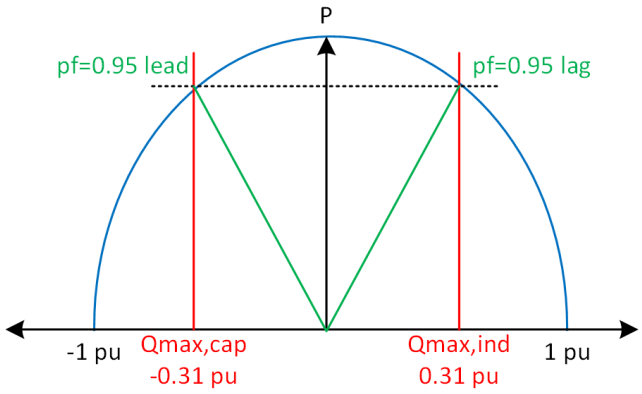

Figure 4.12: PV system reactive power capability.

Voltage control via the injection of reactive power is required by DNOs across the world, depending on the capacity of the DG. An example of Q(U) droop characteristic, as defined by the German Grid Code, is illustrated in Fig. 4.13 [19]. However, according to G99 the only requirement for a PGM of Type A is to demonstrate immunity to

voltage changes of ± 10% [18]. Therefore, it is not possible to define specific Q(U) droop control setpoints at the PV system models used in the simulation scenarios of this section.

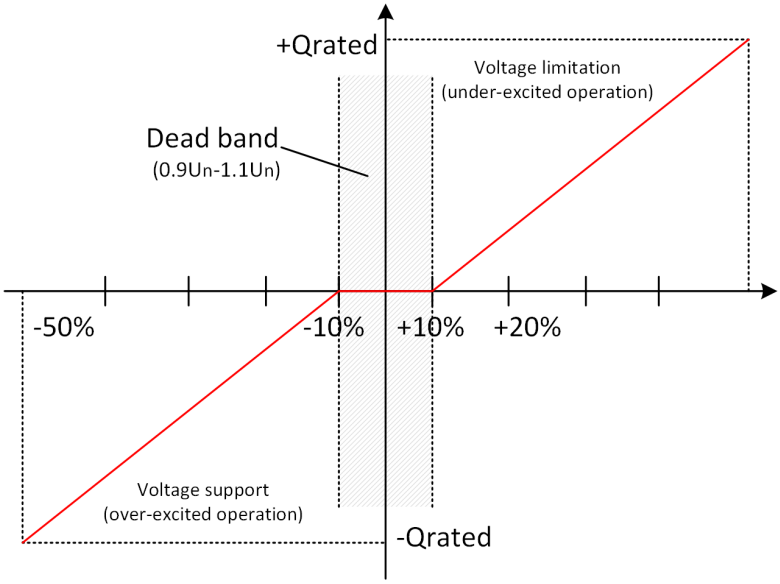

Figure 4.13: Voltage support of PV system during fault event [19].

4.3.4.2 Dynamic modelling of a commercially available inverter

The increasing penetration of PVs in the bulk power system has led to the growing need for better understanding the behaviour of PV inverters during fault conditions. On top of that, the evident inconsistencies in inverter operation across LV connected PV inverters of various manufacturers indicate the risk of invalid assumptions when system studies are conducted [20–23].

An increasing number of bench testing studies reported in the literature examine the behaviour of LV grid-tied PV inverters against grid disturbances. A Loss of Mains (LoM) oriented hardware based study [20] evaluated the PV inverters' grid connection stability during frequency and voltage phase shift events. The Devices Under Test (DUTs) performed similarly with regards to sensitivity and stability during the applied scenarios however, discrepancies were noticed at their active and reactive power output. In addition, several off-the-shelf LV-connected PV inverters of different manufacturers exhibited a wide range of behaviours in [21] and [22], when experimentally tested under

faults and voltage disturbances.

The PV inverters examined in [21] were also tested under voltage magnitude and vector shift (VS) variations in [23]. The findings of [23], collected under the scope of this study, validate the aforementioned concerns regarding the variation in terms of fault response among the different small scale inverters. The testing and resulting inverter connection stability characteristics (VS-retained voltage) are described in Appendix B.

Moreover, the literature has reported a number of studies that attempted to reflect the response of inverters under fault conditions with the aid of simulation models. [24] and [25] implemented bench testing results to validate inverter models for power system dynamic studies. The inverter model presented in [24] operated only at 1 p.u. pre-fault loading level of inverter rating. Furthermore, General Electric (GE) [26], Electric Power Research Institute (EPRI) [27] and the Western Electricity Coordinating Council (WECC) [28, 29] provide guidelines for the development of generic dynamic simulation models emulating transmission connected PV inverters or distribution installed PV plants. However, this approach cannot be inherited for individual small scale PV inverters due to the noted variation of fault responses among different manufacturers.

Therefore, the noted lack of modelling schemes accurately emulating LV-connected PV inverters of various manufacturers, due to the observed inconsistency among the latter, highlights the need of further investigation. This section introduces a novel dynamic model which is implemented to represent real small scale grid-tied PV inverters under fault conditions. The structure and defined adjustable parameters constitute the model flexible to reflect the behaviour of different inverter types, however only one type is used throughout this study. Essential requirement to achieve accurate emulation is the empirical characterisation of the actual inverter supporting both tuning and validation of the model. The ultimate objective of this task is to evaluate the FS location technique in a realistic active distribution network dominated by inverter connected generation under various asymmetrical fault scenarios (scenarios 4.25 - 4.48).

4.3.4.2.1 Proposed methodology

Fig. 4.14 presents the methodology, proposed in this section, which enables the ac-

curate emulation of small scale commercial PV inverters. In particular the steps from the real inverter physical testing to the development and validation of the dynamic model are clearly listed and can be followed for modelling inverters of different manufacturers. The proposed structure and adjustable parameters (i.e. PI gains, P_{ref} and Q_{ref}) constitute the model flexible to reflect the behaviour of different inverter types [9].

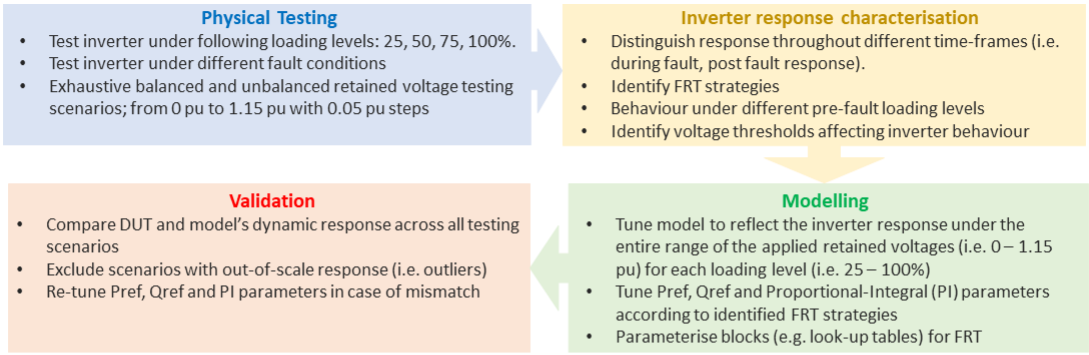

Figure 4.14: Overview of the developed methodology [9].

Physical testing: The experimental testing is an important task supporting both tuning and validation of the model. The inverter is examined under a wide range of voltage scenarios and fault conditions while loaded with different levels (i.e. 25, 50, 75, 100%). This step is an essential requirement in order to achieve empirical characterization of the actual inverter.

Inverter response characterisation: The results extracted during physical testing provide valuable information in order to effectively characterize the fault response of the inverter throughout the various time frames (i.e. during fault, post fault period) of the imposed events. Moreover, this task will enable the identification of the available inverter FRT or Low Voltage Ride Through (LVRT) strategy and the network conditions, such as thresholds of voltage depression, which lead the inverter to the activation of such functions.

Modelling: The results acquired throughout testing and the empirical characterization of the inverter enable wise tuning of the model. The aim is to accurately reflect the identified FRT response of the real device by adjusting the Pref, Qref and PI parameters

depending on the network conditions identified during the previous task (i.e. voltage depression thresholds). It shall be noted that for the tuning exercise, depending on the application and requirements, it would be beneficial to deploy sophisticated methods to allow auto- and adaptive tuning. This is anticipated to introduce certain benefits accounting for minimisation of tuning effort, elimination of potential instabilities and improvement of transient performance [30, 31].

Validation: Validation of the model is accomplished by comparing its output current against this of the real inverter under test, while simulating all physical testing scenarios. Corrective re-tuning of the model is recommended in case of major discripancies, however scenarios with out-of-scale response should be omitted.

4.3.4.2.2 Description of the developed dynamic PV inverter model

A novel average dynamic model has been developed in MATLAB Simulink for the purpose of this study, emulating the behaviour of a 60 kVA LV connected off-the-shelf PV inverter during faults and voltage dips. This is an RMS average model, which assesses the dynamic response of the PV inverter when faults occur at the AC part of the network [9].

The assembly of an average inverter model requires the injection of AC current set-points shaped by the associated control scheme to a three-phase current source. This differs from the logic of a detailed model which would require the implementation and control of semiconductor switching (i.e. IGBTs, MOSFET). An average dynamic (RMS) model is convenient for simulations of power system dynamics and assessment of the inverter's control operation as in this thesis, while a detailed model would be appropriate if the priority was to evaluate the impact of grid events on the semiconductor switching [32–34].

Essential requirement for accurate model tuning and validation is the empirical characterisation of the actual inverter. During physical testing, network disturbances such as faults and voltage drops were applied at the output of the device with the aid of a Real Time Digital Simulator (RTDS) [35]. Section B.2 of Appendix B outlines the physical testing procedure and set-up implemented to characterise the commercially

available inverter. Initially, the data extracted during the physical testing were used to observe and characterise the FRT behaviour of the real inverter. This exercise aided the model tuning in terms of PI gains as well as active and reactive power setpoints. Then, all physical testing scenarios were simulated in MATLAB/Simulink, with a time-step of 100 μs, in order to compare the resulting output of the PV inverter model with those collected during the testing of the real inverter. Effectively, a portion of the experimental data were used to tune the model while all the experimental data were used for validation purposes.

The PV inverter under test performed two distinct FRT responses, FRT 1 and FRT 2, depending on the network conditions and its loading level at the time of the event. During FRT 1, the inverter increases its output current within admissible thermal limits. Moreover, when FRT 2 is activated the inverter immediately stops feeding in current during the event (voltage dip or fault). After the disturbance is cleared, the inverter gradually increases the output current towards the pre-fault rate [9].

Fig. 4.15 and Fig. 4.16 depict the FRT 1 and FRT 2 operation modes of the 60 kVA inverter under slightly different conditions.

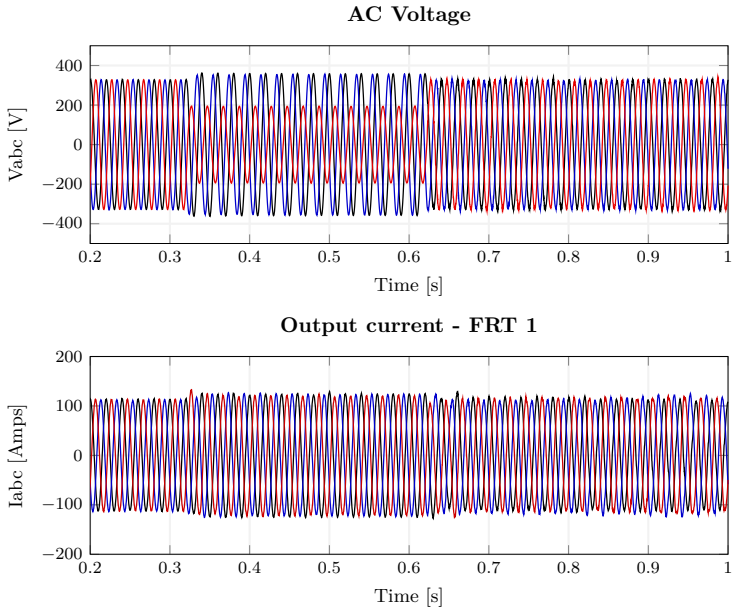

Figure 4.15: 100% Loading – Fault response test (phase-to-earth, 0° PoW, 0.1 Ω) - FRT 1.

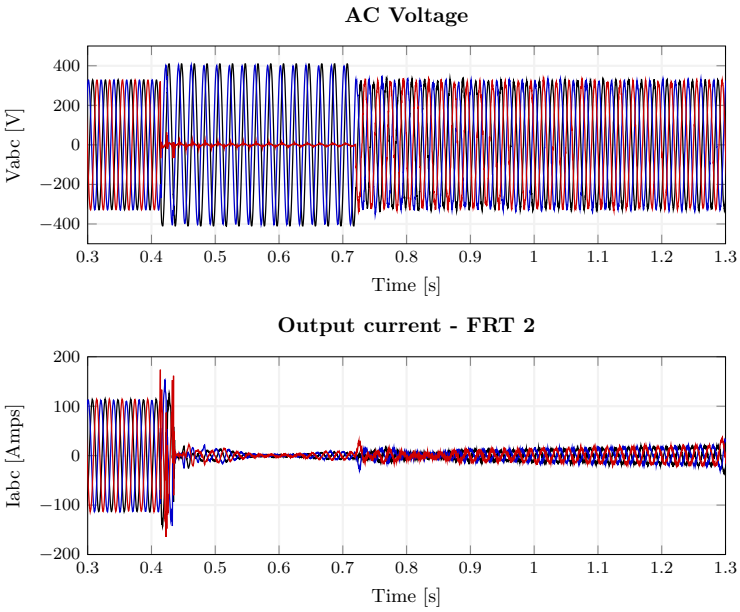

Figure 4.16: 100% Loading – Fault response test (phase-to-earth, 90° PoW, 0 Ω) - FRT 2.

In both cases, the DUT was 100% loaded while phase-to-earth fault conditions are applied. The fault introduced in the first scenario depicted in Fig. 4.15 is resistive (0.1 Ω) and initiated at 0° Point-on-Wave (PoW). During this case the inverter followed the FRT 1 strategy. Moreover, Fig. 4.16 shows measurements captured during a solid fault applied at 90° PoW. These conditions lead the inverter to initiate FRT 2 operation.

During unbalanced faults, the positive sequence component of voltage decreases while the negative rises. In some cases, the inverters support the grid by injecting both positive and negative sequence reactive currents. The negative sequence reactive current contributes to the suppression of the negative sequence voltage, whereas the positive sequence reactive current aids the recovery of the positive sequence voltage [36].

Therefore, the response of LV-connected PV inverters in terms of negative sequence output current and reactive power may be critical for the accurate operation of the FS location technique, which is based on both positive and negative sequence components of voltage. In this case, physical testing showed that the inverter under examination does not produce negative sequence current during unbalanced faults. Instead, the

inverter provided reactive power (or absorbs less reactive power) during the imposed events, which has been captured throughout all testing scenarios.

Fig. 4.17 illustrates a simplified 'equivalent' circuit of the model when integrated into a simple 2-bus system. The schematic shows a current source-based average model fed by the three-phase reference current waveforms, $I_{pv\text{-}a}$, $I_{pv\text{-}b}$ and $I_{pv\text{-}c}$. The PV inverter AC current output, I_{pv}, is produced with the aid of the inverter controllers which process the decomposed active and reactive current components, I_d and I_q. These are depicted in the vector diagram of Fig. 4.17. Both are used to control the active and reactive power respectively, during steady state and grid disturbance conditions.

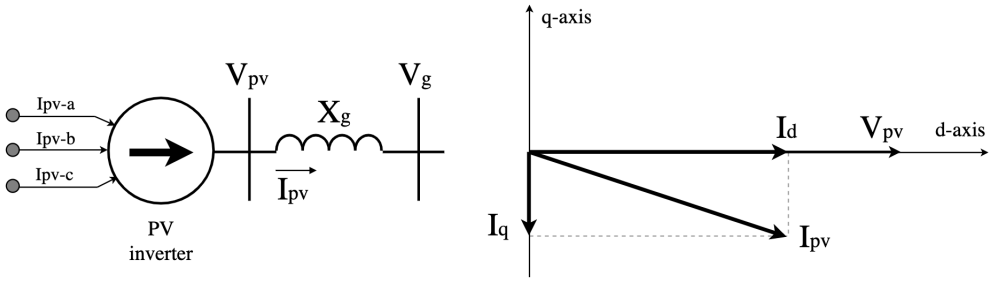

Figure 4.17: Equivalent circuit of a current source representing the PV inverter connected to the grid and the output current phasor I_{pv} decoupled into active and reactive power components, I_d and I_q.

The main structure of the average PV inverter model control logic is presented in Fig. 4.18. It consists of three major stages: i) the steady state and FRT 1 control part, ii) the FRT 2 and iii) the dq-abc output current transformation. The inputs of this control scheme are the active and reactive power setpoints P_{ref} and Q_{ref} as well as the measured voltage and power values V_{pv}, P_{pv} and Q_{pv}.

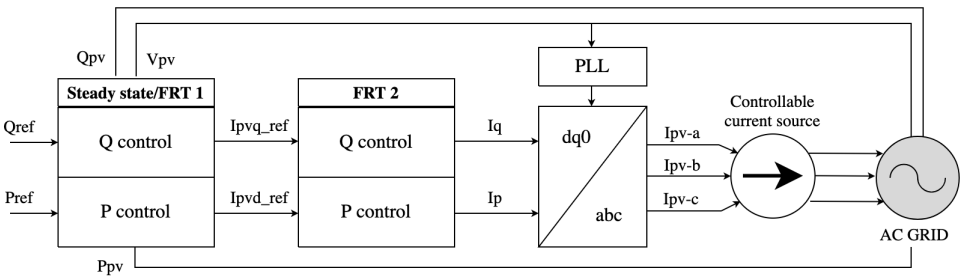

Figure 4.18: Average model control structure.

FRT 1 control strategy is applied during voltage disturbances or faults, leading the inverter to increase its current output within admissible thermal limits. The P and Q control parts of first stage, depicted in Fig. 4.18, provide the reference values I_{pvd_ref} and I_{pvq_ref}, which form the output during steady state or FRT 1 operation. Fig. 4.19 introduces the particular control scheme. A PI based control loop feedback mechanism is used to continuously calculate the P and Q errors (P_{error} and Q_{error}) between the desired power set-points P_{ref}, Q_{ref} and the corresponding measured values, P_{pv} and Q_{pv}. The I_{pvd_ref} and I_{pvq_ref} are then affected by the error correction of the PI controllers and the RMS voltage at the output of the inverter. It is clarified that standard PLL, *DQ0-ABC* and PI blocks have been used, as the aim of this study is the replicability of the model and not the introduction of new blocks and other modelling elements.

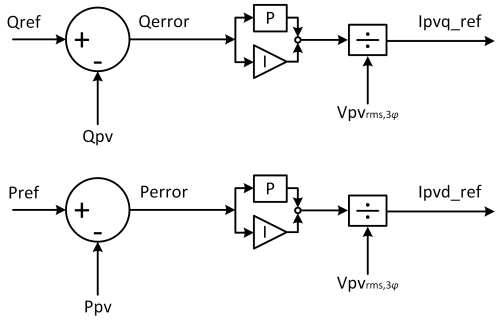

Figure 4.19: Steady state control scheme.

The adjustment of the FRT 1 control scheme depends on the AC voltage conditions and the loading level of the inverter. This strategy uses the steady state control architecture, presented in Fig. 4.19, although a number of parameters are tuned. The PI controller variables, K_p and T_i, the upper and lower PI limits (P_{upper}, Q_{upper}, P_{lower}, Q_{lower}) as well as the P and Q reference values (P_{ref} and Q_{ref}) are adaptive to the various loading levels of the inverter and the AC voltage RMS conditions. Tables 4.7, 4.8, 4.9 and 4.10 list the aforementioned conditions and variables.

Table 4.7: FRT 1 - K_p parameters

Vrms (pu)	0	0.1	0.3	0.4	0.6	0.9	1.0	1.1
$\boldsymbol{K_p}$	0.6	0.6	0.5	0.5	0.5	2.0	2.0	1.0

Table 4.8: FRT 1 - T_i parameters

Loading	25%	50%	75%	100%
$\boldsymbol{T_i}$	0.0033	0.0011	0.0011	0.0011

Table 4.9: FRT 1 - PI upper/lower limits (pu)

Loading	$\boldsymbol{V_{rms}}$	$\boldsymbol{P_{upper}}$	$\boldsymbol{Q_{upper}}$	$\boldsymbol{P_{lower}}$	$\boldsymbol{Q_{lower}}$
100%	0 - 0.8	8	0.8	-8	-0.8
	0.9 - 1	10	1	-10	-1
75%	0 - 0.8	7	0.7	-7	-0.7
	0.9 - 1	10	1	-10	-1
50%	0 - 0.8	8	0.8	-8	-0.8
	0.9 - 1	10	1	-10	-1
25%	0 - 1	8	0.04	-8	-0.04

Table 4.10: FRT 1 - Active/Reactive power setpoints (pu)

Loading	$\boldsymbol{V_{rms}}$	$\boldsymbol{P_{ref}}$	$\boldsymbol{Q_{ref}}$
100%	0	0	0
	0.8	0.7	0.875
	0.9	1	0.125
	1	1	0.125
75%	0	0	0
	0.29	0	0
	0.3	0.7	0.875
	0.4	0.8	0.1
	0.6	1	0.125
	1	1	0.125
50%	0	0	0
	0.29	0	0
	0.3	0.6	0.75
	0.5	0.8	0.1
	1	1	0.125
25%	0	1	0.125
	1	1	0.125

Fig. 4.20 illustrates the output active and reactive power of both the inverter and

the model along with the power setpoints during a network disturbance with retained voltage at 0.75 pu. It can be seen that during FRT 1 reactive power is injected, which can potentially have an effect on the positive sequence voltage and thus on k_s (positive over negative sequence voltage ratio) of the FS location algorithm.

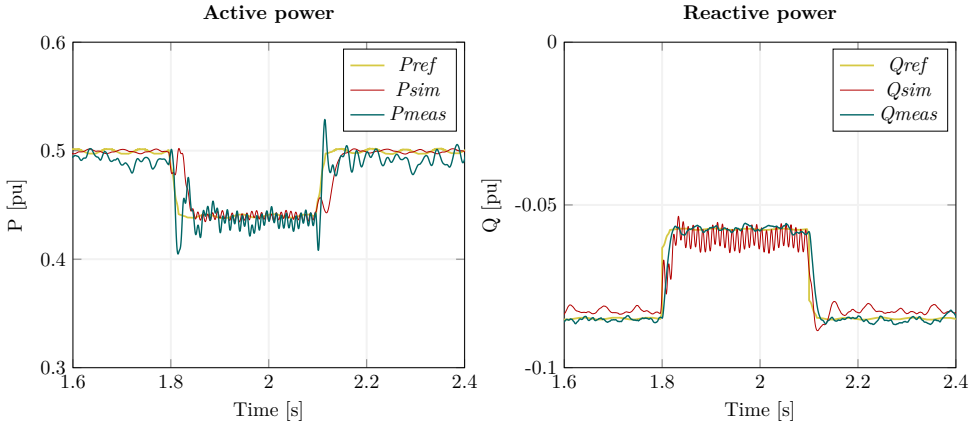

Figure 4.20: Inverter active and reactive power output: 50% Loading - 0.75 pu retained voltage - FRT 1.

FRT 2 strategy is activated in case certain AC voltage thresholds are exceeded during a grid-side event. The main characteristic of the FRT 2 strategy is that the PV inverter immediately stops feeding in current during the voltage disturbance or fault. The observations captured during physical testing revealed the specific parameters and corresponding thresholds initiating the FRT 2 operation mode.

Table 4.11 contains the AC voltage network conditions triggering FRT 2 operation mode [9]. In addition to the output current depression to zero during the event, gradual recovery is performed by the model after the disturbance clearance. The network parameters determining the activation of FRT 2 are the three-phase RMS voltage ($V_{3\phi}$), the single-phase RMS voltage ($V_{1\phi}$) and the voltage unbalance (V_2/V_1) [37]:

- $V_{3\phi}$: This parameter refers to the minimum threshold of the three-phase voltage RMS calculated using equation (4.6):

$$V_{rms,3\phi_{(pu)}} = \frac{1}{3}({V_{AB_{(pu)}}}^2 + {V_{BC_{(pu)}}}^2 + {V_{CA_{(pu)}}}^2) \tag{4.6}$$

- $V_{1\phi}$ and $V_{3\phi}$: FRT 2 operation is triggered when both parameters are lower than the pre-defined limits.

- V_2/V_1 and $V_{3\phi}$: The level of voltage unbalance observed at the output of the inverter is quantified using the negative to positive sequence components ratio [37]. Similar to the previous condition, the three-phase RMS voltage is also taken into account for the FRT 2 activation.

Table 4.11: AC voltage network conditions activating FRT 2

PV inverter loading level:	25%	50%	75%	100%
$V_{3\phi}$ *[pu]* $\leq$	0.05	0.29	0.3	0.65
$V_{1\phi}$ *[pu]* $<$	N/A	N/A	0.15	0.15
$V_{3\phi}$ *[pu]* $\leq$			0.69	0.81
$V_2/V_1>$	N/A	N/A	0.8	0.3
$V_{3\phi}$ *[pu]* $\leq$			0.6	0.9

According to Table 4.11, the activation of FRT 2, highly depends on both the AC network conditions and the loading level of the PV inverter. For instance, when the PV inverter is loaded at 50% of its nominal capacity, FRT 2 is initiated if the three-phase RMS voltage, $V_{rms,3\phi}$, is less than or equal to 0.29 pu. However, when the PV inverter is 100% loaded, the FRT 2 control part is triggered if any of the three conditions listed in the last column of Table 4.11 are met.

Hence, depending on the grid conditions, the I_d and I_q components imported in the *dq0-abc* block are generated either by the steady state control scheme, which matches this of the FRT 1, (depicted in Fig. 4.19) or by the FRT 2. Eventually, the referred time-domain current direct and quadrature (d-q axis) components are fed to the Inverse Park Transform block, as shown in Fig. 4.18. The latter converts I_d and I_q to a three-phase system in an a-b-c reference frame. The *dq0-abc* block uses equation (4.7) to generate the PV inverter's three-phase current output.

$$\begin{bmatrix} \mathrm{a} \\ \mathrm{b} \\ \mathrm{c} \end{bmatrix} = \begin{bmatrix} \sin(\theta) & \cos(\theta) & 1 \\ \sin(\theta - \frac{2\pi}{3}) & \cos(\theta - \frac{2\pi}{3}) & 1 \\ \sin(\theta - \frac{2\pi}{3}) & \cos(\theta - \frac{2\pi}{3}) & 1 \end{bmatrix} \begin{bmatrix} d \\ q \\ 0 \end{bmatrix} \tag{4.7}$$

The successful operation of the developed model was validated by comparing the simulation results with the measurements extracted during the physical examination of the real PV inverter [9]. For the same purpose, the AC voltage measurements captured during testing are applied at the grid side with the aid of an emulated voltage source. The green and red coloured curves in Fig. 4.21 - Fig. 4.22, present the output RMS current of the simulation model and the DUT to better visualize and compare the performance of the model against the output of the real PV inverter during the imposed grid disturbances.

The first example scenarios are used to highlight the impact of the PV inverter's loading level to the FRT response. In this case, the voltage disturbance scenarios were artificially applied by the ideal voltage source model created in RSCAD. Fig. 4.21 and Fig. 4.22 show the varying behaviours of the inverter during a 0.5 pu balanced retained voltage event when this is 25% and 75% loaded respectively. It is observed that the inverter activates FRT 1 strategy when lightly loaded, whereas it follows FRT 2 when loaded by 75% of its nominal rating. The model successfully switches from steady state to FRT 1 and FRT 2 operation mode depending on the voltage conditions seen at its output.

The current spikes observed at the output of the inverter are emanating from the dynamic adjustment of K_p and T_i gains, transitioning from steady state rates to FRT (due to the model parametrization) and vice versa. It shall be highlighted that most of the control structures within commercial converters are not accessible, and therefore any corrective measure (e.g. bump-less transfer) cannot be directly applied (unless it is integrated by the manufacturer). However, since this study focuses primarily on the dynamic features of the model, any transient phenomena of such kind are considered out of scope.

The validation of the model was achieved by comparing the RMS output current

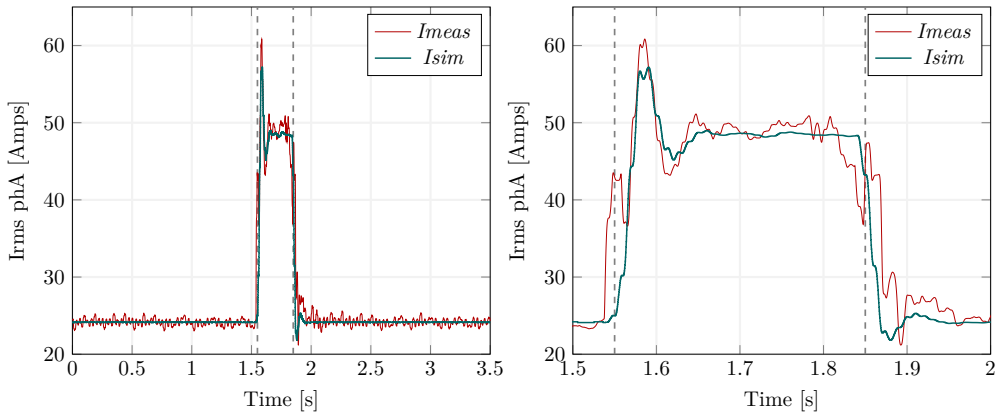

Figure 4.21: Inverter output current: 25% Loading – 0.5 pu retained balanced voltage – FRT 1

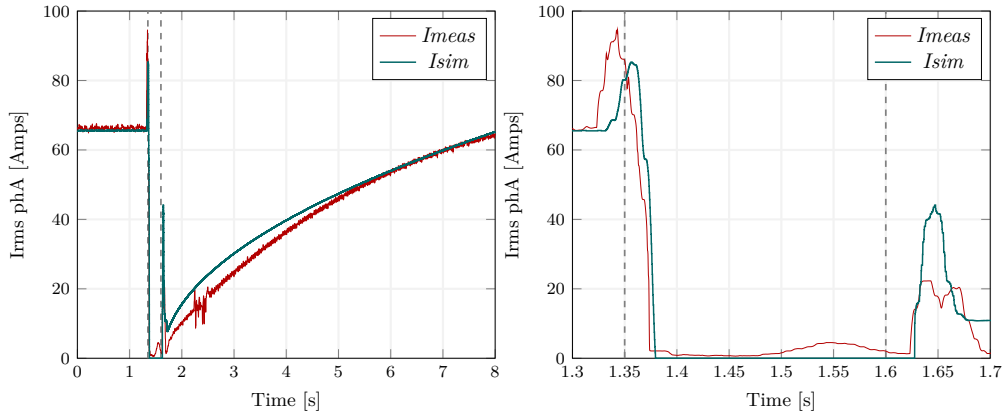

Figure 4.22: Inverter output current: 75% Loading – 0.5 pu retained balanced voltage – FRT 2

of the model with this of the real inverter under test for each of the physical testing scenarios. The convergence of simulation and physical testing data and thus the inverter emulation accuracy is quantified with aid of the coefficient R-squared expressed by Eq. 4.8. The equation utilizes the measurement data y, the model response $\hat{y}$ and the mean value $\overline{y}$:

$$R - squared = 1 - \frac{\sum(y - \hat{y})^2}{\sum(y - \overline{y})^2} \tag{4.8}$$

The R-squared is used to show the degree of similarity between the simulation results and the target data (response of real inverter). R-squared close to 1 implies that the simulation results are very similar to the physical testing data. The R-squared

Table 4.12: PV inverters

PV inverter	**Loading level**	**Power output (kVA)**
PV_1	100 %	60
PV_2	25 %	15
PV_3	75 %	45
PV_4	100 %	60
PV_5	25 %	15
PV_6	100 %	60
PV_7	50 %	30
PV_8	50 %	30
PV_9	100 %	60
PV_{10}	25 %	15
PV_{11}	25 %	15
PV_{12}	50 %	30
PV_{13}	50 %	30
PV_{14}	50 %	30

values calculated for scenarios of Fig. 4.21 and Fig. 4.22, which were chosen as two representative examples of this study, are equal to 0.938 and 0.976. The above shows that the model performed with high accuracy for the referred scenarios.

4.3.4.2.3 Network integration of the dynamic PV inverter model

The inverter model is integrated in the distribution network represented by model C (Fig. 4.3), which is developed in MATLAB Simulink for the purpose of the fault location study [9]. Multiple PV systems are connected at the LV side of the grid covering the 85.3% of the total demand. The 60 kVA inverter model is the grid interface of the mentioned PVs, operating in various loading levels which range from 25% to 100% of its nominal capacity. The deployed inverters are listed in Table 4.12.

Throughout simulation scenarios 4.25-4.48 and the examination of the FS algorithm, the resulted FRT responses of the PV inverters have been reported. Based on the observations acquired during the laboratory assessment of the actual PV inverter, the resulting FRT strategy depends on the AC voltage and loading level of the device. It is therefore expected that, the fault location and point of PV inverter connection across the network are factors affecting the behaviour of the developed model during

the various fault scenarios.

4.4 Chapter summary

This chapter described the modelling methodology followed to assess the performance of the proposed FS location algorithm. It included information with regards to the several network topologies implemented and all associated variants such as MV laterals, unbalanced loads and distributed generation. A number of asymmetrical fault scenarios have been introduced in multiple locations across the modelled networks.

Special emphasis is put on the presence of inverter based generation, such as PVs connected at the LV part of the network where the algorithm measurements are taken. Sections 4.3.4.2.2-4.3.4.2.3 refer to the formation and network integration of a realistic model emulating the fault ride through operation of a real 60 kVA off-the-shelf PV inverter. Information with regards to the physical testing results of the inverter are provided in Appendix B.

4.5 References

[1] "DIgSILENT PowerFactory." `https://www.digsilent.de/en/`.

[2] "Matlab Simulink." `https://www.mathworks.com/solutions/utilities-energy/power-system-studies.html`.

[3] "Alberta Reliability Standard Disturbance Monitoring and Reporting Requirements PRC-002-AB-2," Oct 2019.

[4] P. Bountouris, H. Guo, I. Abdulhadi, and F. Coffele, "Medium voltage fault location using distributed LV measurements," in *14th International Conference on Developments in Power System Protection (DPSP)*, pp. 1–6, March 2018.

[5] P. Bountouris, H. Guo, D. Tzelepis, I. Abdulhadi, F. Coffele, and C. Booth, "MV faulted section location in distribution systems based on unsynchronized LV

measurements," *International Journal of Electrical Power and Energy Systems*, vol. 119, 2020.

[6] "HV and LV Phase Imbalance Assessment," Sep 2015.

[7] M. C. Rodríguez Paz, R. G. Ferraz, A. S. Bretas, and R. C. Leborgne, "System unbalance and fault impedance effect on faulted distribution networks," *Computers and Mathematics with Applications*, vol. 60, no. 4, pp. 1105–1114, 2010.

[8] K. W. Park, O. S. Kwon, H. C. Seo, and C. H. Kim, "A calculation of neutral current for two step type pole in distribution line," in *GMSARN International Journal*, vol. 1, pp. 29–34, 2007.

[9] P. Bountouris, I. Abdulhadi, and F. Coffele, "Dynamic model of commercially available inverters with validation against hardware testing," *IEEE Transactions on Power Systems*, 2022.

[10] DIgSILENT PowerFactory User Manual, *Technical Reference Documentation Synchronous Machine*. 2011.

[11] "IEC 60909-0:2016, short-circuit currents in three-phase a.c. systems - part 0: Calculation of currents," Jan 2016.

[12] DIgSILENT PowerFactory User Manual, *Technical Reference Documentation PV System*. 2011.

[13] E. Muljadi, M. Singh, R. Bravo, and V. Gevorgian, "Dynamic model validation of pv inverters under short-circuit conditions," in *2013 IEEE Green Technologies Conference (GreenTech)*, pp. 98–104, 2013.

[14] North American Electric Reliability Corporation, "Key Takeaways: Inverter manufacturer and relay manufacturer coordination meeting.," April 2019.

[15] G. Kou, J. Jordan, B. Cockerham, R. Patterson, and P. VanSant, "Negative-sequence current injection of transmission solar farms," *IEEE Transactions on Power Delivery*, vol. 35, no. 6, pp. 2740–2743, 2020.

[16] E. Buraimoh and I. E. Davidson, "Overview of fault ride-through requirements for photovoltaic grid integration, design and grid code compliance," in *2020 9th International Conference on Renewable Energy Research and Application (ICRERA)*, pp. 332–336, 2020.

[17] National Grid Electricity System Operator, "The Grid Code," 3 2022.

[18] Energy Networks Association, "ER G99: Requirements for the connection of generation equipment in parallel with public distribution networks on or after 27 april 2019.," March 2020.

[19] "TransmissionCode 2007: Network and System Rules of the German Transmission System Operators.," Aug 2007.

[20] I. Abdulhadi and A. Dyśko, "Hardware testing of photovoltaic inverter loss of mains protection performance," in *13th International Conference on Development in Power System Protection 2016 (DPSP)*, pp. 1–6, 2016.

[21] I. Abdulhadi, F. Coffele, A. Dyśko, C. Foote, C. Kungu, and M. Lee, "Hardware-based characterisation of LV inverter fault response," *CIRED - Open Access Proceedings Journal*, vol. 2017, no. 1, pp. 1167–1171, 2017.

[22] L. Callegaro, G. Konstantinou, C. A. Rojas, N. F. Avila, and J. E. Fletcher, "Testing evidence and analysis of rooftop pv inverters response to grid disturbances," *IEEE Journal of Photovoltaics*, vol. 10, no. 6, pp. 1882–1891, 2020.

[23] P. Bountouris, I. Abdulhadi, A. Dysco, and F. Coffele, "Characterising grid connection stability of low voltage PV inverters through real-time hardware testing," pp. 1–5, June 2019.

[24] E. Muljadi, M. Singh, R. Bravo, and V. Gevorgian, "Dynamic model validation of pv inverters under short-circuit conditions," in *2013 IEEE Green Technologies Conference (GreenTech)*, pp. 98–104, 2013.

[25] R. J. Bravo, R. Yinger, and S. Robles, "Three phase solar photovoltaic inverter testing," in *2013 IEEE Power Energy Society General Meeting*, pp. 1–5, 2013.

[26] Kara Clark, Nicholas W. Miller, Reigh Walling, "Modeling of GE solar photovoltaic plants for grid studies," April 2016.

[27] Electric Power Research Institute (EPRI), "Technical update on generic wind and solar PV model development and validation," 2014.

[28] Western Electricity Coordinating Council, "Generic solar photovoltaic system dynamic simulation model specification," 2012.

[29] Western Electricity Coordinating Council, "WECC solar plant dynamic modelling guidelines," 2014.

[30] I. R. S. Priyamvada and S. Das, "Adaptive tuning of pv generator control to improve stability constrained power transfer capability limit," *IEEE Transactions on Power Systems*, pp. 1–1, 2021.

[31] L. M. Kandasamy, J. Kanakaraj, and S. J, "Artificial neural network based intelligent controller design for grid-tied inverters of microgrid under load variation and disturbance," in *2021 4th International Conference on Recent Developments in Control, Automation Power Engineering (RDCAPE)*, pp. 148–153, 2021.

[32] A. Ellis, M. R. Behnke, and R. T. Elliott, "Generic solar photovoltaic system dynamic simulation model specification." `https://www.osti.gov/servlets/purl/1177082`, 2013.

[33] Z. Jankovic, B. Novakovic, V. Bhavaraju, and A. Nasiri, "Average modeling of a three-phase inverter for integration in a microgrid," in *2014 IEEE Energy Conversion Congress and Exposition (ECCE)*, pp. 793–799, 2014.

[34] A. Ekic, M. Maharjan, B. Strombeck, and D. Wu, "Impact of inverter modeling on sub-cycle dynamics in grid-connected solar pv systems," in *2021 IEEE 48th Photovoltaic Specialists Conference (PVSC)*, pp. 1173–1175, 2021.

[35] "RTDS, "Real Time Digital Power System Simulator • RTDS Technologies Inc.." `https://www.rtds.com/`. Accessed: 2020-02-09.

[36] M. B. Shamseh, R. Inzunza, I. Fukasawa, T. Tanaka, and T. Ambo, "Grid support during asymmetrical faults using negative sequence current injection," in *2019 IEEE 4th International Future Energy Electronics Conference (IFEEC)*, pp. 1–6, 2019.

[37] F. Ghassemi and M. Perry, "Review of voltage unbalance limit in the GB Grid Code CC.6.1.5 (b)," p. 35, 10 2014.

Chapter 5

Analysis of simulation results

5.1 Chapter overview

This chapter summarises the results of the dynamic simulations realised for the validation of the proposed FS location technique. Each section of this chapter refers to the results of different group of simulation scenarios. The presented results include plots of the ratios of positive to negative sequence components, k_s, which were captured from the various LV measurement points throughout all the executed scenarios. In addition, the performance of the algorithm is examined by listing the faulted sections that are identified and proposed by the system for all simulation cases.

Sections 5.2-5.5.1 concentrate the results of the fault location study performed in DIgSILENT Powerfactory. Different network conditions are considered such as radial and ring topologies, the connection of a MV lateral, the presence of unbalanced loads as well as the connection of DGs [1–3]. Furthermore, Section 5.5.2 presents the fault location study results acquired from the simulations undertaken in MATLAB Simulink, where the realistic inverter model is integrated in an active distribution network dominated by LV connected PV generation.

5.2 The PNDC electricity network

5.2.1 Radial topology

This section presents the results of the simulated fault scenarios 1.1 - 1.12 performed using model A, which in this case emulated the radially configured PNDC network [1, 2]. Fig. 5.1 depicts the single line diagram of the mentioned simulated network where a phase-to-earth fault is introduced at location F_1. The red frame at the LV side represents the 3-points window indicating the FS (orange dashed frame).

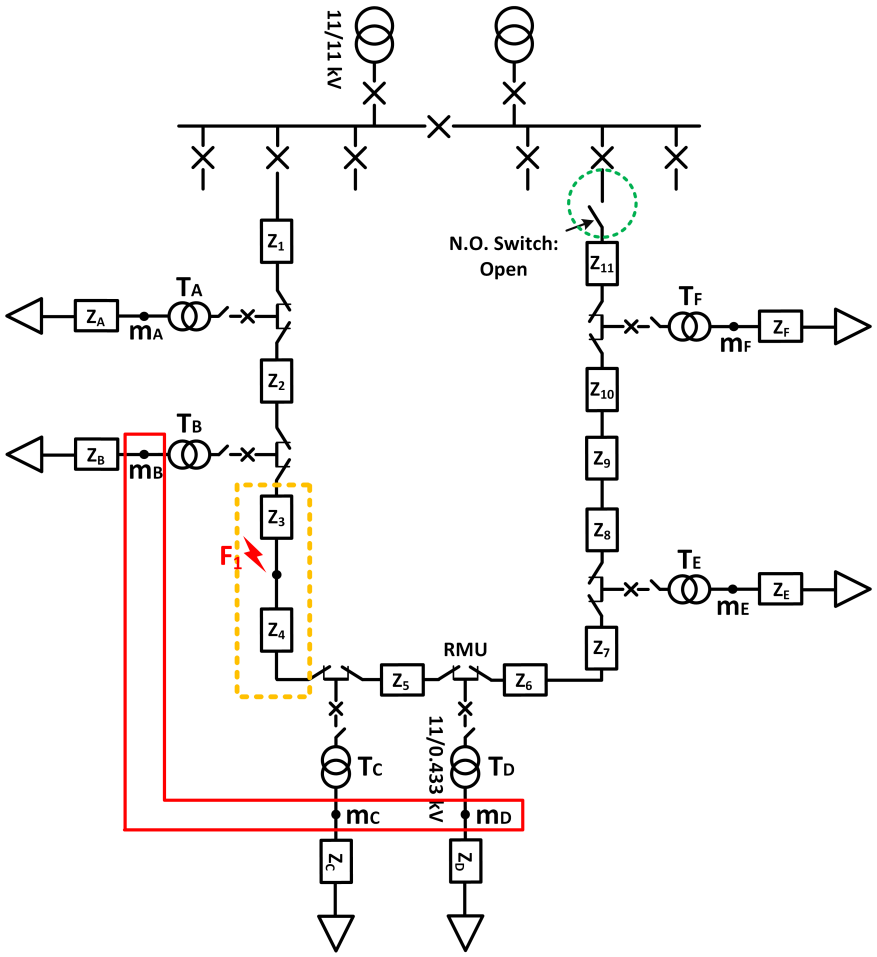

Figure 5.1: Model of radial PNDC network with fault at F_1.

Plots in Fig. 5.2 illustrate the k_s profiles captured at the LV part of the simulated PNDC radial network when applying asymmetrical solid and resistive faults at locations

F_1 - F_3.

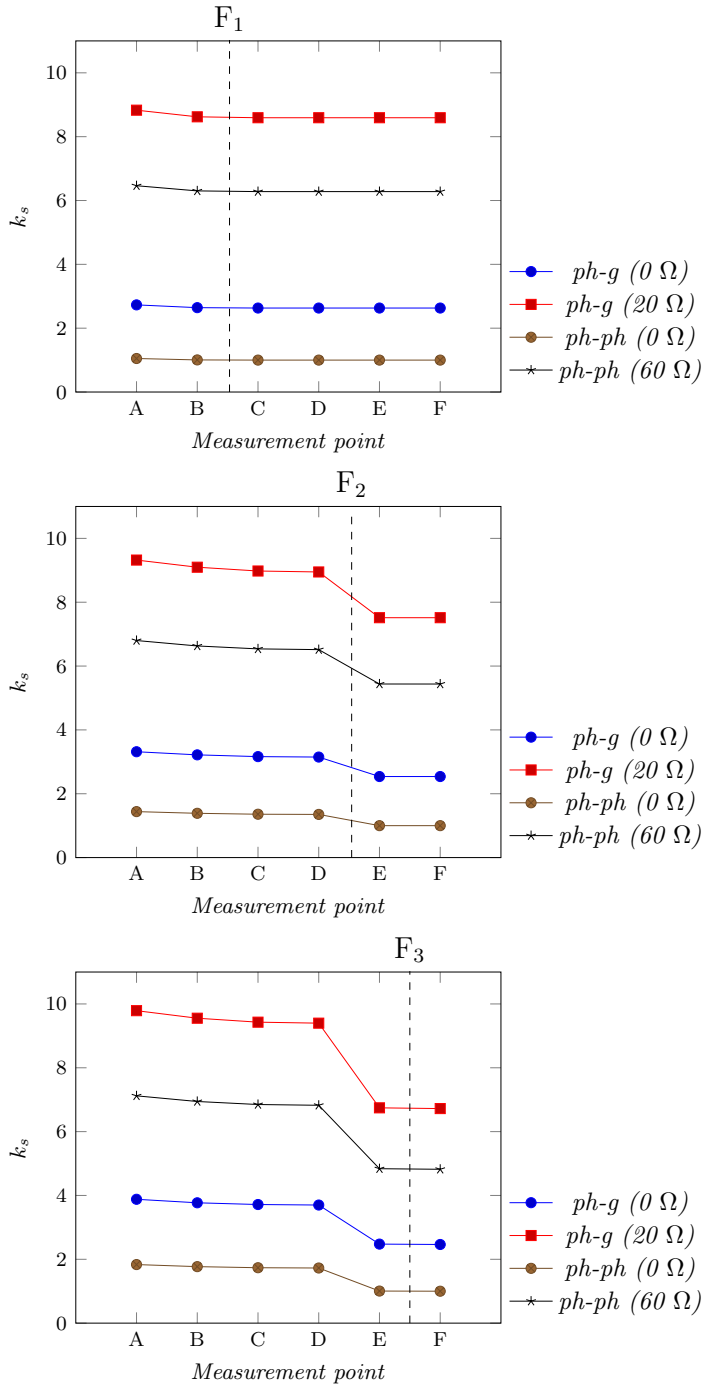

Figure 5.2: k_s profiles captured at PNDC radial network when applying MV asymmetrical faults at locations F_1 - F_3.

Table 5.1 lists the FS located by the algorithm for each of the asymmetrical MV fault simulation scenarios 1.1 - 1.12. It is noted that the proposed technique performs with 100% accuracy throughout the selected simulation cases. The measured parameters of the associated 3-points windows are reported in Appendix C.

Table 5.1: Performance of the algorithm for all simulation scenarios conducted in the radial topology of model A.

Scenario	Fault type	Fault resistance	Fault location	Topology	Identified FS
1.1	ph-earth	0 Ω	F_1	radial	B-C
1.2	ph-earth	20 Ω	F_1	radial	B-C
1.3	ph-ph	0 Ω	F_1	radial	B-C
1.4	ph-ph	60 Ω	F_1	radial	B-C
1.5	ph-earth	0 Ω	F_2	radial	D-E
1.6	ph-earth	20 Ω	F_2	radial	D-E
1.7	ph-ph	0 Ω	F_2	radial	D-E
1.8	ph-ph	60 Ω	F_2	radial	D-E
1.9	ph-earth	0 Ω	F_3	radial	E-F
1.10	ph-earth	20 Ω	F_3	radial	E-F
1.11	ph-ph	0 Ω	F_3	radial	E-F
1.12	ph-ph	60 Ω	F_3	radial	E-F

5.2.2 Ring topology

In this section, the ring topology of model A is achieved by closing the normally open switch, as it can be seen in Fig. 5.3 [1, 2]. The same figure depicts the 3-points window indicating the FS when a fault occurs at location F_2.

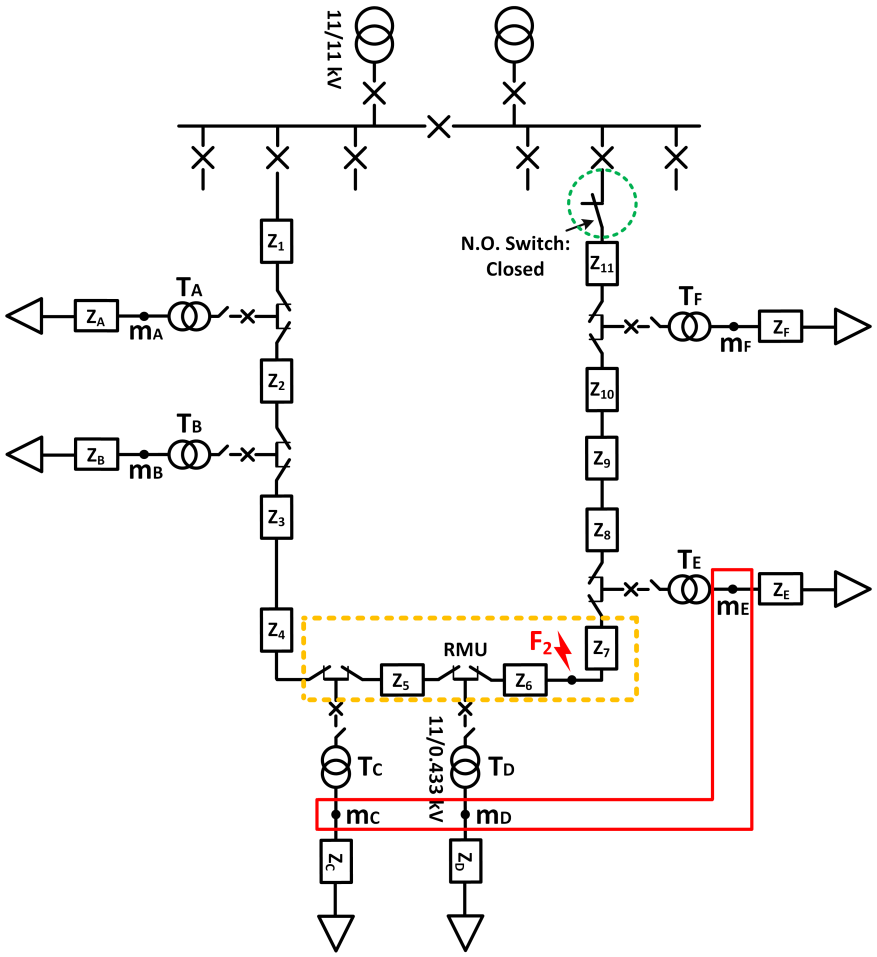

Figure 5.3: Model of ring PNDC network with fault at F_2.

The resultant LV k_s profiles recorded during the simulated fault scenarios 1.13 - 1.24 are presented in Fig. 5.4.

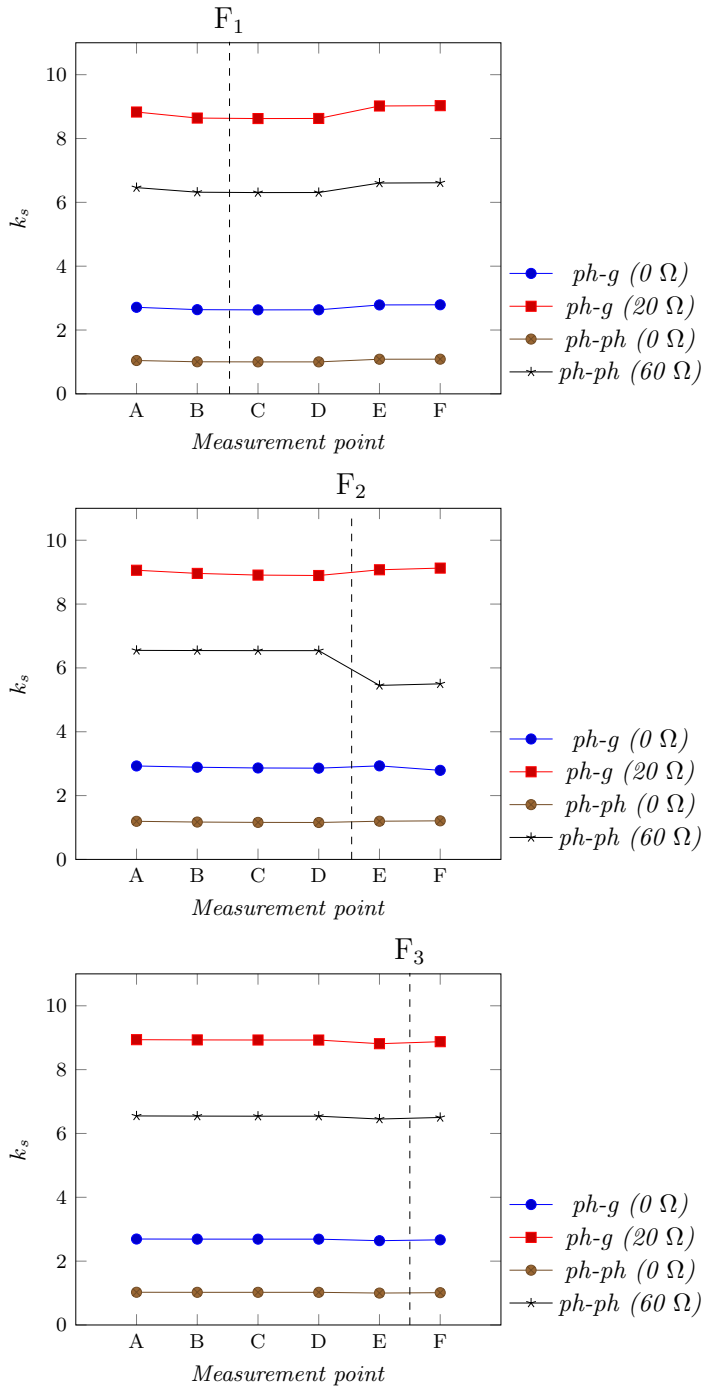

Figure 5.4: k_s profiles captured at PNDC ring network when applying MV asymmetrical faults at locations F_1 - F_3.

Similarly with section 5.2.1, the performance of the algorithm during 12 different

asymmetrical MV fault scenarios, using the ring topology of model A, has been recorded in Table 5.2. The technique locates correctly the FS for the total of the selected simulation cases. It is noted that the capability of the algorithm in FS location in ring topologies is limited to MV sections among three step-down transformers.

Table 5.2: Performance of the algorithm for all simulation scenarios conducted in the ring topology of model A.

Scenario	Fault type	Fault resistance	Fault location	Topology	Identified FS
1.13	ph-earth	0 Ω	F_1	ring	B-C-D
1.14	ph-earth	20 Ω	F_1	ring	B-C-D
1.15	ph-ph	0 Ω	F_1	ring	B-C-D
1.16	ph-ph	60 Ω	F_1	ring	B-C-D
1.17	ph-earth	0 Ω	F_2	ring	C-D-E
1.18	ph-earth	20 Ω	F_2	ring	C-D-E
1.19	ph-ph	0 Ω	F_2	ring	C-D-E
1.20	ph-ph	60 Ω	F_2	ring	C-D-E
1.21	ph-earth	0 Ω	F_3	ring	D-E-F
1.22	ph-earth	20 Ω	F_3	ring	D-E-F
1.23	ph-ph	0 Ω	F_3	ring	D-E-F
1.24	ph-ph	60 Ω	F_3	ring	D-E-F

5.3 Network topologies with MV lateral

5.3.1 Radial topology

This section presents the results of the simulation scenarios 2.1 - 2.24 [2]. Fig. 5.5 illustrates the single line diagram of model B emulating a distribution network with a connected MV lateral and a fault occurring at location F_5. The radial topology is achieved by maintaining the marked switch at open position.

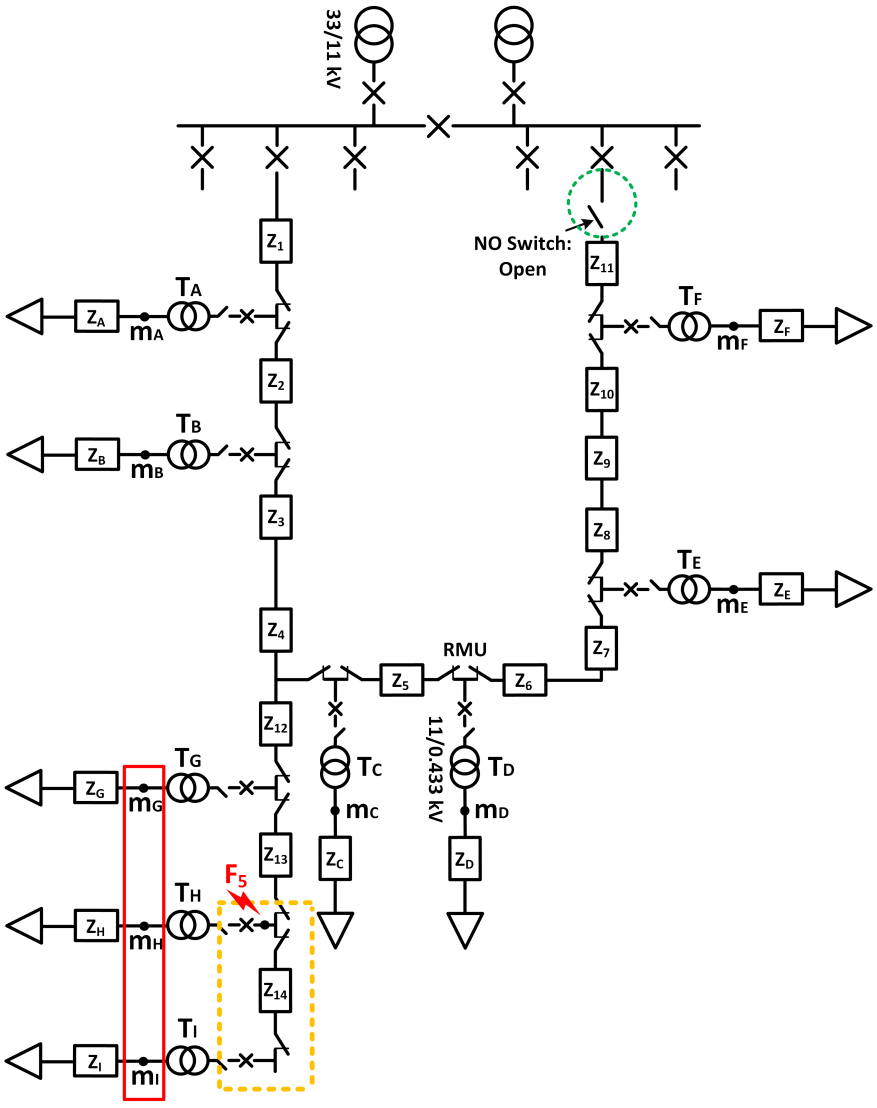

Figure 5.5: Radial configuration of distribution network with MV lateral and fault at F_5.

The k_s profiles extracted from the LV monitoring points and corresponding "slaves" can be found in the following plots of Fig. 5.6.

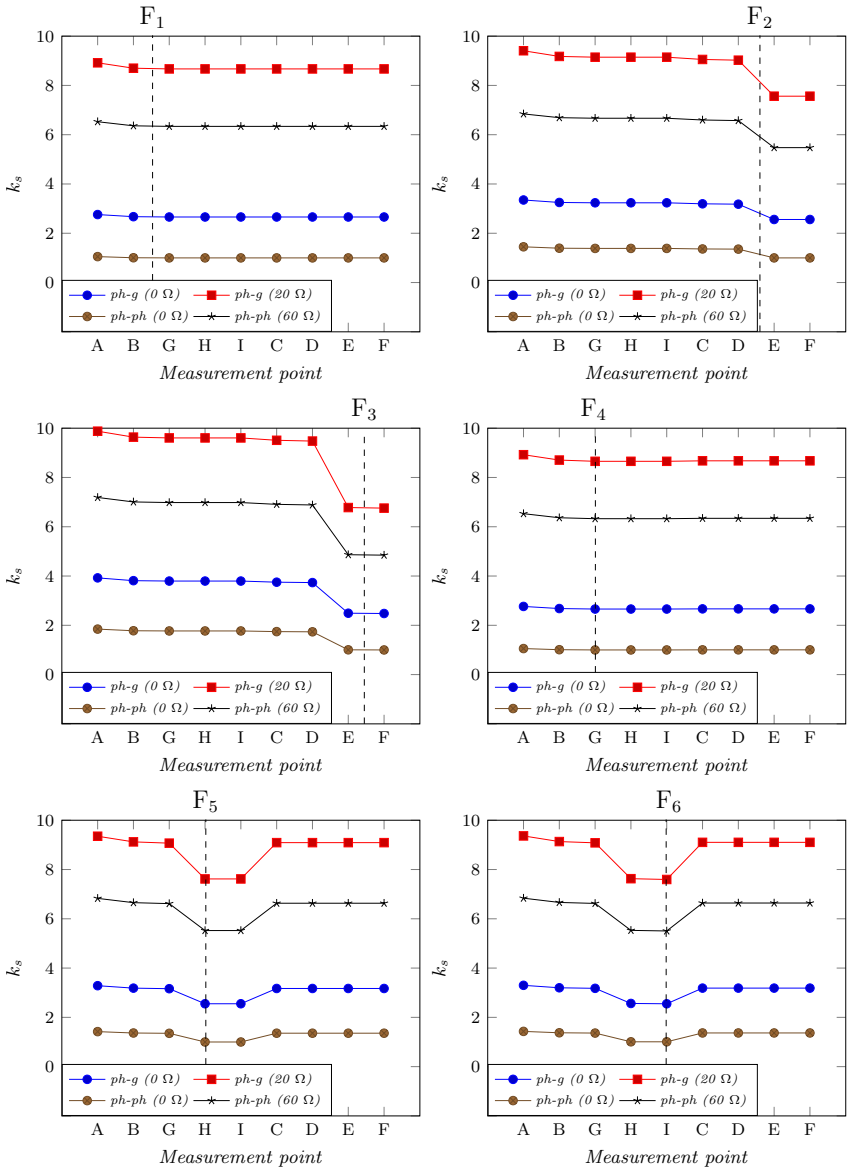

Figure 5.6: k_s profiles during asymmetrical faults applied at locations F_1 - F_6 of the radial distribution network with MV lateral.

Table 5.3 demonstrates the FS location algorithm performance during the 24 different fault scenarios, 2.1 - 2.24, simulated at the radial topology of model B. The technique locates the FS with 100% accuracy, throughout the total of the selected

simulation cases.

Table 5.3: Performance of the algorithm for simulation scenarios 2.1-2.24 conducted in the radial topology of model B.

Scenario	Fault type	Fault resistance	Fault location	Topology	Identified FS
2.1	ph-earth	0 Ω	F_1	radial	B-G
2.2	ph-earth	20 Ω	F_1	radial	B-G
2.3	ph-ph	0 Ω	F_1	radial	B-G
2.4	ph-ph	60 Ω	F_1	radial	B-G
2.5	ph-earth	0 Ω	F_2	radial	D-E
2.6	ph-earth	20 Ω	F_2	radial	D-E
2.7	ph-ph	0 Ω	F_2	radial	D-E
2.8	ph-ph	60 Ω	F_2	radial	D-E
2.9	ph-earth	0 Ω	F_3	radial	E-F
2.10	ph-earth	20 Ω	F_3	radial	E-F
2.11	ph-ph	0 Ω	F_3	radial	E-F
2.12	ph-ph	60 Ω	F_3	radial	E-F
2.13	ph-earth	0 Ω	F_4	radial	B-G
2.14	ph-earth	20 Ω	F_4	radial	B-G
2.15	ph-ph	0 Ω	F_4	radial	B-G
2.16	ph-ph	60 Ω	F_4	radial	B-G
2.17	ph-earth	0 Ω	F_5	radial	G-H
2.18	ph-earth	20 Ω	F_5	radial	G-H
2.19	ph-ph	0 Ω	F_5	radial	G-H
2.20	ph-ph	60 Ω	F_5	radial	G-H
2.21	ph-earth	0 Ω	F_6	radial	H-I
2.22	ph-earth	20 Ω	F_6	radial	H-I
2.23	ph-ph	0 Ω	F_6	radial	H-I
2.24	ph-ph	60 Ω	F_6	radial	H-I

5.3.2 Ring topology

This section demonstrates the performance of the FS location technique in a ring network with MV lateral [2]. Fig. 5.7 shows a fault occurring at location F_6 of the ring topology. The 3-points window G-H-I reveals the FS sitting between the transformers T_G and T_I.

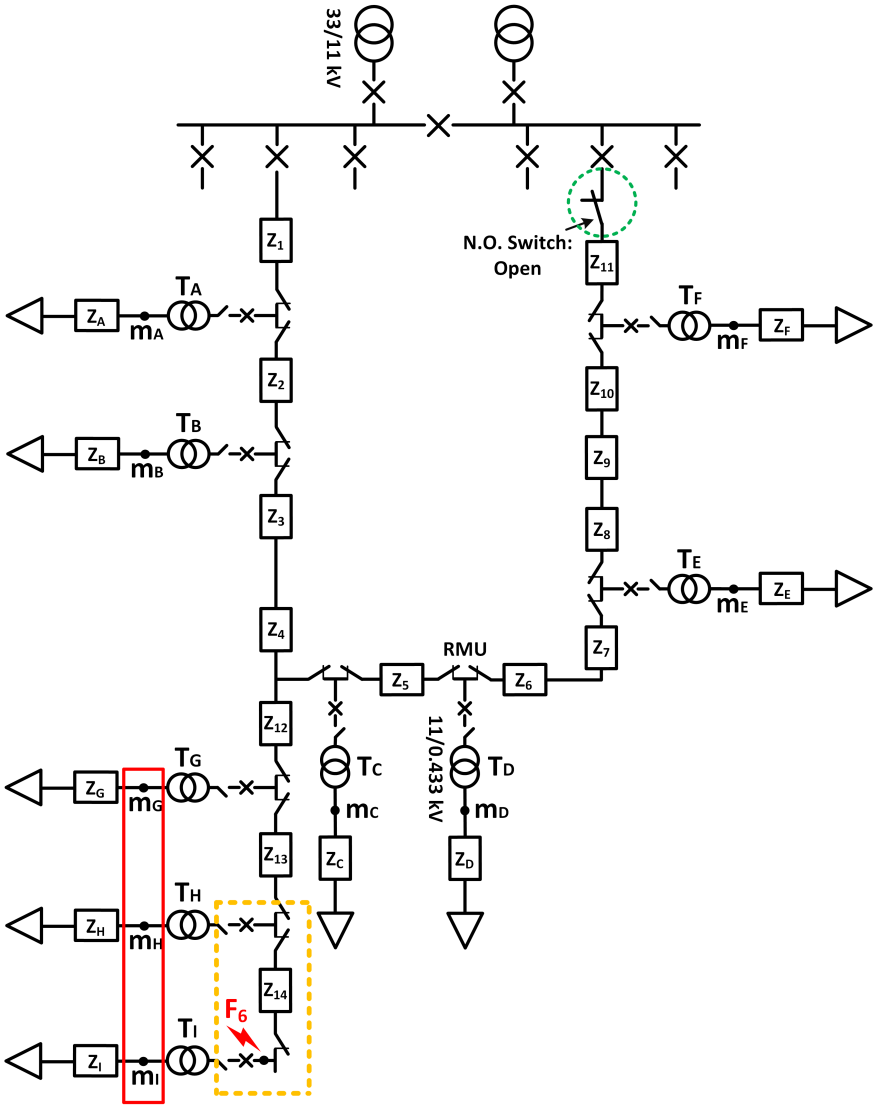

Figure 5.7: Fault at location F_6 of the ring distribution network with MV lateral.

The k_s profiles acquired during scenarios 2.25 - 2.48 are depicted in Fig. 5.8

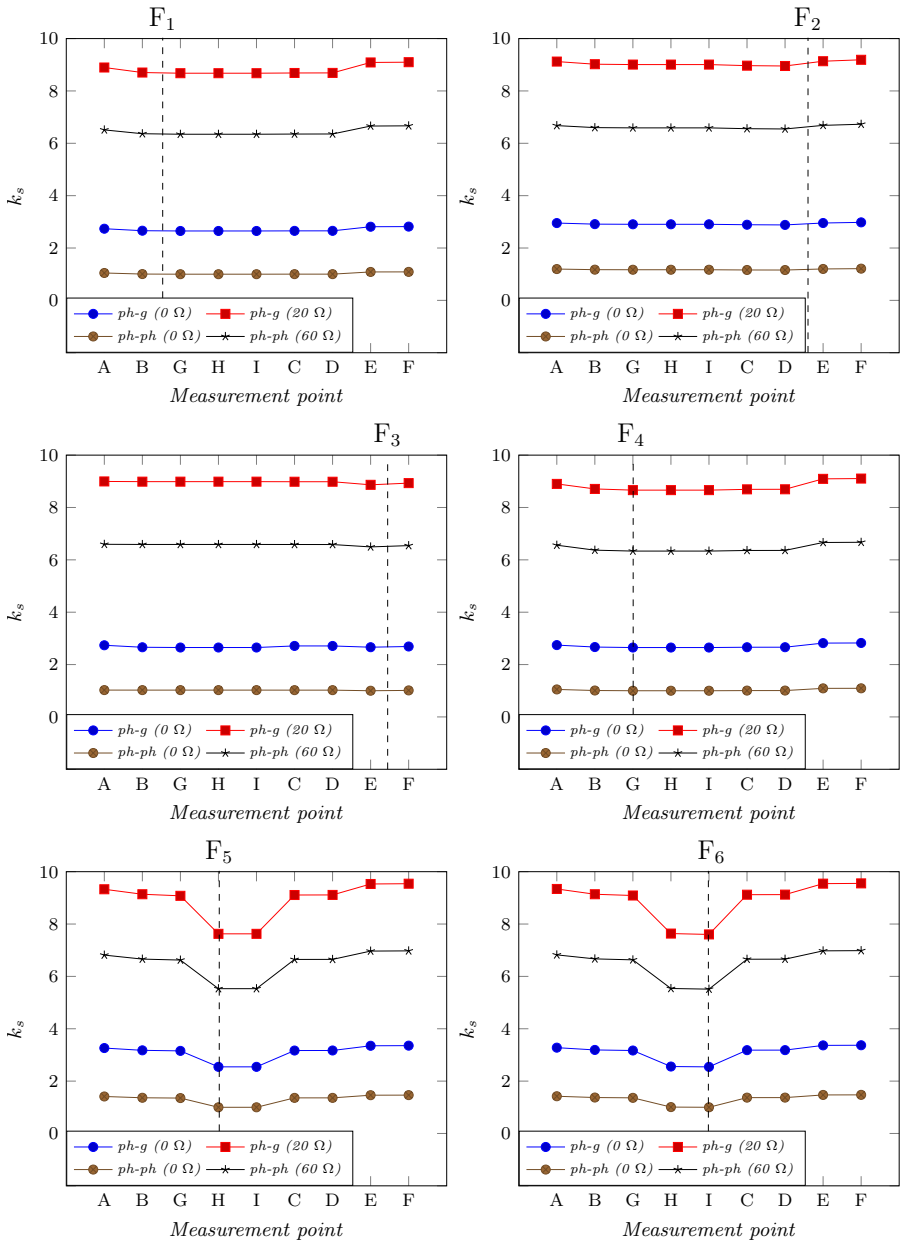

Figure 5.8: k_s profiles in ring distribution network with MV lateral emulated via model B.

Table 5.4 presents the identified FS during the 24 asymmetrical fault scenarios, 2.25 - 2.48, emulated at the ring topology of model B. The algorithm performs 100% accurately throughout the total of the simulation cases.

Table 5.4: Performance of the algorithm for simulation scenarios 2.25-2.48 conducted in the ring topology of model B.

Scenario	Fault type	Fault resistance	Fault location	Topology	Identified FS
2.25	ph-earth	0 Ω	F_1	ring	B-C-D
2.26	ph-earth	20 Ω	F_1	ring	B-C-D
2.27	ph-ph	0 Ω	F_1	ring	B-C-D
2.28	ph-ph	60 Ω	F_1	ring	B-C-D
2.29	ph-earth	0 Ω	F_2	ring	C-D-E
2.30	ph-earth	20 Ω	F_2	ring	C-D-E
2.31	ph-ph	0 Ω	F_2	ring	C-D-E
2.32	ph-ph	60 Ω	F_2	ring	C-D-E
2.33	ph-earth	0 Ω	F_3	ring	D-E-F
2.34	ph-earth	20 Ω	F_3	ring	D-E-F
2.35	ph-ph	0 Ω	F_3	ring	D-E-F
2.36	ph-ph	60 Ω	F_3	ring	D-E-F
2.37	ph-earth	0 Ω	F_4	ring	B-G
2.38	ph-earth	20 Ω	F_4	ring	B-G
2.39	ph-ph	0 Ω	F_4	ring	B-G
2.40	ph-ph	60 Ω	F_4	ring	B-G
2.41	ph-earth	0 Ω	F_5	ring	G-H
2.42	ph-earth	20 Ω	F_5	ring	G-H
2.43	ph-ph	0 Ω	F_5	ring	G-H
2.44	ph-ph	60 Ω	F_5	ring	G-H
2.45	ph-earth	0 Ω	F_6	ring	H-I
2.46	ph-earth	20 Ω	F_6	ring	H-I
2.47	ph-ph	0 Ω	F_6	ring	H-I
2.48	ph-ph	60 Ω	F_6	ring	H-I

5.4 Network topologies with unbalanced loads

The simulations performed with the aid of Powerfactory DIgSILENT, involved 1%, 2%, 3% and 4% of pre-fault load unbalance [2]. Fig. 5.9 depicts a fault happening at location F_1 of a radial network with 1% load unbalance.

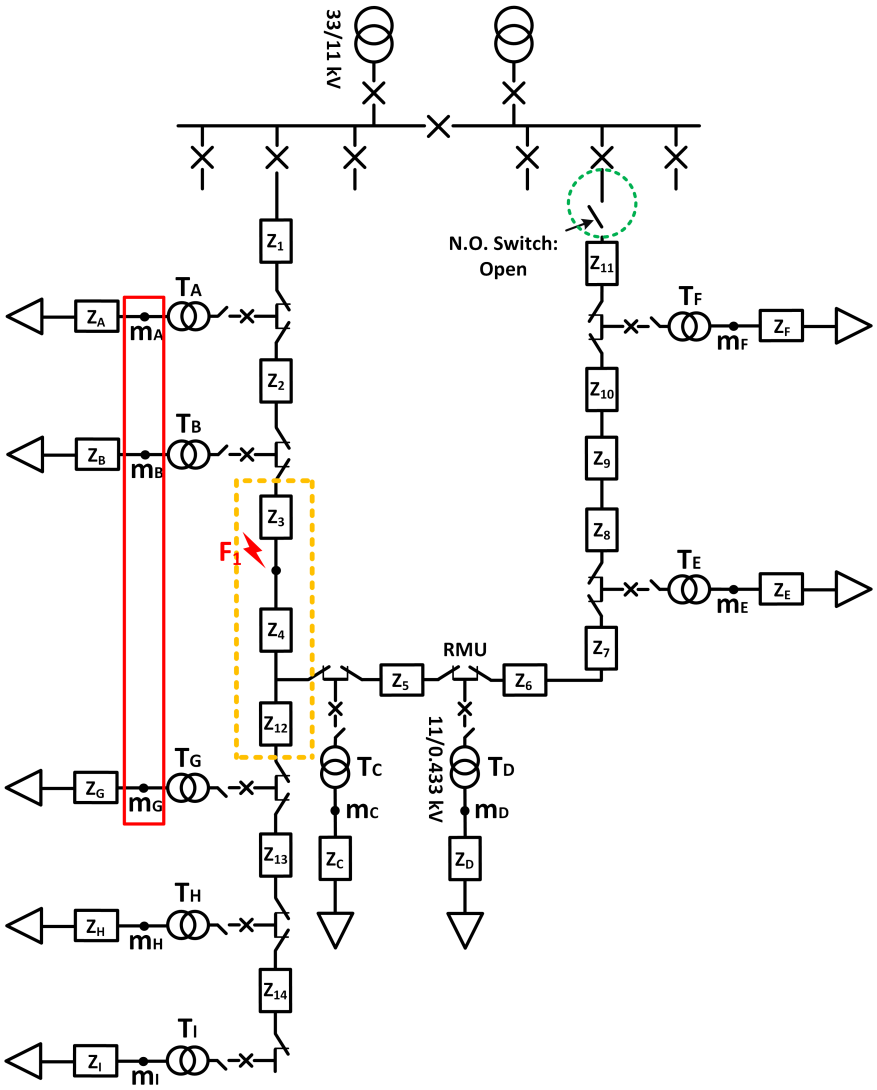

Figure 5.9: Radial distribution network with unbalanced LV loads and fault at F_1.

The graphs in Fig. 5.10-5.13 provide useful insights of the k_s deviation across all the LV measurement points with respect to the different levels of unbalance, 0%, 1%, 2%, 3% and 4%.

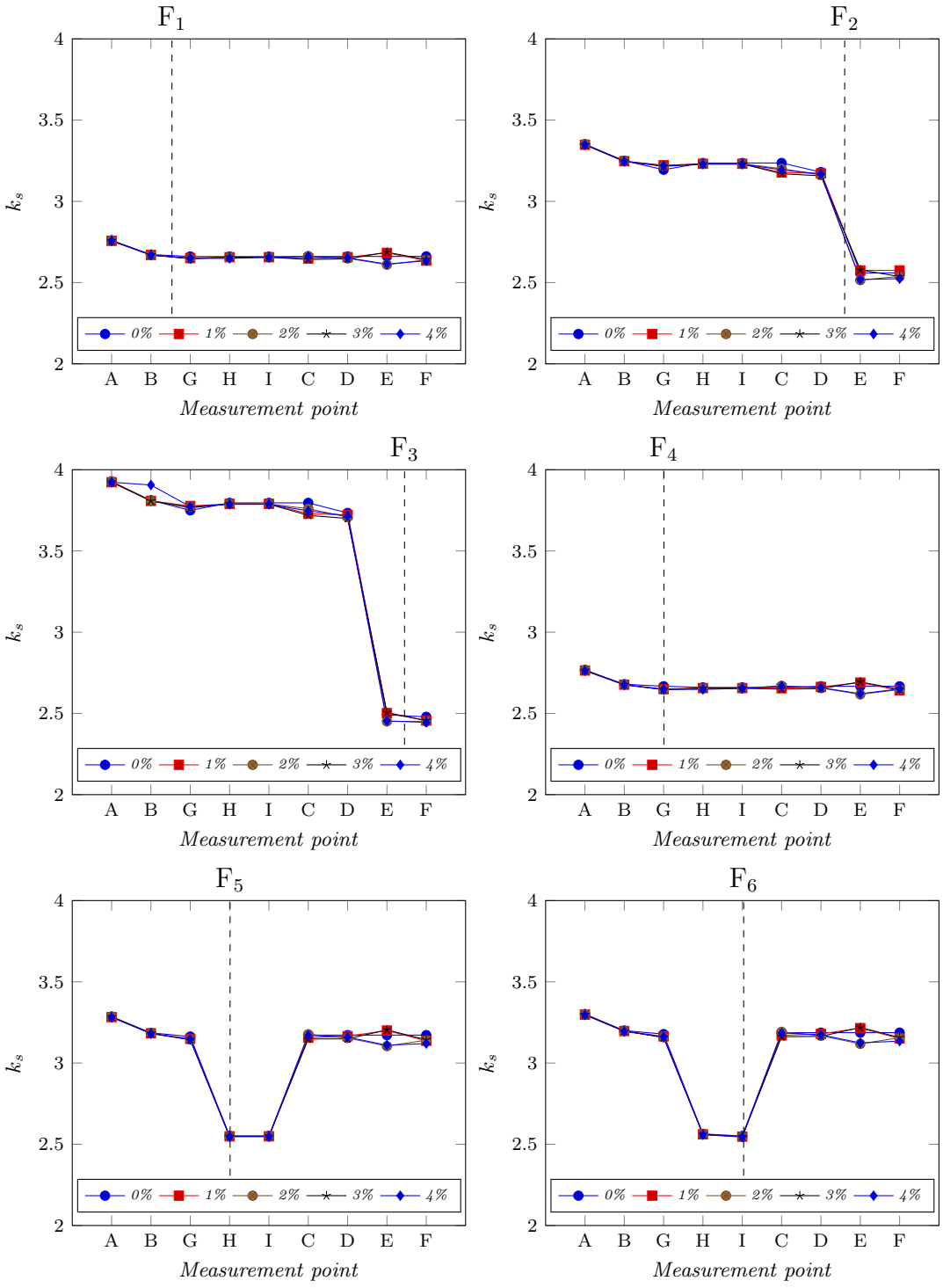

Figure 5.10: Impact of load unbalance on k_s profile. Radial topology / Phase to ground (0 Ω) fault / F_1 - F_6.

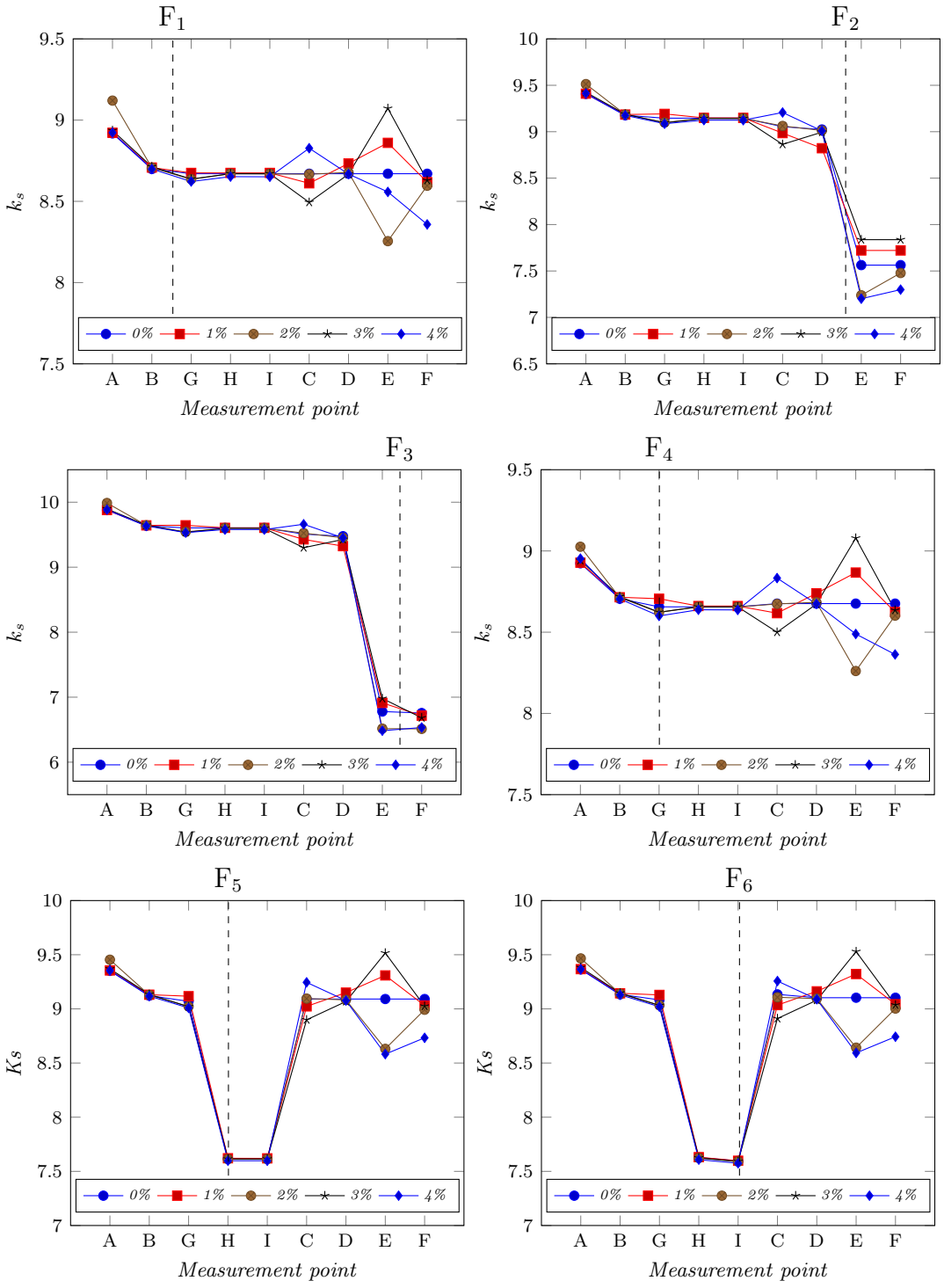

Figure 5.11: Impact of load unbalance on k_s profile. Radial topology / Phase to ground (20 Ω) fault / F_1 - F_6.

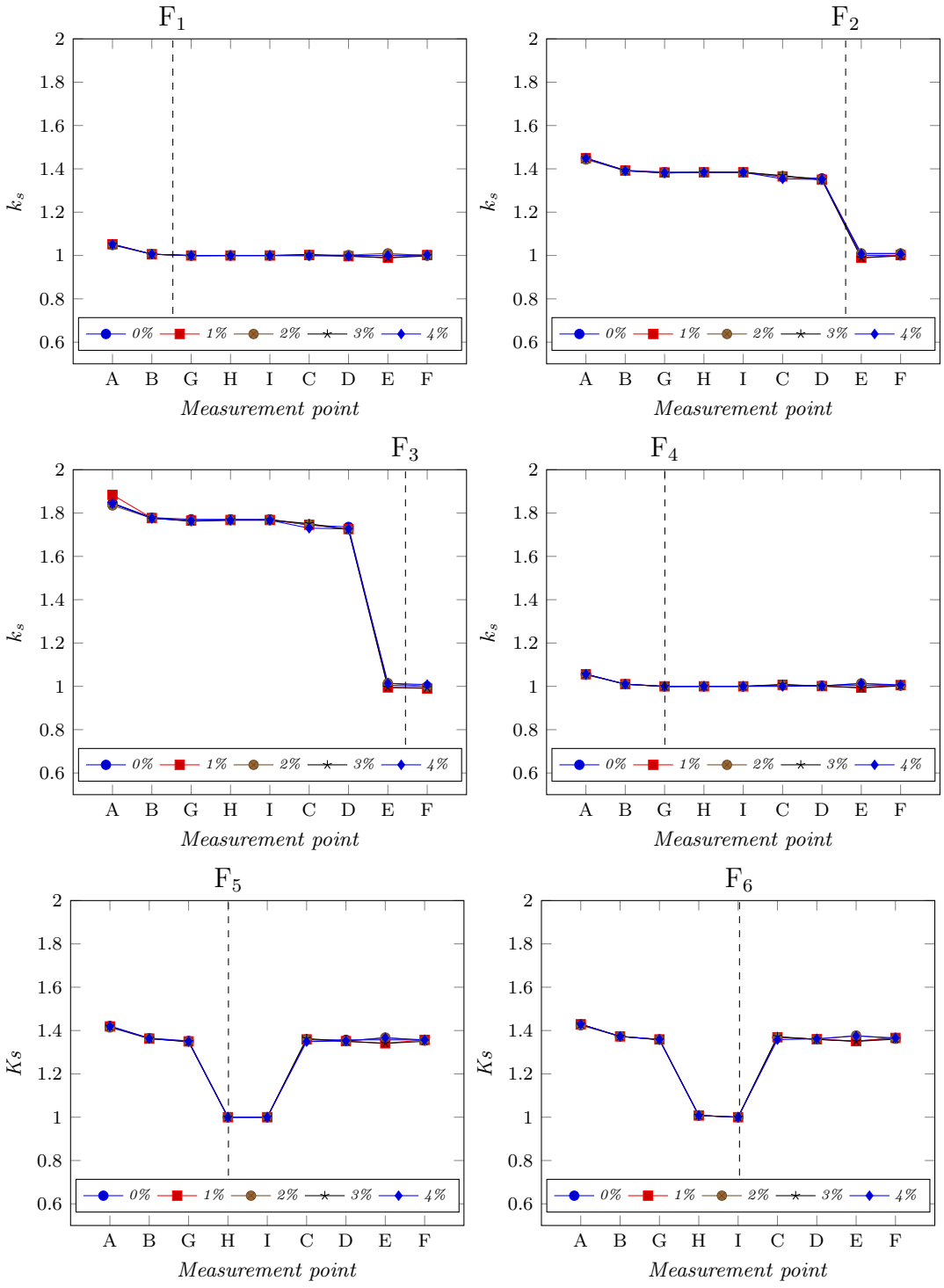

Figure 5.12: Impact of load unbalance on k_s profile. Radial topology / Phase to phase (0 Ω) fault / F_1 - F_6.

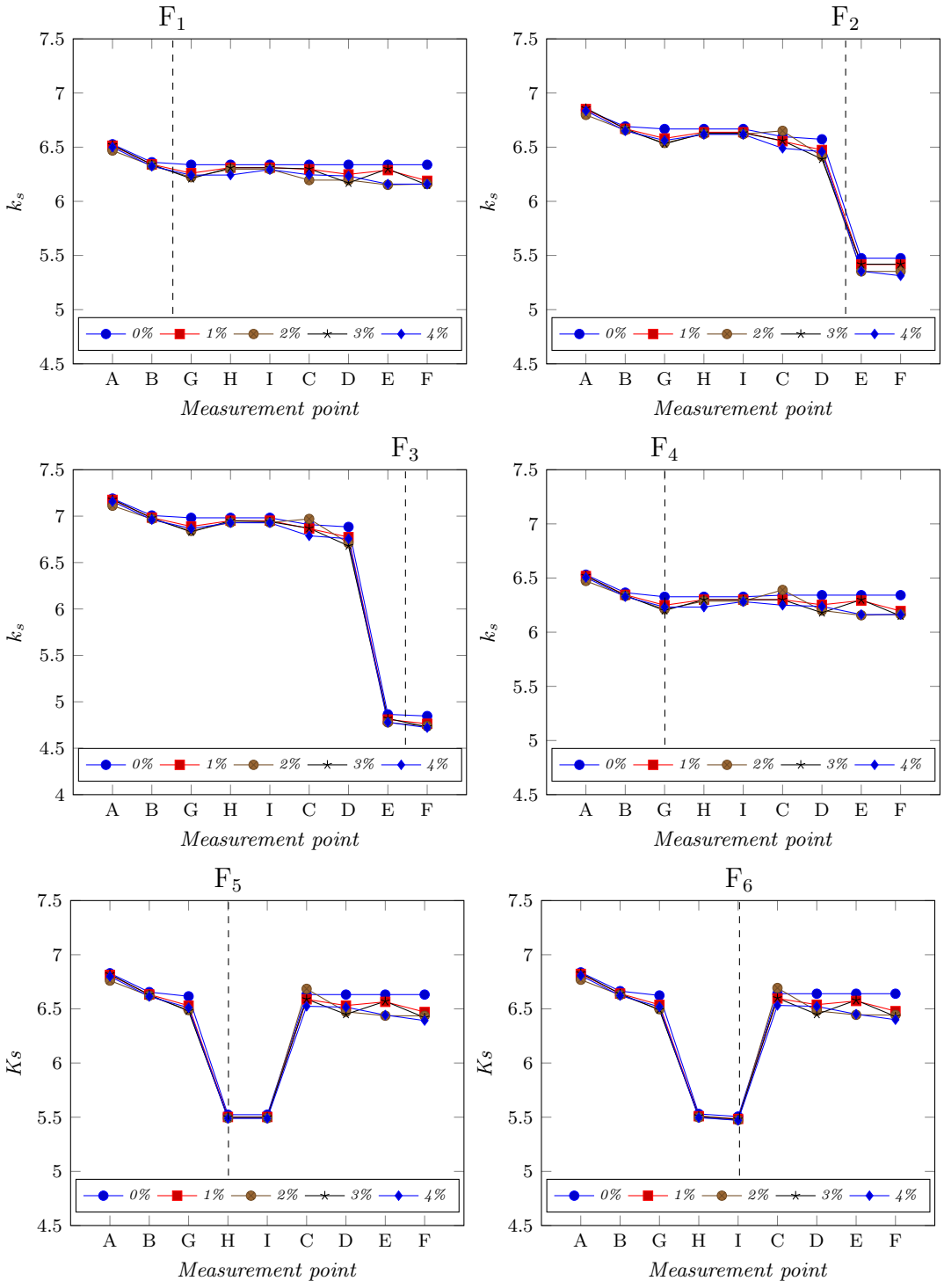

Figure 5.13: Impact of load unbalance on k_s profile. Radial topology / Phase to phase (60 Ω) fault / F_1 - F_6.

The k_s profiles depicted in Fig. 5.10 - Fig. 5.13 demonstrate consistency across the various scenarios, however the load unbalance seems to have greater impact on the parameter k_s, during the resistive 20 Ω phase-to-earth and 60 Ω phase-to-phase faults.

In the equivalent circuit of Fig. 5.14, it can be observed that when a highly resistive, i.e. Z_F=60 Ω, fault occurs then the fault current I_F is low and so the voltage drop at the MV side is not significant. Also, the pre-fault LV load currents, i.e. $I_{LD_A,1}$ and $I_{LD_A,2}$ (in case of load unbalance), are not considered negligible. As a result, the positive sequence of voltage at LV side is retained close to pre-fault levels (i.e. 0.95 p.u.) and the negative sequence is subject to variations in case of load unbalance.

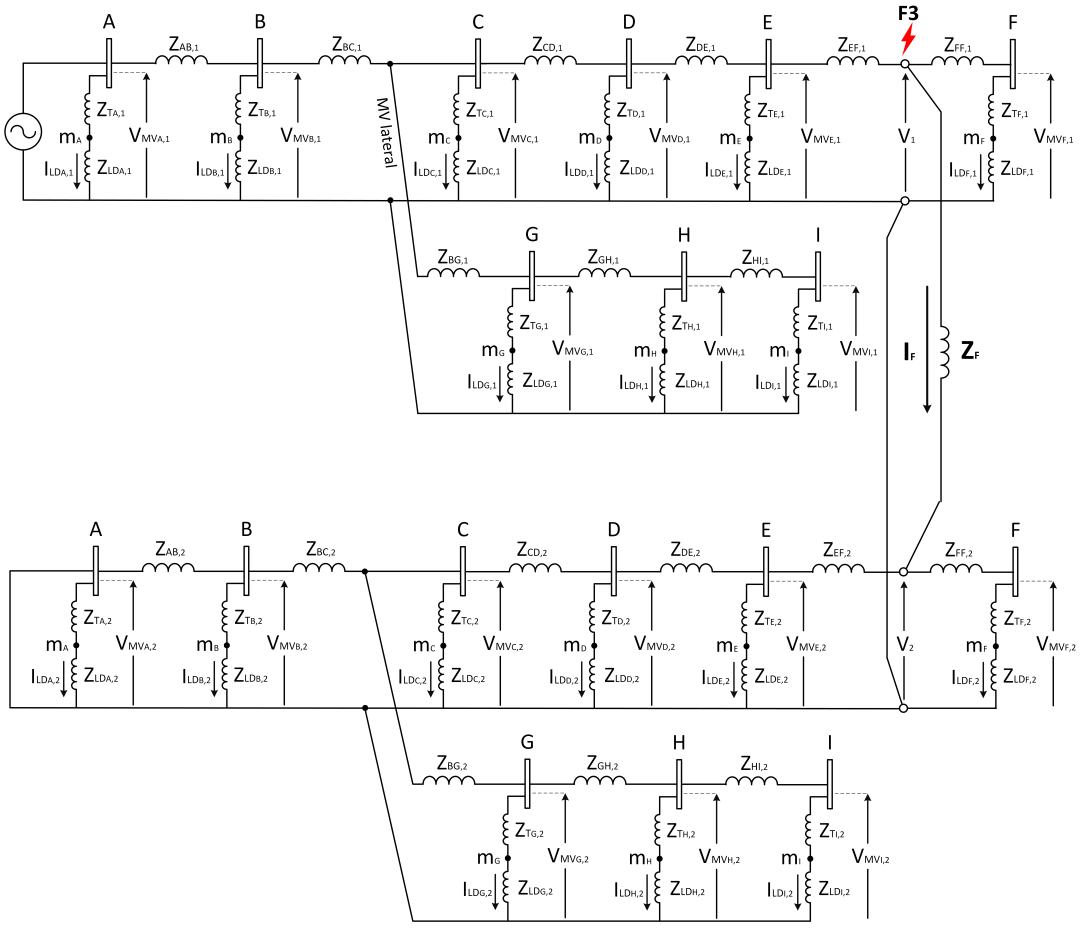

Figure 5.14: Equivalent circuit of radial topology during phase to phase fault at location F_3.

Moreover, by applying KVL during the example phase-to-phase fault depicted in

Fig. 5.14 we get:

$$V_1 = V_2 + I_F Z_F \tag{5.1}$$

So, in case of high fault resistance, i.e. Z_F=60 Ω, then V_1>>V_2. It is therefore inferred that, the insignificant negative sequence voltage observed at the LV side of the step-down transformers, due to the high fault resistance, is susceptible to variations when load unbalance is present at the LV side. This also translates to k_s variations across the various LV measurement points - especially for those installed far from the fault location - as it can be observed in Fig. 5.11 and Fig. 5.13.

Furthermore, the LV load unbalance does not affect the k_s profile significantly during solid faults. When fault impedance, i.e. Z_F in Fig. 5.14, is zero the fault current, I_F, reaches maximum levels. This leads to significant voltage drop across both MV and LV side of the network regardless the LV pre-fault conditions (i.e. load unbalance). Moreover, if during the example phase-to-phase fault, Z_F=0 then V_1=V_2 (Fig. 5.14). This reflects on the k_s profiles illustrated in Fig. 5.10 and Fig. 5.12, where k_s reaches values close to 1, especially at measurement nodes near fault location (i.e. k_s measured at m_E and m_F when fault happens at F_3).

Tables 5.5-5.8 encompass the total of the located FS during 72 different fault scenarios simulated at the radial topology of model B while applying load unbalance of 1%, 2%, 3% and 4% respectively. The algorithm is proved tolerant for up to 3% of pre-fault load unbalance and able to locate the FS successfully during scenarios 3.1 - 3.48 [2]. However, misleading results were remarked when applying 4% of load unbalance, specifically during scenarios 3.56 and 3.58, where resistive faults are applied at locations F_2 and F_3 respectively. Handling the combination of highly resistive faults of low current and minimum of 4% pre-fault load unbalance is therefore a limitation of the proposed FS location technique. All the results are presented in Appendix C.

Table 5.5: Performance of the algorithm for all simulation scenarios conducted in the radial topology of model B with load unbalance of 1%.

Scenario	Fault type	Fault resistance	Fault location	Topology	Identified FS
3.1	ph-earth	0 Ω	F_1	radial	B-C
3.2	ph-earth	20 Ω	F_1	radial	B-G
3.3	ph-ph	0 Ω	F_1	radial	B-G
3.4	ph-ph	60 Ω	F_1	radial	B-G
3.5	ph-earth	0 Ω	F_2	radial	D-E
3.6	ph-earth	20 Ω	F_2	radial	D-E
3.7	ph-ph	0 Ω	F_2	radial	D-E
3.8	ph-ph	60 Ω	F_2	radial	D-E
3.9	ph-earth	0 Ω	F_3	radial	E-F
3.10	ph-earth	20 Ω	F_3	radial	E-F
3.11	ph-ph	0 Ω	F_3	radial	E-F
3.12	ph-ph	60 Ω	F_3	radial	E-F
3.13	ph-earth	0 Ω	F_4	radial	B-G
3.14	ph-earth	20 Ω	F_4	radial	G-H
3.15	ph-ph	0 Ω	F_4	radial	B-G
3.16	ph-ph	60 Ω	F_4	radial	B-G
3.17	ph-earth	0 Ω	F_5	radial	G-H
3.18	ph-earth	20 Ω	F_5	radial	G-H
3.19	ph-ph	0 Ω	F_5	radial	G-H
3.20	ph-ph	60 Ω	F_5	radial	G-H
3.21	ph-earth	0 Ω	F_6	radial	H-I
3.22	ph-earth	20 Ω	F_6	radial	H-I
3.23	ph-ph	0 Ω	F_6	radial	H-I
3.24	ph-ph	60 Ω	F_6	radial	H-I

Table 5.6: Performance of the algorithm for all simulation scenarios conducted in the radial topology of model B with load unbalance of 2%.

Scenario	Fault type	Fault resistance	Fault location	Topology	Identified FS
3.25	ph-earth	0 Ω	F_1	radial	B-C
3.26	ph-earth	20 Ω	F_1	radial	B-G
3.27	ph-ph	0 Ω	F_1	radial	B-G
3.28	ph-ph	60 Ω	F_1	radial	B-C
3.29	ph-earth	0 Ω	F_2	radial	D-E
3.30	ph-earth	20 Ω	F_2	radial	D-E
3.31	ph-ph	0 Ω	F_2	radial	D-E
3.32	ph-ph	60 Ω	F_2	radial	D-E
3.33	ph-earth	0 Ω	F_3	radial	E-F
3.34	ph-earth	20 Ω	F_3	radial	E-F
3.35	ph-ph	0 Ω	F_3	radial	E-F
3.36	ph-ph	60 Ω	F_3	radial	E-F
3.37	ph-earth	0 Ω	F_4	radial	B-G
3.38	ph-earth	20 Ω	F_4	radial	B-G
3.39	ph-ph	0 Ω	F_4	radial	B-G
3.40	ph-ph	60 Ω	F_4	radial	B-G
3.41	ph-earth	0 Ω	F_5	radial	G-H
3.42	ph-earth	20 Ω	F_5	radial	G-H
3.43	ph-ph	0 Ω	F_5	radial	G-H
3.44	ph-ph	60 Ω	F_5	radial	G-H
3.45	ph-earth	0 Ω	F_6	radial	H-I
3.46	ph-earth	20 Ω	F_6	radial	H-I
3.47	ph-ph	0 Ω	F_6	radial	H-I
3.48	ph-ph	60 Ω	F_6	radial	H-I

Table 5.7: Performance of the algorithm for all simulation scenarios conducted in the radial topology of model B with load unbalance of 3%.

Scenario	Fault type	Fault resistance	Fault location	Topology	Identified FS
3.49	ph-earth	0 Ω	F_1	radial	B-C
3.50	ph-earth	20 Ω	F_1	radial	B-C
3.51	ph-ph	0 Ω	F_1	radial	B-G
3.52	ph-ph	60 Ω	F_1	radial	B-G
3.53	ph-earth	0 Ω	F_2	radial	D-E
3.54	ph-earth	20 Ω	F_2	radial	D-E
3.55	ph-ph	0 Ω	F_2	radial	D-E
3.56	ph-ph	60 Ω	F_2	radial	D-E
3.57	ph-earth	0 Ω	F_3	radial	E-F
3.58	ph-earth	20 Ω	F_3	radial	E-F
3.59	ph-ph	0 Ω	F_3	radial	E-F
3.60	ph-ph	60 Ω	F_3	radial	E-F
3.61	ph-earth	0 Ω	F_4	radial	B-G
3.62	ph-earth	20 Ω	F_4	radial	B-G
3.63	ph-ph	0 Ω	F_4	radial	B-G
3.64	ph-ph	60 Ω	F_4	radial	B-G
3.65	ph-earth	0 Ω	F_5	radial	G-H
3.66	ph-earth	20 Ω	F_5	radial	G-H
3.67	ph-ph	0 Ω	F_5	radial	G-H
3.68	ph-ph	60 Ω	F_5	radial	G-H
3.69	ph-earth	0 Ω	F_6	radial	H-I
3.70	ph-earth	20 Ω	F_6	radial	H-I
3.71	ph-ph	0 Ω	F_6	radial	H-I
3.72	ph-ph	60 Ω	F_6	radial	H-I

Table 5.8: Performance of the algorithm for all simulation scenarios conducted in the radial topology of model B with load unbalance of 4%.

Scenario	Fault type	Fault resistance	Fault location	Topology	Identified FS
3.49	ph-earth	0 Ω	F_1	radial	B-G
3.50	ph-earth	20 Ω	F_1	radial	B-G
3.51	ph-ph	0 Ω	F_1	radial	B-G
3.52	ph-ph	60 Ω	F_1	radial	B-G
3.53	ph-earth	0 Ω	F_2	radial	D-E
3.54	ph-earth	20 Ω	F_2	radial	D-E
3.55	ph-ph	0 Ω	F_2	radial	D-E
3.56	ph-ph	60 Ω	F_2	radial	E-F
3.57	ph-earth	0 Ω	F_3	radial	E-F
3.58	ph-earth	20 Ω	F_3	radial	D-E
3.59	ph-ph	0 Ω	F_3	radial	E-F
3.60	ph-ph	60 Ω	F_3	radial	E-F
3.61	ph-earth	0 Ω	F_4	radial	B-G
3.62	ph-earth	20 Ω	F_4	radial	B-G
3.63	ph-ph	0 Ω	F_4	radial	B-G
3.64	ph-ph	60 Ω	F_4	radial	B-G
3.65	ph-earth	0 Ω	F_5	radial	H-I
3.66	ph-earth	20 Ω	F_5	radial	H-I
3.67	ph-ph	0 Ω	F_5	radial	H-I
3.68	ph-ph	60 Ω	F_5	radial	G-H
3.69	ph-earth	0 Ω	F_6	radial	H-I
3.70	ph-earth	20 Ω	F_6	radial	H-I
3.71	ph-ph	0 Ω	F_6	radial	H-I
3.72	ph-ph	60 Ω	F_6	radial	H-I

5.5 Network topologies with distributed generation

5.5.1 Synchronous generation and PV plants

This section assesses the impact of DGs, connected to both MV and LV side of the network, on the operation of the developed fault location algorithm. Specifically, it includes the results of scenarios 4.1 - 4.24 conducted using the DG models in DIgSILENT Powerfactory [2]. Fig. 5.15 illustrates the single line diagram (SLD) of the topology emulated with the aid of model B.

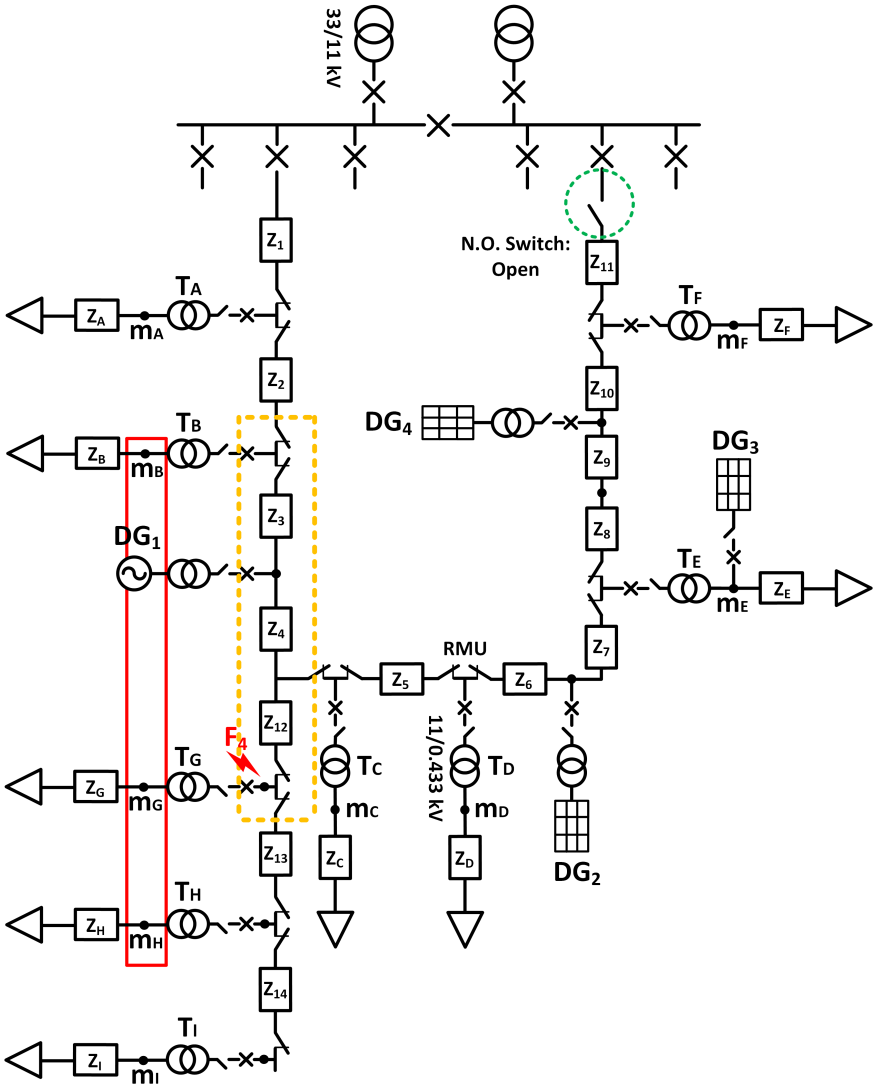

Figure 5.15: Single line diagram of the radial topology simulated with model B.

The above SLD presents the connection points of the various DGs across the deployed MV and LV network, a fault at location F_4 and the 3-points window (red frame) revealing the FS (orange dashed frame).

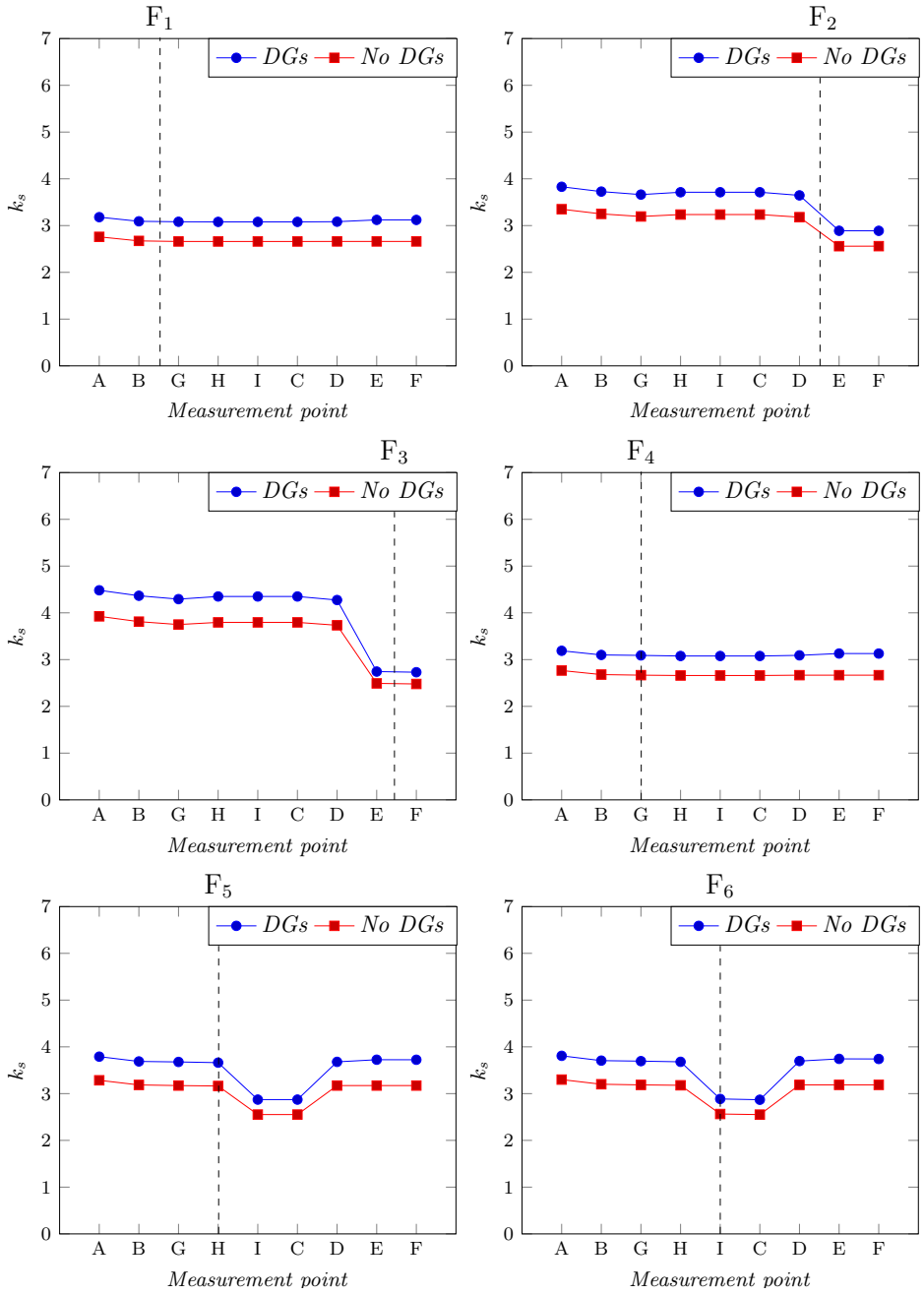

Figure 5.16: DGs impact on k_s profile. Radial topology / Phase to ground 0 Ω / F_1 - F_6.

Fig. 5.16 showcases the impact of the DGs on the k_s profile across the distributed LV measurement points during a solid phase to ground fault. This is achieved by comparing the k_s measurements with those acquired from the same network without DGs. It can be noticed that the implemented distributed generation units (PVs and SG) maintain the ratio k_s in higher levels during the fault event comparing to the measurements collected from the corresponding passive distribution network. However, the "shape" of the profile and trend of the data presents consistency which is beneficial for the performance of the FS location algorithm.

Table 5.9 contains the total of the FS located during the fault scenarios 4.1 - 4.24 simulated at the radial topology of model B. Although distributed generation affected the total of the k_s data, the algorithm accurately located the FS during the total of the imposed scenarios [2].

Table 5.9: Performance of the algorithm for all simulation scenarios conducted in the radial topology of model B with DGs.

Scenario	Fault type	Fault resistance	Fault location	Topology	Identified FS
4.1	ph-earth	0 Ω	F_1	radial	B-G
4.2	ph-earth	20 Ω	F_1	radial	B-G
4.3	ph-ph	0 Ω	F_1	radial	B-G
4.4	ph-ph	60 Ω	F_1	radial	B-G
4.5	ph-earth	0 Ω	F_2	radial	D-E
4.6	ph-earth	20 Ω	F_2	radial	D-E
4.7	ph-ph	0 Ω	F_2	radial	D-E
4.8	ph-ph	60 Ω	F_2	radial	D-E
4.9	ph-earth	0 Ω	F_3	radial	E-F
4.10	ph-earth	20 Ω	F_3	radial	E-F
4.11	ph-ph	0 Ω	F_3	radial	E-F
4.12	ph-ph	60 Ω	F_3	radial	E-F
4.13	ph-earth	0 Ω	F_4	radial	B-G

Continued on next page

Table 5.9 – *Continued from previous page*

Scenario	Fault type	Fault resistance	Fault location	Topology	Identified FS
4.14	ph-earth	20 Ω	F_4	radial	B-G
4.15	ph-ph	0 Ω	F_4	radial	B-G
4.16	ph-ph	60 Ω	F_4	radial	B-G
4.17	ph-earth	0 Ω	F_5	radial	G-H
4.18	ph-earth	20 Ω	F_5	radial	G-H
4.19	ph-ph	0 Ω	F_5	radial	G-H
4.20	ph-ph	60 Ω	F_5	radial	G-H
4.21	ph-earth	0 Ω	F_6	radial	H-I
4.22	ph-earth	20 Ω	F_6	radial	H-I
4.23	ph-ph	0 Ω	F_6	radial	H-I
4.24	ph-ph	60 Ω	F_6	radial	H-I

5.5.2 High penetration of LV connected PV generation

Scenarios 4.25-4.48 involved a dynamic model implemented in MATLAB Simulink to realistically reflect the behaviour of an off-the-shelf PV inverter during faults. Thus, the performance of the FS location technique is examined when this is applied in a faulted active distribution network dominated by LV connected PVs. In particular, the implemented PVs cover the 85.3% of the total demand. The PV inverter dynamic model represents the inverters interfacing the PV_1 - PV_{14} connected at various LV points of the network.

Fig. 5.17 illustrates the single line diagram of the topology emulated with model C in MATLAB Simulink. The mentioned figure indicates the connection points of PV_1-PV_{14} across the deployed network, an example fault at location F_3 and the 3-points window identifying the FS. During the particular fault scenario, the inverters of PV_2, PV_5, PV_{10}, PV_{11} and PV_{12} - yellow colour - activate FRT 1, while the rest of the PV inverters - cyan colour - operate with FRT 2.

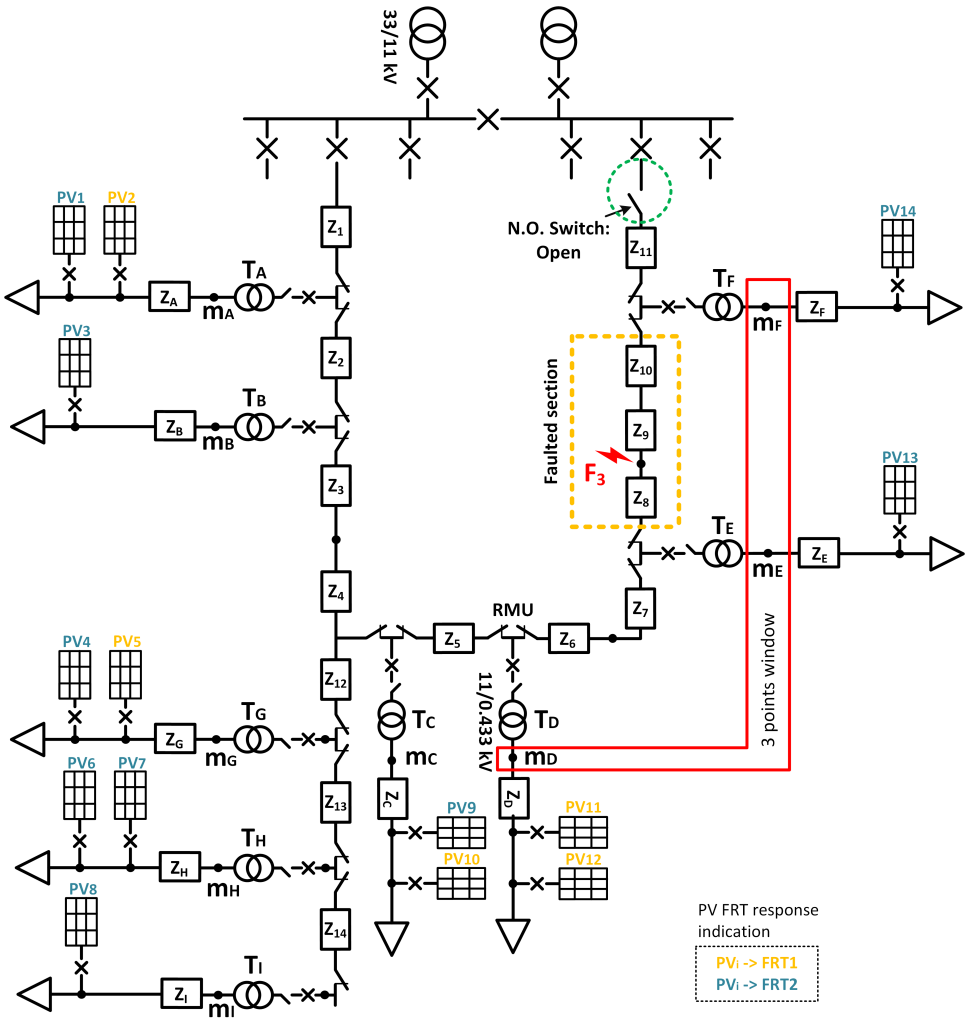

Figure 5.17: Radial topology of network represented by model C under solid phase-to-phase fault at location F_3.

The FRT response of the modelled PV inverter depends on the loading level of the device, the magnitude of the disturbed voltage (single and three phase) and the voltage unbalance measured at its output during the fault [2]. As described in Chapter 4 and Table 4.11, when certain thresholds of the referred AC voltage network conditions ($V_3\phi$, $V_1\phi$, V_2/V_1) are exceeded, the PV inverter ceases to output power (FRT 2). On the contrary, when the said thresholds are not exceeded, the PV inverter injects active and reactive positive sequence current (FRT 1). It is therefore important to observe which particular PVs continued to output power during the applied fault scenarios.

Tables 5.10 and 5.11 provide information regarding the aforementioned network conditions which were captured at the output of each PV inverter during the example phase-to-earth resistive (20 Ω) and phase-to-phase solid (0 Ω) fault scenarios, respectively. The referred faults were repeatedly applied at the locations F_1 - F_6. The table cells with yellow shading denote that the relevant PV inverter activated the FRT 1 strategy under the captured conditions, whereas these with cyan the FRT 2.

The tables demonstrate that the inverter model follows the pre-defined FRT strategy depending on the network conditions such as $V_{3\phi}$, $V_{1\phi}$ and V_2/V_1. They also highlight the diverse FRT response of the PV inverters due to the different loading levels and the various faults applied in the network of different types and locations.

Table 5.10: Network conditions and PV inverters FRT response / Radial topology / Phase to ground (20 Ω) fault.

PV inverter	Loading level	Network conditions	Fault location					
			F_1	F_2	F_3	F_4	F_5	F_6
PV_1	100%	$V_{3\phi}$ [pu]	0.85	0.904	0.926	0.858	0.903	0.903
		$V_{1\phi}$ [pu]	0.835	0.908	0.927	0.846	0.907	0.908
		V_2/V_1	0.083	0.036	0.023	0.075	0.037	0.036
PV_2	25%	$V_{3\phi}$ [pu]	0.85	0.904	0.926	0.858	0.903	0.903
		$V_{1\phi}$ [pu]	0.835	0.908	0.927	0.846	0.907	0.908
		V_2/V_1	0.083	0.036	0.023	0.075	0.037	0.036
PV_3	75%	$V_{3\phi}$ [pu]	0.809	0.892	0.928	0.82	0.889	0.891
		$V_{1\phi}$ [pu]	0.748	0.871	0.902	0.766	0.869	0.871
		V_2/V_1	0.147	0.062	0.039	0.133	0.064	0.063
PV_4	100%	$V_{3\phi}$ [pu]	0.793	0.869	0.91	0.769	0.862	0.864
		$V_{1\phi}$ [pu]	0.746	0.863	0.894	0.725	0.857	0.858
		V_2/V_1	0.153	0.077	0.048	0.175	0.081	0.08
PV_5	25%	$V_{3\phi}$ [pu]	0.793	0.869	0.91	0.769	0.862	0.864
		$V_{1\phi}$ [pu]	0.746	0.863	0.894	0.725	0.857	0.858

Continued on next page

Table 5.10 – *Continued from previous page*

PV inverter	Loading level	Network conditions	Fault location					
			F_1	F_2	F_3	F_4	F_5	F_6
		V_2/V_1	0.153	0.077	0.048	0.175	0.081	0.08
PV_6	100%	$V_{3\phi}$ [pu]	0.788	0.862	0.904	0.764	0.579	0.582
		$V_{1\phi}$ [pu]	0.736	0.846	0.877	0.715	0.548	0.554
		V_2/V_1	0.152	0.076	0.048	0.174	0.338	0.331
PV_7	50%	$V_{3\phi}$ [pu]	0.788	0.862	0.904	0.764	0.579	0.582
		$V_{1\phi}$ [pu]	0.736	0.846	0.877	0.715	0.548	0.554
		V_2/V_1	0.152	0.076	0.048	0.174	0.338	0.331
PV_8	50%	$V_{3\phi}$ [pu]	0.782	0.848	0.894	0.755	0.629	0.628
		$V_{1\phi}$ [pu]	0.742	0.864	0.901	0.717	0.589	0.589
		V_2/V_1	0.161	0.081	0.051	0.184	0.339	0.341
PV_9	100%	$V_{3\phi}$ [pu]	0.794	0.868	0.908	0.775	0.865	0.867
		$V_{1\phi}$ [pu]	0.748	0.847	0.879	0.735	0.844	0.845
		V_2/V_1	0.151	0.076	0.047	0.167	0.078	0.076
PV_{10}	25%	$V_{3\phi}$ [pu]	0.864	0.79	0.904	0.771	0.861	0.849
		$V_{1\phi}$ [pu]	0.748	0.847	0.879	0.735	0.844	0.868
		V_2/V_1	0.151	0.076	0.047	0.167	0.078	0.081
PV_{11}	25%	$V_{3\phi}$ [pu]	0.955	0.98	1.003	0.945	0.982	0.983
		$V_{1\phi}$ [pu]	0.81	0.938	0.969	0.796	0.94	0.942
		V_2/V_1	0.155	0.084	0.053	0.171	0.08	0.079
PV_{12}	50%	$V_{3\phi}$ [pu]	0.955	0.98	1.008	0.95	0.987	0.988
		$V_{1\phi}$ [pu]	0.81	0.938	0.969	0.796	0.94	0.942
		V_2/V_1	0.155	0.084	0.053	0.171	0.08	0.079
PV_{13}	50%	$V_{3\phi}$ [pu]	0.786	0.633	0.606	0.764	0.847	0.849
		$V_{1\phi}$ [pu]	0.749	0.601	0.59	0.731	0.867	0.868
		V_2/V_1	0.159	0.334	0.377	0.175	0.082	0.081

Continued on next page

Table 5.10 – *Continued from previous page*

PV inverter	Loading level	Network conditions	Fault location					
			F_1	F_2	F_3	F_4	F_5	F_6
PV_{14}	50%	$V_{3\phi}$ [pu]	0.785	0.627	0.596	0.763	0.852	0.854
		$V_{1\phi}$ [pu]	0.751	0.587	0.572	0.732	0.879	0.881
		V_2/V_1	0.166	0.351	0.405	0.183	0.086	0.084

Table 5.10 reveals that only the inverter of PV_6, operating at 100% of its total capacity, triggered FRT 2 strategy during 20 Ω faults occurring at locations F_5 and F_6. This is due to the fact that voltage unbalance, V_2/V_1, and RMS voltage, $V_{3\phi}$, exceeded the relevant predefined thresholds during the fault. In particular the ratio V_2/V_1 was measured at 0.338 which is higher than the predefined limit of 0.3. This was combined with the $V_{3\phi}$ of 0.582 pu surpassing the threshold of 0.9 pu, leading the inverter to initiate the FRT 2 operation.

Furthermore, the resultant FRT responses of the various PV inverters in Table 5.11 present higher diversity compared to those of Table 5.10. Specifically, the solid phase to phase fault led more inverters to the activation of FRT 2 strategy in comparison to the previous resistive fault scenario.

Table 5.11: PV inverters FRT responses / Radial topology / Phase to phase (0 Ω) fault.

PV inverter	Loading level	Network conditions	Fault location					
			F_1	F_2	F_3	F_4	F_5	F_6
PV_1	100%	$V_{3\phi}$ [pu]	0.421	0.804	0.874	0.495	0.8	0.803
		$V_{1\phi}$ [pu]	0.44	0.832	0.887	0.533	0.829	0.832
		V_2/V_1	0.278	0.047	0.027	0.207	0.049	0.048
PV_2	25%	$V_{3\phi}$ [pu]	0.421	0.804	0.874	0.495	0.8	0.803
		$V_{1\phi}$ [pu]	0.44	0.832	0.887	0.533	0.829	0.832
		V_2/V_1	0.278	0.047	0.027	0.207	0.049	0.048

Continued on next page

Table 5.11 – *Continued from previous page*

PV inverter	Loading level	Network conditions	Fault location					
			F_1	F_2	F_3	F_4	F_5	F_6
PV_3	75%	$V_{3\phi}$ [pu]	0.223	0.739	0.84	0.326	0.733	0.738
		$V_{1\phi}$ [pu]	0.061	0.751	0.835	0.268	0.746	0.75
		V_2/V_1	0.832	0.085	0.047	0.463	0.088	0.086
PV_4	100%	$V_{3\phi}$ [pu]	0.218	0.682	0.802	0.218	0.665	0.671
		$V_{1\phi}$ [pu]	0.095	0.71	0.816	0.095	0.696	0.701
		V_2/V_1	0.827	0.109	0.057	0.828	0.117	0.114
PV_5	100%	$V_{3\phi}$ [pu]	0.218	0.682	0.802	0.218	0.665	0.671
		$V_{1\phi}$ [pu]	0.095	0.71	0.816	0.095	0.696	0.701
		V_2/V_1	0.827	0.109	0.057	0.828	0.117	0.114
PV_6	100%	$V_{3\phi}$ [pu]	0.193	0.681	0.797	0.193	0.193	0.197
		$V_{1\phi}$ [pu]	0.018	0.7	0.802	0.018	0.018	0.023
		V_2/V_1	1.002	0.109	0.057	1.003	1.002	0.949
PV_7	100%	$V_{3\phi}$ [pu]	0.193	0.681	0.797	0.193	0.193	0.197
		$V_{1\phi}$ [pu]	0.018	0.7	0.802	0.118	0.018	0.023
		V_2/V_1	1.002	0.109	0.057	1.003	1.002	0.949
PV_8	50%	$V_{3\phi}$ [pu]	0.211	0.662	0.787	0.211	0.211	0.211
		$V_{1\phi}$ [pu]	0.012	0.703	0.817	0.012	0.012	0.012
		V_2/V_1	1	0.117	0.062	1.001	1.001	1.001
PV_9	100%	$V_{3\phi}$ [pu]	0.212	0.687	0.809	0.221	0.682	0.687
		$V_{1\phi}$ [pu]	0.144	0.708	0.812	0.147	0.704	0.708
		V_2/V_1	0.802	0.109	0.057	0.748	0.112	0.109
PV_{10}	25%	$V_{3\phi}$ [pu]	0.211	0.684	0.805	0.22	0.679	0.683
		$V_{1\phi}$ [pu]	0.144	0.708	0.812	0.147	0.704	0.708
		V_2/V_1	0.802	0.109	0.057	0.748	0.112	0.109
PV_{11}	25%	$V_{3\phi}$ [pu]	0.312	0.815	0.955	0.335	0.898	0.903

Continued on next page

Table 5.11 – *Continued from previous page*

PV inverter	Loading level	Network conditions	Fault location					
			F_1	F_2	F_3	F_4	F_5	F_6
		$V_{1\phi}$ [pu]	0.202	0.77	0.9	0.175	0.815	0.82
		V_2/V_1	0.782	0.122	0.064	0.726	0.116	0.113
PV_{12}	50%	$V_{3\phi}$ [pu]	0.314	0.818	0.96	0.337	0.902	0.907
		$V_{1\phi}$ [pu]	0.202	0.77	0.9	0.175	0.815	0.82
		V_2/V_1	0.782	0.122	0.064	0.726	0.116	0.113
PV_{13}	50%	$V_{3\phi}$ [pu]	0.207	0.208	0.21	0.214	0.66	0.666
		$V_{1\phi}$ [pu]	0.014	0.014	0.019	0.031	0.704	0.709
		V_2/V_1	1	1.001	0.967	0.917	0.118	0.116
PV_{14}	50%	$V_{3\phi}$ [pu]	0.219	0.22	0.22	0.227	0.655	0.661
		$V_{1\phi}$ [pu]	0.004	0.004	0.003	0.003	0.707	0.712
		V_2/V_1	0.999	1	1	0.916	0.124	0.121

Fig 5.18 and Fig 5.19 illustrate the three-phase AC inverter output current of PV_4 and PV_2 respectively, during a phase to phase (0 Ω) at location F_1.

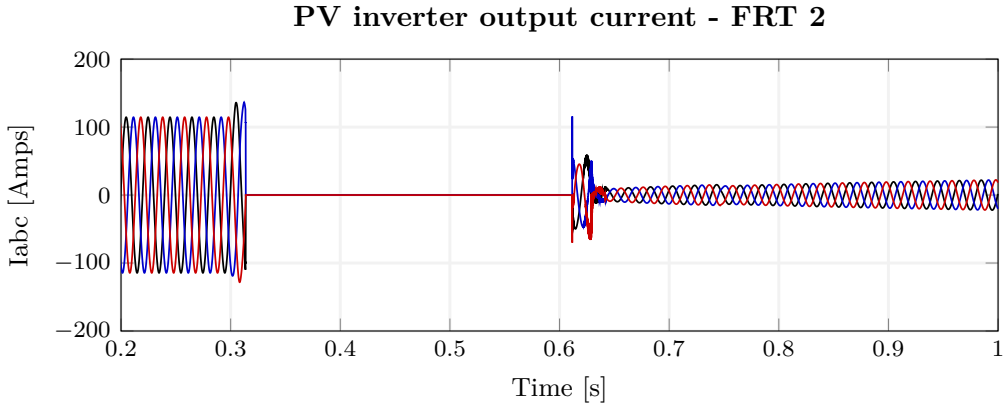

Figure 5.18: PV_4 output current during a phase to phase (0 Ω) at location F_1 - 100% Loading - FRT 2

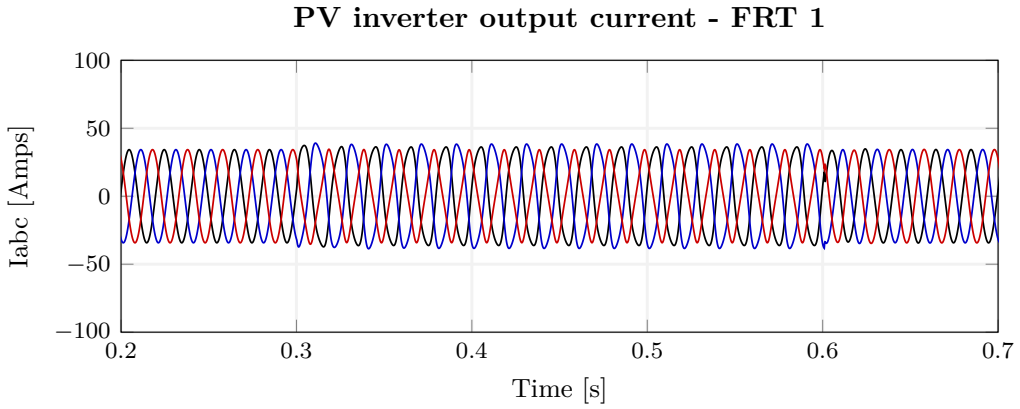

Figure 5.19: PV_2 output current during a phase to phase (0 Ω) at location F_1 - 25% Loading - FRT 1

Fig. 5.20 illustrates the impact of the grid-tied PVs on the k_s profile by comparing it with the corresponding captured from the passive (no DGs) distribution network. It can be seen that, the former is prone to remarkable changes depending on the fault location. In most cases, it is clear from visual inspection that the k_s values recorded at the LV measurement points around the FS have been significantly disturbed.

Evidently, the high percentage (85.3%) of DGs penetration against maximum demand has an effect on the k_s status during the occurrence of a fault. Fig. 5.20 demonstrates that the ratios k_s upstream the fault are larger than those extracted during simulations without the incorporation of DGs. Another observation is the significantly larger percentage differences, $\Delta k_{s_{13}}\%$, related to the FS (i.e. range between 72.5% and 202.67% in resistive phase-to-earth faults) compared to those collected in previous sections (i.e 2.57% - 37.67% in resistive phase-to-earth faults). This is due to the fact that the PV inverters produce only positive sequence active and reactive currents during faults. As a result, the further away the PV inverter is from the fault location the closer to the pre-fault rate the positive sequence voltage will be retained and thus larger deviations are observed between k_{s_1} and k_{s_3}. The mentioned $\Delta k_{s_{13}}\%$ values can be found in Appendix C. This is a very important fact for the effectiveness of the introduced FS location algorithm because the "path" towards the identification of the faulted MV zone becomes even more distinct.

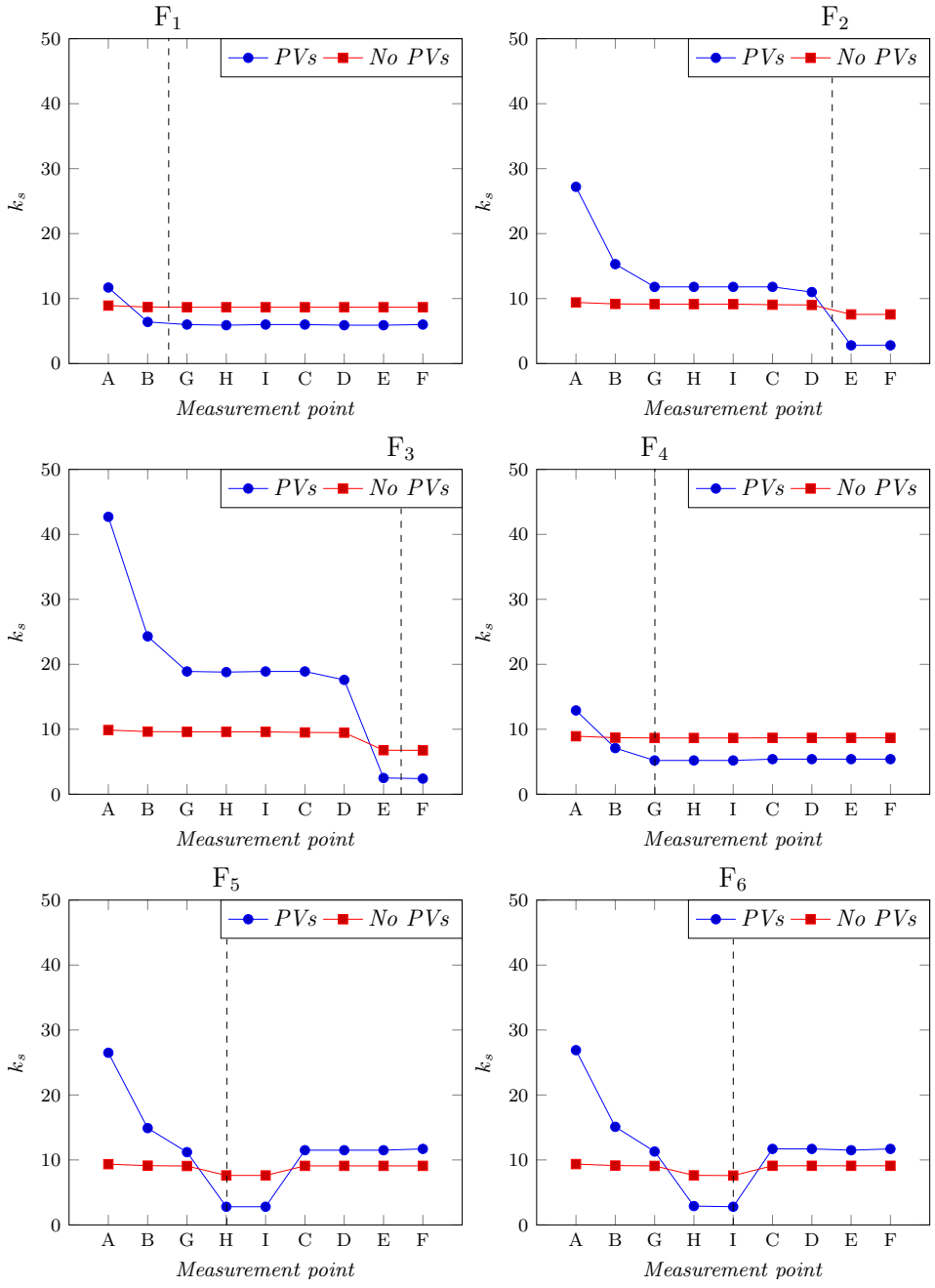

Figure 5.20: PVs impact on k_s profile. Radial topology / Phase to ground 20 Ω / F_1 - F_6.

Table 5.12 includes all the FS located by the algorithm after 24 different fault scenarios simulated at the radial topology of model C. The proposed technique was proved immune to the effect of the numerous LV connected PVs and located the FS

with 100% accuracy throughout the total of the imposed scenarios.

Table 5.12: Performance of the algorithm for all simulation scenarios conducted in the radial topology of model C with high pentration of LV connected PVs.

Scenario	Fault type	Fault resistance	Fault location	Topology	Identified FS
4.25	ph-earth	0 Ω	F_1	radial	B-G
4.26	ph-earth	20 Ω	F_1	radial	B-C
4.27	ph-ph	0 Ω	F_1	radial	B-G
4.28	ph-ph	60 Ω	F_1	radial	B-C
4.29	ph-earth	0 Ω	F_2	radial	D-E
4.30	ph-earth	20 Ω	F_2	radial	D-E
4.31	ph-ph	0 Ω	F_2	radial	D-E
4.32	ph-ph	60 Ω	F_2	radial	D-E
4.33	ph-earth	0 Ω	F_3	radial	E-F
4.34	ph-earth	20 Ω	F_3	radial	E-F
4.35	ph-ph	0 Ω	F_3	radial	E-F
4.36	ph-ph	60 Ω	F_3	radial	E-F
4.37	ph-earth	0 Ω	F_4	radial	B-G
4.38	ph-earth	20 Ω	F_4	radial	B-G
4.39	ph-ph	0 Ω	F_4	radial	B-G
4.40	ph-ph	60 Ω	F_4	radial	B-G
4.41	ph-earth	0 Ω	F_5	radial	G-H
4.42	ph-earth	20 Ω	F_5	radial	G-H
4.43	ph-ph	0 Ω	F_5	radial	G-H
4.44	ph-ph	60 Ω	F_5	radial	G-H
4.45	ph-earth	0 Ω	F_6	radial	H-I
4.46	ph-earth	20 Ω	F_6	radial	H-I
4.47	ph-ph	0 Ω	F_6	radial	H-I

Continued on next page

Table 5.12 – *Continued from previous page*

Scenario	Fault type	Fault resistance	Fault location	Topology	Identified FS
4.48	ph-ph	60 Ω	F_6	radial	H-I

5.6 Chapter summary

This chapter analysed the results of the simulations conducted for the evaluation of the proposed FS location technique. The study deployed multiple network configurations and challenging characteristics such as load unbalance and high DGs penetration. The latter was supported via the deployment of a dynamic model satisfactorily emulating the response of a commercially available PV inverter during faults. The referred model, developed and validated against physical testing of the actual inverter, was integrated in the network studies.

The FS location algorithm exhibited effective operation under the majority of the imposed asymmetrical fault scenarios. In particular, the developed technique located accurately the FS during 214 out of the 216 simulation scenarios, meaning 99.07% accuracy. The algorithm performance was compromised during resistive faults applied in a network with 4% of pre-fault load unbalance. This remark highlights the need of future work in order the algorithm to compensate the effect of LV load unbalance on the ratio k_s.

5.7 References

[1] P. Bountouris, H. Guo, I. Abdulhadi, and F. Coffele, "Medium voltage fault location using distributed LV measurements," in *14th International Conference on Developments in Power System Protection (DPSP)*, pp. 1–6, March 2018.

[2] P. Bountouris, H. Guo, D. Tzelepis, I. Abdulhadi, F. Coffele, and C. Booth, "MV faulted section location in distribution systems based on unsynchronized LV measurements," *International Journal of Electrical Power and Energy Systems*, vol. 119, 2020.

[3] P. Bountouris, I. Abdulhadi, and F. Coffele, "Dynamic model of commercially available inverters with validation against hardware testing," *IEEE Transactions on Power Systems*, 2022.

Chapter 6

Laboratory experimentation and hardware implementation

6.1 Chapter overview

The purpose of this chapter is to examine the performance of the proposed algorithm through laboratory experiments and further simulations which consider a number of implementation issues [1]. The laboratory tests aim to assess the performance of the algorithm under realistic network fault conditions. These are conducted in the PNDC facilities which provide a realistic environment for the injection of real electrical MV faults. Specifically, 20 Ω phase-to-earth and 60 Ω phase-to-phase faults were applied at three different locations of the PNDC MV network. Moreover, the six MV/LV transformers along with dedicated monitoring equipment are used for the acquisition of the LV measurements. Throughout this chapter, the physical testing procedure, the setup and eventually the algorithm validation are thoroughly described.

In addition, further experimentation is realised using simulation to evaluate the operation of the developed technique under noise interference, loss of communications and alteration of the fault time window length.

6.2 Overview of the physical test

The network configuration used for physical testing is arranged as indicated in Fig. 6.1. Faults are applied at the desired locations, F_1, F_2 and F_3, of the PNDC network with the aid of the 11 kV fault thrower. The proper combination of switches and resistors within the referred equipment provides the option of different fault types i.e. phase-to-earth and phase-to-phase faults. The minimum fault resistance that can be applied in the particular MV network is 20 Ω for phase-to-earth and 60 Ω for phase-to-phase faults respectively. This limitation does not compromise the validation of the algorithm, since resistive faults have been proven more challenging than solidly-connected faults during the simulation studies. Radial topology of the network is achieved when the indicated normal open switch (Fig. 6.1) remains open and ring when this is closed. The hardware testing scenarios, shown in Table 6.1, are numbered in such a way to match the corresponding simulation cases introduced in Chapter 4.

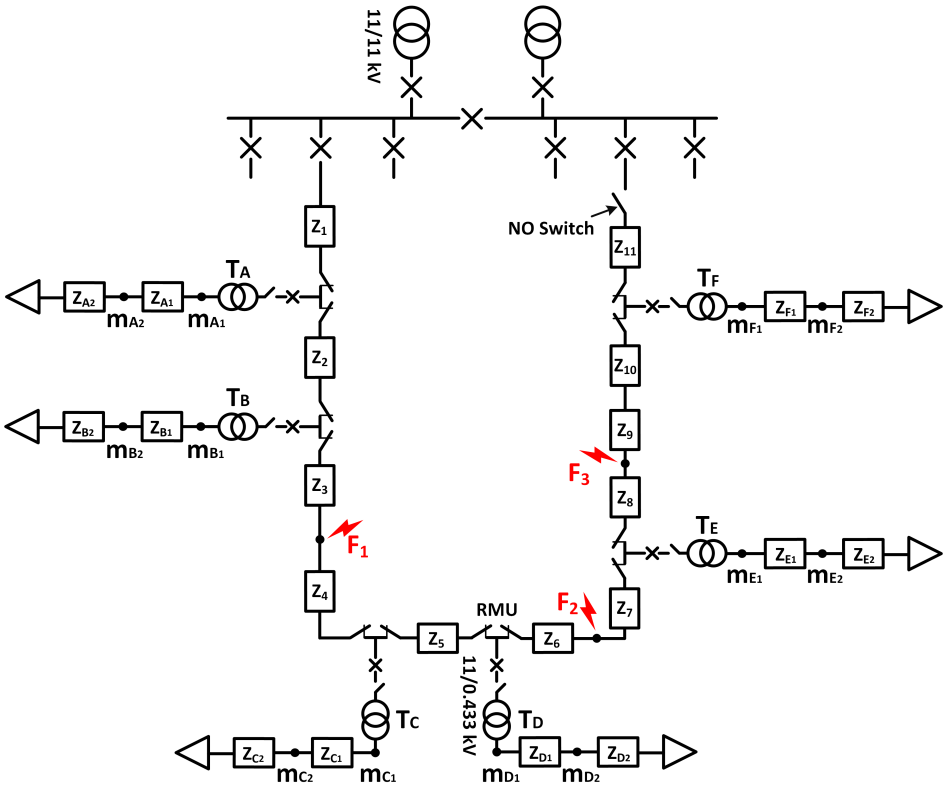

Figure 6.1: The PNDC network configuration [1].

Table 6.1: Hardware testing scenarios.

Scenario	Topology	Fault type	Fault resistance	Fault location
Distribution network of PNDC				
1.4-1.6	radial	ph-earth	20 Ω	F_1-F_3
1.10-1.12	radial	ph-ph	60 Ω	F_1-F_3
1.16-1.18	ring	ph-earth	20 Ω	F_1-F_3
1.22-1.24	ring	ph-ph	60 Ω	F_1-F_3

Moreover, in Fig. 6.1 two possible LV monitoring points, i.e. m_{A_1} and m_{A_2}, are shown. Ideally, the monitoring devices would be directly installed at the secondary side of the transformers, i.e. m_{A_1} – m_{F_1}. However, since the LV take-off cabinets of the PNDC secondary substations do not have exposed busbars or test points, connecting the LV monitors would be more complicated. Therefore, the LV monitors record instantaneous voltage values while connected to the LV test bays denoted by points m_{A_2} – m_{F_2}.

6.3 LV measurement devices and setup

The deployment of secondary substations LV monitoring infrastructure is still a concept under development, even though DNOs have already rolled out a number of LV monitoring devices in their distribution networks [2–4]. It is expected that, LV monitors from various vendors will be used, so it is reasonable to deploy more than one type of devices during the evaluation, to emulate a realistic implementation scenario. Hence, the two types of LV monitoring equipment available in PNDC have been used: Fluke 435-II power quality analyser [5] and Beckhoff voltage monitor [6]. The Fluke device is a portable monitoring unit whereas the Beckhoff system comprises of a master unit (i.e. an industrial PC running Windows operating system) and a number of distributed voltage measurement modules. Fig. 6.2 depicts the hardware testing and monitoring set-up.

Table 6.2 reports the key characteristics of both measuring devices [5],[6]. The two

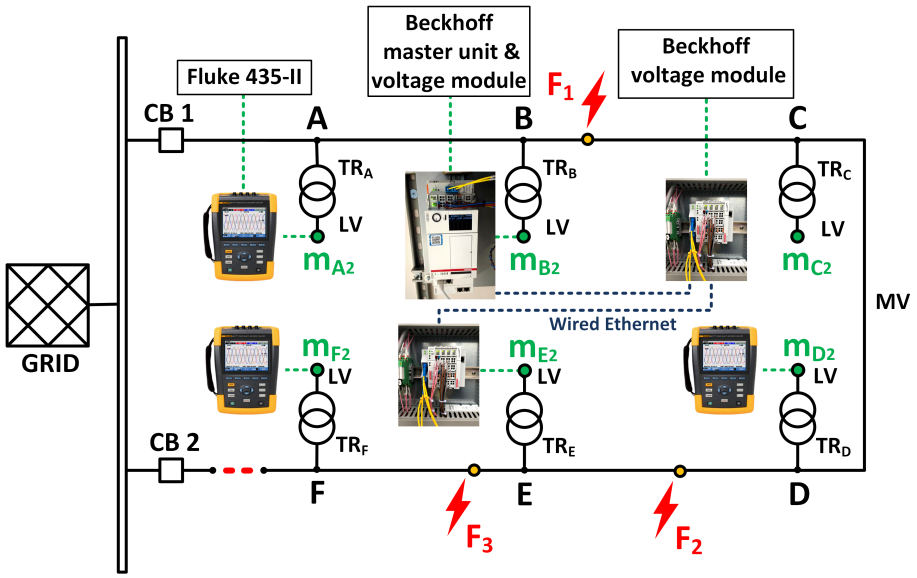

Figure 6.2: Hardware testing set-up.

monitoring devices provide instantaneous values which are used for voltage magnitude, angle and sequence components calculations. The Fluke 435 II samples the instantaneous voltage with frequency of 3.75 kHz, which corresponds to 75 samples/cycle at 50 Hz. The Beckhoff device provides sampling frequency of 10 kHz. Two example three-phase voltage waveforms captured by Fluke 435 II and Beckhoff measurement units during a phase-to-phase and phase-to-earth fault respectively, are presented in Fig. 6.3.

Table 6.2: Characteristics of measurement devices

Monitoring device	**Fluke 435-II Power Quality Analyser**	**Beckhoff**
Measurement method	Instantaneous voltage	Instantaneous voltage
Measurement range	1-1400 V phase to neutral peak voltage	Up to 288 V phase to neutral peak voltage
Measurement accuracy	±0.2 % of nominal voltage	±0.5 % to full scale value
Sampling frequency	3.75 kHz	10 kHz

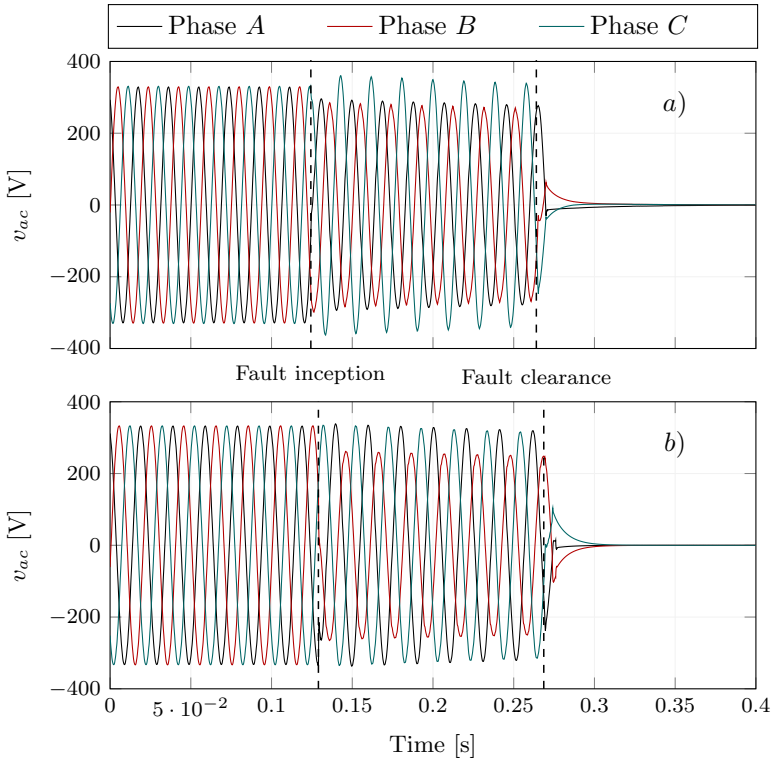

Figure 6.3: a) Voltage waveforms during a phase-to-phase fault captured by Fluke 435-II, b) Voltage waveforms during a phase-to-earth fault captured by Beckhoff technology.

Voltage magnitude and angle can be derived by applying FFT to the raw voltage waveforms data. It is important to clarify that the calculated phase angles express the angular deviation among the three phases measured at each individual LV meter. The aim is the computation of the positive and negative sequence components with the aid of equations (6.1) and (6.2), in order to quantify the three-phases unbalance at each of the aforementioned measurement points. Therefore, it is emphasised that no use of Phasor Measurement Units (PMUs) and Global Positioning System (GPS) synchronisation is dictated by the developed technique.

$$|V_1| = \sqrt{\begin{array}{l}[V_A \cdot cos(phA) + V_B \cdot cos(phB + 120°) + V_C \cdot cos(phC + 240°)]^2 \\ +[V_A \cdot sin(phA) + V_B \cdot sin(phB + 120°) + V_C \cdot sin(phC + 240°)]^2\end{array}} \quad (6.1)$$

$$|V_2| = \sqrt{\begin{array}{l}[V_A \cdot cos(phA) + V_B \cdot cos(phB + 240°) + V_C \cdot cos(phC + 120°)]^2 \\ +[V_A \cdot sin(phA) + V_B \cdot sin(phB + 240°) + V_C \cdot sin(phC + 120°)]^2\end{array}} \quad (6.2)$$

6.4 Voltage measurements compensation

As discussed previously, the LV measurement units are connected at the PNDC LV test-bays, $m_{2_{A\text{-}F}}$, to record the instantaneous voltage values during a fault event, and not at the secondary side of the transformers ($m_{1_{A\text{-}F}}$). Thus, it can be inferred that the cable impedance between m_1 and m_2, shown in Fig. 6.4, will cause a voltage drop which has to be estimated and subsequently compensated in order the proposed fault location algorithm to operate properly.

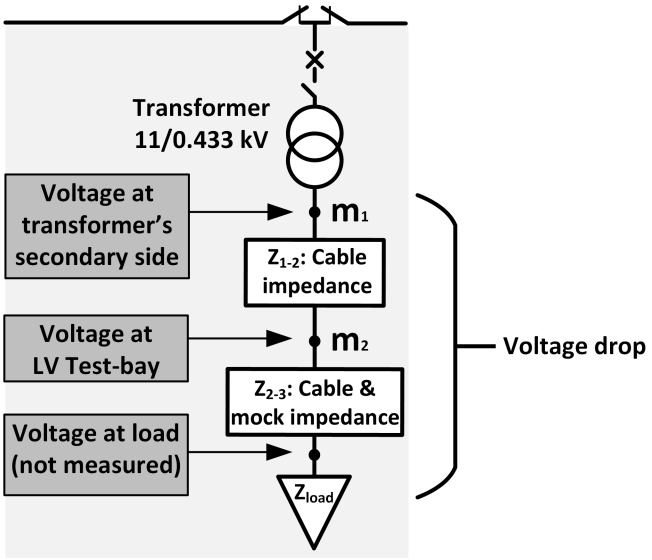

Figure 6.4: Overview of LV measurement in PNDC.

To achieve the above, a number of assumptions needs to be undertaken. First, the overall load of the LV network is considered to be equally shared to the individual load-banks, as there is no current measurement at the LV side of the transformers. It is noted, that the loading (kVA) - at the LV network - is determined by a specialised API software, which is capable to control the total capacity of the load-banks and not each piece individually. Also, since all load-banks have the same power factor of 0.95 lagging,

the X/R ratio is the same for all of them. In addition, due to the fact that there are no voltage measurements at the PNDC load connection points, the simulated model was used to obtain the corresponding data. Specifically, the load values captured during physical testing were used in simulations to calculate the voltage at the particular points of the network. The aforementioned assumptions are adopted in order to calculate the load impedance magnitude $|Z_{\text{load}}|$ (Eq. 6.3).

$$|Z_{load}| = \frac{3|V_{load}|^2}{|S_{load}|} \tag{6.3}$$

The magnitude of the total impedance from the secondary side of the MV/LV transformer to the load is calculated with the aid of Eq. 6.4.

$$|Z_{total}| = |Z_{1-2}| + |Z_{2-3}| + |Z_{load}| \tag{6.4}$$

Therefore, the voltage magnitude and angle at point m_1 can be derived using Eq. 6.5 and 6.6. The referred equations utilize the voltage magnitude and angle, V_{m_2} and $ph_{V_{m_2}}$, measured at point m_2, the magnitude of total impedance Z_{load} and the cable impedance, $Z_{1\text{-}2}$, between m_1 and m_2. Table 6.3 contains the calculations with the compensation values for all the measurement points.

$$|V_{m_1}| = |V_{m_2}| * \frac{|Z_{total}|}{|Z_{total}| - |Z_{1-2}|} \tag{6.5}$$

$$ph_{V_{m_1}} = ph_{V_{m_2}} + ph_{Z_{1-2}} \tag{6.6}$$

6.5 Algorithm evaluation against real data

This section assesses the performance of the FS location algorithm when asymmetrical faults occur in the real PNDC network. It is important to highlight that some difference at the magnitude of ratios, k_s, is expected between physical testing and software based simulations results. The main reason is that it was not possible to emulate identically

Table 6.3: Compensation of voltage measurements retrieved during physical testing.

Measurement point where compensation is applied	**Radial topology**	**Ring topology**
m_{A_2}	$V_{m_{A_1}} = \frac{1.0838}{1.0838-0.0326} V_{m_{A_2}}$ $ph_{V_{m_{A_1}}} = ph_{V_{m_{A_2}}} + 0.031°$	$V_{m_{A_1}} = \frac{1.0838}{1.0838-0.0326} V_{A_{m_2}}$ $ph_{V_{m_{A_1}}} = ph_{V_{m_{A_2}}} + 0.031°$
m_{B_2}	$V_{m_{B_1}} = \frac{2.0979}{2.0979-0.0248} V_{m_{B_2}}$ $ph_{V_{m_{B_1}}} = ph_{V_{m_{B_2}}} + 0.021°$	$V_{m_{B_1}} = \frac{2.0979}{2.0979-0.0248} V_{m_{B_2}}$ $ph_{V_{m_{B_1}}} = ph_{V_{m_{B_2}}} + 0.021°$
m_{C_2}	$V_{m_{C_1}} = \frac{2.0384}{2.0384-0.0338} V_{m_{C_2}}$ $ph_{m_{C_{m_1}}} = ph_{V_{m_{C_2}}} + 0.0291°$	$V_{m_{C_1}} = \frac{2.0384}{2.0384-0.0338} V_{m_{C_2}}$ $ph_{V_{m_{C_1}}} = ph_{V_{m_{C_2}}} + 0.0291°$
m_{D_2}	$V_{m_{D_1}} = \frac{4.2981}{4.2981-0.036} V_{m_{D_2}}$ $ph_{V_{m_{D_1}}} = ph_{V_{m_{D_2}}} + 0.0084°$	$V_{m_{D_1}} = \frac{4.2981}{4.2981-0.036} V_{m_{D_2}}$ $ph_{V_{m_{D_1}}} = ph_{V_{m_{D_2}}} + 0.0084°$
m_{E_2}	$V_{m_{E_1}} = \frac{4.2357}{4.2357-0.04} V_{m_{E_2}}$ $ph_{V_{m_{E_1}}} = ph_{V_{m_{E_2}}} + 0.0345°$	$V_{m_{E_1}} = \frac{4.2704}{4.2704-0.04} V_{m_{E_2}}$ $ph_{V_{m_{E_1}}} = ph_{V_{m_{E_2}}} + 0.0343°$
m_{F_2}	$V_{m_{F_1}} = \frac{4.4011}{4.4011-0.0428} V_{m_{F_2}}$ $ph_{V_{m_{F_1}}} = ph_{V_{m_{F_2}}} + 0.01846°$	$V_{m_{F_1}} = \frac{4.4738}{4.4738-0.0428} V_{m_{F_2}}$ $ph_{V_{m_{F_1}}} = ph_{V_{m_{F_2}}} + 0.0181°$

a number of physical components (i.e. cable parts, connectors) implemented in the real network, for which technical specifications were not available. Fig. 6.5 presents the variance between the ratios, k_s, captured from the real network studies and software simulations, during a 20 Ω phase-to-earth fault at location F_3.

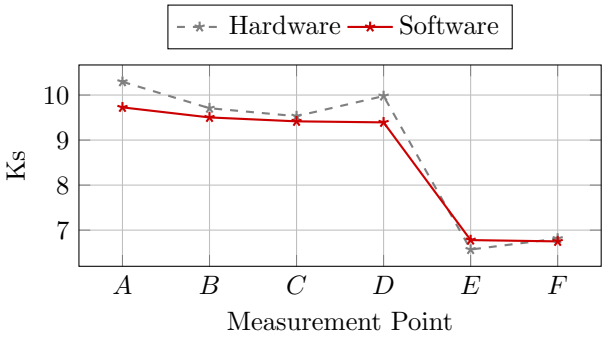

Figure 6.5: Comparison between software and hardware derived k_s values.

Tables 6.4 and 6.5 report the the 3-points-windows data required for the accurate FS

location after a 20 Ω phase-to-earth and a 60 Ω phase-to-phase fault occurred in location F_1, correspondingly. In both cases the percentage difference, $\Delta k_{s_{13}}\%$, with the highest value is identified in the 3-points-window A-B-C. As the radial topologies associated algorithm's logic dictates, the first window containing the comparison indicators pair '1'-'0' will provide the FS. In both mentioned paradigms (Tables 6.4 and 6.5), the window B-C-D correctly locates the FS which is among the transformers T_B and T_C.

Table 6.4: Physical testing results
Radial topology / Phase to ground (20 Ω) fault. / F_1.

3-points window	k_{s_1}	k_{s_2}	k_{s_3}	$\Delta k_{s_{13}}\%$	FS search	$k_{s_1} > k_{s_2}$	$k_{s_2} > k_{s_3}$
A-B-C	9.23	8.98	8.91	3.65%	↓	'1'	'1'
B-C-D	8.98	8.91	9.17	2.11%	→	'1'	'0'
C-D-E	8.91	9.17	8.99	0.88%		'0'	'1'
D-E-F	9.17	8.99	9.35	1.96%		'1'	'0'

Table 6.5: Physical testing results
Radial topology / Phase to phase (60 Ω) fault. / F_1.

3-points window	k_{s_1}	k_{s_2}	k_{s_3}	$\Delta k_{s_{13}}\%$	FS search	$k_{s_1} > k_{s_2}$	$k_{s_2} > k_{s_3}$
A-B-C	7.81	7.67	7.6	2.33%	↓	'1'	'1'
B-C-D	7.67	7.6	7.71	0.52%	→	'1'	'0'
C-D-E	7.6	7.71	7.64	0.52%		'0'	'1'
D-E-F	7.71	7.64	7.62	1.18%		'1'	'1'

As described in Section 3, the outcome of a comparative analysis of the balance factor, k_s, values across a ring network, determines the FS location. It is emphasised that, since the algorithm is merely based on voltage measurements and the impedance of the MV conductors is not known, the FS is considered within three step-down transformers when examining ring configurations. The results of the ring topology study are captured and presented in Tables 6.6 - 6.7. The results show that the algorithm can correctly locate the FS at the MV section B-D (green coloured cells in Table 6.6), where the 20 Ω phase-to-earth fault occurred.

Table 6.6 shows that when faults were injected at the locations F2 and F3 multiple

'1' to '0' transitions were observed, in opposition with the scenario of a fault occurrence at F1. Under such circumstances, the largest $|\Delta k_{s_{13}}\%|$ should be identified among the two three-point windows B-C-D and D-E-F, which will determine the FS. The particular values are highlighted in Table 6.7, which both correspond to the 3-points window D-E-F indicating the correct FS, D-F.

Table 6.6: Physical testing results: k_s comparisons indexes
Ring topology / Phase to ground (20 Ω) fault.

DG	Fault location	A>B	B>C	C>D	D>E	E>F
No	F_1	1	1	0	0	0
	F_2	1	1	0	1	0
	F_3	1	1	0	1	0

Table 6.7: Physical testing results: $|\Delta k_{s_{13}}\%|$ comparisons
Ring topology / Phase to ground (20 Ω) fault.

Fault location	$\lvert\Delta k_{s_{BD}}\rvert$	$\lvert\Delta k_{s_{DF}}\rvert$
F_2	0.96%	2.58%
F_3	1.3%	18.09%

Table 6.8 contains the results acquired during the selected scenarios 1.2 - 1.24. The algorithm identified the FS accurately throughout all scenarios.

Table 6.8: Algorithm's performance across all physical testing scenarios conducted in the PNDC network.

Scenario	Fault type	Fault resistance	Fault location	Topology	Identified FS
1.4	ph-earth	20 Ω	F_1	radial	B-C
1.5	ph-earth	20 Ω	F_2	radial	D-E
1.6	ph-earth	20 Ω	F_3	radial	E-F
1.10	ph-ph	60 Ω	F_1	radial	B-C
1.11	ph-ph	60 Ω	F_2	radial	D-E

Continued on next page

Table 6.8 – *Continued from previous page*

Scenario	Fault type	Fault resistance	Fault location	Topology	Identified FS
1.12	ph-ph	60 Ω	F_3	radial	E-F
1.16	ph-earth	20 Ω	F_1	ring	B-C-D
1.17	ph-earth	20 Ω	F_2	ring	C-D-E
1.18	ph-earth	20 Ω	F_3	ring	D-E-F
1.22	ph-ph	60 Ω	F_1	ring	B-C-D
1.23	ph-ph	60 Ω	F_2	ring	C-D-E
1.24	ph-ph	60 Ω	F_3	ring	D-E-F

6.6 Influence of noise

In active networks, the high penetration of converter based distributed generation and active loads can lead to the injection of harmonics content to the system. The maximum output voltage Total Harmonic Distortion (THD%) given by the most inverter specifications is 5% [7]. However, the proposed technique is expected to present high level of tolerance under normal harmonics contamination. The algorithm operates in the RMS domain and the latter is calculated by extracting only the fundamental (50 Hz) voltage components due to the use of FFT. Hence, the rest of the harmonics are filtered out.

Therefore, the influence of the LV measurement units background noise and A/D errors on sequence components and the parameter k_s is only examined in this section. The noise level of a measurement system can vary depending on the measurement bandwidth, environmental conditions and measurement techniques. A typical noise level for a LV RMS measurement system could be between 0.1% - 0.5% or less of the full-scale measurement [8–10]. In this case random noise of ±5% maximum deviation is added to the positive and negative voltage sequence components acquired during the simulations. Fig. 6.6 depicts an example of a 0 Ω phase-to-earth fault occurred at location F_1 where the fault period of both healthy and noisy positive and negative

voltage sequence components are captured.

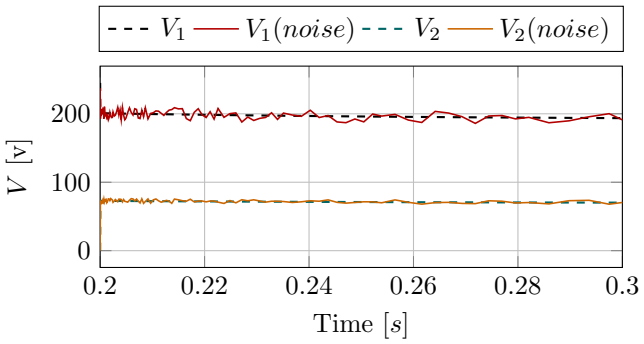

Figure 6.6: Voltage positive and negative sequence components with and without noise.

Although the positive and negative sequence components of Fig. 6.6 seem to be slightly deformed by the added noise, the algorithm is not affected as it requires the average value of the calculated k_s during the fault period. By this way, the derived error is eliminated and so the developed FS location technique is considered immune even under the extreme conditions of ±5% background noise. Table 6.9 demonstrates the negligible impact of random ±1% to ±5% added noise on a k_s measurement captured from a specific LV point during a phase-to-earth fault. The largest deviation of k_s equal to 0.065% was recorded when ±4% of random noise was applied.

Table 6.9: ±1% to ±5% noise influence on random k_s measurement during a phase-to-earth fault.

Noise:	0%	±1%	±2%	±3%	±4%	±5%
k_s***:***	2.7589	2.7592	2.7601	2.7602	2.7607	2.7606
k_s ***deviation (%):***	-	0.011	0.043	0.047	0.065	0.062

It is also noted that, the measurement units have already passed electromagnetic interference and accuracy tests before they are launched in the market.

6.7 Influence of communications failures

The developed technique is based on the availability of monitoring devices and communication system in order to acquire and process the LV sparse measurements. Failures

often introduced by the various components of these technologies, such as communication links, servers, measurement devices etc. lead to partial or complete loss of data, latency and synchronisation issues. It is therefore important to investigate any potential impact these issues may have on the functionality of the FS location algorithm.

Increased latency and loss of synchronisation cause significant problems to various functionalities of electrical networks such as protection and automation systems [11]. However fault location does not require instant response, therefore synchronisation of the measurements can be performed after the fault is detected. As discussed in section 3.3.2, the algorithm is able to discriminate the fault period from each individual dataset acquired from the various monitoring units. Afterwards, the average k_s value is calculated with the aid of the fault period data samples. It is therefore inferred that synchronisation or increased letancy issues would present no effect on the effectiveness of the algorithm.

Furthemore, the algorithm needs to be examined when a communication failure leads to complete loss of data expected from a measurement unit. For this purpose, a number of simulations were repeated while excluding the captured results from random monitoring units.

The example of missing data from m_C when a 20 Ω phase-to-earth fault occurred in location F_1 is demonstrated with the aid of Fig. 6.7 and Table 6.10. In this case, the percentage difference, $\Delta k_{s_{13}}\%$, of window A-B-D matches the one of A-B-G. Similarly, the $\Delta k_{s_{13}}\%$ of the following '1'-'0' windows are the same for both separate radial circuits. However, it is expected that if m_C was operational, window A-B-C would have replaced the A-B-D and then the corresponding value of $\Delta k_{s_{13}}\%$ would have been even smaller (due to the smaller impedance of section B-C compared to B-D). Therefore, the window B-G-H is considered the most impacted one indicating the MV zone B-G as the one including the FS. In this case, the algorithm performs accurately as normally and the performance is not compromised.

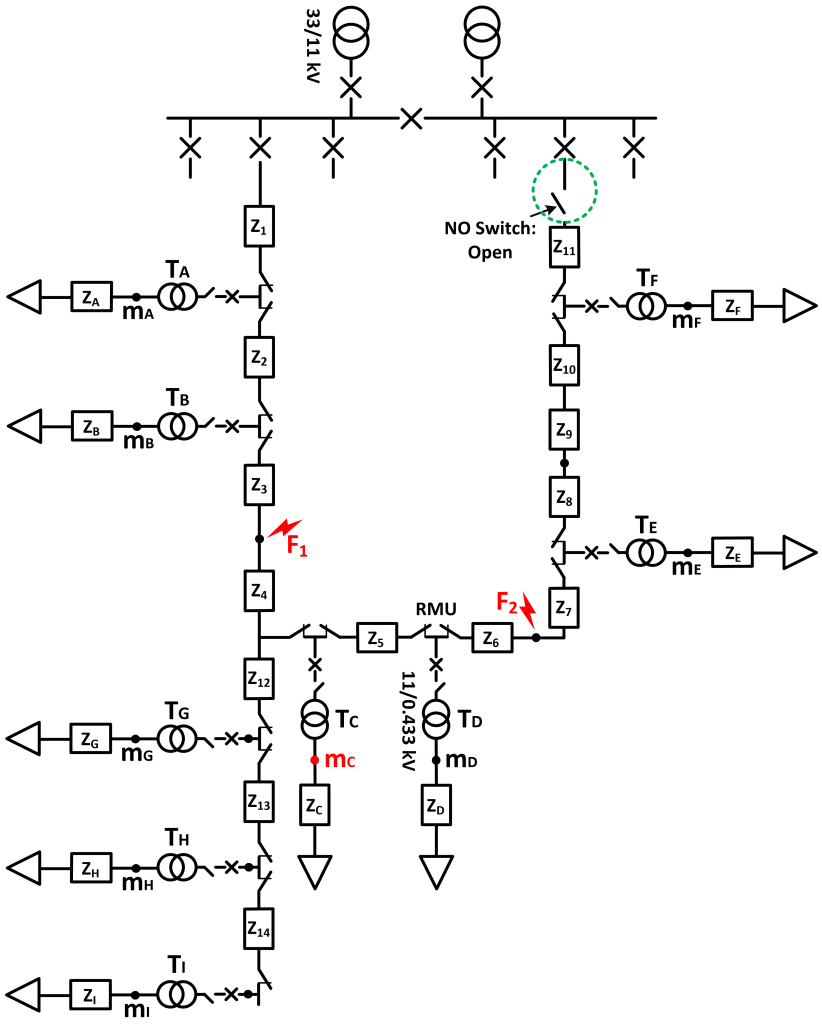

Figure 6.7: Radial configuration with failure at monitoring unit m_C.

Table 6.10: Communication loss with m_C
Radial topology / Phase to ground (20 Ω) fault / F_1.

3-points window	k_{s_1}	k_{s_2}	k_{s_3}	$\Delta k_{s_{13}}\%$	$k_{s_1} > k_{s_2}$	$k_{s_2} > k_{s_3}$
A-B-D	8.92	8.7	8.67	2.83%	'1'	'1'
B-D-E	8.7	8.67	8.67	0.33%	'1'	'0'
A-B-G	8.92	8.7	8.67	2.83%	'1'	'1'
B-G-H	8.7	8.67	8.67	0.33%	'1'	'0'

Moreover, a different paradigm is described with the aid of Table 6.11, where the

loss of communication with the measurement device m_D is assumed during a 20 Ω phase-to-earth fault occurred in location F_2. Similarly with the above example (Table 6.10), the technique deploys the normal radial topologies logic "ignoring" the absence of the missed m_D data. In particular, the 3-points window B-C-E provides the highest percentage difference, $\Delta k_{s_{13}}\%$, among all the created windows and the C-E-F is the one indicating the FS C-E. The obvious drawback of missing the m_D data is that the identified FS is wider than normally is, including the MV zones between two adjacent pairs of step-down transformers, C-D and D-E. In other words, the proposed FS location technique is operational even under the potential hazard of communications loss and the worst case scenario is a longer derived FS than in normal conditions.

Table 6.11: Communication loss with m_D
Radial topology / Phase to ground (20 Ω) fault / F_2.

3-points window	k_{s_1}	k_{s_2}	k_{s_3}	$\Delta k_{s_{13}}\%$	$k_{s_1} > k_{s_2}$	$k_{s_2} > k_{s_3}$
B-C-E	9.18	9.05	7.56	18.77%	'1'	'1'
C-E-F	9.05	7.56	7.56	18.5%	'1'	'0'
B-G-H	9.18	9.15	9.15	0.34%	'1'	'0'

6.8 Impact of time window length

The section 3.3.2 described how the time indices t_F and t_{CB} are used to identify the fault time window W. In this section, the performance of the proposed algorithm is investigated considering shorter fault time windows. In particular, new windows with lengths 75%, 50% and 25% of the initial time window W have been utilised for the analysis (refer to Table 6.12 for window length details).

The analysis revealed that the performance of the proposed algorithm has not been compromised even when the fault time window has been reduced to 25%. Table 6.13, Table 6.14 and Table 6.15 present the results for faults at locations F_1, F_2 and F_3 respectively. It is evident that the comparison of k_s values has initiated correct binary outputs leading to correct operation of the scheme for all the faults.

Table 6.12: Fault time window (W) lengths
Radial topology / Phase to ground (20 Ω) fault.

Fault location	75% of W (ms)	50% of W (ms)	25% of W (ms)
F_1	86.9	57.9	29.1
F_2	78.7	52.3	23
F_3	75.5	50.4	25.1

Table 6.13: Radial topology / Phase to ground (20 Ω) fault / F_1.

3-points window	k_{s_1}	k_{s_2}	k_{s_3}	$\Delta k_{s_{13}}$%	$k_{s_1} > k_{s_2}$	$k_{s_2} > k_{s_3}$
A-B-G	8.92	8.7	8.67	2.83%	'1'	'1'
B-G-H	8.7	8.67	8.67	0.33%	'1'	'0'
A-B-C	8.92	8.7	8.67	2.83%	'1'	'1'
B-C-D	8.7	8.67	8.67	0.33%	'1'	'0'

Table 6.14: Radial topology / Phase to ground (20 Ω) fault / F_2.

3-points window	k_{s_1}	k_{s_2}	k_{s_3}	$\Delta k_{s_{13}}$%	$k_{s_1} > k_{s_2}$	$k_{s_2} > k_{s_3}$
A-B-G	9.407	9.177	9.146	2.82%	'1'	'1'
B-G-H	9.177	9.146	9.146	0.34%	'1'	'0'
A-B-C	9.407	9.177	9.054	3.83%	'1'	'1'
B-C-D	9.177	9.054	9.024	1.68%	'1'	'1'
C-D-E	9.054	9.024	7.563	17.44%	'1'	'1'
D-E-F	9.024	7.563	7.563	18.15%	'1'	'0'

Table 6.15: Radial topology / Phase to ground (20 Ω) fault / F_3.

3-points window	k_{s_1}	k_{s_2}	k_{s_3}	$\Delta k_{s_{13}}$%	$k_{s_1} > k_{s_2}$	$k_{s_2} > k_{s_3}$
A-B-G	9.878	9.637	9.605	2.81%	'1'	'1'
B-G-H	9.637	9.605	9.605	0.33%	'1'	'0'
A-B-C	9.878	9.637	9.51	3.81%	'1'	'1'
B-C-D	9.637	9.51	9.477	1.68%	'1'	'1'
C-D-E	9.51	9.477	6.78	31.79%	'1'	'1'
D-E-F	9.477	6.78	6.756	35.47%	'1'	'1'

6.9 Hardware and software implementation

The proposed algorithm is based on monitoring the LV part of the distribution network to locate the FS at the MV side. The technique can be integrated into the Distribution Management System (DMS) of the DNO to allow automatic FLISR and thus self-healing capability of the network. Fig. 6.8 illustrates an example architecture and the various software and hardware components of a centralised FLISR approach using the developed FS location technique.

The depicted solution relies on telemetry and remote control for automatic network operation. The FS location algorithm resides on the DMS of the control centre, among other distribution automation applications such as Volt/VAr control, congestion management, load/generation forecasting, state estimation, etc.

The SCADA communicates with the Remote Terminal Units (RTU) of the various secondary substations via Modbus TCP protocol. It provides the analogue and status measurements captured by the RTUs in secondary and primary substations to the SCADA/DMS and specifically to the "slaves" of the FS location algorithm. When the MV CB opens due to a fault on the MV conductor, a status indication of the CB is transmitted from the RTU located in the primary substation to the SCADA. Then the "slaves" retrieve the voltage measurements which are collected from the LV voltage sensors and the RTUs of the secondary substations via SCADA and the selected communication protocol (i.e. Modbus). The FS location technique can still operate even when a measurement point is lost due to communication failure. In such a case the identified FS would be larger than normally.

As soon as the technique locates the FS, the FLISR of SCADA/DMS issues a control command to open the switches and completely isolate the damaged section. Once the FS is properly isolated, FLISR restores the service to as many "healthy" parts of the feeder as possible, via normally-open, remotely controlled tie switches that have spare capacity to carry additional load.

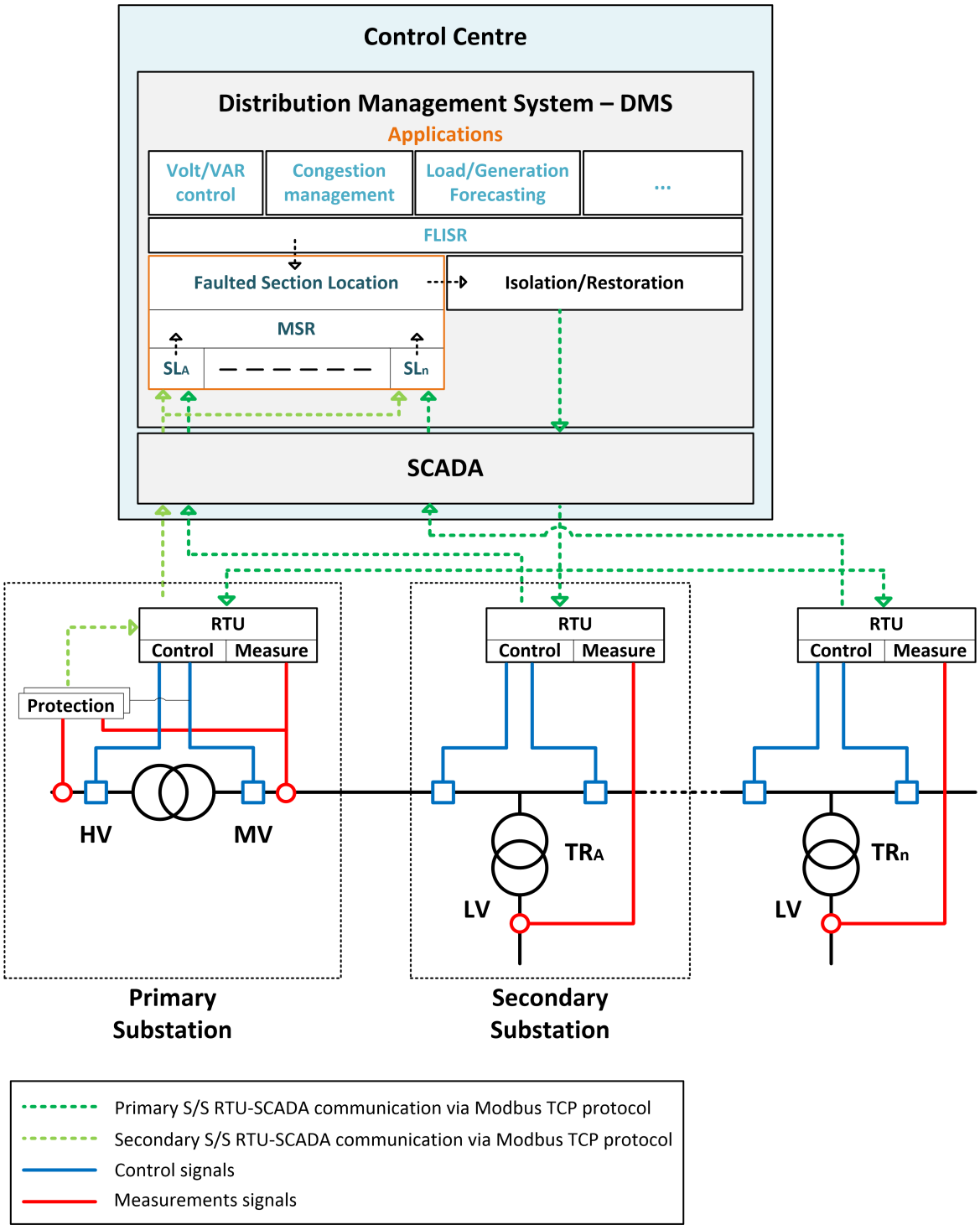

Figure 6.8: Example FS location technique deployment architecture.

6.10 Chapter summary

This chapter elaborated on certain implementation aspects which can have an impact on the applicability of the introduced FS algorithm. A hardware based study as well as additional modelling simulations were conducted to validate the effectiveness of the developed scheme. The technique was capable to solve the problem of faulted segment location under the imposed realistic conditions. Last, an example architecture of a complete FLISR scheme using the developed FS location technique is proposed presenting the various software and hardware components.

6.11 References

[1] P. Bountouris, H. Guo, D. Tzelepis, I. Abdulhadi, F. Coffele, and C. Booth, "MV faulted section location in distribution systems based on unsynchronized LV measurements," *International Journal of Electrical Power and Energy Systems*, vol. 119, 2020.

[2] SP Energy Networks, "LV Network Monitoring - ED2 Engineering Justification Paper," 2021.

[3] UK Power Networks, "Application to Innovation Roll-Out Mechanism - LV Network Visibility and Control," 2017.

[4] Western Power Distribution Networks, "Next Generation Networks - LV Current Sensor Technology Evaluation," 2016.

[5] FLUKE, "Fluke 434-II/435-II/437-II Three Phase Energy and Power Quality Analyzer Users Manual." `goo.gl/KFrdVJ`. Accessed: 2018-03-02.

[6] BECKHOFF, "EL3773 — Power monitoring oversampling terminal." `goo.gl/Nex6Z5`. Accessed: 2020-11-06.

[7] S. Manias, *Power Electronics and Motor Drive Systems*. 12 2016.

[8] LEM, *Voltage transducer DVL 750/SP5*, 9 2022. Version 5.

[9] FLUKE, *Fluke 87 True RMS Multimeter*, 8 1988. Rev. 8.

[10] J. Williams, "High Voltage, Low Noise, DC/DC Converters," tech. rep., LINEAR TECNOLOGY, 3 2008.

[11] B. Falahati and E. Chua, "Failure modes in iec 61850-enabled substation automation systems," in *2016 IEEE/PES Transmission and Distribution Conference and Exposition (T D)*, pp. 1–5, 2016.

Chapter 7

Conclusions and Future Work

7.1 Conclusions

This thesis has proposed and described a novel MV faulted section location technique exploiting the increasing deployment of monitoring technologies in LV networks by DSOs. The developed method implements the ratio of positive over negative sequence voltages as the main parameter to localise the MV section where an asymmetrical fault occurred.

The proposed technique provides a cost effective solution to the problem of localising asymmetrical faults at the MV part of the distribution network using only distributed LV voltage measurements as input, with no requirement for any additional MV measurements. This measurement data would be acquired from LV monitoring infrastructure which is planned to play a critical role in the management of active distribution networks and can be utilised for multiple functions and applications in the future. This is in contrast with fault location techniques (i.e. one-ended and double-ended impedance measurement) which depend on expensive MV monitoring equipment and their infrastructure is exclusively used for the purpose of fault location i.e. FPIs. Moreover, in comparison with the knowledge based methods, the proposed FS location technique does not require training. Instead, it can be applied in all types of distribution networks including different topologies such as radial or ring, connection of MV laterals and the presence of DGs. Depending on the conditions and characteristics of

the concerned distribution network, hybrid schemes can also be implemented combining the proposed method and existing techniques (i.e. FPIs) to achieve optimal FS location. The evaluation of the algorithm has been realised via both simulations and physical testing results.

Chapter 2 presented a comprehensive literature review of traditional and modern fault location techniques implemented and proposed by both industry and academia. The review included conventional methods utilised by DNOs for both overhead lines and underground cables, single and multi-ended impedance-based methods, as well as travelling wave and knowledge based techniques. The chapter outlined the key characteristics, requirements, advantages and disadvantages of the discussed methodologies. Some of the main challenges include the need of time-synchronised measurements, the presence of DGs as well as the multi-lateral and meshed configurations of the distribution networks.

The proposed FS location technique deals with all the above shortcomings. The algorithm is able to identify the fault inception and fault clearance time and thus distinguish fault period within the data acquired from each LV measurement device. Since the algorithm is based on sequence components and there is no need to process the extracted data in time domain, no requirement for time-synchronised monitoring devices is imposed. Moreover, the algorithm demonstrated high accuracy when applied in radial, ring and multi-lateral network topologies including connection of DGs and specifically inverter-based generation.

Chapter 3 described the novel MV FS location technique deploying distributed LV measurements, which is the major contribution of this thesis. Initially, the results of a data driven study are collected and illustrated to highlight the impact of MV faults to the voltage signatures - RMS, phase angle, positive and negative sequence components - captured at the LV side of six step-down transformers. The analysis of the data driven study results generated the following observations:

- Using exclusively voltage RMS or angle values at multiple LV points, does not provide sufficient information for locating the fault.

- Positive and negative sequence components captured at various LV measurement points provide a more distinct trend which can be leveraged for MV faulted section localisation purposes.

- Zero sequence components are not observed at the LV network during 11 kV faults due to the delta/star connection of the MV/LV transformers.

Moreover, the unbalanced fault analysis described in section 3.2 infers that the ratio of positive over negative sequence components at multiple points constitute a strong parameter for locating faults at the MV part of distribution networks. The comprehensive LV profile characterisation and the asymmetrical fault analysis presented in this chapter acted as preliminary knowledge for the development of a novel faulted section location algorithm. The main characteristics of the proposed technique are listed below:

- The developed technique utilizes distributed LV voltage magnitude and angle measurements to calculate the required sequence components.

- Signal processing techniques have been used for the effective operation of the method. In particular, Fourier transform has been deployed for the calculation of RMS and phase angle values. In addition, DWT has been proven effective for the identification of the fault event initiation aiding the fault period discrimination. The latter is considered one of the most critical parts of the algorithm process, as it provides the capability for offline measurements synchronisation avoiding the implementation of expensive GPS infrastructure.

- The logic and the capability of the method differs depending on the radial or ring type of network configuration. In case of radial topology, the algorithm is able to locate the FS between two adjacent MV/LV transformers. However, the algorithm's FS location capability is limited to the MV zone among three step-down transformers when ring topology is the case. This limitation arises from the fact that the cable impedance data is deliberately ignored, with the objective of

maximising the applicability of the algorithm regardless the availability of cable impedance data.

Chapter 4 presents the methodology followed to thorough evaluate the algorithm via modelling simulations. The proposed FS location technique has been assessed in both software and hardware environments. The latter is the real PNDC MV/LV network of the University of Strathclyde, which was also modelled exposing the algorithm to the same fault scenarios with those of the hardware investigations.

Furthermore, the simulations software provided the opportunity of further exploration by expanding the models in various ends. First, the additional connection of an MV lateral with three more MV/LV transformers connected has been examined. Also, the phenomenon of LV load unbalance has been taken into account aiming to challenge the algorithm, which relies on the LV sequence components profile. Moreover, the influence of DGs connected at multiple points across the network was investigated by implementing the default modelling components (synchronous generators, PVs) available in the simulations software package.

Further studies aimed to the evaluation of the algorithm when applied in an active distribution network dominated by LV connected PV systems. First, a physical experiment-based study was realised to better understand the behaviour of seven off-the-shelf LV grid-connected PV inverters during fault conditions. The synopsis of the physical testing set-up, procedure and results are presented in Appendix B. The main findings were used to characterise the stability of the inverters under test against grid disturbances that impose voltage magnitude and VS changes. Analysis of the results led to the following key observations and recommendations:

- The diversity among the inverters' responses as observed during the testing indicates a risk of loss of PV generation during typical MV and HV level faults. Furthermore, the lack of specific guidelines in the UK Grid Code (GC) of the National Electricity Transmission System and the relevant Engineering Recommendations targeting the small scale generation units' fault ride through strategy explains the inverters inconsistency under the above testing conditions.

- The majority of the observed inverters' disconnections at lower retained voltages occurred during the fault clearance when the voltage magnitude and angle recovered. The above contrasts with the requirement of the G83 type test procedure application at nominal voltage, where no VS recovery is proposed to be applied during a type test. Therefore, some revision of the proposed VS type testing and engagement with the inverter manufacturers is necessary to address the concerns of instability during MV and HV faults in the future.

- Moreover, the wide variety of inverters connection stability limits as well as the observed reduction of active power when they remained connected, raise two risks. First, the former case indicates possible PV generation connection loss during both typical transmission and distribution level faults, while the latter may magnify the severity of a major Rate of Change of Frequency (RoCoF) associated system incident, compromising the stability of the RoCoF based LOM protection. The above revealed the need for further analysis of the penetration levels of various types of inverters in the network, aiding a more reliable estimation of the potential worst-case scenario.

The aforementioned remarks and the seemingly inconsistent behaviour, particularly with regards to FRT strategies, of LV grid-interfaced PV inverters across various manufacturers can lead to unreliable or outdated modelling assumptions. Thus, the development of a representative model reflecting the output of real PV inverters under fault conditions is considered important. Such a model can be properly tuned to represent different manufacturers' products and implemented for the purpose of this investigation and other studies assessing the stability and reliability of the network.

In this study, the development of the referred dynamic model was based on the characterisation of a 60 kVA inverter response under varied short circuit and voltage depression testing conditions. Appendix B presents the results of the mentioned PV inverter physical testing. The structure and performance of the developed model can be found in Chapter 4. The tests involved varying the retained voltage across the inverter output while altering the pre-event loading level of the inverter from 25% to 100% in

steps of 25%. The inverter exhibited two distinct FRT strategies mainly depending on the loading level and the amount of voltage depression at the AC output. The following characteristics were observed throughout the physical testing and adopted during the modelling procedure.

- A significant output of this experiment was the identification of the diverse FRT responses along with their different stages. The inverter under test exhibited two types of fault ride through strategies when voltage disturbances and fault conditions were applied at the AC network. FRT 1 resulted in a slight increase of the inverter's current output (within thermal limits) and it was activated when the conditions listed in Table 4.11 were not met. FRT 2 strategy initiated when the thresholds in Table 4.11 were exceeded, depressing the current output to near zero values followed by a gradual recovery of the pre-event current output just after the end of the event (fault clearance, grid voltage recovery).

- It is more likely the inverter increases its output current (FRT 1), maintaining the pre-fault active power output level and providing reactive power to the grid when it's not fully loaded, i.e. 0.25 and 0.5 pu of loading level, prior to the fault. FRT 2 is observed more often in cases when the inverter loading level is 1.0 pu. This logic prevents the inverter's output current to exceed certain limits leading to inverter disconnection or even damage.

- There is no clear evidence that the Point on Wave (PoW) at which the fault is introduced has a systematic impact on the sustained inverter current output during a fault, although only a few cases of 90° PoW initiated faults, at high inverter loading levels (75%, 100%), caused the inverter to activate the FRT 2.

- The level of voltage unbalance affected the behaviour of the inverter during asymmetrical faults and applied voltage asymmetries and thus the control strategy of the developed model. The ratio V_2/V_1 was used to measure the level of voltage unbalance at the AC side of the inverter model. A threshold of this ratio along with the amount of total voltage depression determined when the inverter

switches from steady state to FRT 1 or FRT 2 response. The particular control scheme was used mainly for the higher loading levels (75% and 100%) as it was observed that voltage unbalance did not affect the inverter's FRT behaviour when it was lightly loaded.

- In addition to the above, the FRT operation mode was also affected by the amount of voltage depression at each individual phase. Certain retained voltage thresholds per phase have also been defined in order to ensure that the inverter does not exceed any thermal limits, especially when loaded at 75% and 100% of maximum capacity (Table 4.11).

The developed dynamic inverter model reflected satisfactorily the behaviour of the real inverter under voltage disturbances and fault conditions. The key modelling parameters affecting the resulted performance were identified and can be implemented to tune the dynamic model and represent PV inverters of different manufacturers.

Chapter 5 presented the results of the modelling simulations study conducted to evaluate the proposed FS location scheme. A wide range of fault scenarios was implemented including both phase-to-phase and phase-to-earth faults with resistances up to 60 Ω. The evaluation of the proposed scheme generated the following conclusions:

- It was verified that the length of the located FS varies depending on the network configuration. In radial topologies, the algorithm identified the FS between two adjacent MV/LV transformers whereas in ring configurations the FS is located among three transformers.

- The technique was able to discriminate the data samples associated to the fault period from all the LV measurements captured throughout the simulations based analysis. This is a very important feature as distributed monitoring devices do not require GPS synchronisation mitigating the deployment costs significantly.

- The algortihm presented 100% accurate performance when evaluated in both radial and ring topologies of the emulated PNDC distribution network.

- 100% level of success was also noted when the developed technique was applied in a modelled network with an additional MV lateral.
- The effectiveness of the FS location algorithm was maintained when load unbalance reached the maximum of 3%. However, the performance of the technique was compromised when resistive faults were applied in the network with 4% of load unbalance. Overall, the technique performed with a success rate of 98% (94 out of 96 simulation scenarios) under LV load unbalance conditions.
- The proposed FS location algorithm demonstrated 100% accuracy when DGs provided by the software DIgSILENT PowerFactory were connected at both MV and LV side of the network.
- The algorithm presented 100% accuracy when assessed in an active distribution network dominated by LV connected PV inverters of various loading levels. The latter were emulated with the aid of the developed dynamic model introduced in Chapter 4.

Chapter 6 examined several implementation aspects which can possibly affect the applicability of the proposed FS scheme. A hardware based study as well as extended simulations were performed to scrutinise the successful operation of the proposed technique. The performance of the algorithm was proven robust on solving the problem of FS location under the imposed realistic conditions and the following remarks were noted:

- The FS scheme identified correctly the faulted MV section during the physical examination in the PNDC network. 100% accuracy was reported for both radial and ring topologies of the network where faults with maximum resistance of 60 Ω were implemented.
- The synchronisation the LV measurements was successfully achieved offline with data retrieved during hardware testing.
- The LV monitoring devices used by the FS location technique should ideally be connected directly at the LV side of the step-down transformers. Otherwise,

technical details of the LV cable and compensation of the voltage measurements are required, in order to avoid the generation of misleading results due to the intermediate impedance between the secondary substation and the measurement point.

- The positive and negative sequence components seem to be slightly deformed when random background noise is added. However, the algorithm is not affected because its function is based on average values of the calculated k_s during the fault period. By this way, the derived error is eliminated and so the developed FS location technique is accurate even under the extreme conditions of $\pm 5\%$ background noise.

- The proposed FS location technique is operational under the potential hazard of communications loss and the worst case scenario is to derive a longer FS than this with healthy communications infrastructure.

- Last but not least, the performance of the proposed algorithm was evaluated considering shorter fault time windows. The analysis revealed that the performance of the technique has not been compromised even when the fault time window has been reduced to 25%.

7.2 Future work

After the successful development and evaluation of the proposed faulted section location scheme, it has been identified that there are still several research directions to be explored. For further work with regards to the localisation of MV faults in active distribution networks the following remarks may be consulted:

- The proposed faulted section location scheme presented in this thesis is based on the ratio of positive to negative sequence voltages, so it focuses exclusively on asymmetrical faults. Further investigation of the LV profile and development of an additional FS location algorithm should be carried out considering MV symmetrical faults. The latter cannot be based on negative sequence voltage

measurements. In this case, a fault classification algorithm will be required to distinguish between unbalanced and balanced faults in order the proper algorithm to be utilized.

- The limitation of the algorithm to locate the FS between two step-down transformers when applied in ring topologies, can be overcome if the impedance of the MV cables or OHLs are available. Therefore, a more advanced version of the proposed algorithm will be capable to understand which MV section of the two identified, has been affected more depending on the combination of the voltage drop and the impedance.

- The algorithm performed satisfactorily during pre-fault load unbalance conditions with accuracy of 97.92% in 96 fault scenarios. Further mitigation of the LV load unbalance effect on the performance of the technique, especially during resistive faults, could be investigated via the deployment of current sensors (i.e. Rogowski coils) at the MV feeders, which are connected at the MV side of the transformers [1]. This approach could leverage the measurements of negative sequence currents at secondary substations and potentially indicate the difference between fault and load unbalance currents. A drawback of this practice would be the additional cost required for the deployment of the current sensors.

- In addition to the load unbalance, the impact of the pre-fault phase unbalance due to the presence of single-phase PV inverters in the LV part of the distribution network, depending on the FRT strategy they follow, should be explored.

- Faults on the LV part of the system should be studied aiming to get the most out of the monitoring technologies connected at the LV side of the transformers. One possible approach to locate faults at the LV network is to leverage the voltage sensors installed at the secondary substations and the voltage sag readings acquired from smart meters installed at the consumers premises [2].

- Simulation scenarios examining different grid fault levels in addition to this of the PNDC network as well as operation of the FS location technique in islanded mode

when only DG is present, are recommended for future work to further assess the effectiveness of the proposed method.

- Physical testing and simulation scenarios were limited to the PNDC network capabilities in terms of fault resistance to 20 Ω and 60 Ω for phase to earth and phase to phase faults respectively. Additional simulations involving a wider range of fault resistance values are recommended to broaden the evaluation of the FS location algorithm. In this sense, the effect of arc resistance on the performance of the algorithm should be also examined. In addition, higher load level than 500 kVA, which is the maximum rate that can be achieved in PNDC shall be also investigated.

- Asymmetrical faults often degenerate into three-phase faults. This condition would challenge the algorithm since it is able to operate only with unbalanced faults. Further work is recommended to develop the algorithm's capability of distinguishing the fault duration portion which corresponds to the asymmetrical fault.

- LV interconnection should be examined in the future. This rare type of distribution network configuration could possibly affect the LV measurements of two LV interconnected step-down transformers. The impact of such network configuration could be maximised in case of DG connection at the LV part.

- In this study only solid grounding has been taken into account since this is the most dominant type of grounding in MV distribution networks of GB. The FS location algorithm should also be assessed in systems with different earthing arrangements including high-impedance and resonant grounding.

- The transformer vector group configuration of Dyn11, which was used for the purpose of this study, is the most commonly implemented in secondary substations. The potential impact of other transformer vector groups, such as Ynd1 or Yyn0, should also be investigated.

- The key parameters shaping the behaviour of the developed PV inverter model

were identified during this study. They can be adjusted to properly tune the dynamic model and represent PV inverters of various manufacturers. This task can be a future extension of this work leading to the development of a generic model, which will be a great tool for DSOs network planning purposes.

- The physical testing data was measured with an accuracy of ±0.5%. This is in line with the accuracy specification of most LV monitoring projects conducted by DNOs. However, the minimum requirement for measurement accuracy will require further investigation.

- Also, the minimum sampling rate for viable LV monitoring allowing successful operation of the FS location algorithm needs to be quantified in the future. It is expected that next-generation LV meters will be capable of capturing even fast transient events, which would require sample rates of 33,000 samples per cycle or faster, although such a feature will considerably increase the cost [3]. It is also important to ensure that the minimum sampling frequency will correspond to a DWT frequency band, which will allow to successfully distinguish the initiation of the fault.

- The creation of a prototype and conduction of a pilot study are significant future steps to validate the operation of the developed technique under real fault conditions.

7.3 References

[1] A. Farughian, L. Kumpulainen, and K. Kauhaniemi, "Earth fault location using negative sequence currents," *Energies*, vol. 12, no. 19, 2019.

[2] F. A. Albasri, Z. Al Zaki, E. Al Nainoon, H. Alawi, and R. Ayyad, "A fault location system using GIS and smart meters for the LV distribution system," in *2019 International Conference on Innovation and Intelligence for Informatics, Computing, and Technologies (3ICT)*, pp. 1–6, 2019.

[3] EATON, "Next-generation power quality meters."

Appendix A

Network parameters

Table A.1: MV & LV lines/cables characteristics

Impedance	***Length (km)***	***Resistance (Ω)***	***Inductance (mH)***	***Reactance (Ω)***
Z_{m1}	2.13	0.213	0.668	0.21
Z_{m2}	2.05	0.181	0.637	0.2
Z_{m3}	0.25	0.037	0.08	0.025
Z_{m4}	0.74	0.106	0.239	0.075
Z_{m5}	0.138	0.059	0.063	0.019
Z_{m6}	5.125	1.066	5.03	1.58
Z_{m7}	5.093	1.061	5.05	1.586
Z_{m8}	0.15	0.057	0.066	0.02
Z_{m9}	0.41	0.036	0.128	0.04
Z_{m10}	0.12	0.05	0.047	0.015
Z_{m11}	0.56	0.098	0.187	0.058
Z_{mA}	0.215	0.046	0.051	0.016
Z_{mB}	0.785	0.156	0.174	0.055
Z_{mC}	0.895	0.18	0.2	0.063
Z_{mD}	0.9	0.181	0.201	0.063
Z_{mE}	1.069	0.22	0.249	0.078
Z_{mF}	0.2	0.042	0.047	0.0147

Table A.2: Step-down transformers impedances

Transformer	***Voltage levels (kV)***	***Rated power (kVA)***	***Impedance (%)***
Isolation Transformer	11/11	2000	7.69
Primary Transformer	33/11	5000	7.15
T_A	11/0.433	315	4.66
T_B	11/0.433	200	4.88
T_C	11/0.433	100	4.14
T_D	11/0.433	50	4.5
T_E	11/0.433	50	4.31
T_F	11/0.433	500	4.81

Table A.3: LV loads

Load	***Loading level (kVA)***	***pf***
Load A	160	0.95
Load B	80	0.95
Load C	80	0.95
Load D	40	0.95
Load E	40	0.95
Load F	40	0.95

Table A.4: MV lateral lines/cables characteristics

Impedance	***Length (km)***	***Resistance (Ω)***	***Inductance (mH)***	***Reactance (Ω)***
Z_{m12}	0.2	0.016	0.06	0.019
Z_{m13}	5	1.015	4.98	1.56
Z_{m14}	0.4	0.032	0.1241	0.039
Z_{mG}	0.6	0.117	0.13	0.04
Z_{mH}	0.6	0.117	0.13	0.04
Z_{mI}	0.6	0.117	0.13	0.04

Table A.5: MV lateral step-down transformers impedances

Transformer	***Voltage levels (kV)***	***Rated power (kVA)***	***Impedance (%)***
T_G	11/0.433	315	4.14
T_H	11/0.433	315	4.88
T_I	11/0.433	315	4.31

Table A.6: MV lateral connected LV loads

Load	***Loading level (kVA)***	***pf***
Load G	50	0.95
Load H	100	0.95
Load I	40	0.95

Table A.7: Synchronous generator parameters

Parameters description	***Symbol***	***Value***
Nominal apparent power	S_n (kVA)	50
Nominal voltage	V_n (kV)	11
Frequency	f (Hz)	50
Power factor	pf	0.8
Synchronous reactance d-axis	Xd (pu)	2
Synchronous reactance q-axis	Xq (pu)	2
Transient reactance d-axis	Xd' (pu)	0.3
Transient reactance q-axis	Xq' (pu)	0.3
Subtransient reactance d-axis	Xd" (pu)	0.2
Subtransient reactance q-axis	Xq" (pu)	0.2
Transient time constant d-axis	Td' (s)	1
Transient time constant q-axis	Tq' (s)	1
Subtransient time constant d-axis	Td" (s)	0.05
Subtransient time constant q-axis	Tq" (s)	0.05

Table A.8: PV plants parameters

Parameters description	***Symbol***	***Value (DG_2/DG_3/DG_4)***
Nominal apparent power	S_n (kVA)	500/50/300
Nominal voltage	V_n (kV)	11/0.433/11
Frequency	f (Hz)	50
Min Power factor	pf	0.95
Negative sequence resistance	r_2 (pu)	99999
Negative sequence reactance	x_2 (pu)	99999

Appendix B

Physical testing of PV inverters

B.1 Grid connection stability of LV-connected PV inverters under fault conditions

The objective of this work is to characterise the connection stability limits of seven off-the-shelf small scale grid-tied PV inverters under a variety of network disturbances represented by step changes in voltage magnitude and phase angle (VS). Such conditions, often caused by faults in the MV and HV network, can compromise the connection stability of the PV inverters and potentially exacerbate the network instability if large loss of PV generation ensues. The results of this study demonstrate and highlight the level of diverseness of the connection stability profiles among the various PV inverter manufacturers [1].

Table B.1 lists the various inverters under test. Fig. B.1) illustrates the test set up incorporating a RTDS [2] a PV emulator and Triphase [3]. The latter is a configurable power-electronics based device which can operate either as a (AC or DC) voltage or current source. For this testing, Triphase was configured as a 3-phase AC voltage source and it was able to sink the currents produced by the PV inverter.

The tests were systematically carried out to identify the PV inverters stability margin in terms of voltage VS with a simultaneous short-term voltage dip lasting 140 ms. The testing process generated a vector shift angle vs. retained voltage characteristic

Table B.1: List of inverters under test.

Phases	PV inverter	Rated Power	Inverter settings
Single Phase	Inverter A	5 kVA	G59/3 [4], G83/2 [5]
	Inverter B	5 kVA	G59/3, G83/2
	Inverter C	5 kVA	G59/2 [6], G83/1 [7]
	Inverter D	3 kVA	G83/1
	Inverter E	5 kVA	G59/3, G83/2
Single Phase	Inverter F	20 kVA	G59/3
	Inverter G	10 kVA	G59/3, G83/2

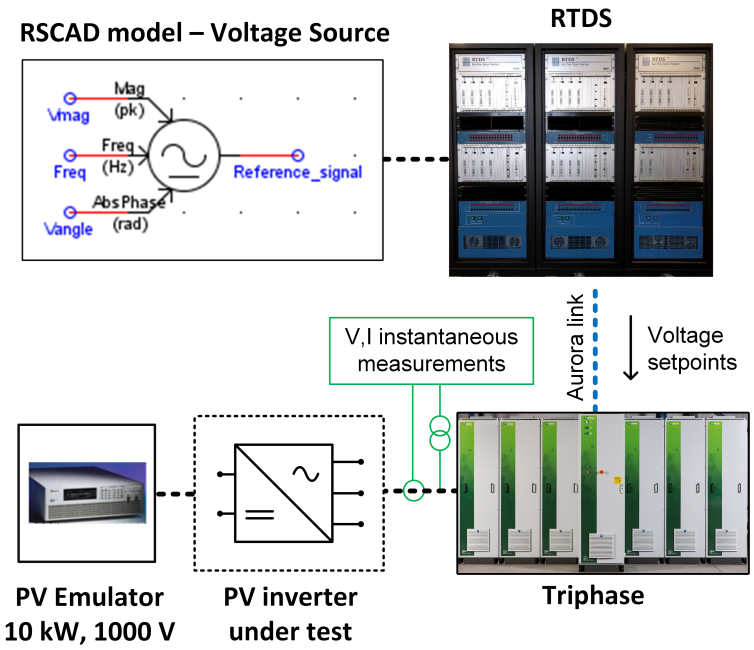

Figure B.1: Test configuration for VS and voltage depression tests.

for all inverters showing the trip (orange line) and no trip margins (blue line). The characteristics of all PV inverters under test are shown in Fig. B.2 and B.3.

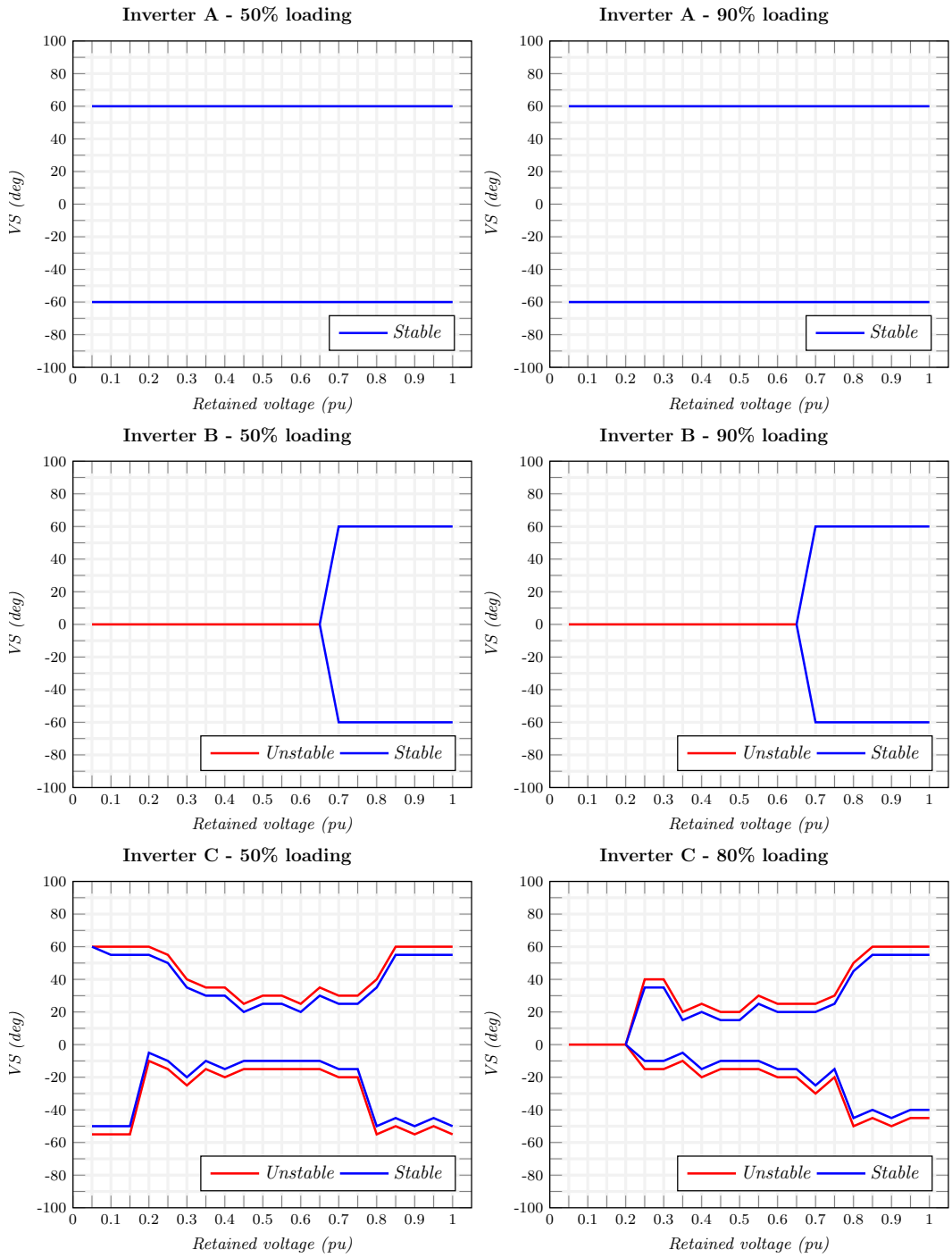

Figure B.2: VS against retained voltage characteristics - Inverters A-C.

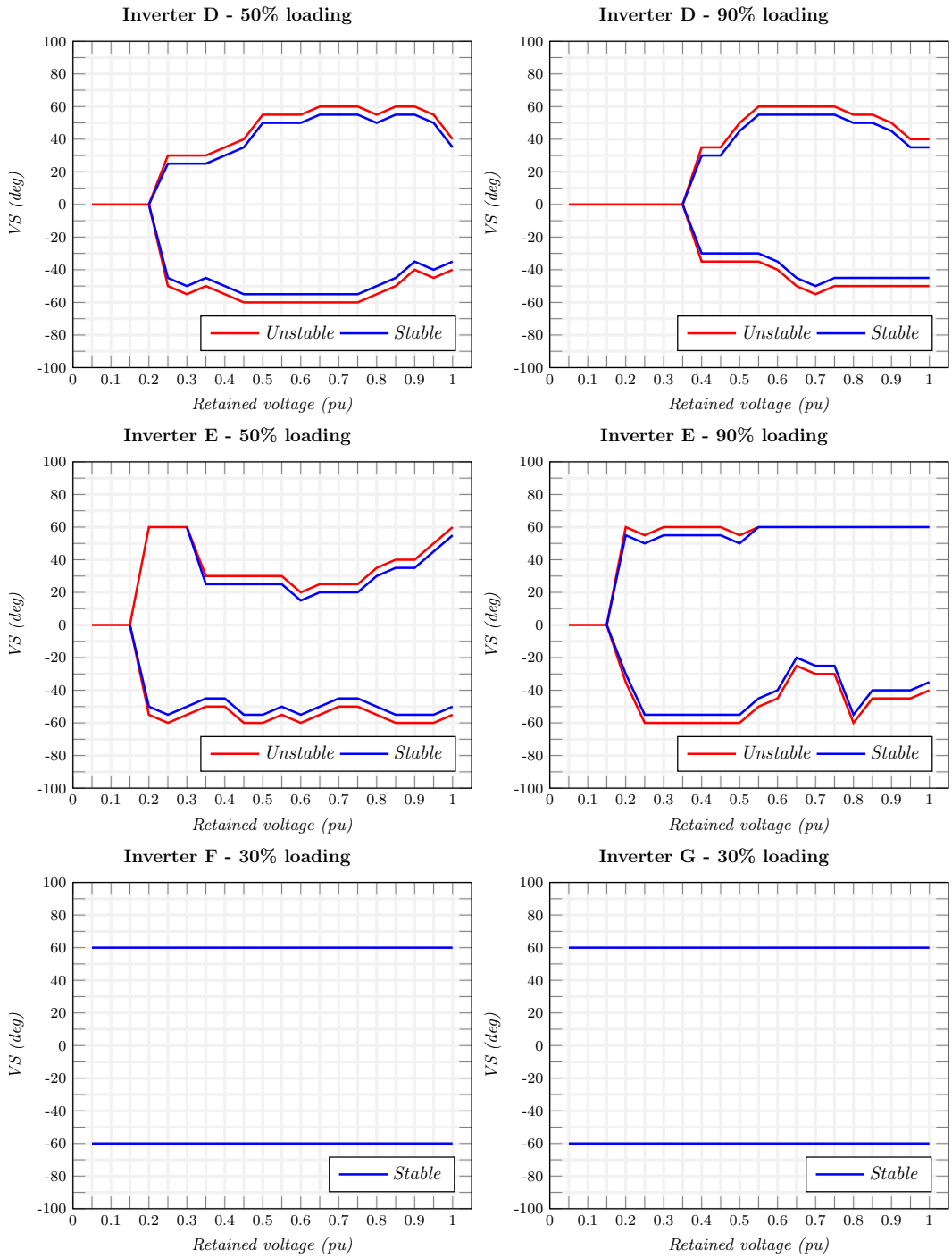

Figure B.3: VS against retained voltage characteristics - Inverters D-G.

B.2 Empirical characterisation of a commercially available PV inverter's FRT strategy

The development of the model presented in section 4.3.4.2 is based on the physical testing of a three phase LV PV inverter rated at 60 kVA. The inverter under test is an off-the-shelf product following the GB ENA Engineering Recommendation G59/3 and the relevant FRT requirements which are defined in the GB Grid Code [8, 9]. The objective of the experimental investigation is to characterise the output and hence the response of the inverter during the imposed conditions. The DUT was subject to various voltage profiles, reflecting different conditions of the grid. The following factors were considered throughout the numerous testing scenarios:

- Voltage magnitude at inverter's output
- Inverter loading prior to the fault/voltage disturbance
- Voltage point on wave (PoW) at fault inception

B.2.1 Test setup

The test setup shown in Fig. B.4 was implemented to apply LV voltage disturbances and fault conditions at the output of the PV inverter, with the aid of RTDS [10] and Triphase [11]. The latter is a configurable power-electronics based device which can operate either as a (AC or DC) voltage or current source. For this testing, Triphase was configured as a 3-phase AC voltage source and it was able to sink the currents produced by the PV inverter. Its voltage output can be controlled through voltage set-points provided by RTDS. In particular, the AC network conditions are simulated in RTDS and the resulting voltage profiles at the position of interest, have been extracted and applied to the inverter under-test via the Triphase unit. The Aurora link has been used to transfer the numerical values of voltage from the RTDS to Triphase. Effectively, the Triphase unit was utilized as a means to impose the network conditions to the inverter under-test.

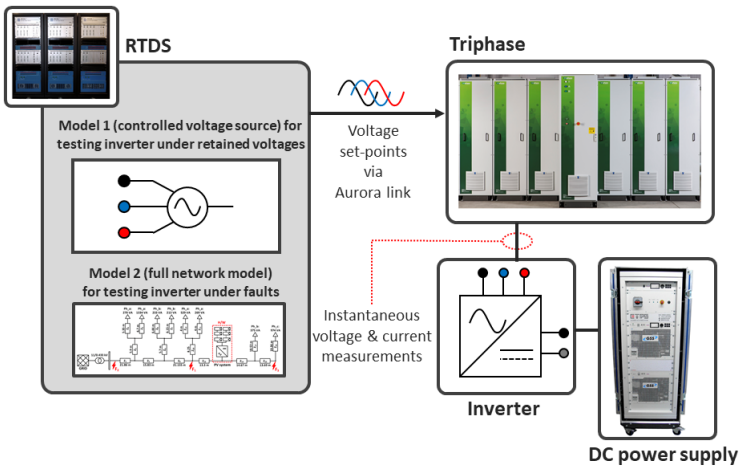

Figure B.4: Test network setup for voltage disturbance testing and faults.

The PV inverter was supplied by a PV emulator [12] rated at 64 kW maximum power and 1000 V maximum DC voltage. The particular equipment allowed to examine the DUT under a wide range of loading levels (25-100%). Moreover, a monitoring system based on Beckhoff analogue acquisition cards was deployed to acquire the instantaneous voltage and current measurements at the output of the PV inverter. The reporting rate was set at 5 kHz, although the terminal of the referred measuring device is able to measure at significantly shorter intervals through oversampling with maximum measuring error of ±0.5% relative to the full scale value ($U_{L\text{-}L}$max.:500V, $U_{L\text{-}N}$max.:288V, U_{DC}max.:410V) [13]. It is highlighted that, the inverter modelling exercise will be based on the data extracted during the physical testing. The time-step of 0.2 ms corresponding to the referred sampling frequency, is considered sufficient for the required modelling simulations according to [14, 15].

During the laboratory assessment, the voltage at the terminals of the PV inverter was determined by the simulated AC conditions in RTDS. This was achieved via two ways. First, voltage disturbances were artificially applied with the aid of a fully controllable three-phase voltage source (Model 1). By this way, the inverter was tested under a wide range of predetermined balance and unbalanced AC network voltage scenarios,

which are reported in Table B.2.

Table B.2: Voltage disturbances test schedule

Loading (%)	***Balanced Retained Voltage (pu)***		
25, 50, 75, 100	0 - 1.15 (with step of 0.05)		
Loading (%)	***Retained Phase Voltages (pu)***		
	Va	Vb	Vc
	1	1	0
	1	1	0.25
	1	1	0.5
	1	1	0.75
	1	1	1.15
	1	0	0
25, 50, 75, 100	1	0.25	0.25
	1	0.5	0.5
	1	0.75	0.75
	1	1.15	1.15
	1	0	1.15
	1	0.25	0.75
	1	0.75	0.25
	1	1.15	0

In addition, fault conditions were created via a second RSCAD model (Model 2) representing a real LV distribution network, using parameters published by Electricity North West [16]. Thus, the inverter is also examined under a wide range of voltage depressions caused by different fault types, fault locations and PoW scenarios. With respect to voltage PoW, it shall be noted that depending on the voltage value upon the fault inception, different signatures may be observed at the converter terminals accounting for voltages and currents. Additionally, since most of the converter controls are based on PLL elements, PoW has been found to have an impact on the ability of inverters to stay synchronized to the main grid [17, 18]. Even PoW is not the main focus of this work, due to its potential impact on the inverter behaviour, several PoW scenarios have been considered in the tests.

Fig. B.5 depicts the AC network topology modelled in the RTDS, indicating the

point of connection of the PV inverter hardware (H/W). The same single-line-diagram (SLD) includes the cable feeder lengths, the LV loads per phase, the MV/LV step-down transformer as well as the locations of the applied faults (F_1, F_2 and F_3). Detailed information the LV feeders impedance is provided in Table B.3.

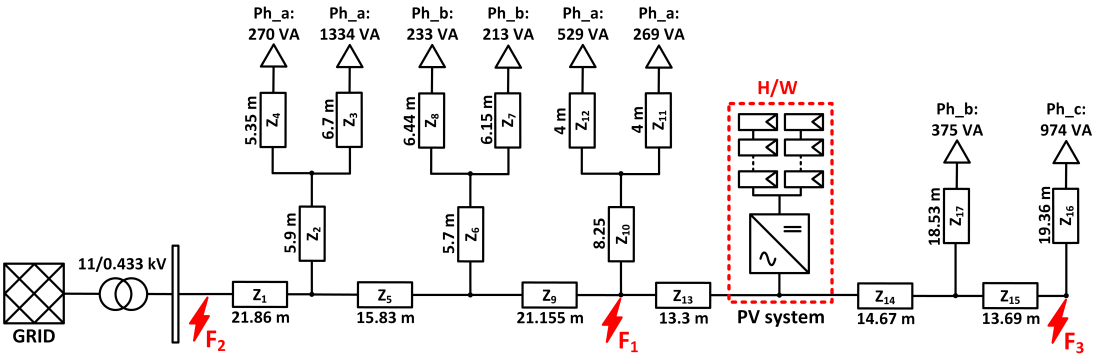

Figure B.5: LV AC network modelled in RSCAD.

Table B.3: LV feeders characteristics

Feeder section	***R*** *(mΩ)*	***X*** *(mΩ)*	***R0*** *(mΩ)*	***X0*** *(mΩ)*
Z_1	9.75	1.55206	32.8993	1.81438
Z_2	6.785	0.5192	32.8993	0.5192
Z_3	7.705	0.5896	8.04	0.5896
Z_4	6.1525	0.4708	6.42	0.4708
Z_5	7.06018	1.12393	23.82415	1.31389
Z_6	6.555	0.5016	6.84	0.5016
Z_7	7.073	0.5412	7.38	0.5412
Z_8	7.406	0.56672	7.728	0.56672
Z_9	9.43513	1.502005	31.838275	1.755865
Z_{10}	9.4875	0.726	9.9	0.726
Z_{11}	4.6	0.352	4.8	0.352
Z_{12}	4.6	0.352	4.8	0.352
Z_{13}	5.9318	0.9443	20.0165	1.1039
Z_{14}	1.30563	0.990225	4.67973	1.11492
Z_{15}	1.21841	0.924075	4.36711	1.04044
Z_{16}	22.264	1.70368	23.232	1.70368
Z_{17}	21.3095	1.63064	22.236	1.63064

Table B.4 lists the implemented fault cases. Fault period of 300 ms is considered a

typical fault duration given the fact that the fault clearance time ranges among 100 – 400 ms, depending on the protection zone.

Table B.4: Fault scenarios

Fault locations	F_1, F_2, F_3
Fault types	p-g, p-p, p-p-g, 3-p-g
Fault resistances (Ω)	0, 0.1
Voltage PoW ($^\circ$)	0, 90
Fault duration (ms)	300

B.3 References

[1] P. Bountouris, I. Abdulhadi, A. Dysco, and F. Coffele, "Characterising grid connection stability of low voltage PV inverters through real-time hardware testing," pp. 1–5, June 2019.

[2] "RTDS, "Real Time Digital Power System Simulator • RTDS Technologies Inc.." `https://www.rtds.com/`. Accessed: 2020-02-09.

[3] Triphase, "Programmable Power Conversion for RnD and Education.." `https://triphase.com/`. Accessed: 2020-02-09.

[4] Energy Networks Association, "ER G83/2: Recommendations for the connection of type tested small-scale embedded generators (up to 16a per phase) in parallel with low-voltage distribution systems.," 2012.

[5] Energy Networks Association, "Engineering recommendation G83, issue 2: Recommendations for the connection of generating plant to the distribution systems of licensed distribution network operators.," 2013.

[6] Energy Networks Association, "ER G59/2 recommendations for the connection of generating plant to the distribution systems of licensed distribution network operators.," 2011.

[7] Energy Networks Association, "Recommendations for the connection of small-scale embedded generators (up to 16 a per phase) in parallel with public low-voltage distribution networks.," 2008.

[8] Energy Networks Association, "ER G83/2: Recommendations for the connection of type tested small-scale embedded generators (up to 16a per phase) in parallel with low-voltage distribution systems.," 2012.

[9] National Grid Electricity Transmission, "The Grid Code - Issue 5," 03 2017.

[10] "RTDS, "Real Time Digital Power System Simulator, RTDS Technologies Inc." `https://www.rtds.com/`. Accessed: 2020-02-09.

[11] Triphase, "Programmable Power Conversion for RnD and Education." `https://triphase.com/`. Accessed: 2020-02-09.

[12] ETPS, "Grid-tied bidirectional DC supply." `https://bit.ly/3nOMP3X`. Accessed: 2020-11-06.

[13] Beckhoff, "EL3773 power monitoring oversampling terminal."

[14] N. Hatziargyriou, J. Milanovic, C. Rahmann, V. Ajjarapu, C. Canizares, I. Erlich, D. Hill, I. Hiskens, I. Kamwa, B. Pal, P. Pourbeik, J. Sanchez-Gasca, A. Stankovic, T. Van Cutsem, V. Vittal, and C. Vournas, "Definition and classification of power system stability – revisited amp; extended," *IEEE Transactions on Power Systems*, vol. 36, no. 4, pp. 3271–3281, 2021.

[15] N. Hatziargyriou, J. Milanovic, C. Rahmann, V. Ajjarapu, C. Canizares, I. Erlich, D. Hill, I. Hiskens, I. Kamwa, B. Pal, P. Pourbeik, J. Sanchez-Gasca, A. Stankovic, T. Van Cutsem, V. Vittal, and C. Vournas, "Stability definitions and characterization of dynamic behavior in systems with high penetration of power electronic interfaced technologies," *Power System Dynamic Performance Committee (PSDP)*, 2020.

[16] ENWL, "Low Voltage Network Solutions (LVNS)." `https://bit.ly/3BtJ7V4`. Accessed: 2020-11-06.

[17] F. Blaabjerg, R. Teodorescu, M. Liserre, and A. Timbus, "Overview of control and grid synchronization for distributed power generation systems," *IEEE Transactions on Industrial Electronics*, vol. 53, no. 5, pp. 1398–1409, 2006.

[18] S. Ma, H. Geng, L. Liu, G. Yang, and B. C. Pal, "Grid-synchronization stability improvement of large scale wind farm during severe grid fault," *IEEE Transactions on Power Systems*, vol. 33, no. 1, pp. 216–226, 2018.

Appendix C

Faulted section location results

This appendix includes all the results associated with the performance of the FS location algorithm captured throughout the total of the simulation and hardware testing scenarios.

C.1 Distribution network of PNDC

C.1.1 Radial topology

Tables C.1-C.12 include the data associated to the radial topology of PNDC network simulated with the aid of model A.

Table C.1: Phase to ground (0 Ω) fault / F_1.

3-points window	k_{s_1}	k_{s_2}	k_{s_3}	$\Delta k_{s_{13}}\%$	FS search	$k_{s_1} > k_{s_2}$	$k_{s_2} > k_{s_3}$
A-B-C	2.703	2.623	2.616	3.29%	↓	'1'	'1'
B-C-D	2.623	2.616	2.616	0.28%	→	'1'	'0'
C-D-E	2.616	2.616	2.616	0%		'0'	'0'
D-E-F	2.616	2.616	2.616	0%		'0'	'0'

Table C.2: Phase to ground (20 Ω) fault / F_1.

3-points window	k_{s_1}	k_{s_2}	k_{s_3}	$\Delta k_{s_{13}}\%$	FS search	$k_{s_1} > k_{s_2}$	$k_{s_2} > k_{s_3}$
A-B-C	8.83	8.63	8.61	2.57%	↓	'1'	'1'
B-C-D	8.63	8.61	8.61	0.23%	→	'1'	'0'
C-D-E	8.61	8.61	8.61	0%		'0'	'0'
D-E-F	8.61	8.61	8.61	0%		'0'	'0'

Table C.3: Phase to phase (0 Ω) fault / F_1.

3-points window	k_{s_1}	k_{s_2}	k_{s_3}	$\Delta k_{s_{13}}\%$	FS search	$k_{s_1} > k_{s_2}$	$k_{s_2} > k_{s_3}$
A-B-C	1.047	1.004	1	4.63%	↓	'1'	'1'
B-C-D	1.004	1	1	0.41%	→	'1'	'0'
C-D-E	1	1	1	0%		'0'	'0'
D-E-F	1	1	1	0%		'0'	'0'

Table C.4: Phase to phase (60 Ω) fault / F_1.

3-points window	k_{s_1}	k_{s_2}	k_{s_3}	$\Delta k_{s_{13}}\%$	FS search	$k_{s_1} > k_{s_2}$	$k_{s_2} > k_{s_3}$
A-B-C	6.466	6.312	6.297	2.66%	↓	'1'	'1'
B-C-D	6.312	6.297	6.297	0.23%	→	'1'	'0'
C-D-E	6.297	6.297	6.297	0%		'0'	'0'
D-E-F	6.297	6.297	6.297	0%		'0'	'0'

Table C.5: Phase to ground (0 Ω) fault / F_2.

3-points window	k_{s_1}	k_{s_2}	k_{s_3}	$\Delta k_{s_{13}}\%$	FS search	$k_{s_1} > k_{s_2}$	$k_{s_2} > k_{s_3}$
A-B-C	3.25	3.158	3.122	4.01%		'1'	'1'
B-C-D	3.158	3.122	3.112	1.47%		'1'	'1'
C-D-E	3.122	3.112	2.517	20.74%		'1'	'1'
D-E-F	3.112	2.517	2.517	21.91%	→	'1'	'0'

Table C.6: Phase to ground (20 Ω) fault / F_2.

3-points window	k_{s_1}	k_{s_2}	k_{s_3}	$\Delta k_{s_{13}}\%$	FS search	$k_{s_1} > k_{s_2}$	$k_{s_2} > k_{s_3}$
A-B-C	6.772	6.610	6.548	2.66%		'1'	'1'
B-C-D	6.610	6.548	6.531	1.21%		'1'	'1'
C-D-E	6.548	6.531	5.468	17.47%		'1'	'1'
D-E-F	6.531	5.468	5.468	18.26%	→	'1'	'0'

Table C.7: Phase to phase (0 Ω) fault / F_2.

3-points window	k_{s_1}	k_{s_2}	k_{s_3}	$\Delta k_{s_{13}}\%$	FS search	$k_{s_1} > k_{s_2}$	$k_{s_2} > k_{s_3}$
A-B-C	1.424	1.371	1.351	4.63%		'1'	'1'
B-C-D	1.371	1.351	1.346	1.89%		'1'	'1'
C-D-E	1.351	1.346	1	28.49%		'1'	'1'
D-E-F	1.346	1	1	31%	→	'1'	'0'

Table C.8: Phase to phase (60 Ω) fault / F_2.

3-points window	k_{s_1}	k_{s_2}	k_{s_3}	$\Delta k_{s_{13}}\%$	FS search	$k_{s_1} > k_{s_2}$	$k_{s_2} > k_{s_3}$
A-B-C	6.772	6.61	6.548	3.37%		'1'	'1'
B-C-D	6.61	6.548	6.531	1.21%		'1'	'1'
C-D-E	6.548	6.531	5.468	17.47%		'1'	'1'
D-E-F	6.531	5.468	5.468	18.26%	→	'1'	'0'

Table C.9: Phase to ground (0 Ω) fault / F_3.

3-points window	k_{s_1}	k_{s_2}	k_{s_3}	$\Delta k_{s_{13}}\%$	FS search	$k_{s_1} > k_{s_2}$	$k_{s_2} > k_{s_3}$
A-B-C	3.811	3.706	3.666	3.88%		'1'	'1'
B-C-D	3.706	3.666	3.655	1.4%		'1'	'1'
C-D-E	3.666	3.655	2.459	37.04%		'1'	'1'
D-E-F	3.655	2.459	2.444	42.43%	→	'1'	'1'

Table C.10: Phase to ground (20 Ω) fault / F_3.

3-points window	k_{s_1}	k_{s_2}	k_{s_3}	$\Delta k_{s_{13}}\%$	FS search	$k_{s_1} > k_{s_2}$	$k_{s_2} > k_{s_3}$
A-B-C	9.726	9.503	9.416	3.247%		'1'	'1'
B-C-D	9.503	9.416	9.393	1.166%		'1'	'1'
C-D-E	9.416	9.393	6.779	30.92%		'1'	'1'
D-E-F	9.393	6.779	6.75	34.59%	→	'1'	'1'

Table C.11: Phase to phase (0 Ω) fault / F_3.

3-points window	k_{s_1}	k_{s_2}	k_{s_3}	$\Delta k_{s_{13}}\%$	FS search	$k_{s_1} > k_{s_2}$	$k_{s_2} > k_{s_3}$
A-B-C	1.809	1.748	1.724	4.85%		'1'	'1'
B-C-D	1.748	1.724	1.718	1.74%		'1'	'1'
C-D-E	1.724	1.718	1.007	48.31%		'1'	'1'
D-E-F	1.718	1.007	1	57.79%	→	'1'	'1'

Table C.12: Phase to phase (60 Ω) fault / F_3.

3-points window	k_{s_1}	k_{s_2}	k_{s_3}	$\Delta k_{s_{13}}\%$	FS search	$k_{s_1} > k_{s_2}$	$k_{s_2} > k_{s_3}$
A-B-C	7.083	6.915	6.849	3.37%		'1'	'1'
B-C-D	6.915	6.849	6.832	1.21%		'1'	'1'
C-D-E	6.849	6.832	4.872	31.97%		'1'	'1'
D-E-F	6.832	4.872	4.849	35.93%	→	'1'	'1'

C.1.2 Ring topology

Tables C.13-C.24 include the data associated to the ring topology of PNDC network simulated with the aid of model A.

Table C.13: Phase to ground (20 Ω) fault / F_1.

3-points window	k_{s_1}	k_{s_2}	k_{s_3}	$\Delta k_{s_{13}}\%$	FS search	$k_{s_1} > k_{s_2}$	$k_{s_2} > k_{s_3}$
A-B-C	2.692	2.621	2.619	2.77%		'1'	'1'
B-C-D	2.621	2.619	2.620	0.06%	→	'1'	'0'
C-D-E	2.619	2.620	2.759	5.25%		'0'	'0'
D-E-F	2.62	2.759	2.762	5.27%		'0'	'0'

Table C.14: Phase to ground (0 Ω) fault / F_1.

3-points window	k_{s_1}	k_{s_2}	k_{s_3}	$\Delta k_{s_{13}}\%$	FS search	$k_{s_1} > k_{s_2}$	$k_{s_2} > k_{s_3}$
A-B-C	8.833	8.652	8.643	2.18%		'1'	'1'
B-C-D	8.652	8.643	8.645	0.081%	→	'1'	'0'
C-D-E	8.643	8.645	9.005	4.13%		'0'	'0'
D-E-F	8.645	9.005	9.014	0%		'0'	'0'

Table C.15: Phase to phase (0 Ω) fault / F_1.

3-points window	k_{s_1}	k_{s_2}	k_{s_3}	$\Delta k_{s_{13}}\%$	FS search	$k_{s_1} > k_{s_2}$	$k_{s_2} > k_{s_3}$
A-B-C	1.042	1.004	1.001	3.99%		'1'	'1'
B-C-D	1.004	1.001	1.002	0.18%	→	'1'	'0'
C-D-E	1.001	1.002	1.079	7.51%		'0'	'0'
D-E-F	1.002	1.079	1.080	7.46%		'0'	'0'

Table C.16: Phase to phase (60 Ω) fault / F_1.

3-points window	k_{s_1}	k_{s_2}	k_{s_3}	$\Delta k_{s_{13}}\%$	FS search	$k_{s_1} > k_{s_2}$	$k_{s_2} > k_{s_3}$
A-B-C	6.467	6.329	6.323	2.26%		'1'	'1'
B-C-D	6.329	6.323	6.324	0.08%	→	'1'	'0'
C-D-E	6.323	6.324	6.597	4.28%		'0'	'0'
D-E-F	6.324	6.597	6.604	4.3%		'0'	'0'

Table C.17: Phase to ground (0 Ω) fault / F_2.

3-points window	k_{s_1}	k_{s_2}	k_{s_3}	$\Delta k_{s_{13}}\%$	FS search	$k_{s_1} > k_{s_2}$	$k_{s_2} > k_{s_3}$
A-B-C	2.906	2.868	2.846	2.11%		'1'	'1'
B-C-D	2.868	2.846	2.841	0.95%		'1'	'1'
C-D-E	2.846	2.841	2.915	2.42%	→	'1'	'0'
D-E-F	3.841	2.915	2.935	3.24%		'0'	'0'

Table C.18: Phase to ground (20 Ω) fault / F_2.

3-points window	k_{s_1}	k_{s_2}	k_{s_3}	$\Delta k_{s_{13}}\%$	FS search	$k_{s_1} > k_{s_2}$	$k_{s_2} > k_{s_3}$
A-B-C	9.057	8.963	8.914	1.59%		'1'	'1'
B-C-D	8.963	8.914	8.904	0.661%		'1'	'1'
C-D-E	8.914	8.904	9.081	1.863%	→	'1'	'0'
D-E-F	8.904	9.081	9.129	2.489%		'0'	'0'

Table C.19: Phase to phase (0 Ω) fault / F_2.

3-points window	k_{s_1}	k_{s_2}	k_{s_3}	$\Delta k_{s_{13}}\%$	FS search	$k_{s_1} > k_{s_2}$	$k_{s_2} > k_{s_3}$
A-B-C	1.188	1.167	1.157	3.99%		'1'	'1'
B-C-D	1.167	1.157	1.154	1.06%		'1'	'1'
C-D-E	1.157	1.154	1.194	3.2%	→	'1'	'0'
D-E-F	1.154	1.194	1.205	4.23%		'0'	'0'

Table C.20: Phase to phase (60 Ω) fault / F_2.

3-points window	k_{s_1}	k_{s_2}	k_{s_3}	$\Delta k_{s_{13}}\%$	FS search	$k_{s_1} > k_{s_2}$	$k_{s_2} > k_{s_3}$
A-B-C	6.628	6.557	6.518	1.68%		'1'	'1'
B-C-D	6.557	6.518	6.51	0.71%		'1'	'1'
C-D-E	6.518	6.51	5.646	1.95%	→	'1'	'0'
D-E-F	6.51	5.646	5.683	2.61%		'0'	'0'

Table C.21: Phase to ground (0 Ω) fault / F_3.

3-points window	k_{s_1}	k_{s_2}	k_{s_3}	$\Delta k_{s_{13}}\%$	FS search	$k_{s_1} > k_{s_2}$	$k_{s_2} > k_{s_3}$
A-B-C	2.653	2.652	2.651	0.08%		'1'	'1'
B-C-D	2.652	2.651	2.650	0.08%		'1'	'1'
C-D-E	2.651	2.650	2.624	1.02%		'1'	'1'
D-E-F	2.650	2.624	2.639	0.42%	→	'1'	'0'

Table C.22: Phase to ground (20 Ω) fault / F_3.

3-points window	k_{s_1}	k_{s_2}	k_{s_3}	$\Delta k_{s_{13}}\%$	FS search	$k_{s_1} > k_{s_2}$	$k_{s_2} > k_{s_3}$
A-B-C	8.912	8.908	8.906	0.07%		'1'	'1'
B-C-D	8.908	8.906	8.905	0.034%		'1'	'1'
C-D-E	8.906	8.905	8.835	0.8%		'1'	'1'
D-E-F	8.905	8.835	8.876	0.338%	→	'1'	'0'

Table C.23: Phase to phase (0 Ω) fault / F_3.

3-points window	k_{s_1}	k_{s_2}	k_{s_3}	$\Delta k_{s_{13}}\%$	FS search	$k_{s_1} > k_{s_2}$	$k_{s_2} > k_{s_3}$
A-B-C	1.016	1.0151	1.0147	0.13%		'1'	'1'
B-C-D	1.0151	1.0147	1.0146	0.05%		'1'	'1'
C-D-E	1.0147	1.0146	1.0002	1.44%		'1'	'1'
D-E-F	1.0146	1.0002	1.0084	0.62%	→	'1'	'1'

Table C.24: Phase to phase (60 Ω) fault / F_3.

3-points window	k_{s_1}	k_{s_2}	k_{s_3}	$\Delta k_{s_{13}}\%$	FS search	$k_{s_1} > k_{s_2}$	$k_{s_2} > k_{s_3}$
A-B-C	6.533	6.530	6.528	0.08%		'1'	'1'
B-C-D	6.530	6.5283	6.5279	0.03%		'1'	'1'
C-D-E	6.5283	6.5279	6.475	0.82%		'1'	'1'
D-E-F	6.5279	6.475	6.505	0.35%	→	'1'	'1'

C.2 Distribution network with MV lateral

C.2.1 Radial topology

Tables C.25-C.48 contain the data associated to the radial topology of a distribution network including a MV lateral, simulated with the aid of model B.

Table C.25: Radial topology / Phase to ground (0 Ω) fault / F_1.

Circuit	3-points window	k_{s_1}	k_{s_2}	k_{s_3}	$\Delta k_{s_{13}}\%$	FS search	$k_{s_1} > k_{s_2}$	$k_{s_2} > k_{s_3}$
Radial A-I	A-B-G	2.759	2.673	2.66	3.67%	↓↓	'1'	'1'
	B-G-H	2.73	2.66	2.66	0.49%	→	'1'	'0'
	G-H-I	2.66	2.66	2.66	0%		'0'	'0'
Radial A-F	A-B-C	2.759	2.673	2.66	3.67%	↓↓	'1'	'1'
	B-C-D	2.673	2.66	2.66	0.49%	→	'1'	'0'
	C-D-E	2.66	2.66	2.66	0%		'0'	'0'
	D-E-F	2.66	2.66	2.66	0%		'0'	'0'

Table C.26: Radial topology / Phase to ground (20 Ω) fault / F_1.

Circuit	3-points window	k_{s_1}	k_{s_2}	k_{s_3}	$\Delta k_{s_{13}}\%$	FS search	$k_{s_1} > k_{s_2}$	$k_{s_2} > k_{s_3}$
Radial A-I	A-B-G	8.918	8.699	8.67	2.83%	↓↓	'1'	'1'
	B-G-H	8.699	8.67	8.67	0.33%	→	'1'	'0'
	G-H-I	8.67	8.67	8.67	0%		'0'	'0'
Radial A-F	A-B-C	8.918	8.699	8.67	2.83%	↓↓	'1'	'1'
	B-C-D	8.699	8.67	8.67	0.33%	→	'1'	'0'
	C-D-E	8.67	8.67	8.67	0%		'0'	'0'
	D-E-F	8.67	8.67	8.67	0%		'0'	'0'

Table C.27: Radial topology / Phase to phase (0 Ω) fault / F_1.

Circuit	3-points window	k_{s_1}	k_{s_2}	k_{s_3}	$\Delta k_{s_{13}}\%$	FS search	$k_{s_1} > k_{s_2}$	$k_{s_2} > k_{s_3}$
Radial A-I	A-B-G	1.052	1.006	1	5.07%	↓↓	'1'	'1'
	B-G-H	1.006	1	1	0.59%	→	'1'	'0'
	G-H-I	1	1	1	0%		'0'	'0'
Radial A-F	A-B-C	1.052	1.006	1	5.07%	↓↓	'1'	'1'
	B-C-D	1.006	1	1	0.59%	→	'1'	'0'
	C-D-E	1	1	1	0%		'0'	'0'
	D-E-F	1	1	1	0%		'0'	'0'

Table C.28: Radial topology / Phase to phase (60 Ω) fault / F_1.

Circuit	3-points window	k_{s_1}	k_{s_2}	k_{s_3}	$\Delta k_{s_{13}}\%$	FS search	$k_{s_1} > k_{s_2}$	$k_{s_2} > k_{s_3}$
Radial A-I	A-B-G	6.527	6.361	6.338	2.95%	↓↓	'1'	'1'
	B-G-H	6.361	6.338	6.338	0.36%	→	'1'	'0'
	G-H-I	6.338	6.338	6.338	0%		'0'	'0'
Radial A-F	A-B-C	6.527	6.361	6.338	2.95%	↓↓	'1'	'1'
	B-C-D	6.361	6.338	6.338	0.36%	→	'1'	'0'
	C-D-E	6.338	6.338	6.338	0%		'0'	'0'
	D-E-F	6.338	6.338	6.338	0%		'0'	'0'

Table C.29: Radial topology / Phase to ground (0 Ω) fault / F_2.

Circuit	3-points window	k_{s_1}	k_{s_2}	k_{s_3}	$\Delta k_{s_{13}}\%$	FS search	$k_{s_1} > k_{s_2}$	$k_{s_2} > k_{s_3}$
Radial A-I	A-B-G	3.35	3.25	3.236	3.48%		'1'	'1'
	B-G-H	3.25	3.236	3.236	0.43%		'1'	'0'
	G-H-I	3.236	3.236	3.236	0%		'0'	'0'
Radial A-F	A-B-C	3.35	3.25	3.195	4.75%		'1'	'1'
	B-C-D	3.25	3.195	3.18	2.18%		'1'	'1'
	C-D-E	3.195	3.18	2.559	21.36%		'1'	'1'
	D-E-F	3.18	2.559	2.559	22.45%	→	'1'	'0'

Table C.30: Radial topology / Phase to ground (20 Ω) fault / F_2.

Circuit	3-points window	k_{s_1}	k_{s_2}	k_{s_3}	$\Delta k_{s_{13}}\%$	FS search	$k_{s_1} > k_{s_2}$	$k_{s_2} > k_{s_3}$
Radial A-I	A-B-G	9.407	9.177	9.146	2.82%		'1'	'1'
	B-G-H	9.177	9.146	9.146	0.34%		'1'	'0'
	G-H-I	9.146	9.146	9.146	0%		'0'	'0'
Radial A-F	A-B-C	9.407	9.177	9.054	3.83%		'1'	'1'
	B-C-D	9.177	9.054	9.024	1.68%		'1'	'1'
	C-D-E	9.054	9.024	7.563	17.44%		'1'	'1'
	D-E-F	9.024	7.563	7.563	18.15%	→	'1'	'0'

Table C.31: Radial topology / Phase to phase (0 Ω) fault / F_2.

Circuit	3-points window	k_{s_1}	k_{s_2}	k_{s_3}	$\Delta k_{s_{13}}\%$	FS search	$k_{s_1} > k_{s_2}$	$k_{s_2} > k_{s_3}$
Radial A-I	A-B-G	1.45	1.393	1.385	4.56%		'1'	'1'
	B-G-H	1.393	1.385	1.385	0.54%		'1'	'1'
	G-H-I	1.385	1.385	1.385	0%		'0'	'0'
Radial A-F	A-B-C	1.45	1.393	1.363	6.17%		'1'	'1'
	B-C-D	1.393	1.363	1.356	2.69%		'1'	'1'
	C-D-E	1.363	1.356	1	29.3%		'1'	'1'
	D-E-F	1.356	1	1	31.83%	→	'1'	'0'

Table C.32: Radial topology / Phase to phase (60 Ω) fault / F_2.

Circuit	3-points window	k_{s_1}	k_{s_2}	k_{s_3}	$\Delta k_{s_{13}}\%$	FS search	$k_{s_1} > k_{s_2}$	$k_{s_2} > k_{s_3}$
Radial A-I	A-B-G	6.844	6.691	6.668	2.62%		'1'	'1'
	B-G-H	6.691	6.668	6.668	0.36%		'1'	'0'
	G-H-I	6.668	6.668	6.668	0%		'0'	'0'
Radial A-F	A-B-C	6.844	6.691	6.597	3.68%		'1'	'1'
	B-C-D	6.691	6.597	6.573	1.78%		'1'	'1'
	C-D-E	6.597	6.573	5.475	18.05%		'1'	'1'
	D-E-F	6.573	5.475	5.475	18.8%	→	'1'	'0'

Table C.33: Radial topology / Phase to ground (0 Ω) fault / F_3.

Circuit	3-points window	k_{s_1}	k_{s_2}	k_{s_3}	$\Delta k_{s_{13}}\%$	FS search	$k_{s_1} > k_{s_2}$	$k_{s_2} > k_{s_3}$
Radial A-I	A-B-G	3.925	3.812	3.796	3.36%		'1'	'1'
	B-G-H	3.812	3.796	3.796	0.42%		'1'	'0'
	G-H-I	3.796	3.796	3.796	0%		'0'	'0'
Radial A-F	A-B-C	3.925	3.812	3.750	4.57%		'1'	'1'
	B-C-D	3.812	3.750	3.734	2.07%		'1'	'1'
	C-D-E	3.750	3.734	2.491	37.86%		'1'	'1'
	D-E-F	3.734	2.491	2.479	43.26%	→	'1'	'1'

Table C.34: Radial topology / Phase to ground (20 Ω) fault / F_3.

Circuit	3-points window	k_{s_1}	k_{s_2}	k_{s_3}	$\Delta k_{s_{13}}\%$	FS search	$k_{s_1} > k_{s_2}$	$k_{s_2} > k_{s_3}$
Radial A-I	A-B-G	9.878	9.637	9.605	2.81%		'1'	'1'
	B-G-H	9.637	9.605	9.605	0.33%		'1'	'0'
	G-H-I	9.605	9.605	9.605	0%		'0'	'0'
Radial A-F	A-B-C	9.878	9.637	9.509	3.81%		'1'	'1'
	B-C-D	9.637	9.509	9.477	1.68%		'1'	'1'
	C-D-E	9.509	9.477	6.779	31.79%		'1'	'1'
	D-E-F	9.477	6.779	6.756	35.47%	→	'1'	'1'

Table C.35: Radial topology / Phase to phase (0 Ω) fault / F_3.

Circuit	3-points window	k_{s_1}	k_{s_2}	k_{s_3}	$\Delta k_{s_{13}}\%$	FS search	$k_{s_1} > k_{s_2}$	$k_{s_2} > k_{s_3}$
Radial A-I	A-B-G	1.846	1.779	1.771	4.17%		'1'	'1'
	B-G-H	1.779	1.771	1.771	0.45%		'1'	'0'
	G-H-I	1.771	1.771	1.771	0%		'0'	'0'
Radial A-F	A-B-C	1.846	1.779	1.744	5.7%		'1'	'1'
	B-C-D	1.779	1.744	1.736	2.45%		'1'	'1'
	C-D-E	1.744	1.736	1.005	49.43%		'1'	'1'
	D-E-F	1.736	1.005	1	59.02%	→	'1'	'1'

Table C.36: Radial topology / Phase to phase (60 Ω) fault / F_3.

Circuit	3-points window	k_{s_1}	k_{s_2}	k_{s_3}	$\Delta k_{s_{13}}\%$	FS search	$k_{s_1} > k_{s_2}$	$k_{s_2} > k_{s_3}$
Radial A-I	A-B-G	7.189	7.007	6.982	2.93%		'1'	'1'
	B-G-H	7.007	6.982	6.982	0.36%		'1'	'0'
	G-H-I	6.982	6.982	6.982	0%		'0'	'0'
Radial A-F	A-B-C	7.189	7.007	6.909	3.98%		'1'	'1'
	B-C-D	7.007	6.909	6.884	1.77%		'1'	'1'
	C-D-E	6.909	6.884	4.865	32.87%		'1'	'1'
	D-E-F	6.884	4.865	4.847	36.82%	→	'1'	'1'

Table C.37: Radial topology / Phase to ground (0 Ω) fault / F_4.

Circuit	3-points window	k_{s_1}	k_{s_2}	k_{s_3}	$\Delta k_{s_{13}}\%$	FS search	$k_{s_1} > k_{s_2}$	$k_{s_2} > k_{s_3}$
Radial A-I	A-B-G	2.766	2.68	2.66	3.92%	↓↓	'1'	'1'
	B-G-H	2.68	2.66	2.66	0.75%	→	'1'	'0'
	G-H-I	2.66	2.66	2.66	0%		'0'	'0'
Radial A-F	A-B-C	2.766	2.68	2.667	3.66%		'1'	'1'
	B-C-D	2.68	2.667	2.667	0.49%	→	'1'	'0'
	C-D-E	2.667	2.667	2.667	0%		'0'	'0'
	D-E-F	2.667	2.667	2.667	0%		'0'	'0'

Table C.38: Radial topology / Phase to ground (20 Ω) fault / F_4.

Circuit	3-points window	k_{s_1}	k_{s_2}	k_{s_3}	$\Delta k_{s_{13}}\%$	FS search	$k_{s_1} > k_{s_2}$	$k_{s_2} > k_{s_3}$
Radial A-I	A-B-G	8.924	8.706	8.656	3.06%	↓↓	'1'	'1'
	B-G-H	8.706	8.656	8.656	0.58%	→	'1'	'0'
	G-H-I	8.656	8.656	8.656	0%		'0'	'0'
Radial A-F	A-B-C	8.924	8.706	8.676	2.83%		'1'	'1'
	B-C-D	8.706	8.676	8.676	0.35%	→	'1'	'0'
	C-D-E	8.676	8.676	8.676	0%		'0'	'0'
	D-E-F	8.676	8.676	8.676	0%		'0'	'0'

Table C.39: Radial topology / Phase to phase (0 Ω) fault / F_4.

Circuit	3-points window	k_{s_1}	k_{s_2}	k_{s_3}	$\Delta k_{s_{13}}\%$	FS search	$k_{s_1} > k_{s_2}$	$k_{s_2} > k_{s_3}$
Radial A-I	A-B-G	1.056	1.01	1	5.48%	↓↓	'1'	'1'
	B-G-H	1.01	1	1	1%	→	'1'	'0'
	G-H-I	1	1	1	0%		'0'	'0'
Radial A-F	A-B-C	1.056	1.01	1.004	5.08%		'1'	'1'
	B-C-D	1.01	1.004	1.004	0.6%	→	'1'	'0'
	C-D-E	1.004	1.004	1.004	0%		'0'	'0'
	D-E-F	1.004	1.004	1.004	0%		'0'	'0'

Table C.40: Radial topology / Phase to phase (60 Ω) fault / F_4.

Circuit	3-points window	k_{s_1}	k_{s_2}	k_{s_3}	$\Delta k_{s_{13}}\%$	FS search	$k_{s_1} > k_{s_2}$	$k_{s_2} > k_{s_3}$
Radial A-I	A-B-G	6.531	6.365	6.327	3.18%	↓↓	'1'	'1'
	B-G-H	6.365	6.327	6.327	0.6%	→	'1'	'0'
	G-H-I	6.327	6.327	6.327	0%		'0'	'0'
Radial A-F	A-B-C	6.531	6.365	6.342	2.95%		'1'	'1'
	B-C-D	6.365	6.342	6.342	0.36%	→	'1'	'0'
	C-D-E	6.342	6.342	6.342	0%		'0'	'0'
	D-E-F	6.342	6.342	6.342	0%		'0'	'0'

Table C.41: Radial topology / Phase to ground (0 Ω) fault / F_5.

Circuit	3-points window	k_{s_1}	k_{s_2}	k_{s_3}	$\Delta k_{s_{13}}\%$	FS search	$k_{s_1} > k_{s_2}$	$k_{s_2} > k_{s_3}$
Radial A-I	A-B-G	3.285	3.186	3.163	3.8%		'1'	'1'
	B-G-H	3.186	3.163	2.552	21.37%		'1'	'1'
	G-H-I	3.163	2.552	2.552	22.17%	→	'1'	'0'
Radial A-F	A-B-C	3.285	3.186	3.172	3.52%		'1'	'1'
	B-C-D	3.186	3.172	3.172	0.44%		'1'	'0'
	C-D-E	3.172	3.172	3.172	0%		'0'	'0'
	D-E-F	3.172	3.172	3.172	0%		'0'	'0'

Table C.42: Radial topology / Phase to ground (20 Ω) fault / F_5.

Circuit	3-points window	k_{s_1}	k_{s_2}	k_{s_3}	$\Delta k_{s_{13}}\%$	FS search	$k_{s_1} > k_{s_2}$	$k_{s_2} > k_{s_3}$
Radial A-I	A-B-G	9.351	9.122	9.070	3.06%		'1'	'1'
	B-G-H	9.122	9.070	7.618	17.48%		'1'	'1'
	G-H-I	9.070	7.618	7.618	17.92%	→	'1'	'0'
Radial A-F	A-B-C	9.351	9.122	9.091	2.83%		'1'	'1'
	B-C-D	9.122	9.091	9.091	0.34%		'1'	'0'
	C-D-E	9.091	9.091	9.091	0%		'0'	'0'
	D-E-F	9.091	9.091	9.091	0%		'0'	'0'

Table C.43: Radial topology / Phase to phase (0 Ω) fault / F_5.

Circuit	3-points window	k_{s_1}	k_{s_2}	k_{s_3}	$\Delta k_{s_{13}}\%$	FS search	$k_{s_1} > k_{s_2}$	$k_{s_2} > k_{s_3}$
Radial A-I	A-B-G	1.421	1.365	1.352	5%		'1'	'1'
	B-G-H	1.365	1.352	1	29.46%		'1'	'1'
	G-H-I	1.352	1	1	31.5%	→	'1'	'0'
Radial A-F	A-B-C	1.421	1.365	1.357	4.63%		'1'	'1'
	B-C-D	1.365	1.357	1.357	0.59%		'1'	'0'
	C-D-E	1.357	1.357	1.357	0%		'0'	'0'
	D-E-F	1.357	1.357	1.357	0%		'0'	'0'

Table C.44: Radial topology / Phase to phase (60 Ω) fault / F_5.

Circuit	3-points window	k_{s_1}	k_{s_2}	k_{s_3}	$\Delta k_{s_{13}}\%$	FS search	$k_{s_1} > k_{s_2}$	$k_{s_2} > k_{s_3}$
Radial A-I	A-B-G	6.829	6.655	6.616	3.18%		'1'	'1'
	B-G-H	6.655	6.616	5.523	18.07%		'1'	'1'
	G-H-I	6.616	5.523	5.523	18.57%	→	'1'	'0'
Radial A-F	A-B-C	6.829	6.655	6.632	2.94%		'1'	'1'
	B-C-D	6.655	6.632	6.632	0.35%		'1'	'0'
	C-D-E	6.632	6.632	6.632	0%		'0'	'0'
	D-E-F	6.632	6.632	6.632	0%		'0'	'0'

Table C.45: Radial topology / Phase to ground (0 Ω) fault / F_6.

Circuit	3-points window	k_{s_1}	k_{s_2}	k_{s_3}	$\Delta k_{s_{13}}\%$	FS search	$k_{s_1} > k_{s_2}$	$k_{s_2} > k_{s_3}$
Radial A-I	A-B-G	3.3	3.2	3.178	3.78%		'1'	'1'
	B-G-H	3.2	3.178	2.564	21.34%		'1'	'1'
	G-H-I	3.178	2.564	2.551	22.68%	→	'1'	'1'
Radial A-F	A-B-C	3.3	3.2	3.187	3.5%		'1'	'1'
	B-C-D	3.2	3.187	3.187	0.41%		'1'	'0'
	C-D-E	3.187	3.187	3.187	0%		'0'	'0'
	D-E-F	3.187	3.187	3.187	0%		'0'	'0'

Table C.46: Radial topology / Phase to ground (20 Ω) fault / F_6.

Circuit	3-points window	k_{s_1}	k_{s_2}	k_{s_3}	$\Delta k_{s_{13}}\%$	FS search	$k_{s_1} > k_{s_2}$	$k_{s_2} > k_{s_3}$
Radial A-I	A-B-G	9.364	9.134	9.083	3.06%		'1'	'1'
	B-G-H	9.134	9.083	7.628	17.48%		'1'	'1'
	G-H-I	9.083	7.628	7.596	18.35%	→	'1'	'1'
Radial A-F	A-B-C	9.364	9.134	9.103	2.84%		'1'	'1'
	B-C-D	9.134	9.103	9.103	0.34%		'1'	'0'
	C-D-E	9.103	9.103	9.103	0%		'0'	'0'
	D-E-F	9.103	9.103	9.103	0%		'0'	'0'

Table C.47: Radial topology / Phase to phase (0 Ω) fault / F_6.

Circuit	3-points window	k_{s_1}	k_{s_2}	k_{s_3}	$\Delta k_{s_{13}}\%$	FS search	$k_{s_1} > k_{s_2}$	$k_{s_2} > k_{s_3}$
Radial A-I	A-B-G	1.43	1.374	1.362	4.9%		'1'	'1'
	B-G-H	1.374	1.362	1.008	29.33%		'1'	'1'
	G-H-I	1.362	1.008	1	32.23%	→	'1'	'1'
Radial A-F	A-B-C	1.43	1.374	1.367	4.53%		'1'	'1'
	B-C-D	1.374	1.367	1.367	0.51%		'1'	'0'
	C-D-E	1.367	1.367	1.367	0%		'0'	'0'
	D-E-F	1.367	1.367	1.367	0%		'0'	'0'

Table C.48: Radial topology / Phase to phase (60 Ω) fault / F_6.

Circuit	3-points window	k_{s_1}	k_{s_2}	k_{s_3}	$\Delta k_{s_{13}}\%$	FS search	$k_{s_1} > k_{s_2}$	$k_{s_2} > k_{s_3}$
Radial A-I	A-B-G	6.837	6.664	6.624	3.18%		'1'	'1'
	B-G-H	6.664	6.624	5.530	18.08%		'1'	'1'
	G-H-I	6.624	5.530	5.506	18.99%	→	'1'	'1'
Radial A-F	A-B-C	6.837	6.664	6.64	2.93%		'1'	'1'
	B-C-D	6.664	6.64	6.64	0.36%		'1'	'1'
	C-D-E	6.64	6.64	6.64	0%		'0'	'0'
	D-E-F	6.64	6.64	6.64	0%		'0'	'0'

C.2.2 Ring topology

Tables C.49-C.72 gather the data associated to the ring topology of a distribution network including a MV lateral, simulated with the aid of model B.

Table C.49: Ring topology / Phase to ground (0 Ω) fault / F_1.

Circuit	3-points window	k_{s_1}	k_{s_2}	k_{s_3}	$\lvert\Delta k_{s_{13}}\%\rvert$	FS search	$k_{s_1} > k_{s_2}$	$k_{s_2} > k_{s_3}$
Ring A-F	A-B-C	2.737	2.661	2.655	3.05%		'1'	'1'
	B-C-D	2.661	2.655	2.656	0.19%	↓↓	'1'	'0'
	C-D-E	2.655	2.656	2.813	5.83%		'0'	'0'
	D-E-F	2.656	2.813	2.818	5.68%		'0'	'0'
Radial B-I	B-G-H	2.661	2.651	2.651	0.38%	→	'1'	'0'
Radial D-I	D-C-G	2.656	2.655	2.651	0.19%	↓	'1'	'1'
	C-G-H	2.655	2.651	2.651	0.151%	→	'1'	'0'
B-I & D-I	G-H-I	2.651	2.651	2.651	0%		'0'	'0'

Table C.50: Ring topology / Phase to ground (20 Ω) fault / F_1.

Circuit	3-points window	k_{s_1}	k_{s_2}	k_{s_3}	$\lvert\Delta k_{s_{13}}\%\rvert$	FS search	$k_{s_1} > k_{s_2}$	$k_{s_2} > k_{s_3}$
Ring A-F	A-B-C	6.512	6.366	6.353	2.48%		'1'	'1'
	B-C-D	6.366	6.353	6.356	0.16%	↓↓	'1'	'0'
	C-D-E	6.353	6.356	6.659	4.74%		'0'	'0'
	D-E-F	6.356	6.659	6.667	4.74%		'0'	'0'
Radial B-I	B-G-H	6.366	6.346	6.346	0.31%	→	'1'	'0'
Radial D-I	D-C-G	6.356	6.353	6.346	0.16%	↓	'1'	'1'
	C-G-H	6.353	6.346	6.346	0.11%	→	'1'	'0'
B-I & D-I	G-H-I	6.346	6.346	6.346	0%		'0'	'0'

Table C.51: Ring topology / Phase to phase (0 Ω) fault / F_1.

Circuit	3-points window	k_{s_1}	k_{s_2}	k_{s_3}	$\lvert\Delta k_{s_{13}}\%\rvert$	FS search	$k_{s_1} > k_{s_2}$	$k_{s_2} > k_{s_3}$
Ring A-F	A-B-C	1.046	1.005	1.002	4.324%		'1'	'1'
	B-C-D	1.005	1.002	1.002	0.3%	↓↓	'1'	'0'
	C-D-E	1.002	1.002	1.086	8.16%		'0'	'0'
	D-E-F	1.002	1.086	11.088	8.12%		'0'	'0'
Radial B-I	B-G-H	1.005	1	1	0.5%	→	'1'	'0'
Radial D-I	D-C-G	1.002	1.002	1	0.2%	↓	'1'	'1'
	C-G-H	1.002	1	1	0.2%	→	'1'	'0'
B-I & D-I	G-H-I	1	1	1	0%		'0'	'0'

Table C.52: Ring topology / Phase to phase (60 Ω) fault / F_1.

Circuit	3-points window	k_{s_1}	k_{s_2}	k_{s_3}	$\lvert\Delta k_{s_{13}}\%\rvert$	FS search	$k_{s_1} > k_{s_2}$	$k_{s_2} > k_{s_3}$
Ring A-F	A-B-C	6.512	6.366	6.353	2.48%		'1'	'1'
	B-C-D	6.366	6.353	6.356	0.16%	↓↓	'1'	'0'
	C-D-E	6.353	6.356	6.659	4.74%		'0'	'0'
	D-E-F	6.356	6.659	6.67	4.74%		'0'	'0'
Radial B-I	B-G-H	6.366	6.346	6.346	0.31%	→	'1'	'0'
Radial D-I	D-C-G	6.356	6.353	6.346	0.16%	↓	'1'	'1'
	C-G-H	6.353	6.346	6.346	0.11%	→	'1'	'0'
B-I & D-I	G-H-I	6.346	6.346	6.346	0%		'0'	'0'

Table C.53: Ring topology / Phase to ground (0 Ω) fault / F_2.

Circuit	3-points window	k_{s_1}	k_{s_2}	k_{s_3}	$\lvert\Delta k_{s_{13}}\%\rvert$	FS search	$k_{s_1} > k_{s_2}$	$k_{s_2} > k_{s_3}$
Ring A-F	A-B-C	2.95	2.912	2.889	2.19%		'1'	'1'
	B-C-D	2.912	2.889	2.882	1.04%		'1'	'1'
	C-D-E	2.889	2.882	2.955	2.27%	→	'1'	'0'
	D-E-F	2.882	2.955	2.98	3.33%		'0'	'0'

Table C.54: Ring topology / Phase to ground (20 Ω) fault / F_2.

Circuit	3-points window	k_{s_1}	k_{s_2}	k_{s_3}	$\lvert\Delta k_{s_{13}}\%\rvert$	FS search	$k_{s_1} > k_{s_2}$	$k_{s_2} > k_{s_3}$
Ring A-F	A-B-C	9.122	9.021	8.966	1.73%		'1'	'1'
	B-C-D	9.021	8.966	8.953	0.76%		'1'	'1'
	C-D-E	8.966	8.953	9.135	1.87%	→	'1'	'0'
	D-E-F	8.953	9.135	9.19	2.61%		'0'	'0'

Table C.55: Ring topology / Phase to phase (0 Ω) fault / F_2.

Circuit	3-points window	k_{s_1}	k_{s_2}	k_{s_3}	$\lvert\Delta k_{s_{13}}\%\rvert$	FS search	$k_{s_1} > k_{s_2}$	$k_{s_2} > k_{s_3}$
Ring A-F	A-B-C	1.196	1.173	1.161	2.97%		'1'	'1'
	B-C-D	1.173	1.161	1.159	1.2%		'1'	'1'
	C-D-E	1.161	1.159	1.2	3.32%	→	'1'	'0'
	D-E-F	1.159	1.2	1.212	4.45%		'0'	'0'

Table C.56: Ring topology / Phase to phase (60 Ω) fault / F_2.

Circuit	3-points window	k_{s_1}	k_{s_2}	k_{s_3}	$\lvert\Delta k_{s_{13}}\%\rvert$	FS search	$k_{s_1} > k_{s_2}$	$k_{s_2} > k_{s_3}$
Ring A-F	A-B-C	6.676	6.599	6.558	2.97%		'1'	'1'
	B-C-D	6.599	6.558	6.547	0.79%		'1'	'1'
	C-D-E	6.558	6.547	6.685	1.93%	→	'1'	'0'
	D-E-F	6.547	6.685	6.728	2.72%		'0'	'0'

Table C.57: Ring topology / Phase to ground (0 Ω) fault / F_3.

Circuit	3-points window	k_{s_1}	k_{s_2}	k_{s_3}	$\lvert\Delta k_{s_{13}}\%\rvert$	FS search	$k_{s_1} > k_{s_2}$	$k_{s_2} > k_{s_3}$
Ring A-F	A-B-C	2.716	2.713	2.712	0.15%		'1'	'1'
	B-C-D	2.713	2.712	2.711	0.07%		'1'	'1'
	C-D-E	2.712	2.711	2.663	1.82%		'1'	'1'
	D-E-F	2.711	2.663	2.69	0.78%	→	'1'	'0'

Table C.58: Ring topology / Phase to ground (20 Ω) fault / F_3.

Circuit	3-points window	k_{s_1}	k_{s_2}	k_{s_3}	$\lvert\Delta k_{s_{13}}\%\rvert$	FS search	$k_{s_1} > k_{s_2}$	$k_{s_2} > k_{s_3}$
Ring A-F	A-B-C	8.995	8.987	8.984	0.12%		'1'	'1'
	B-C-D	8.987	8.9843	8.9839	0.03%		'1'	'1'
	C-D-E	8.9843	8.9839	8.866	1.32%		'1'	'1'
	D-E-F	8.9839	8.866	8.931	0.59%	→	'1'	'0'

Table C.59: Ring topology / Phase to phase (0 Ω) fault / F_3.

Circuit	3-points window	k_{s_1}	k_{s_2}	k_{s_3}	$\lvert\Delta k_{s_{13}}\%\rvert$	FS search	$k_{s_1} > k_{s_2}$	$k_{s_2} > k_{s_3}$
Ring A-F	A-B-C	1.025	1.024	1.023	0.2%		'1'	'1'
	B-C-D	1.024	1.023	1.0233	0.07%		'1'	'1'
	C-D-E	1.023	1.0233	1	2.29%		'1'	'1'
	D-E-F	1.0233	1	1.013	0.99%	→	'1'	'0'

Table C.60: Ring topology / Phase to phase (60 Ω) fault / F_3.

Circuit	3-points window	k_{s_1}	k_{s_2}	k_{s_3}	$\lvert\Delta k_{s_{13}}\%\rvert$	FS search	$k_{s_1} > k_{s_2}$	$k_{s_2} > k_{s_3}$
Ring A-F	A-B-C	6.594	6.588	6.586	0.12%		'1'	'1'
	B-C-D	6.588	6.586	6.585	0.05%		'1'	'1'
	C-D-E	6.586	6.585	6.494	1.4%		'1'	'1'
	D-E-F	6.585	6.494	6.544	0.63%	→	'1'	'0'

Table C.61: Ring topology / Phase to ground (0 Ω) fault / F_4.

Circuit	3-points window	k_{s_1}	k_{s_2}	k_{s_3}	$\lvert\Delta k_{s_{13}}\%\rvert$	FS search	$k_{s_1} > k_{s_2}$	$k_{s_2} > k_{s_3}$
Ring A-F	A-B-C	2.744	2.669	2.662	3.05%		'1'	'1'
	B-C-D	2.669	2.662	2.663	0.23%	↓↓	'1'	'0'
	C-D-E	2.662	2.663	2.82	5.82%		'0'	'0'
	D-E-F	2.663	2.82	2.825	5.85%		'0'	'0'
Radial B-I	B-G-H	2.669	2.65	2.65	0.72%	→	'1'	'0'
Radial D-I	D-C-G	2.663	2.662	2.65	0.489%	↓	'1'	'1'
	C-G-H	2.662	2.65	2.65	0.452%	→	'1'	'0'
B-I & D-I	G-H-I	2.65	2.65	2.65	0%		'0'	'0'

Table C.62: Ring topology / Phase to ground (20 Ω) fault / F_4.

Circuit	3-points window	k_{s_1}	k_{s_2}	k_{s_3}	$\lvert\Delta k_{s_{13}}\%\rvert$	FS search	$k_{s_1} > k_{s_2}$	$k_{s_2} > k_{s_3}$
Ring A-F	A-B-C	8.901	8.709	8.693	2.37%		'1'	'1'
	B-C-D	8.709	8.693	8.695	0.16%	↓↓	'1'	'0'
	C-D-E	8.693	8.695	9.094	4.54%		'0'	'0'
	D-E-F	8.695	9.094	9.105	4.57%		'0'	'0'
Radial B-I	B-G-H	8.709	8.663	8.663	0.53%	→	'1'	'0'
Radial D-I	D-C-G	8.695	8.693	8.663	0.369%	↓	'1'	'1'
	C-G-H	8.693	8.663	8.663	0.346%	→	'1'	'0'
B-I & D-I	G-H-I	8.663	8.663	8.663	0%		'0'	'0'

Table C.63: Ring topology / Phase to phase (0 Ω) fault / F_4.

Circuit	3-points window	k_{s_1}	k_{s_2}	k_{s_3}	$\lvert\Delta k_{s_{13}}\%\rvert$	FS search	$k_{s_1} > k_{s_2}$	$k_{s_2} > k_{s_3}$
Ring A-F	A-B-C	1.05	1.009	1.006	4.31%		'1'	'1'
	B-C-D	1.009	1.006	1.007	0.2%	↓↓	'1'	'0'
	C-D-E	1.006	1.007	1.091	8.22%		'0'	'0'
	D-E-F	1.007	1.091	1.093	8.09%		'0'	'0'
Radial B-I	B-G-H	1.009	1	1	0.9%	→	'1'	'0'
Radial D-I	D-C-G	1.007	1.006	1	0.7%	↓	'1'	'1'
	C-G-H	1.006	1	1	0.6%	→	'1'	'0'
B-I & D-I	G-H-I	1	1	1	0%		'0'	'0'

Table C.64: Ring topology / Phase to phase (60 Ω) fault / F_4.

Circuit	3-points window	k_{s_1}	k_{s_2}	k_{s_3}	$\lvert\Delta k_{s_{13}}\%\rvert$	FS search	$k_{s_1} > k_{s_2}$	$k_{s_2} > k_{s_3}$
Ring A-F	A-B-C	6.516	6.37	6.358	2.46%		'1'	'1'
	B-C-D	6.37	6.358	6.36	0.16%	↓↓	'1'	'0'
	C-D-E	6.358	6.36	6.663	4.72%		'0'	'0'
	D-E-F	6.36	6.663	6.671	4.74%		'0'	'0'
Radial B-I	B-G-H	6.37	6.335	6.335	0.55%	→	'1'	'0'
Radial D-I	D-C-G	6.36	6.358	6.335	0.39%	↓	'1'	'1'
	C-G-H	6.358	6.335	6.335	0.36%	→	'1'	'0'
B-I & D-I	G-H-I	6.635	6.635	6.635	0%		'0'	'0'

Table C.65: Ring topology / Phase to ground (0 Ω) fault / F_5.

Circuit	3-points window	k_{s_1}	k_{s_2}	k_{s_3}	$\lvert\Delta k_{s_{13}}\%\rvert$	FS search	$k_{s_1} > k_{s_2}$	$k_{s_2} > k_{s_3}$
Ring A-F	A-B-C	3.263	3.176	3.168	2.97%		'1'	'1'
	B-C-D	3.176	3.168	3.17	0.19%	↓↓	'1'	'0'
	C-D-E	3.168	3.17	3.35	5.64%		'0'	'0'
	D-E-F	3.17	3.35	3.355	5.62%		'0'	'0'
Radial B-I	B-G-H	3.176	3.155	2.545	21.33%	↓	'1'	'1'
Radial D-I	D-C-G	3.17	3.168	3.155	0.474%	↓	'1'	'1'
	C-G-H	3.168	3.155	2.545	21.076%	↓	'1'	'1'
B-I & D-I	G-H-I	3.155	2.545	2.545	22.2%	→→	'1'	'0'

Table C.66: Ring topology / Phase to ground (20 Ω) fault / F_5.

Circuit	3-points window	k_{s_1}	k_{s_2}	k_{s_3}	$\lvert\Delta k_{s_{13}}\%\rvert$	FS search	$k_{s_1} > k_{s_2}$	$k_{s_2} > k_{s_3}$
Ring A-F	A-B-C	9.328	9.126	9.109	2.38%		'1'	'1'
	B-C-D	9.126	9.109	9.112	0.15%	↓↓	'1'	'0'
	C-D-E	9.109	9.112	9.53	4.55%		'0'	'0'
	D-E-F	9.112	9.53	9.541	4.57%		'0'	'0'
Radial B-I	B-G-H	9.126	9.078	7.626	17.42%	↓	'1'	'1'
Radial D-I	D-C-G	9.112	9.109	9.078	0.374%	↓	'1'	'1'
	C-G-H	9.109	9.078	7.626	17.236%	↓	'1'	'1'
B-I & D-I	G-H-I	9.078	7.626	7.626	17.9%	→→	'1'	'0'

Table C.67: Ring topology / Phase to phase (0 Ω) fault / F_5.

Circuit	3-points window	k_{s_1}	k_{s_2}	k_{s_3}	$\lvert\Delta k_{s_{13}}\%\rvert$	FS search	$k_{s_1} > k_{s_2}$	$k_{s_2} > k_{s_3}$
Ring A-F	A-B-C	1.413	1.364	1.36	3.84%	↓↓	'1'	'1'
	B-C-D	1.364	1.36	1.36	0.29%		'1'	'0'
	C-D-E	1.36	1.36	1.462	7.32%		'0'	'0'
	D-E-F	1.36	1.462	1.465	7.35%		'0'	'0'
Radial B-I	B-G-H	1.364	1.352	1	29.39%	↓	'1'	'1'
Radial D-I	D-C-G	1.36	1.36	1.352	0.59%	↓	'1'	'1'
	C-G-H	1.36	1.352	1	29.09%	↓	'1'	'1'
B-I & D-I	G-H-I	1.352	1	1	31.5%	→ →	'1'	'0'

Table C.68: Ring topology / Phase to phase (60 Ω) fault / F_5.

Circuit	3-points window	k_{s_1}	k_{s_2}	k_{s_3}	$\lvert\Delta k_{s_{13}}\%\rvert$	FS search	$k_{s_1} > k_{s_2}$	$k_{s_2} > k_{s_3}$
Ring A-F	A-B-C	6.814	6.661	6.648	2.47%	↓↓	'1'	'1'
	B-C-D	6.661	6.648	6.65	0.17%		'1'	'0'
	C-D-E	6.648	6.65	6.967	4.72%		'0'	'0'
	D-E-F	6.65	6.967	6.975	4.73%		'0'	'0'
Radial B-I	B-G-H	6.661	6.624	5.51	18.02%	↓	'1'	'1'
Radial D-I	D-C-G	6.648	6.624	6.624	0.39%	↓	'1'	'1'
	C-G-H	6.648	6.624	5.531	17.82%	↓	'1'	'1'
B-I & D-I	G-H-I	6.624	5.531	5.531	18.54%	→ →	'1'	'0'

Table C.69: Ring topology / Phase to ground (0 Ω) fault / F_6.

Circuit	3-points window	k_{s_1}	k_{s_2}	k_{s_3}	$\lvert\Delta k_{s_{13}}\%\rvert$	FS search	$k_{s_1} > k_{s_2}$	$k_{s_2} > k_{s_3}$
Ring A-F	A-B-C	3.278	3.191	3.18	2.95%	↓↓	'1'	'1'
	B-C-D	3.191	3.183	3.184	0.22%		'1'	'0'
	C-D-E	3.183	3.184	3.365	5.61%		'0'	'0'
	D-E-F	3.184	3.365	3.37	5.63%		'0'	'0'
Radial B-I	B-G-H	3.191	3.169	2.557	21.33%	↓	'1'	'1'
Radial D-I	D-C-G	3.184	3.183	3.169	0.472%	↓	'1'	'1'
	C-G-H	3.183	3.169	2.557	21.08%	↓	'1'	'1'
B-I & D-I	G-H-I	3.169	2.557	2.544	22.67%	→ →	'1'	'1'

Table C.70: Ring topology / Phase to ground (20 Ω) fault / F_6.

Circuit	3-points window	k_{s_1}	k_{s_2}	k_{s_3}	$\lvert\Delta k_{s_{13}}\%\rvert$	FS search	$k_{s_1} > k_{s_2}$	$k_{s_2} > k_{s_3}$
Ring A-F	A-B-C	9.34	9.138	9.121	2.38%	↓↓	'1'	'1'
	B-C-D	9.138	9.121	9.124	0.15%		'1'	'0'
	C-D-E	9.121	9.124	9.543	4.56%		'0'	'0'
	D-E-F	9.124	9.543	9.553	4.56%		'0'	'0'
Radial B-I	B-G-H	9.138	9.09	7.636	17.42%	↓	'1'	'1'
Radial D-I	D-C-G	9.124	9.121	9.09	0.373%	↓	'1'	'1'
	C-G-H	9.121	9.09	7.636	17.236%	↓	'1'	'1'
B-I & D-I	G-H-I	9.09	7.636	7.603	18.34%	→→	'1'	'1'

Table C.71: Ring topology / Phase to phase (0 Ω) fault / F_6.

Circuit	3-points window	k_{s_1}	k_{s_2}	k_{s_3}	$\lvert\Delta k_{s_{13}}\%\rvert$	FS search	$k_{s_1} > k_{s_2}$	$k_{s_2} > k_{s_3}$
Ring A-F	A-B-C	1.422	1.373	1.369	3.82%	↓↓	'1'	'1'
	B-C-D	1.373	1.369	1.37	0.22%		'1'	'0'
	C-D-E	1.369	1.37	1.472	7.34%		'0'	'0'
	D-E-F	1.37	1.472	1.475	7.35%		'0'	'0'
Radial B-I	B-G-H	1.364	1.352	1	29.39%	↓	'1'	'1'
Radial D-I	D-C-G	1.37	1.369	1.361	0.66%	↓	'1'	'1'
	C-G-H	1.369	1.361	1.008	28.97%	↓	'1'	'1'
B-I & D-I	G-H-I	1.361	1.008	1	32.15%	→→	'1'	'1'

Table C.72: Ring topology / Phase to phase (60 Ω) fault / F_6.

Circuit	3-points window	k_{s_1}	k_{s_2}	k_{s_3}	$\lvert\Delta k_{s_{13}}\%\rvert$	FS search	$k_{s_1} > k_{s_2}$	$k_{s_2} > k_{s_3}$
Ring A-F	A-B-C	6.822	6.669	6.656	2.47%	↓↓	'1'	'1'
	B-C-D	6.669	6.656	6.658	0.17%		'1'	'0'
	C-D-E	6.656	6.658	6.976	4.73%		'0'	'0'
	D-E-F	6.658	6.976	6.984	4.74%		'0'	'0'
Radial B-I	B-G-H	6.669	6.632	5.538	18.01%	↓	'1'	'1'
Radial D-I	D-C-G	6.658	6.656	6.632	0.39%	↓	'1'	'1'
	C-G-H	6.656	6.632	5.538	17.82%	↓	'1'	'1'
B-I & D-I	G-H-I	6.632	5.538	5.513	18.98%	→→	'1'	'1'

C.3 Network loads

C.3.1 1% Load unbalance

Table C.73: Radial topology / Phase to ground (0 Ω) fault / F_1.

Circuit	3-points window	k_{s_1}	k_{s_2}	k_{s_3}	$\Delta k_{s_{13}}\%$	FS search	$k_{s_1} > k_{s_2}$	$k_{s_2} > k_{s_3}$
Radial A-I	A-B-G	2.757	2.67	2.651	3.93%	↓↓	'1'	'1'
	B-G-H	2.67	2.651	2.656	0.5%	→	'1'	'0'
	G-H-I	2.651	2.656	2.656	0.21%		'0'	'0'
Radial A-F	A-B-C	2.757	2.67	2.648	4.044%	↓↓	'1'	'1'
	B-C-D	2.67	2.648	2.656	0.52%	→	'1'	'0'
	C-D-E	2.648	2.656	2.683	1.33%		'0'	'0'
	D-E-F	2.656	2.683	2.635	0.78%		'0'	'1'

Table C.74: Radial topology / Phase to ground (20 Ω) fault / F_1.

Circuit	3-points window	k_{s_1}	k_{s_2}	k_{s_3}	$\Delta k_{s_{13}}\%$	FS search	$k_{s_1} > k_{s_2}$	$k_{s_2} > k_{s_3}$
Radial A-I	A-B-G	8.922	8.708	8.675	2.81%	↓↓	'1'	'1'
	B-G-H	8.708	8.675	8.675	0.38%	→	'1'	'0'
	G-H-I	8.675	8.675	8.675	0%		'0'	'0'
Radial A-F	A-B-C	8.922	8.708	8.611	3.56%	↓↓	'1'	'1'
	B-C-D	8.708	8.611	8.733	0.285%	→	'1'	'0'
	C-D-E	8.611	8.733	8.86	2.86%		'0'	'0'
	D-E-F	8.733	8.86	8.618	1.32%		'0'	'1'

Table C.75: Radial topology / Phase to phase (0 Ω) fault / F_1.

Circuit	3-points window	k_{s_1}	k_{s_2}	k_{s_3}	$\Delta k_{s_{13}}\%$	FS search	$k_{s_1} > k_{s_2}$	$k_{s_2} > k_{s_3}$
Radial A-I	A-B-G	1.052	1.006	1	5.1%	↓↓	'1'	'1'
	B-G-H	1.006	1	1	0.58%	→	'1'	'0'
	G-H-I	1	1	1	0%		'0'	'0'
Radial A-F	A-B-C	1.052	1.006	1.002	4.8%	↓↓	'1'	'1'
	B-C-D	1.006	1.002	0.997	0.85%	↓	'1'	'1'
	C-D-E	1.002	0.997	0.99	1.26%	↓	'1'	'1'
	D-E-F	0.997	0.99	1.002	0.475%	→	'1'	'0'

Table C.76: Radial topology / Phase to phase (60 Ω) fault / F_1.

Circuit	3-points window	k_{s_1}	k_{s_2}	k_{s_3}	$\Delta k_{s_{13}}\%$	FS search	$k_{s_1} > k_{s_2}$	$k_{s_2} > k_{s_3}$
Radial A-I	A-B-G	6.514	6.341	6.26	3.98%	↓↓	'1'	'1'
	B-G-H	6.341	6.26	6.311	0.47%	→	'1'	'0'
	G-H-I	6.26	6.311	6.311	0%		'0'	'0'
Radial A-F	A-B-C	6.514	6.341	6.296	3.41%	↓↓	'1'	'1'
	B-C-D	6.341	6.296	6.249	1.46%	↓	'1'	'1'
	C-D-E	6.296	6.249	6.288	0.14%	→	'1'	'0'
	D-E-F	6.249	6.288	6.19	0.94%		'0'	'1'

Table C.77: Radial topology / Phase to ground (0 Ω) fault / F_2.

Circuit	3-points window	k_{s_1}	k_{s_2}	k_{s_3}	$\Delta k_{s_{13}}\%$	FS search	$k_{s_1} > k_{s_2}$	$k_{s_2} > k_{s_3}$
Radial A-I	A-B-G	3.348	3.246	3.222	3.86%		'1'	'1'
	B-G-H	3.246	3.222	3.231	0.49%		'1'	'0'
	G-H-I	3.222	3.231	3.231	0.28%		'0'	'0'
Radial A-F	A-B-C	3.348	3.246	3.178	4.62%		'1'	'1'
	B-C-D	3.246	3.178	3.172	2.33%		'1'	'1'
	C-D-E	3.178	3.172	2.575	20.07%		'1'	'1'
	D-E-F	3.172	2.575	2.575	21.53%	→	'1'	'0'

Table C.78: Radial topology / Phase to ground (20 Ω) fault / F_2.

Circuit	3-points window	k_{s_1}	k_{s_2}	k_{s_3}	$\Delta k_{s_{13}}\%$	FS search	$k_{s_1} > k_{s_2}$	$k_{s_2} > k_{s_3}$
Radial A-I	A-B-G	9.41	9.185	9.192	2.356%		'1'	'0'
	B-G-H	9.185	9.192	9.149	0.39%		'0'	'1'
	G-H-I	9.192	9.149	9.149	0.46%		'1'	'0'
Radial A-F	A-B-C	9.41	9.185	8.985	4.62%		'1'	'1'
	B-C-D	9.185	8.985	8.822	4.03%		'1'	'1'
	C-D-E	8.985	8.822	7.721	14.85%		'1'	'1'
	D-E-F	8.822	7.721	7.721	13.61%	→	'1'	'0'

Table C.79: Radial topology / Phase to phase (0 Ω) fault / F_2.

Circuit	3-points window	k_{s_1}	k_{s_2}	k_{s_3}	$\Delta k_{s_{13}}\%$	FS search	$k_{s_1} > k_{s_2}$	$k_{s_2} > k_{s_3}$
Radial A-I	A-B-G	1.449	1.392	1.383	4.68%		'1'	'1'
	B-G-H	1.392	1.383	1.384	0.54%		'1'	'0'
	G-H-I	1.383	1.384	1.384	0.112%		'0'	'0'
Radial A-F	A-B-C	1.449	1.392	1.365	5.94%		'1'	'1'
	B-C-D	1.392	1.365	1.35	3.04%		'1'	'1'
	C-D-E	1.365	1.35	0.99	30.38%		'1'	'1'
	D-E-F	1.35	0.99	1.002	31.24%	→	'1'	'0'

Table C.80: Radial topology / Phase to phase (60 Ω) fault / F_2.

Circuit	3-points window	k_{s_1}	k_{s_2}	k_{s_3}	$\Delta k_{s_{13}}\%$	FS search	$k_{s_1} > k_{s_2}$	$k_{s_2} > k_{s_3}$
Radial A-I	A-B-G	6.852	6.67	6.581	4.04%		'1'	'1'
	B-G-H	6.67	6.581	6.638	0.47%		'1'	'0'
	G-H-I	6.581	6.638	6.638	0.86%		'0'	'0'
Radial A-F	A-B-C	6.852	6.67	6.555	4.43%		'1'	'1'
	B-C-D	6.67	6.555	6.474	2.98%		'1'	'1'
	C-D-E	6.555	6.474	5.417	18.51%		'1'	'1'
	D-E-F	6.474	5.417	5.417	18.32%	→	'1'	'0'

Table C.81: Radial topology / Phase to ground (0 Ω) fault / F_3.

Circuit	3-points window	k_{s_1}	k_{s_2}	k_{s_3}	$\Delta k_{s_{13}}\%$	FS search	$k_{s_1} > k_{s_2}$	$k_{s_2} > k_{s_3}$
Radial A-I	A-B-G	3.923	3.808	3.777	3.82%		'1'	'1'
	B-G-H	3.808	3.777	3.79	0.48%		'1'	'0'
	G-H-I	3.777	3.79	3.79	0.34%		'0'	'1'
Radial A-F	A-B-C	3.923	3.808	3.729	5.08%		'1'	'1'
	B-C-D	3.808	3.729	3.722	2.29%		'1'	'1'
	C-D-E	3.729	3.722	2.502	36.98%		'1'	'1'
	D-E-F	3.722	2.502	2.456	43.76%	→	'1'	'1'

Table C.82: Radial topology / Phase to ground (20 Ω) fault / F_3.

Circuit	3-points window	k_{s_1}	k_{s_2}	k_{s_3}	$\Delta k_{s_{13}}\%$	FS search	$k_{s_1} > k_{s_2}$	$k_{s_2} > k_{s_3}$
Radial A-I	A-B-G	9.88	9.644	9.645	2.413%		'1'	'0'
	B-G-H	9.644	9.645	9.606	0.397%		'0'	'1'
	G-H-I	9.645	9.606	9.606	0.41%		'1'	'0'
Radial A-F	A-B-C	9.88	9.644	9.428	4.68%		'1'	'1'
	B-C-D	9.644	9.428	9.324	3.384%		'1'	'1'
	C-D-E	9.428	9.324	6.912	29.4%		'1'	'1'
	D-E-F	9.324	6.912	6.716	34.09%	→	'1'	'1'

Table C.83: Radial topology / Phase to phase (0 Ω) fault / F_3.

Circuit	3-points window	k_{s_1}	k_{s_2}	k_{s_3}	$\Delta k_{s_{13}}\%$	FS search	$k_{s_1} > k_{s_2}$	$k_{s_2} > k_{s_3}$
Radial A-I	A-B-G	1.844	1.777	1.765	4.37%		'1'	'1'
	B-G-H	1.777	1.765	1.768	0.51%		'1'	'0'
	G-H-I	1.765	1.768	1.768	0.163%		'0'	'0'
Radial A-F	A-B-C	1.844	1.777	1.746	5.46%		'1'	'1'
	B-C-D	1.777	1.746	1.726	2.93%		'1'	'1'
	C-D-E	1.746	1.726	0.995	50.42%		'1'	'1'
	D-E-F	1.726	0.995	0.99	59.49%	→	'1'	'1'

Table C.84: Radial topology / Phase to phase (60 Ω) fault / F_3.

Circuit	3-points window	k_{s_1}	k_{s_2}	k_{s_3}	$\Delta k_{s_{13}}\%$	FS search	$k_{s_1} > k_{s_2}$	$k_{s_2} > k_{s_3}$
Radial A-I	A-B-G	7.175	6.984	6.866	3.98%		'1'	'1'
	B-G-H	6.984	6.889	6.951	0.48%		'1'	'0'
	G-H-I	6.889	6.951	6.951	0.9%		'0'	'0'
Radial A-F	A-B-C	7.175	6.984	6.866	4.43%		'1'	'1'
	B-C-D	6.984	6.866	6.774	3.06%		'1'	'1'
	C-D-E	6.866	6.774	4.809	33.46%		'1'	'1'
	D-E-F	6.774	4.809	4.764	36.88%	→	'1'	'1'

Table C.85: Radial topology / Phase to ground (0 Ω) fault / F_4.

Circuit	3-points window	k_{s_1}	k_{s_2}	k_{s_3}	$\Delta k_{s_{13}}$%	FS search	$k_{s_1} > k_{s_2}$	$k_{s_2} > k_{s_3}$
Radial A-I	A-B-G	2.764	2.677	2.655	4.22%	↓↓	'1'	'1'
	B-G-H	2.677	2.65	2.656	0.8%	→	'1'	'0'
	G-H-I	2.65	2.656	2.656	0.214%		'0'	'1'
Radial A-F	A-B-C	2.764	2.677	2.655	4.04%	↓↓	'1'	'1'
	B-C-D	2.677	2.655	2.663	0.52%	→	'1'	'0'
	C-D-E	2.655	2.663	2.69	1.33%		'0'	'0'
	D-E-F	2.663	2.69	2.642	0.79%		'0'	'1'

Table C.86: Radial topology / Phase to ground (20 Ω) fault / F_4.

Circuit	3-points window	k_{s_1}	k_{s_2}	k_{s_3}	$\Delta k_{s_{13}}$%	FS search	$k_{s_1} > k_{s_2}$	$k_{s_2} > k_{s_3}$
Radial A-I	A-B-G	8.928	8.715	8.706	2.53%	↓↓	'1'	'1'
	B-G-H	8.715	8.706	8.661	0.616%	↓	'1'	'1'
	G-H-I	8.706	8.661	8.661	0.52%	→	'1'	'0'
Radial A-F	A-B-C	8.928	8.715	8.617	3.56%	↓↓	'1'	'1'
	B-C-D	8.715	8.617	8.739	0.284%	→	'1'	'0'
	C-D-E	8.617	8.739	8.867	2.86%		'0'	'0'
	D-E-F	8.739	8.867	8.624	1.32%		'0'	'1'

Table C.87: Radial topology / Phase to phase (0 Ω) fault / F_4.

Circuit	3-points window	k_{s_1}	k_{s_2}	k_{s_3}	$\Delta k_{s_{13}}$%	FS search	$k_{s_1} > k_{s_2}$	$k_{s_2} > k_{s_3}$
Radial A-I	A-B-G	1.056	1.01	1	5.51%	↓↓	'1'	'1'
	B-G-H	1.01	1	1	0.99%	→	'1'	'0'
	G-H-I	1	1	1	0%		'0'	'0'
Radial A-F	A-B-C	1.056	1.01	1.007	4.81%	↓↓	'1'	'1'
	B-C-D	1.01	1.007	1.001	0.86%	↓	'1'	'1'
	C-D-E	1.007	1.001	0.994	1.26%	↓	'1'	'1'
	D-E-F	1.001	0.994	1.006	0.47%	→	'1'	'0'

Table C.88: Radial topology / Phase to phase (60 Ω) fault / F_4.

Circuit	3-points window	k_{s_1}	k_{s_2}	k_{s_3}	$\Delta k_{s_{13}}\%$	FS search	$k_{s_1} > k_{s_2}$	$k_{s_2} > k_{s_3}$
Radial A-I	A-B-G	6.518	6.345	6.249	4.22%	↓↓	'1'	'1'
	B-G-H	6.345	6.249	6.3	0.71%	→	'1'	'0'
	G-H-I	6.249	6.3	6.3	0.81%		'0'	'0'
Radial A-F	A-B-C	6.518	6.345	6.3	3.41%	↓↓	'1'	'1'
	B-C-D	6.345	6.3	6.253	1.46%	↓	'1'	'1'
	C-D-E	6.3	6.253	6.292	0.14%	→	'1'	'0'
	D-E-F	6.253	6.292	6.195	0.94%		'0'	'1'

Table C.89: Radial topology / Phase to ground (0 Ω) fault / F_5.

Circuit	3-points window	k_{s_1}	k_{s_2}	k_{s_3}	$\Delta k_{s_{13}}\%$	FS search	$k_{s_1} > k_{s_2}$	$k_{s_2} > k_{s_3}$
Radial A-I	A-B-G	3.283	3.183	3.149	4.16%		'1'	'1'
	B-G-H	3.183	3.149	2.549	21.41%		'1'	'1'
	G-H-I	3.149	2.549	2.549	21.84%	→	'1'	'0'
Radial A-F	A-B-C	3.283	3.183	3.156	3.95%		'1'	'1'
	B-C-D	3.183	3.156	3.165	0.57%		'1'	'0'
	C-D-E	3.156	3.165	3.2	1.4%		'0'	'0'
	D-E-F	3.165	3.2	3.137	0.88%		'0'	'1'

Table C.90: Radial topology / Phase to ground (20 Ω) fault / F_5.

Circuit	3-points window	k_{s_1}	k_{s_2}	k_{s_3}	$\Delta k_{s_{13}}\%$	FS search	$k_{s_1} > k_{s_2}$	$k_{s_2} > k_{s_3}$
Radial A-I	A-B-G	9.355	9.131	9.117	2.6%		'1'	'1'
	B-G-H	9.131	9.117	7.621	17.52%		'1'	'1'
	G-H-I	9.117	7.621	7.621	18.43%	→	'1'	'0'
Radial A-F	A-B-C	9.355	9.131	9.023	3.62%		'1'	'1'
	B-C-D	9.131	9.023	9.15	0.205%		'1'	'0'
	C-D-E	9.023	9.15	9.309	3.12%		'0'	'0'
	D-E-F	9.15	9.309	9.031	1.3%		'0'	'1'

Table C.91: Radial topology / Phase to phase (0 Ω) fault / F_5.

Circuit	3-points window	k_{s_1}	k_{s_2}	k_{s_3}	$\Delta k_{s_{13}}\%$	FS search	$k_{s_1} > k_{s_2}$	$k_{s_2} > k_{s_3}$
Radial A-I	A-B-G	1.419	1.363	1.35	5.05%		'1'	'1'
	B-G-H	1.363	1.35	1	29.36%		'1'	'1'
	G-H-I	1.35	1	1	31.32%	→	'1'	'0'
Radial A-F	A-B-C	1.419	1.363	1.359	4.35%		'1'	'1'
	B-C-D	1.363	1.359	1.351	0.9%		'1'	'1'
	C-D-E	1.359	1.351	1.341	1.33%		'1'	'1'
	D-E-F	1.351	1.341	1.357	0.41%		'1'	'0'

Table C.92: Radial topology / Phase to phase (60 Ω) fault / F_5.

Circuit	3-points window	k_{s_1}	k_{s_2}	k_{s_3}	$\Delta k_{s_{13}}\%$	FS search	$k_{s_1} > k_{s_2}$	$k_{s_2} > k_{s_3}$
Radial A-I	A-B-G	6.814	6.633	6.53	4.27%		'1'	'1'
	B-G-H	6.633	6.53	5.502	18.17%		'1'	'1'
	G-H-I	6.53	5.502	5.502	17.59%	→	'1'	'0'
Radial A-F	A-B-C	6.814	6.633	6.588	3.39%		'1'	'1'
	B-C-D	6.633	6.588	6.531	1.55%		'1'	'1'
	C-D-E	6.588	6.531	6.565	0.35%		'1'	'0'
	D-E-F	6.531	6.565	6.471	0.91%		'0'	'1'

Table C.93: Radial topology / Phase to ground (0 Ω) fault / F_6.

Circuit	3-points window	k_{s_1}	k_{s_2}	k_{s_3}	$\Delta k_{s_{13}}\%$	FS search	$k_{s_1} > k_{s_2}$	$k_{s_2} > k_{s_3}$
Radial A-I	A-B-G	3.298	3.197	3.164	4.15%		'1'	'1'
	B-G-H	3.197	3.164	2.561	21.39%		'1'	'1'
	G-H-I	3.164	2.561	2.547	22.36%	→	'1'	'1'
Radial A-F	A-B-C	3.298	3.197	3.170	3.95%		'1'	'1'
	B-C-D	3.197	3.170	3.179	0.57%		'1'	'0'
	C-D-E	3.170	3.179	3.215	1.4%		'0'	'0'
	D-E-F	3.179	3.215	3.151	0.88%		'0'	'1'

Table C.94: Radial topology / Phase to ground (20 Ω) fault / F_6.

Circuit	3-points window	k_{s_1}	k_{s_2}	k_{s_3}	$\Delta k_{s_{13}}\%$	FS search	$k_{s_1} > k_{s_2}$	$k_{s_2} > k_{s_3}$
Radial A-I	A-B-G	9.367	9.144	9.129	2.59%		'1'	'1'
	B-G-H	9.144	9.129	7.631	17.522%		'1'	'1'
	G-H-I	9.129	7.631	7.598	18.85%	→	'1'	'1'
Radial A-F	A-B-C	9.367	9.144	9.035	3.62%		'1'	'1'
	B-C-D	9.144	9.035	9.162	0.203%		'1'	'0'
	C-D-E	9.035	9.162	9.322	3.12%		'0'	'0'
	D-E-F	9.162	9.322	9.043	1.29%		'0'	'1'

Table C.95: Radial topology / Phase to phase (0 Ω) fault / F_6.

Circuit	3-points window	k_{s_1}	k_{s_2}	k_{s_3}	$\Delta k_{s_{13}}\%$	FS search	$k_{s_1} > k_{s_2}$	$k_{s_2} > k_{s_3}$
Radial A-I	A-B-G	1.429	1.373	1.359	5.05%		'1'	'1'
	B-G-H	1.373	1.359	1.008	29.29%		'1'	'1'
	G-H-I	1.359	1.008	1	31.98%	→	'1'	'1'
Radial A-F	A-B-C	1.429	1.373	1.369	4.34%		'1'	'1'
	B-C-D	1.373	1.369	1.36	0.9%		'1'	'1'
	C-D-E	1.369	1.36	1.351	1.33%		'1'	'1'
	D-E-F	1.36	1.351	1.366	0.41%		'1'	'0'

Table C.96: Radial topology / Phase to phase (60 Ω) fault / F_6.

Circuit	3-points window	k_{s_1}	k_{s_2}	k_{s_3}	$\Delta k_{s_{13}}\%$	FS search	$k_{s_1} > k_{s_2}$	$k_{s_2} > k_{s_3}$
Radial A-I	A-B-G	6.823	6.641	6.538	4.27%		'1'	'1'
	B-G-H	6.641	6.538	5.509	18.17%		'1'	'1'
	G-H-I	6.538	5.509	5.484	18.04%	→	'1'	'1'
Radial A-F	A-B-C	6.823	6.641	6.596	3.39%		'1'	'1'
	B-C-D	6.641	6.596	6.539	1.55%		'1'	'1'
	C-D-E	6.596	6.539	6.573	0.35%		'1'	'0'
	D-E-F	6.539	6.573	6.479	0.91%		'0'	'1'

C.3.2 2% Load unbalance

Table C.97: Radial topology / Phase to ground (0 Ω) fault / F_1.

Circuit	3-points window	k_{s_1}	k_{s_2}	k_{s_3}	$\Delta k_{s_{13}}\%$	FS search	$k_{s_1} > k_{s_2}$	$k_{s_2} > k_{s_3}$
Radial A-I	A-B-G	2.761	2.67	2.648	4.197%	↓↓	'1'	'1'
	B-G-H	2.67	2.648	2.656	0.53%	→	'1'	'0'
	G-H-I	2.648	2.656	2.656	0.295%		'0'	'1'
Radial A-F	A-B-C	2.761	2.67	2.663	3.65%	↓↓	'1'	'1'
	B-C-D	2.67	2.663	2.663	0.8%	→	'1'	'0'
	C-D-E	2.663	2.663	2.61	2%		'0'	'1'
	D-E-F	2.649	2.61	2.64	0.35%		'1'	'0'

Table C.98: Radial topology / Phase to ground (20 Ω) fault / F_1.

Circuit	3-points window	k_{s_1}	k_{s_2}	k_{s_3}	$\Delta k_{s_{13}}\%$	FS search	$k_{s_1} > k_{s_2}$	$k_{s_2} > k_{s_3}$
Radial A-I	A-B-G	9.12	8.707	8.636	5.48%	↓↓	'1'	'1'
	B-G-H	8.707	8.636	8.67	0.43%	→	'1'	'0'
	G-H-I	8.636	8.67	8.669	0.37%		'0'	'1'
Radial A-F	A-B-C	9.12	8.707	8.667	5.12%	↓↓	'1'	'1'
	B-C-D	8.707	8.667	8.678	0.339%	→	'1'	'0'
	C-D-E	8.667	8.678	8.255	4.83%		'0'	'1'
	D-E-F	8.678	8.255	8.596	0.96%		'1'	'0'

Table C.99: Radial topology / Phase to phase (0 Ω) fault / F_1.

Circuit	3-points window	k_{s_1}	k_{s_2}	k_{s_3}	$\Delta k_{s_{13}}\%$	FS search	$k_{s_1} > k_{s_2}$	$k_{s_2} > k_{s_3}$
Radial A-I	A-B-G	1.048	1.006	0.999	4.82%	↓↓	'1'	'1'
	B-G-H	1.006	0.999	1	0.57%	→	'1'	'0'
	G-H-I	0.999	1	1	0.082%		'0'	'0'
Radial A-F	A-B-C	1.048	1.006	1.002	4.556%	↓↓	'1'	'1'
	B-C-D	1.006	1.002	1.002	0.37%	→	'1'	'0'
	C-D-E	1.002	1.002	1.01	0.81%		'0'	'0'
	D-E-F	1.002	1.01	0.999	0.26%		'0'	'1'

Table C.100: Load unbalance 2% / Radial topology / Phase to phase (60 Ω) fault / F_1.

Circuit	3-points window	k_{s_1}	k_{s_2}	k_{s_3}	$\Delta k_{s_{13}}\%$	FS search	$k_{s_1} > k_{s_2}$	$k_{s_2} > k_{s_3}$
Radial A-I	A-B-G	6.469	6.33	6.223	3.88%	↓↓	'1'	'1'
	B-G-H	6.33	6.223	6.297	0.5%	→	'1'	'0'
	G-H-I	6.223	6.297	6.297	1.18%		'0'	'0'
Radial A-F	A-B-C	6.469	6.33	6.196	4.31%	↓↓	'1'	'1'
	B-C-D	6.33	6.196	6.196	2.15%	→	'1'	'0'
	C-D-E	6.196	6.196	6.152	0.71%		'0'	'1'
	D-E-F	6.196	6.152	6.16	0.58%		'1'	'0'

Table C.101: Radial topology / Phase to ground (0 Ω) fault / F_2.

Circuit	3-points window	k_{s_1}	k_{s_2}	k_{s_3}	$\Delta k_{s_{13}}\%$	FS search	$k_{s_1} > k_{s_2}$	$k_{s_2} > k_{s_3}$
Radial A-I	A-B-G	3.353	3.248	3.218	4.132%		'1'	'1'
	B-G-H	3.248	3.218	3.231	0.52%		'1'	'0'
	G-H-I	3.218	3.231	3.231	0.39%		'0'	'1'
Radial A-F	A-B-C	3.353	3.248	3.201	4.66%		'1'	'1'
	B-C-D	3.248	3.201	3.162	2.67%		'1'	'1'
	C-D-E	3.201	3.162	2.515	23.16%		'1'	'1'
	D-E-F	3.162	2.515	2.538	22.8%	→	'1'	'0'

Table C.102: Radial topology / Phase to ground (20 Ω) fault / F_2.

Circuit	3-points window	k_{s_1}	k_{s_2}	k_{s_3}	$\Delta k_{s_{13}}\%$	FS search	$k_{s_1} > k_{s_2}$	$k_{s_2} > k_{s_3}$
Radial A-I	A-B-G	9.513	9.185	9.099	4.47%		'1'	'1'
	B-G-H	9.185	9.099	9.144	0.45%		'1'	'0'
	G-H-I	9.099	9.144	9.143	0.489%		'0'	'1'
Radial A-F	A-B-C	9.513	9.185	9.062	4.88%		'1'	'1'
	B-C-D	9.185	9.062	9.013	1.89%		'1'	'1'
	C-D-E	9.062	9.013	7.238	21.61%		'1'	'1'
	D-E-F	9.013	7.238	7.478	19.4%	→	'1'	'0'

Table C.103: Radial topology / Phase to phase (0 Ω) fault / F_2.

Circuit	3-points window	k_{s_1}	k_{s_2}	k_{s_3}	$\Delta k_{s_{13}}\%$	FS search	$k_{s_1} > k_{s_2}$	$k_{s_2} > k_{s_3}$
Radial A-I	A-B-G	1.443	1.391	1.381	4.39%		'1'	'1'
	B-G-H	1.391	1.381	1.384	0.53%		'1'	'0'
	G-H-I	1.381	1.384	1.384	0.182%		'0'	'0'
Radial A-F	A-B-C	1.443	1.391	1.366	5.51%		'1'	'1'
	B-C-D	1.391	1.366	1.35	3.03%		'1'	'1'
	C-D-E	1.366	1.35	1.01	28.65%		'1'	'1'
	D-E-F	1.35	1.01	1.01	30.24%	→	'1'	'0'

Table C.104: Radial topology / Phase to phase (60 Ω) fault / F_2.

Circuit	3-points window	k_{s_1}	k_{s_2}	k_{s_3}	$\Delta k_{s_{13}}\%$	FS search	$k_{s_1} > k_{s_2}$	$k_{s_2} > k_{s_3}$
Radial A-I	A-B-G	6.798	6.657	6.539	3.89%		'1'	'1'
	B-G-H	6.657	6.539	6.622	0.53%		'1'	'0'
	G-H-I	6.539	6.622	6.621	1.24%		'0'	'1'
Radial A-F	A-B-C	6.798	6.657	6.651	2.19%		'1'	'1'
	B-C-D	6.657	6.651	6.416	3.67%		'1'	'1'
	C-D-E	6.651	6.416	5.353	21.14%		'1'	'1'
	D-E-F	6.416	5.353	5.353	18.63%	→	'1'	'0'

Table C.105: Radial topology / Phase to ground (0 Ω) fault / F_3.

Circuit	3-points window	k_{s_1}	k_{s_2}	k_{s_3}	$\Delta k_{s_{13}}\%$	FS search	$k_{s_1} > k_{s_2}$	$k_{s_2} > k_{s_3}$
Radial A-I	A-B-G	3.929	3.809	3.771	4.104%		'1'	'1'
	B-G-H	3.809	3.771	3.789	0.52%		'1'	'0'
	G-H-I	3.771	3.789	3.789	0.483%		'0'	'1'
Radial A-F	A-B-C	3.929	3.809	3.76	4.38%		'1'	'1'
	B-C-D	3.809	3.76	3.708	2.69%		'1'	'1'
	C-D-E	3.76	3.708	2.451	39.59%		'1'	'1'
	D-E-F	3.708	2.451	2.45	43.84%	→	'1'	'1'

Table C.106: Radial topology / Phase to ground (20 Ω) fault / F_3.

Circuit	3-points window	k_{s_1}	k_{s_2}	k_{s_3}	$\Delta k_{s_{13}}\%$	FS search	$k_{s_1} > k_{s_2}$	$k_{s_2} > k_{s_3}$
Radial A-I	A-B-G	9.988	9.645	9.543	4.58%		'1'	'1'
	B-G-H	9.645	9.543	9.601	0.466%		'1'	'0'
	G-H-I	9.543	9.601	9.6	0.596%		'0'	'1'
Radial A-F	A-B-C	9.988	9.645	9.525	4.762%		'1'	'1'
	B-C-D	9.645	9.525	9.451	2.034%		'1'	'1'
	C-D-E	9.525	9.451	6.516	35.42%		'1'	'1'
	D-E-F	9.451	6.516	6.512	39.226%	→	'1'	'1'

Table C.107: Radial topology / Phase to phase (0 Ω) fault / F_3.

Circuit	3-points window	k_{s_1}	k_{s_2}	k_{s_3}	$\Delta k_{s_{13}}\%$	FS search	$k_{s_1} > k_{s_2}$	$k_{s_2} > k_{s_3}$
Radial A-I	A-B-G	1.835	1.776	1.763	4.05%		'1'	'1'
	B-G-H	1.776	1.763	1.767	0.5%		'1'	'0'
	G-H-I	1.763	1.767	1.767	0.257%		'0'	'0'
Radial A-F	A-B-C	1.835	1.776	1.748	4.88%		'1'	'1'
	B-C-D	1.776	1.748	1.724	2.95%		'1'	'1'
	C-D-E	1.748	1.724	1.015	48.984%		'1'	'1'
	D-E-F	1.724	1.015	0.999	58.19%	→	'1'	'1'

Table C.108: Radial topology / Phase to phase (60 Ω) fault / F_3.

Circuit	3-points window	k_{s_1}	k_{s_2}	k_{s_3}	$\Delta k_{s_{13}}\%$	FS search	$k_{s_1} > k_{s_2}$	$k_{s_2} > k_{s_3}$
Radial A-I	A-B-G	7.112	6.969	6.841	3.89%		'1'	'1'
	B-G-H	6.969	6.841	6.932	0.54%		'1'	'0'
	G-H-I	6.841	6.932	6.932	1.32%		'0'	'0'
Radial A-F	A-B-C	7.112	6.969	6.97	2.02%		'0'	'0'
	B-C-D	6.969	6.97	6.71	3.76%		'0'	'1'
	C-D-E	6.97	6.71	4.778	35.63%		'1'	'1'
	D-E-F	6.71	4.778	4.738	36.46%	→	'1'	'1'

Table C.109: Radial topology / Phase to ground (0 Ω) fault / F_4.

Circuit	3-points window	k_{s_1}	k_{s_2}	k_{s_3}	$\Delta k_{s_{13}}\%$	FS search	$k_{s_1} > k_{s_2}$	$k_{s_2} > k_{s_3}$
Radial A-I	A-B-G	2.769	2.677	2.647	4.48%	↓↓	'1'	'1'
	B-G-H	2.677	2.647	2.655	0.83%	→	'1'	'0'
	G-H-I	2.647	2.655	2.655	0.296%		'0'	'1'
Radial A-F	A-B-C	2.769	2.677	2.67	3.651%	↓↓	'1'	'1'
	B-C-D	2.677	2.67	2.656	0.8%	→	'1'	'1'
	C-D-E	2.67	2.656	2.617	2.004%		'1'	'1'
	D-E-F	2.656	2.617	2.647	0.35%		'1'	'0'

Table C.110: Radial topology / Phase to ground (20 Ω) fault / F_4.

Circuit	3-points window	k_{s_1}	k_{s_2}	k_{s_3}	$\Delta k_{s_{13}}\%$	FS search	$k_{s_1} > k_{s_2}$	$k_{s_2} > k_{s_3}$
Radial A-I	A-B-G	9.026	8.713	8.622	4.59%	↓↓	'1'	'1'
	B-G-H	8.713	8.622	8.656	0.665%	↓	'1'	'0'
	G-H-I	8.622	8.656	8.655	0.379%	→	'0'	'1'
Radial A-F	A-B-C	9.026	8.713	8.674	4.0021%	↓↓	'1'	'1'
	B-C-D	8.713	8.674	8.684	0.34%	→	'1'	'0'
	C-D-E	8.674	8.684	8.261	4.835%		'0'	'1'
	D-E-F	8.684	8.261	8.602	0.964%		'1'	'0'

Table C.111: Radial topology / Phase to phase (0 Ω) fault / F_4.

Circuit	3-points window	k_{s_1}	k_{s_2}	k_{s_3}	$\Delta k_{s_{13}}\%$	FS search	$k_{s_1} > k_{s_2}$	$k_{s_2} > k_{s_3}$
Radial A-I	A-B-G	1.053	1.01	0.999	5.23%	↓↓	'1'	'1'
	B-G-H	1.01	0.999	1	0.98%	→	'1'	'0'
	G-H-I	0.999	1	1	0.082%		'0'	'0'
Radial A-F	A-B-C	1.053	1.01	1.006	4.55%	↓↓	'1'	'1'
	B-C-D	1.01	1.006	1.002	0.8%	↓	'1'	'1'
	C-D-E	1.006	1.002	1.014	0.81%	→	'1'	'0'
	D-E-F	1.002	1.014	1.003	0.166%		'0'	'1'

Table C.112: Radial topology / Phase to phase (60 Ω) fault / F_4.

Circuit	3-points window	k_{s_1}	k_{s_2}	k_{s_3}	$\Delta k_{s_{13}}\%$	FS search	$k_{s_1} > k_{s_2}$	$k_{s_2} > k_{s_3}$
Radial A-I	A-B-G	6.473	6.4	6.212	4.1%	↓↓	'1'	'1'
	B-G-H	6.4	6.212	6.286	1.81%	→	'1'	'0'
	G-H-I	6.212	6.286	6.286	1.18%		'0'	'0'
Radial A-F	A-B-C	6.473	6.4	6.39	1.29%	↓↓	'1'	'1'
	B-C-D	6.4	6.39	6.2	3.16%	↓	'1'	'1'
	C-D-E	6.39	6.2	6.156	3.74%	↓	'1'	'1'
	D-E-F	6.2	6.156	6.164	0.58%	→	'1'	'0'

Table C.113: Radial topology / Phase to ground (0 Ω) fault / F_5.

Circuit	3-points window	k_{s_1}	k_{s_2}	k_{s_3}	$\Delta k_{s_{13}}\%$	FS search	$k_{s_1} > k_{s_2}$	$k_{s_2} > k_{s_3}$
Radial A-I	A-B-G	3.287	3.183	3.145	4.42%		'1'	'1'
	B-G-H	3.183	3.145	2.548	21.44%		'1'	'1'
	G-H-I	3.145	2.548	2.548	21.73%	→	'1'	'0'
Radial A-F	A-B-C	3.287	3.183	3.177	3.4%		'1'	'1'
	B-C-D	3.183	3.177	3.154	0.91%		'1'	'1'
	C-D-E	3.177	3.154	3.104	2.33%		'1'	'1'
	D-E-F	3.154	3.104	3.141	0.4%		'1'	'0'

Table C.114: Radial topology / Phase to ground (20 Ω) fault / F_5.

Circuit	3-points window	k_{s_1}	k_{s_2}	k_{s_3}	$\Delta k_{s_{13}}\%$	FS search	$k_{s_1} > k_{s_2}$	$k_{s_2} > k_{s_3}$
Radial A-I	A-B-G	9.454	9.128	9.022	4.69%		'1'	'1'
	B-G-H	9.128	9.022	7.613	17.645%	↓	'1'	'1'
	G-H-I	9.022	7.613	7.613	17.428%	→	'1'	'0'
Radial A-F	A-B-C	9.454	9.128	9.095	3.89%		'1'	'1'
	B-C-D	9.128	9.095	9.083	0.491%		'1'	'1'
	C-D-E	9.095	9.083	8.631	5.194%		'1'	'1'
	D-E-F	9.083	8.631	8.992	1.027%		'1'	'0'

Table C.115: Radial topology / Phase to phase (0 Ω) fault / F_5.

Circuit	3-points window	k_{s_1}	k_{s_2}	k_{s_3}	$\Delta k_{s_{13}}\%$	FS search	$k_{s_1} > k_{s_2}$	$k_{s_2} > k_{s_3}$
Radial A-I	A-B-G	1.414	1.363	1.349	4.76%		'1'	'1'
	B-G-H	1.363	1.349	1	29.35%		'1'	'1'
	G-H-I	1.349	1	1	31.23%	→	'1'	'0'
Radial A-F	A-B-C	1.414	1.363	1.36	3.93%		'1'	'1'
	B-C-D	1.363	1.36	1.351	0.9%		'1'	'1'
	C-D-E	1.36	1.351	1.368	0.58%		'1'	'0'
	D-E-F	1.351	1.368	1.353	0.127%		'0'	'1'

Table C.116: Radial topology / Phase to phase (60 Ω) fault / F_5.

Circuit	3-points window	k_{s_1}	k_{s_2}	k_{s_3}	$\Delta k_{s_{13}}\%$	FS search	$k_{s_1} > k_{s_2}$	$k_{s_2} > k_{s_3}$
Radial A-I	A-B-G	6.761	6.621	6.489	4.11%		'1'	'1'
	B-G-H	6.621	6.489	5.491	18.22%	↓	'1'	'1'
	G-H-I	6.489	5.491	5.491	17.14%	→	'1'	'0'
Radial A-F	A-B-C	6.761	6.621	6.685	1.14%		'1'	'0'
	B-C-D	6.621	6.685	6.473	2.24%		'0'	'1'
	C-D-E	6.685	6.473	6.437	3.8%		'1'	'1'
	D-E-F	6.473	6.437	6.435	0.59%		'1'	'1'

Table C.117: Radial topology / Phase to ground (0 Ω) fault / F_6.

Circuit	3-points window	k_{s_1}	k_{s_2}	k_{s_3}	$\Delta k_{s_{13}}\%$	FS search	$k_{s_1} > k_{s_2}$	$k_{s_2} > k_{s_3}$
Radial A-I	A-B-G	3.302	3.197	3.159	4.42%		'1'	'1'
	B-G-H	3.197	3.159	2.561	21.42%		'1'	'1'
	G-H-I	3.159	2.561	2.547	22.235%	→	'1'	'1'
Radial A-F	A-B-C	3.302	3.197	3.192	3.4%		'1'	'1'
	B-C-D	3.197	3.192	3.168	0.91%		'1'	'1'
	C-D-E	3.192	3.168	3.118	2.342%		'1'	'1'
	D-E-F	3.168	3.118	3.156	0.4%		'1'	'0'

Table C.118: Radial topology / Phase to ground (20 Ω) fault / F_6.

Circuit	3-points window	k_{s_1}	k_{s_2}	k_{s_3}	$\Delta k_{s_{13}}\%$	FS search	$k_{s_1} > k_{s_2}$	$k_{s_2} > k_{s_3}$
Radial A-I	A-B-G	9.466	9.14	9.033	4.7%		'1'	'1'
	B-G-H	9.14	9.033	7.623	17.646%		'1'	'1'
	G-H-I	9.033	7.623	7.59	17.86%	→	'1'	'1'
Radial A-F	A-B-C	9.466	9.14	9.107	3.885%		'1'	'1'
	B-C-D	9.14	9.107	9.095	0.494%		'1'	'1'
	C-D-E	9.107	9.095	8.642	5.203%		'1'	'1'
	D-E-F	9.095	8.642	9.003	1.029%		'1'	'0'

Table C.119: Radial topology / Phase to phase (0 Ω) fault / F_6.

Circuit	3-points window	k_{s_1}	k_{s_2}	k_{s_3}	$\Delta k_{s_{13}}\%$	FS search	$k_{s_1} > k_{s_2}$	$k_{s_2} > k_{s_3}$
Radial A-I	A-B-G	1.424	1.373	1.358	4.75%		'1'	'1'
	B-G-H	1.373	1.358	1.008	29.28%		'1'	'1'
	G-H-I	1.358	1.008	1	31.9%	→	'1'	'1'
Radial A-F	A-B-C	1.424	1.373	1.369	3.91%		'1'	'1'
	B-C-D	1.373	1.369	1.36	0.9%		'1'	'1'
	C-D-E	1.369	1.36	1.377	0.57%		'1'	'0'
	D-E-F	1.36	1.377	1.362	0.126%		'0'	'1'

Table C.120: Radial topology / Phase to phase (60 Ω) fault / F_6.

Circuit	3-points window	k_{s_1}	k_{s_2}	k_{s_3}	$\Delta k_{s_{13}}\%$	FS search	$k_{s_1} > k_{s_2}$	$k_{s_2} > k_{s_3}$
Radial A-I	A-B-G	6.769	6.629	6.497	4.1%		'1'	'1'
	B-G-H	6.629	6.497	5.498	18.22%	↓	'1'	'1'
	G-H-I	6.497	5.498	5.473	17.59%	→	'1'	'1'
Radial A-F	A-B-C	6.769	6.629	6.693	1.13%		'1'	'0'
	B-C-D	6.629	6.693	6.481	2.24%		'0'	'1'
	C-D-E	6.693	6.481	6.445	3.79%		'1'	'1'
	D-E-F	6.481	6.445	6.443	0.59%		'1'	'1'

C.3.3 3% Load unbalance

Table C.121: Radial topology / Phase to ground (0 Ω) fault / F_1.

Circuit	3-points window	k_{s_1}	k_{s_2}	k_{s_3}	$\Delta k_{s_{13}}\%$	FS search	$k_{s_1} > k_{s_2}$	$k_{s_2} > k_{s_3}$
Radial A-I	A-B-G	2.758	2.67	2.647	4.12%	↓↓	'1'	'1'
	B-G-H	2.67	2.647	2.656	0.53%	→	'1'	'0'
	G-H-I	2.647	2.656	2.656	0.355%		'0'	'1'
Radial A-F	A-B-C	2.758	2.67	2.642	4.31%	↓↓	'1'	'1'
	B-C-D	2.67	2.642	2.646	0.91%	→	'1'	'0'
	C-D-E	2.642	2.646	2.687	1.69%		'0'	'0'
	D-E-F	2.646	2.687	2.641	0.19%		'0'	'1'

Table C.122: Radial topology / Phase to ground (20 Ω) fault / F_1.

Circuit	3-points window	k_{s_1}	k_{s_2}	k_{s_3}	$\Delta k_{s_{13}}\%$	FS search	$k_{s_1} > k_{s_2}$	$k_{s_2} > k_{s_3}$
Radial A-I	A-B-G	8.936	8.713	8.637	3.41%	↓↓	'1'	'1'
	B-G-H	8.713	8.637	8.67	0.489%	→	'1'	'0'
	G-H-I	8.637	8.67	8.67	0.379%		'0'	'1'
Radial A-F	A-B-C	8.936	8.713	8.494	5.068%	↓↓	'1'	'1'
	B-C-D	8.713	8.494	8.667	0.527%	→	'1'	'0'
	C-D-E	8.494	8.667	9.072	6.616%		'0'	'0'
	D-E-F	8.667	9.072	8.629	0.434%		'0'	'1'

Table C.123: Radial topology / Phase to phase (0 Ω) fault / F_1.

Circuit	3-points window	k_{s_1}	k_{s_2}	k_{s_3}	$\Delta k_{s_{13}}\%$	FS search	$k_{s_1} > k_{s_2}$	$k_{s_2} > k_{s_3}$
Radial A-I	A-B-G	1.051	1.006	0.999	5.16%	↓↓	'1'	'1'
	B-G-H	1.006	0.999	1	0.57%	→	'1'	'0'
	G-H-I	0.999	1	1	0.114%		'0'	'0'
Radial A-F	A-B-C	1.051	1.006	1.005	4.572%	↓↓	'1'	'1'
	B-C-D	1.006	1.005	0.997	0.85%	↓	'1'	'1'
	C-D-E	1.005	0.997	0.989	1.556%	↓	'1'	'1'
	D-E-F	0.997	0.989	0.998	0.078%	→	'1'	'0'

Table C.124: Radial topology / Phase to phase (60 Ω) fault / F_1.

Circuit	3-points window	k_{s_1}	k_{s_2}	k_{s_3}	$\Delta k_{s_{13}}\%$	FS search	$k_{s_1} > k_{s_2}$	$k_{s_2} > k_{s_3}$
Radial A-I	A-B-G	6.52	6.34	6.21	4.87%	↓↓	'1'	'1'
	B-G-H	6.34	6.21	6.31	0.48%	→	'1'	'0'
	G-H-I	6.21	6.31	6.31	1.59%		'0'	'0'
Radial A-F	A-B-C	6.52	6.34	6.3	3.444%	↓↓	'1'	'1'
	B-C-D	6.34	6.3	6.17	2.71%	↓	'1'	'1'
	C-D-E	6.3	6.17	6.3	0%	→	'1'	'0'
	D-E-F	6.17	6.3	6.15	0.32%		'0'	'1'

Table C.125: Radial topology / Phase to ground (0 Ω) fault / F_2.

Circuit	3-points window	k_{s_1}	k_{s_2}	k_{s_3}	$\Delta k_{s_{13}}\%$	FS search	$k_{s_1} > k_{s_2}$	$k_{s_2} > k_{s_3}$
Radial A-I	A-B-G	3.349	3.247	3.215	4.106%		'1'	'1'
	B-G-H	3.247	3.215	3.23	0.51%		'1'	'0'
	G-H-I	3.215	3.23	3.23	0.472%		'0'	'0'
Radial A-F	A-B-C	3.349	3.247	3.17	5.49%		'1'	'1'
	B-C-D	3.247	3.17	3.157	2.82%		'1'	'1'
	C-D-E	3.17	3.157	2.578	19.95%		'1'	'1'
	D-E-F	3.157	2.578	2.578	20.88%	→	'1'	'0'

Table C.126: Radial topology / Phase to ground (20 Ω) fault / F_2.

Circuit	3-points window	k_{s_1}	k_{s_2}	k_{s_3}	$\Delta k_{s_{13}}\%$	FS search	$k_{s_1} > k_{s_2}$	$k_{s_2} > k_{s_3}$
Radial A-I	A-B-G	9.425	9.189	9.095	3.57%		'1'	'1'
	B-G-H	9.189	9.095	9.143	0.504%		'1'	'0'
	G-H-I	9.095	9.143	9.142	0.513%		'0'	'1'
Radial A-F	A-B-C	9.425	9.189	8.864	6.13%		'1'	'1'
	B-C-D	9.189	8.864	8.995	2.14%		'1'	'0'
	C-D-E	8.864	8.995	7.837	11.99%		'0'	'1'
	D-E-F	8.995	7.837	7.837	14.087%	→	'1'	'0'

Table C.127: Radial topology / Phase to phase (0 Ω) fault / F_2.

Circuit	3-points window	k_{s_1}	k_{s_2}	k_{s_3}	$\Delta k_{s_{13}}\%$	FS search	$k_{s_1} > k_{s_2}$	$k_{s_2} > k_{s_3}$
Radial A-I	A-B-G	1.449	1.392	1.381	4.82%		'1'	'1'
	B-G-H	1.392	1.381	1.384	0.54%		'1'	'0'
	G-H-I	1.381	1.384	1.384	0.241%		'0'	'0'
Radial A-F	A-B-C	1.449	1.392	1.369	5.69%		'1'	'1'
	B-C-D	1.392	1.369	1.349	3.12%		'1'	'1'
	C-D-E	1.369	1.349	0.989	30.69%		'1'	'1'
	D-E-F	1.349	0.989	0.998	31.53%	→	'1'	'0'

Table C.128: Radial topology / Phase to phase (60 Ω) fault / F_2.

Circuit	3-points window	k_{s_1}	k_{s_2}	k_{s_3}	$\Delta k_{s_{13}}\%$	FS search	$k_{s_1} > k_{s_2}$	$k_{s_2} > k_{s_3}$
Radial A-I	A-B-G	6.86	6.67	6.53	4.94%		'1'	'1'
	B-G-H	6.67	6.53	6.63	0.61%		'1'	'0'
	G-H-I	6.53	6.63	6.63	1.52%		'0'	'0'
Radial A-F	A-B-C	6.86	6.67	6.56	4.48%		'1'	'1'
	B-C-D	6.67	6.56	6.39	4.28%		'1'	'1'
	C-D-E	6.56	6.39	5.42	18.62%		'1'	'1'
	D-E-F	6.39	5.42	5.42	16.89%	→	'1'	'0'

Table C.129: Radial topology / Phase to ground (0 Ω) fault / F_3.

Circuit	3-points window	k_{s_1}	k_{s_2}	k_{s_3}	$\Delta k_{s_{13}}\%$	FS search	$k_{s_1} > k_{s_2}$	$k_{s_2} > k_{s_3}$
Radial A-I	A-B-G	3.924	3.808	3.766	4.128%		'1'	'1'
	B-G-H	3.808	3.766	3.789	0.51%		'1'	'0'
	G-H-I	3.766	3.789	3.788	0.588%		'0'	'1'
Radial A-F	A-B-C	3.924	3.808	3.719	5.38%		'1'	'1'
	B-C-D	3.808	3.719	3.7	2.89%		'1'	'1'
	C-D-E	3.719	3.7	2.505	36.7%		'1'	'1'
	D-E-F	3.7	2.505	2.456	43.09%	→	'1'	'1'

Table C.130: Radial topology / Phase to ground (20 Ω) fault / F_3.

Circuit	3-points window	k_{s_1}	k_{s_2}	k_{s_3}	$\Delta k_{s_{13}}\%$	FS search	$k_{s_1} > k_{s_2}$	$k_{s_2} > k_{s_3}$
Radial A-I	A-B-G	9.897	9.647	9.536	3.72%		'1'	'1'
	B-G-H	9.647	9.536	9.598	0.518%		'1'	'0'
	G-H-I	9.536	9.598	9.597	0.64%		'0'	'1'
Radial A-F	A-B-C	9.897	9.647	9.3	6.2%		'1'	'1'
	B-C-D	9.647	9.3	9.427	2.333%		'1'	'0'
	C-D-E	9.3	9.427	6.98	27.08%		'0'	'1'
	D-E-F	9.427	6.98	6.683	35.65%	→	'1'	'1'

Table C.131: Radial topology / Phase to phase (0 Ω) fault / F_3.

Circuit	3-points window	k_{s_1}	k_{s_2}	k_{s_3}	$\Delta k_{s_{13}}\%$	FS search	$k_{s_1} > k_{s_2}$	$k_{s_2} > k_{s_3}$
Radial A-I	A-B-G	1.844	1.777	1.762	4.56%		'1'	'1'
	B-G-H	1.777	1.762	1.768	0.5%		'1'	'0'
	G-H-I	1.762	1.768	1.768	0.336%		'0'	'0'
Radial A-F	A-B-C	1.844	1.777	1.751	5.19%		'1'	'1'
	B-C-D	1.777	1.751	1.723	3.08%		'1'	'1'
	C-D-E	1.751	1.723	0.995	50.75%		'1'	'1'
	D-E-F	1.723	0.995	0.993	59.02%	→	'1'	'1'

Table C.132: Radial topology / Phase to phase (60 Ω) fault / F_3.

Circuit	3-points window	k_{s_1}	k_{s_2}	k_{s_3}	$\Delta k_{s_{13}}\%$	FS search	$k_{s_1} > k_{s_2}$	$k_{s_2} > k_{s_3}$
Radial A-I	A-B-G	7.18	6.98	6.83	5%		'1'	'1'
	B-G-H	6.98	6.83	6.95	0.43%		'1'	'0'
	G-H-I	6.83	6.95	6.94	1.59%		'0'	'1'
Radial A-F	A-B-C	7.18	6.98	6.87	4.42%		'1'	'1'
	B-C-D	6.98	6.87	6.68	4.38%		'1'	'1'
	C-D-E	6.87	6.68	4.82	33.48%		'1'	'1'
	D-E-F	6.68	4.82	4.73	36.04%	→	'1'	'1'

Table C.133: Radial topology / Phase to ground (0 Ω) fault / F_4.

Circuit	3-points window	k_{s_1}	k_{s_2}	k_{s_3}	$\Delta k_{s_{13}}\%$	FS search	$k_{s_1} > k_{s_2}$	$k_{s_2} > k_{s_3}$
Radial A-I	A-B-G	2.765	2.677	2.646	4.41%	↓↓	'1'	'1'
	B-G-H	2.677	2.646	2.655	0.82%	→	'1'	'0'
	G-H-I	2.646	2.655	2.655	0.35%		'0'	'1'
Radial A-F	A-B-C	2.765	2.677	2.649	4.31%	↓↓	'1'	'1'
	B-C-D	2.677	2.649	2.653	0.91%	→	'1'	'0'
	C-D-E	2.649	2.653	2.694	1.69%		'0'	'0'
	D-E-F	2.653	2.694	2.648	0.19%		'0'	'1'

Table C.134: Radial topology / Phase to ground (20 Ω) fault / F_4.

Circuit	3-points window	k_{s_1}	k_{s_2}	k_{s_3}	$\Delta k_{s_{13}}\%$	FS search	$k_{s_1} > k_{s_2}$	$k_{s_2} > k_{s_3}$
Radial A-I	A-B-G	8.942	8.719	8.623	3.64%	↓↓	'1'	'1'
	B-G-H	8.719	8.623	8.656	0.72%	→	'1'	'0'
	G-H-I	8.623	8.656	8.656	0.38%		'0'	'1'
Radial A-F	A-B-C	8.942	8.719	8.5	5.069%	↓↓	'1'	'1'
	B-C-D	8.719	8.5	8.673	0.529%	→	'1'	'0'
	C-D-E	8.5	8.673	9.079	6.618%		'0'	'0'
	D-E-F	8.673	9.079	8.635	0.435%		'0'	'1'

Table C.135: Radial topology / Phase to phase (0 Ω) fault / F_4.

Circuit	3-points window	k_{s_1}	k_{s_2}	k_{s_3}	$\Delta k_{s_{13}}\%$	FS search	$k_{s_1} > k_{s_2}$	$k_{s_2} > k_{s_3}$
Radial A-I	A-B-G	1.056	1.01	0.999	5.57%	↓↓	'1'	'1'
	B-G-H	1.01	0.999	1	0.98%	→	'1'	'0'
	G-H-I	0.999	1	1	0.082%		'0'	'0'
Radial A-F	A-B-C	1.056	1.01	1.009	4.57%	↓↓	'1'	'1'
	B-C-D	1.01	1.009	1.001	0.85%	↓	'1'	'1'
	C-D-E	1.009	1.001	0.993	1.556%	↓	'1'	'1'
	D-E-F	1.001	0.993	1.002	0.077%	→	'1'	'0'

Table C.136: Radial topology / Phase to phase (60 Ω) fault / F_4.

Circuit	3-points window	k_{s_1}	k_{s_2}	k_{s_3}	$\Delta k_{s_{13}}\%$	FS search	$k_{s_1} > k_{s_2}$	$k_{s_2} > k_{s_3}$
Radial A-I	A-B-G	6.52	6.34	6.2	5.04%	↓↓	'1'	'1'
	B-G-H	6.34	6.2	6.3	0.64%	→	'1'	'0'
	G-H-I	6.2	6.3	6.3	1.6%		'0'	'0'
Radial A-F	A-B-C	6.52	6.34	6.3	3.44%	↓↓	'1'	'1'
	B-C-D	6.34	6.3	6.18	2.55%	↓	'1'	'1'
	C-D-E	6.3	6.18	6.3	0%	→	'1'	'0'
	D-E-F	6.18	6.3	6.15	0.48%		'0'	'1'

Table C.137: Radial topology / Phase to ground (0 Ω) fault / F_5.

Circuit	3-points window	k_{s_1}	k_{s_2}	k_{s_3}	$\Delta k_{s_{13}}\%$	FS search	$k_{s_1} > k_{s_2}$	$k_{s_2} > k_{s_3}$
Radial A-I	A-B-G	3.284	3.183	3.143	4.4%		'1'	'1'
	B-G-H	3.183	3.143	2.549	21.44%		'1'	'1'
	G-H-I	3.143	2.549	2.549	21.61%	→	'1'	'0'
Radial A-F	A-B-C	3.284	3.183	3.148	4.23%		'1'	'1'
	B-C-D	3.183	3.148	3.149	1.05%		'1'	'0'
	C-D-E	3.148	3.149	3.204	1.77%		0'	'0'
	D-E-F	3.149	3.204	3.143	0.22%		'0'	'1'

Table C.138: Radial topology / Phase to ground (20 Ω) fault / F_5.

Circuit	3-points window	k_{s_1}	k_{s_2}	k_{s_3}	$\Delta k_{s_{13}}\%$	FS search	$k_{s_1} > k_{s_2}$	$k_{s_2} > k_{s_3}$
Radial A-I	A-B-G	9.369	9.134	9.02	3.8%		'1'	'1'
	B-G-H	9.134	9.02	7.614	17.7%	↓	'1'	'1'
	G-H-I	9.02	7.614	7.614	17.4%	→	'1'	'0'
Radial A-F	A-B-C	9.369	9.134	8.899	5.14%		'1'	'1'
	B-C-D	9.134	8.899	9.068	0.725%		'1'	'0'
	C-D-E	8.899	9.068	9.516	6.736%		'0'	'0'
	D-E-F	9.068	9.516	9.025	0.47%		'0'	'1'

Table C.139: Radial topology / Phase to phase (0 Ω) fault / F_5.

Circuit	3-points window	k_{s_1}	k_{s_2}	k_{s_3}	$\Delta k_{s_{13}}\%$	FS search	$k_{s_1} > k_{s_2}$	$k_{s_2} > k_{s_3}$
Radial A-I	A-B-G	1.419	1.363	1.348	5.18%		'1'	'1'
	B-G-H	1.363	1.348	1	29.37%		'1'	'1'
	G-H-I	1.348	1	1	31.18%	→	'1'	'0'
Radial A-F	A-B-C	1.419	1.363	1.362	4.1%		'1'	'1'
	B-C-D	1.363	1.363	1.35	0.98%		'1'	'1'
	C-D-E	1.363	1.35	1.341	0.63%		'1'	'1'
	D-E-F	1.35	1.341	1.35	0.041%		'1'	'0'

Table C.140: Radial topology / Phase to phase (60 Ω) fault / F_5.

Circuit	3-points window	k_{s_1}	k_{s_2}	k_{s_3}	$\Delta k_{s_{13}}\%$	FS search	$k_{s_1} > k_{s_2}$	$k_{s_2} > k_{s_3}$
Radial A-I	A-B-G	6.82	6.63	6.48	5.12%		'1'	'1'
	B-G-H	6.63	6.48	5.5	18.22%	↓	'1'	'1'
	G-H-I	6.48	5.5	5.5	16.82%	→	'1'	'0'
Radial A-F	A-B-C	6.82	6.63	6.59	3.44%		'1'	'1'
	B-C-D	6.63	6.59	6.45	2.75%		'1'	'1'
	C-D-E	6.59	6.45	6.57	0.31%		'1'	'0'
	D-E-F	6.45	6.57	6.42	0.46%		'0'	'1'

Table C.141: Radial topology / Phase to ground (0 Ω) fault / F_6.

Circuit	3-points window	k_{s_1}	k_{s_2}	k_{s_3}	$\Delta k_{s_{13}}\%$	FS search	$k_{s_1} > k_{s_2}$	$k_{s_2} > k_{s_3}$
Radial A-I	A-B-G	3.299	3.197	3.157	4.4%		'1'	'1'
	B-G-H	3.197	3.157	2.561	21.42%		'1'	'1'
	G-H-I	3.157	2.561	2.547	22.15%	→	'1'	'1'
Radial A-F	A-B-C	3.299	3.197	3.162	4.23%		'1'	'1'
	B-C-D	3.197	3.162	3.164	1.06%		'1'	'0'
	C-D-E	3.162	3.164	3.219	2.78%		'0'	'0'
	D-E-F	3.164	3.219	3.157	0.22%		'0'	'1'

Table C.142: Radial topology / Phase to ground (20 Ω) fault / F_6.

Circuit	3-points window	k_{s_1}	k_{s_2}	k_{s_3}	$\Delta k_{s_{13}}\%$	FS search	$k_{s_1} > k_{s_2}$	$k_{s_2} > k_{s_3}$
Radial A-I	A-B-G	9.382	9.146	9.032	3.8%		'1'	'1'
	B-G-H	9.146	9.032	7.624	17.7%		'1'	'1'
	G-H-I	9.032	7.624	7.591	17.83%	→	'1'	'1'
Radial A-F	A-B-C	9.382	9.146	8.911	5.14%		'1'	'1'
	B-C-D	9.146	8.911	9.08	0.729%		'1'	'0'
	C-D-E	8.911	9.08	9.529	6.74%		'0'	'0'
	D-E-F	9.08	9.529	9.036	0.47%		'0'	'1'

Table C.143: Radial topology / Phase to phase (0 Ω) fault / F_6.

Circuit	3-points window	k_{s_1}	k_{s_2}	k_{s_3}	$\Delta k_{s_{13}}\%$	FS search	$k_{s_1} > k_{s_2}$	$k_{s_2} > k_{s_3}$
Radial A-I	A-B-G	1.429	1.373	1.357	5.17%		'1'	'1'
	B-G-H	1.373	1.357	1.008	29.29%		'1'	'1'
	G-H-I	1.357	1.008	1	31.84%	→	'1'	'1'
Radial A-F	A-B-C	1.429	1.373	1.372	4.09%		'1'	'1'
	B-C-D	1.373	1.372	1.359	0.99%		'1'	'1'
	C-D-E	1.372	1.359	1.35	1.629%		'1'	'1'
	D-E-F	1.359	1.35	1.36	0.04%		'1'	'0'

Table C.144: Radial topology / Phase to phase (60 Ω) fault / F_6.

Circuit	3-points window	k_{s_1}	k_{s_2}	k_{s_3}	$\Delta k_{s_{13}}\%$	FS search	$k_{s_1} > k_{s_2}$	$k_{s_2} > k_{s_3}$
Radial A-I	A-B-G	6.83	6.64	6.49	5.11%		'1'	'1'
	B-G-H	6.64	6.49	5.51	18.19%		'1'	'1'
	G-H-I	6.49	5.51	5.48	17.33%	→	'1'	'1'
Radial A-F	A-B-C	6.83	6.64	6.6	3.44%		'1'	'1'
	B-C-D	6.64	6.6	6.45	2.89%		'1'	'1'
	C-D-E	6.6	6.45	6.58	0.31%		'1'	'0'
	D-E-F	6.45	6.58	6.43	0.31%		'0'	'1'

C.3.4 4% Load unbalance

Table C.145: Radial topology / Phase to ground (0 Ω) fault / F_1.

Circuit	3-points window	k_{s_1}	k_{s_2}	k_{s_3}	$\Delta k_{s_{13}}$%	FS search	$k_{s_1} > k_{s_2}$	$k_{s_2} > k_{s_3}$
Radial A-I	A-B-G	2.756	2.67	2.649	3.99%	↓↓	'1'	'1'
	B-G-H	2.67	2.649	2.649	0.75%	→	'1'	'0'
	G-H-I	2.649	2.649	2.655	0.22%		'0'	'1'
Radial A-F	A-B-C	2.756	2.67	2.661	3.51%	↓↓	'1'	'1'
	B-C-D	2.67	2.661	2.652	0.62%	↓↓	'1'	'1'
	C-D-E	2.661	2.652	2.614	1.77%	↓↓	'1'	'1'
	D-E-F	2.652	2.614	2.634	0.7%	→	'1'	'0'

Table C.146: Radial topology / Phase to ground (20 Ω) fault / F_1.

Circuit	3-points window	k_{s_1}	k_{s_2}	k_{s_3}	$\Delta k_{s_{13}}$%	FS search	$k_{s_1} > k_{s_2}$	$k_{s_2} > k_{s_3}$
Radial A-I	A-B-G	8.923	8.699	8.622	3.43%	↓↓	'1'	'1'
	B-G-H	8.699	8.622	8.652	0.54%	→	'1'	'0'
	G-H-I	8.622	8.652	8.651	0.33%		'0'	'1'
Radial A-F	A-B-C	8.923	8.699	8.827	1.08%	↓↓	'1'	'0'
	B-C-D	8.699	8.827	8.668	0.36%		'0'	'1'
	C-D-E	8.827	8.668	8.558	3.09%		'1'	'1'
	D-E-F	8.668	8.558	8.358	3.63%		'1'	'1'

Table C.147: Radial topology / Phase to phase (0 Ω) fault / F_1.

Circuit	3-points window	k_{s_1}	k_{s_2}	k_{s_3}	$\Delta k_{s_{13}}$%	FS search	$k_{s_1} > k_{s_2}$	$k_{s_2} > k_{s_3}$
Radial A-I	A-B-G	1.051	1.006	1	5.06%	↓↓	'1'	'1'
	B-G-H	1.006	1	1	0.56%	→	'1'	'0'
	G-H-I	1	1	1	0%		'0'	'0'
Radial A-F	A-B-C	1.051	1.005	0.995	5.49%	↓↓	'1'	'1'
	B-C-D	1.005	0.995	0.998	0.75%	↓	'1'	'1'
	C-D-E	0.995	0.998	1.001	0.2%	→	'1'	'0'
	D-E-F	0.998	1.001	1.003	0.036%		'0'	'0'

Table C.148: Radial topology / Phase to phase (60 Ω) fault / F_1.

Circuit	3-points window	k_{s_1}	k_{s_2}	k_{s_3}	$\Delta k_{s_{13}}\%$	FS search	$k_{s_1} > k_{s_2}$	$k_{s_2} > k_{s_3}$
Radial A-I	A-B-G	6.5	6.324	6.242	4.061%	↓↓	'1'	'1'
	B-G-H	6.324	6.242	6.243	1.29%	→	'1'	'0'
	G-H-I	6.242	6.243	6.293	0.81%		'0'	'0'
Radial A-F	A-B-C	6.5	6.324	6.245	4.02%	↓↓	'1'	'1'
	B-C-D	6.324	6.245	6.234	1.44%	↓	'1'	'1'
	C-D-E	6.245	6.234	6.159	1.38%	↓	'1'	'1'
	D-E-F	6.234	6.159	6.159	1.21%	→	'1'	'0'

Table C.149: Radial topology / Phase to ground (0 Ω) fault / F_2.

Circuit	3-points window	k_{s_1}	k_{s_2}	k_{s_3}	$\Delta k_{s_{13}}\%$	FS search	$k_{s_1} > k_{s_2}$	$k_{s_2} > k_{s_3}$
Radial A-I	A-B-G	3.348	3.245	3.219	3.92%		'1'	'1'
	B-G-H	3.245	3.219	3.229	0.52%		'1'	'0'
	G-H-I	3.219	3.229	3.229	0.29%		'0'	'1'
Radial A-F	A-B-C	3.348	3.245	3.194	4.7%		'1'	'1'
	B-C-D	3.245	3.194	3.168	2.43%		'1'	'1'
	C-D-E	3.194	3.168	2.519	22.85%		'1'	'1'
	D-E-F	3.168	2.519	2.524	23.52%	→	'1'	'0'

Table C.150: Radial topology / Phase to ground (20 Ω) fault / F_2.

Circuit	3-points window	k_{s_1}	k_{s_2}	k_{s_3}	$\Delta k_{s_{13}}\%$	FS search	$k_{s_1} > k_{s_2}$	$k_{s_2} > k_{s_3}$
Radial A-I	A-B-G	9.413	9.176	9.086	3.54%		'1'	'1'
	B-G-H	9.176	9.086	9.125	0.56%		'1'	'0'
	G-H-I	9.086	9.125	9.124	0.41%		'0'	'1'
Radial A-F	A-B-C	9.413	9.176	9.207	2.22%		'1'	'0'
	B-C-D	9.176	9.207	9.009	1.83%		'0'	'1'
	C-D-E	9.207	9.009	7.201	23.66%	↓	'1'	'1'
	D-E-F	9.009	7.201	7.299	21.81%	→	'1'	'0'

Table C.151: Radial topology / Phase to phase (0 Ω) fault / F_2.

Circuit	3-points window	k_{s_1}	k_{s_2}	k_{s_3}	$\Delta k_{s_{13}}\%$	FS search	$k_{s_1} > k_{s_2}$	$k_{s_2} > k_{s_3}$
Radial A-I	A-B-G	1.448	1.391	1.382	4.65%		'1'	'1'
	B-G-H	1.391	1.382	1.384	0.52%		'1'	'0'
	G-H-I	1.382	1.384	1.384	0.102%		'0'	'0'
Radial A-F	A-B-C	1.448	1.391	1.354	6.69%		'1'	'1'
	B-C-D	1.391	1.354	1.351	2.93%		'1'	'1'
	C-D-E	1.354	1.351	1.008	27.95%		'1'	'1'
	D-E-F	1.351	1.008	1.008	30.55%	→	'1'	'0'

Table C.152: Radial topology / Phase to phase (60 Ω) fault / F_2.

Circuit	3-points window	k_{s_1}	k_{s_2}	k_{s_3}	$\Delta k_{s_{13}}\%$	FS search	$k_{s_1} > k_{s_2}$	$k_{s_2} > k_{s_3}$
Radial A-I	A-B-G	6.836	6.651	6.562	4.11%		'1'	'1'
	B-G-H	6.651	6.562	6.618	0.49%		'1'	'0'
	G-H-I	6.562	6.618	6.618	0.85%		'0'	'1'
Radial A-F	A-B-C	6.836	6.651	6.49	5.2%		'1'	'1'
	B-C-D	6.651	6.49	6.459	2.94%		'1'	'1'
	C-D-E	6.49	6.459	5.355	18.61%		'1'	'1'
	D-E-F	6.459	5.355	5.313	20.07%	→	'1'	'1'

Table C.153: Radial topology / Phase to ground (0 Ω) fault / F_3.

Circuit	3-points window	k_{s_1}	k_{s_2}	k_{s_3}	$\Delta k_{s_{13}}\%$	FS search	$k_{s_1} > k_{s_2}$	$k_{s_2} > k_{s_3}$
Radial A-I	A-B-G	3.923	3.806	3.773	3.89%		'1'	'1'
	B-G-H	3.806	3.773	3.787	0.51%		'1'	'0'
	G-H-I	3.773	3.787	3.787	0.35%		'0'	'1'
Radial A-F	A-B-C	3.923	3.806	3.747	4.58%		'1'	'1'
	B-C-D	3.806	3.747	3.716	2.4%		'1'	'1'
	C-D-E	3.747	3.716	2.454	39.1%		'1'	'1'
	D-E-F	3.716	2.454	2.445	44.25%	→	'1'	'1'

Table C.154: Radial topology / Phase to ground (20 Ω) fault / F_3.

Circuit	3-points window	k_{s_1}	k_{s_2}	k_{s_3}	$\Delta k_{s_{13}}\%$	FS search	$k_{s_1} > k_{s_2}$	$k_{s_2} > k_{s_3}$
Radial A-I	A-B-G	9.885	9.635	9.532	3.64%		'1'	'1'
	B-G-H	9.635	9.532	9.580	0.57%		'1'	'0'
	G-H-I	9.532	9.580	9.579	0.48%		'0'	'1'
Radial A-F	A-B-C	9.885	9.635	9.661	2.3%		'1'	'0'
	B-C-D	9.635	9.661	9.452	1.9%		'0'	'1'
	C-D-E	9.661	9.452	6.484	37.23%		'1'	'1'
	D-E-F	9.452	6.484	6.533	38.97%	→	'1'	'0'

Table C.155: Radial topology / Phase to phase (0 Ω) fault / F_3.

Circuit	3-points window	k_{s_1}	k_{s_2}	k_{s_3}	$\Delta k_{s_{13}}\%$	FS search	$k_{s_1} > k_{s_2}$	$k_{s_2} > k_{s_3}$
Radial A-I	A-B-G	1.843	1.776	1.765	4.35%		'1'	'1'
	B-G-H	1.776	1.765	1.767	0.49%		'1'	'0'
	G-H-I	1.765	1.767	1.767	0.151%		'0'	'0'
Radial A-F	A-B-C	1.843	1.776	1.73	6.29%		'1'	'1'
	B-C-D	1.776	1.73	1.727	2.82%		'1'	'1'
	C-D-E	1.73	1.727	1.014	48.09%		'1'	'1'
	D-E-F	1.727	1.014	1.008	57.522%	→	'1'	'1'

Table C.156: Radial topology / Phase to phase (60 Ω) fault / F_3.

Circuit	3-points window	k_{s_1}	k_{s_2}	k_{s_3}	$\Delta k_{s_{13}}\%$	FS search	$k_{s_1} > k_{s_2}$	$k_{s_2} > k_{s_3}$
Radial A-I	A-B-G	7.158	6.963	6.886	4.16%		'1'	'1'
	B-G-H	6.963	6.886	6.929	0.49%		'1'	'0'
	G-H-I	6.886	6.929	6.928	0.9%		'0'	'1'
Radial A-F	A-B-C	7.158	6.963	6.788	5.3%		'1'	'1'
	B-C-D	6.963	6.788	6.757	3%		'1'	'1'
	C-D-E	6.788	6.757	4.779	32.9%		'1'	'1'
	D-E-F	6.757	4.779	4.722	37.56%	→	'1'	'1'

Table C.157: Radial topology / Phase to ground (0 Ω) fault / F_4.

Circuit	3-points window	k_{s_1}	k_{s_2}	k_{s_3}	$\Delta k_{s_{13}}\%$	FS search	$k_{s_1} > k_{s_2}$	$k_{s_2} > k_{s_3}$
Radial A-I	A-B-G	2.763	2.676	2.648	4.28%	↓↓	'1'	'1'
	B-G-H	2.676	2.648	2.648	1.05%	→	'1'	'0'
	G-H-I	2.648	2.648	2.654	0.22%		'0'	'0'
Radial A-F	A-B-C	2.763	2.676	2.668	3.51%	↓↓	'1'	'1'
	B-C-D	2.676	2.668	2.659	0.62%	→	'1'	'1'
	C-D-E	2.668	2.659	2.621	1.77%		'1'	'1'
	D-E-F	2.659	2.621	2.651	0.32%		'1'	'0'

Table C.158: Radial topology / Phase to ground (20 Ω) fault / F_4.

Circuit	3-points window	k_{s_1}	k_{s_2}	k_{s_3}	$\Delta k_{s_{13}}\%$	FS search	$k_{s_1} > k_{s_2}$	$k_{s_2} > k_{s_3}$
Radial A-I	A-B-G	8.953	8.705	8.6	4.03%	↓↓	'1'	'1'
	B-G-H	8.705	8.6	8.638	0.77%	→	'1'	'0'
	G-H-I	8.6	8.638	8.637	0.33%		'0'	'1'
Radial A-F	A-B-C	8.953	8.705	8.833	1.369%	↓↓	'1'	'0'
	B-C-D	8.705	8.833	8.674	0.36%		'0'	'1'
	C-D-E	8.833	8.674	8.489	3.96%		'1'	'1'
	D-E-F	8.674	8.489	8.363	3.64%		'1'	'1'

Table C.159: Radial topology / Phase to phase (0 Ω) fault / F_4.

Circuit	3-points window	k_{s_1}	k_{s_2}	k_{s_3}	$\Delta k_{s_{13}}\%$	FS search	$k_{s_1} > k_{s_2}$	$k_{s_2} > k_{s_3}$
Radial A-I	A-B-G	1.056	1.01	1	5.47%	↓↓	'1'	'1'
	B-G-H	1.01	1	1	0.97%	→	'1'	'0'
	G-H-I	1	1	1	0%		'0'	'0'
Radial A-F	A-B-C	1.056	1.01	0.999	5.49%	↓↓	'1'	'1'
	B-C-D	1.01	0.999	1.002	0.76%	→	'1'	'0'
	C-D-E	0.999	1.002	1.013	1.3%		'0'	'0'
	D-E-F	1.002	1.013	1.007	0.45%		'0'	'1'

Table C.160: Radial topology / Phase to phase (60 Ω) fault / F_4.

Circuit	3-points window	k_{s_1}	k_{s_2}	k_{s_3}	$\Delta k_{s_{13}}\%$	FS search	$k_{s_1} > k_{s_2}$	$k_{s_2} > k_{s_3}$
Radial A-I	A-B-G	6.505	6.328	6.232	4.3%	↓↓	'1'	'1'
	B-G-H	6.328	6.232	6.232	1.54%	→	'1'	'0'
	G-H-I	6.232	6.232	6.282	0.81%		'0'	'0'
Radial A-F	A-B-C	6.505	6.328	6.249	4.03%	↓↓	'1'	'1'
	B-C-D	6.328	6.249	6.238	1.44%	↓	'1'	'1'
	C-D-E	6.249	6.238	6.163	1.38%	↓	'1'	'1'
	D-E-F	6.238	6.163	6.163	1.21%	→	'1'	'0'

Table C.161: Radial topology / Phase to ground (0 Ω) fault / F_5.

Circuit	3-points window	k_{s_1}	k_{s_2}	k_{s_3}	$\Delta k_{s_{13}}\%$	FS search	$k_{s_1} > k_{s_2}$	$k_{s_2} > k_{s_3}$
Radial A-I	A-B-G	3.281	3.181	3.146	4.22%		'1'	'1'
	B-G-H	3.181	3.146	2.547	21.42%		'1'	'1'
	G-H-I	3.146	2.547	2.547	21.81%	→	'1'	'0'
Radial A-F	A-B-C	3.281	3.181	3.17	3.44%		'1'	'1'
	B-C-D	3.181	3.17	3.159	0.67%		'1'	'1'
	C-D-E	3.17	3.159	3.11	1.94%		1'	'1'
	D-E-F	3.159	3.11	3.12	1.25%		'1'	'0'

Table C.162: Radial topology / Phase to ground (20 Ω) fault / F_5.

Circuit	3-points window	k_{s_1}	k_{s_2}	k_{s_3}	$\Delta k_{s_{13}}\%$	FS search	$k_{s_1} > k_{s_2}$	$k_{s_2} > k_{s_3}$
Radial A-I	A-B-G	9.354	9.118	9.009	3.76%		'1'	'1'
	B-G-H	9.118	9.009	7.598	17.72%	↓	'1'	'1'
	G-H-I	9.009	7.598	7.598	17.48%	→	'1'	'0'
Radial A-F	A-B-C	9.354	9.118	9.245	1.17%		'1'	'0'
	B-C-D	9.118	9.245	9.077	0.45%		'0'	'1'
	C-D-E	9.245	9.077	8.582	7.39%		'1'	'1'
	D-E-F	9.077	8.582	8.733	3.91%		'1'	'0'

Table C.163: Radial topology / Phase to phase (0 Ω) fault / F_5.

Circuit	3-points window	k_{s_1}	k_{s_2}	k_{s_3}	$\Delta k_{s_{13}}\%$	FS search	$k_{s_1} > k_{s_2}$	$k_{s_2} > k_{s_3}$
Radial A-I	A-B-G	1.419	1.363	1.35	5.03%		'1'	'1'
	B-G-H	1.363	1.35	1	29.34%		'1'	'1'
	G-H-I	1.35	1	1	31.32%	→	'1'	'0'
Radial A-F	A-B-C	1.419	1.363	1.348	5.1%		'1'	'1'
	B-C-D	1.363	1.348	1.352	0.8%		'1'	'0'
	C-D-E	1.348	1.352	1.366	1.25%		'0'	'0'
	D-E-F	1.352	1.366	1.357	0.33%		'0'	'1'

Table C.164: Radial topology / Phase to phase (60 Ω) fault / F_5.

Circuit	3-points window	k_{s_1}	k_{s_2}	k_{s_3}	$\Delta k_{s_{13}}\%$	FS search	$k_{s_1} > k_{s_2}$	$k_{s_2} > k_{s_3}$
Radial A-I	A-B-G	6.8	6.615	6.511	4.34%		'1'	'1'
	B-G-H	6.615	6.511	5.489	18.15%	↓	'1'	'1'
	G-H-I	6.511	5.489	5.489	17.54%	→	'1'	'1'
Radial A-F	A-B-C	6.8	6.615	6.524	4.14%		'1'	'1'
	B-C-D	6.615	6.524	6.516	1.51%		'1'	'1'
	C-D-E	6.524	6.516	6.443	1.25%		'1'	'1'
	D-E-F	6.516	6.443	6.392	1.91%		'1'	'1'

Table C.165: Radial topology / Phase to ground (0 Ω) fault / F_6.

Circuit	3-points window	k_{s_1}	k_{s_2}	k_{s_3}	$\Delta k_{s_{13}}\%$	FS search	$k_{s_1} > k_{s_2}$	$k_{s_2} > k_{s_3}$
Radial A-I	A-B-G	3.296	3.195	3.161	4.22%		'1'	'1'
	B-G-H	3.195	3.161	2.559	21.4%		'1'	'1'
	G-H-I	3.161	2.559	2.545	22.33%	→	'1'	'1'
Radial A-F	A-B-C	3.296	3.195	3.185	3.44%		'1'	'1'
	B-C-D	3.195	3.185	3.174	0.67%		'1'	'1'
	C-D-E	3.185	3.174	3.124	1.95%		'1'	'1'
	D-E-F	3.174	3.124	3.135	1.25%		'1'	'0'

Table C.166: Radial topology / Phase to ground (20 Ω) fault / F_6.

Circuit	3-points window	k_{s_1}	k_{s_2}	k_{s_3}	$\Delta k_{s_{13}}\%$	FS search	$k_{s_1} > k_{s_2}$	$k_{s_2} > k_{s_3}$
Radial A-I	A-B-G	9.366	9.13	9.02	3.77%		'1'	'1'
	B-G-H	9.13	9.02	7.608	17.724%		'1'	'1'
	G-H-I	9.02	7.608	7.575	17.9%	→	'1'	'1'
Radial A-F	A-B-C	9.366	9.13	8.257	1.17%		'1'	'0'
	B-C-D	9.13	9.257	9.089	0.453%		'0'	'1'
	C-D-E	9.257	9.089	8.593	7.44%		'1'	'1'
	D-E-F	9.089	8.593	8.743	3.92%		'1'	'0'

Table C.167: Radial topology / Phase to phase (0 Ω) fault / F_6.

Circuit	3-points window	k_{s_1}	k_{s_2}	k_{s_3}	$\Delta k_{s_{13}}\%$	FS search	$k_{s_1} > k_{s_2}$	$k_{s_2} > k_{s_3}$
Radial A-I	A-B-G	1.429	1.373	1.359	5.02%		'1'	'1'
	B-G-H	1.373	1.359	1.008	29.26%		'1'	'1'
	G-H-I	1.359	1.008	1	31.99%	→	'1'	'1'
Radial A-F	A-B-C	1.429	1.373	1.358	5.1%		'1'	'1'
	B-C-D	1.373	1.358	1.362	0.8%		'1'	'0'
	C-D-E	1.358	1.362	1.375	1.25%		'0'	'0'
	D-E-F	1.362	1.375	1.366	0.04%		'0'	'1'

Table C.168: Radial topology / Phase to phase (60 Ω) fault / F_6.

Circuit	3-points window	k_{s_1}	k_{s_2}	k_{s_3}	$\Delta k_{s_{13}}\%$	FS search	$k_{s_1} > k_{s_2}$	$k_{s_2} > k_{s_3}$
Radial A-I	A-B-G	6.83	6.64	6.49	5.11%		'1'	'1'
	B-G-H	6.64	6.49	5.51	18.19%		'1'	'1'
	G-H-I	6.49	5.51	5.48	17.33%	→	'1'	'1'
Radial A-F	A-B-C	6.83	6.64	6.6	3.44%		'1'	'1'
	B-C-D	6.64	6.6	6.45	2.89%		'1'	'1'
	C-D-E	6.6	6.45	6.58	0.31%		'1'	'0'
	D-E-F	6.45	6.58	6.43	0.31%		'0'	'1'

C.4 Distributed Generation

Table C.169: Radial topology / Phase to ground (0 Ω) fault / F_1.

Circuit	3-points window	k_{s_1}	k_{s_2}	k_{s_3}	$\Delta k_{s_{13}}\%$	FS search	$k_{s_1} > k_{s_2}$	$k_{s_2} > k_{s_3}$
Radial A-I	A-B-G	3.18	3.091	3.079	3.239%	↓↓	'1'	'1'
	B-G-H	3.091	3.079	3.079	0.4%	→	'1'	'0'
	G-H-I	3.079	3.079	3.079	0%		'0'	'1'
Radial A-F	A-B-C	3.18	3.091	3.082	3.155%	↓↓	'1'	'1'
	B-C-D	3.091	3.082	3.083	0.27%	→	'1'	'0'
	C-D-E	3.082	3.083	3.122	1.3%		'0'	'0'
	D-E-F	3.083	3.122	3.121	1.22%		'0'	'1'

Table C.170: Radial topology / Phase to ground (20 Ω) fault / F_1.

Circuit	3-points window	k_{s_1}	k_{s_2}	k_{s_3}	$\Delta k_{s_{13}}\%$	FS search	$k_{s_1} > k_{s_2}$	$k_{s_2} > k_{s_3}$
Radial A-I	A-B-G	8.89	8.68	8.65	2.74%	↓↓	'1'	'1'
	B-G-H	8.68	8.65	8.65	0.346%	→	'1'	'0'
	G-H-I	8.65	8.65	8.65	0%		'0'	'0'
Radial A-F	A-B-C	8.89	8.68	8.66	2.63%	↓↓	'1'	'1'
	B-C-D	8.68	8.66	8.66	0.23%	→	'1'	'0'
	C-D-E	8.66	8.66	8.76	1.15%		'0'	'0'
	D-E-F	8.66	8.76	8.76	1.14%		'0'	'0'

Table C.171: Radial topology / Phase to phase (0 Ω) fault / F_1.

Circuit	3-points window	k_{s_1}	k_{s_2}	k_{s_3}	$\Delta k_{s_{13}}\%$	FS search	$k_{s_1} > k_{s_2}$	$k_{s_2} > k_{s_3}$
Radial A-I	A-B-G	1.048	1.005	1	4.72%	↓↓	'1'	'1'
	B-G-H	1.005	1	1	0.5%	→	'1'	'0'
	G-H-I	1	1	1	0%		'0'	'0'
Radial A-F	A-B-C	1.048	1.005	1.001	4.617%	↓↓	'1'	'1'
	B-C-D	1.005	1.001	1.002	0.29%	→	'1'	'0'
	C-D-E	1.001	1.002	1.023	2.18%		'0'	'0'
	D-E-F	1.002	1.023	01.024	2.16%		'0'	'0'

Table C.172: Radial topology / Phase to phase (60 Ω) fault / F_1.

Circuit	3-points window	k_{s_1}	k_{s_2}	k_{s_3}	$\Delta k_{s_{13}}\%$	FS search	$k_{s_1} > k_{s_2}$	$k_{s_2} > k_{s_3}$
Radial A-I	A-B-G	7.73	7.551	7.528	2.66%	↓↓	'1'	'1'
	B-G-H	7.551	7.528	7.528	0.31%	→	'1'	'0'
	G-H-I	7.528	7.528	7.528	0%		'0'	'0'
Radial A-F	A-B-C	7.73	7.551	7.533	2.58%	↓↓	'1'	'1'
	B-C-D	7.551	7.533	7.537	0.2%	→	'1'	'0'
	C-D-E	7.533	7.537	7.621	1.15%		'0'	'0'
	D-E-F	7.537	7.621	7.62	1.05%		'0'	'1'

Table C.173: Radial topology / Phase to ground (0 Ω) fault / F_2.

Circuit	3-points window	k_{s_1}	k_{s_2}	k_{s_3}	$\Delta k_{s_{13}}\%$	FS search	$k_{s_1} > k_{s_2}$	$k_{s_2} > k_{s_3}$
Radial A-I	A-B-G	3.83	3.727	3.713	3.113%		'1'	'1'
	B-G-H	3.727	3.713	3.713	0.38%		'1'	'0'
	G-H-I	3.713	3.713	3.713	0%		'0'	'0'
Radial A-F	A-B-C	3.83	3.727	3.66	4.47%		'1'	'1'
	B-C-D	3.727	3.66	3.646	2.21%		'1'	'1'
	C-D-E	3.66	3.646	2.889	22.77%		'1'	'1'
	D-E-F	3.646	2.889	2.889	24.09%	→	'1'	'0'

Table C.174: Radial topology / Phase to ground (20 Ω) fault / F_2.

Circuit	3-points window	k_{s_1}	k_{s_2}	k_{s_3}	$\Delta k_{s_{13}}\%$	FS search	$k_{s_1} > k_{s_2}$	$k_{s_2} > k_{s_3}$
Radial A-I	A-B-G	9.29	9.07	9.05	2.62%		'1'	'1'
	B-G-H	9.07	9.05	9.05	0.22%		'1'	'0'
	G-H-I	9.05	9.05	9.05	0%		'0'	'0'
Radial A-F	A-B-C	9.29	9.07	8.96	3.623%		'1'	'1'
	B-C-D	9.07	8.96	8.94	1.45%		'1'	'1'
	C-D-E	8.96	8.94	7.58	16.24%		'1'	'1'
	D-E-F	8.94	7.58	7.58	16.92%	→	'1'	'0'

Table C.175: Radial topology / Phase to phase (0 Ω) fault / F_2.

Circuit	3-points window	k_{s_1}	k_{s_2}	k_{s_3}	$\Delta k_{s_{13}}\%$	FS search	$k_{s_1} > k_{s_2}$	$k_{s_2} > k_{s_3}$
Radial A-I	A-B-G	1.504	1.449	1.442	4.23%		'1'	'1'
	B-G-H	1.449	1.442	1.442	0.46%		'1'	'0'
	G-H-I	1.442	1.442	1.442	0%		'0'	'0'
Radial A-F	A-B-C	1.504	1.449	1.417	5.97%		'1'	'1'
	B-C-D	1.449	1.417	1.409	2.82%		'1'	'1'
	C-D-E	1.417	1.409	1.006	32.176%		'1'	'1'
	D-E-F	1.409	1.006	1.007	35.24%	→	'1'	'0'

Table C.176: Radial topology / Phase to phase (60 Ω) fault / F_2.

Circuit	3-points window	k_{s_1}	k_{s_2}	k_{s_3}	$\Delta k_{s_{13}}\%$	FS search	$k_{s_1} > k_{s_2}$	$k_{s_2} > k_{s_3}$
Radial A-I	A-B-G	8.052	7.866	7.842	2.65%		'1'	'1'
	B-G-H	7.866	7.842	7.842	0.31%		'1'	'0'
	G-H-I	7.842	7.842	7.842	0%		'0'	'0'
Radial A-F	A-B-C	8.052	7.866	7.754	3.78%		'1'	'1'
	B-C-D	7.866	7.754	7.725	1.81%		'1'	'1'
	C-D-E	7.754	7.725	6.33	19.58%		'1'	'1'
	D-E-F	7.725	6.33	6.33	20.43%	→	'1'	'0'

Table C.177: Radial topology / Phase to ground (0 Ω) fault / F_3.

Circuit	3-points window	k_{s_1}	k_{s_2}	k_{s_3}	$\Delta k_{s_{13}}\%$	FS search	$k_{s_1} > k_{s_2}$	$k_{s_2} > k_{s_3}$
Radial A-I	A-B-G	4.482	4.365	4.35	3.014%		'1'	'1'
	B-G-H	4.365	4.35	4.35	0.36%		'1'	'1'
	G-H-I	4.35	4.35	4.35	08%		'0'	'0'
Radial A-F	A-B-C	4.482	4.365	4.293	4.31%		'1'	'1'
	B-C-D	4.365	4.293	4.274	2.11%		'1'	'1'
	C-D-E	4.293	4.274	2.744	41.074%		'1'	'1'
	D-E-F	4.274	2.744	2.73	47.54%	→	'1'	'1'

Table C.178: Radial topology / Phase to ground (20 Ω) fault / F_3.

Circuit	3-points window	k_{s_1}	k_{s_2}	k_{s_3}	$\Delta k_{s_{13}}\%$	FS search	$k_{s_1} > k_{s_2}$	$k_{s_2} > k_{s_3}$
Radial A-I	A-B-G	9.72	9.49	9.47	2.615%		'1'	'1'
	B-G-H	9.49	9.47	9.47	0.21%		'1'	'0'
	G-H-I	9.47	9.47	9.47	0%		'0'	'0'
Radial A-F	A-B-C	9.72	9.49	9.38	3.57%		'1'	'1'
	B-C-D	9.49	9.38	9.35	1.488%		'1'	'1'
	C-D-E	9.38	9.35	6.78	30.57%		'1'	'1'
	D-E-F	9.35	6.78	6.75	34.09%	→	'1'	'1'

Table C.179: Radial topology / Phase to phase (0 Ω) fault / F_3.

Circuit	3-points window	k_{s_1}	k_{s_2}	k_{s_3}	$\Delta k_{s_{13}}\%$	FS search	$k_{s_1} > k_{s_2}$	$k_{s_2} > k_{s_3}$
Radial A-I	A-B-G	1.968	1.902	1.894	3.85%		'1'	'1'
	B-G-H	1.902	1.894	1.894	0.43%		'1'	'0'
	G-H-I	1.894	1.894	1.894	0%		'0'	'0'
Radial A-F	A-B-C	1.968	1.902	1.863	5.49%		'1'	'1'
	B-C-D	1.902	1.863	1.854	2.59%		'1'	'1'
	C-D-E	1.863	1.854	1.006	54.43%		'1'	'1'
	D-E-F	1.854	1.006	1	66.37%	→	'1'	'1'

Table C.180: Radial topology / Phase to phase (60 Ω) fault / F_3.

Circuit	3-points window	k_{s_1}	k_{s_2}	k_{s_3}	$\Delta k_{s_{13}}\%$	FS search	$k_{s_1} > k_{s_2}$	$k_{s_2} > k_{s_3}$
Radial A-I	A-B-G	8.397	8.204	8.179	2.65%		'1'	'1'
	B-G-H	8.204	8.179	8.179	0.31%		'1'	'1'
	G-H-I	8.179	8.179	8.179	0%		'0'	'0'
Radial A-F	A-B-C	8.397	8.204	8.087	3.77%		'1'	'1'
	B-C-D	8.204	8.087	8.058	1.8%		'1'	'1'
	C-D-E	8.087	8.058	5.484	36.11%		'1'	'1'
	D-E-F	8.058	5.484	5.46	41.03%	→	'1'	'1'

Table C.181: Radial topology / Phase to ground (0 Ω) fault / F_4.

Circuit	3-points window	k_{s_1}	k_{s_2}	k_{s_3}	$\Delta k_{s_{13}}\%$	FS search	$k_{s_1} > k_{s_2}$	$k_{s_2} > k_{s_3}$
Radial A-I	A-B-G	3.189	3.1	3.077	3.569%	↓↓	'1'	'1'
	B-G-H	3.1	3.077	3.077	0.73%	→	'1'	'0'
	G-H-I	3.077	3.077	3.077	0%		'0'	'0'
Radial A-F	A-B-C	3.189	3.1	3.089	3.15%	↓↓	'1'	'1'
	B-C-D	3.1	3.089	3.091	0.27%	→	'1'	'0'
	C-D-E	3.089	3.091	3.13	1.3%		'0'	'0'
	D-E-F	3.091	3.13	3.129	1.22%		'0'	'1'

Table C.182: Radial topology / Phase to ground (20 Ω) fault / F_4.

Circuit	3-points window	k_{s_1}	k_{s_2}	k_{s_3}	$\Delta k_{s_{13}}\%$	FS search	$k_{s_1} > k_{s_2}$	$k_{s_2} > k_{s_3}$
Radial A-I	A-B-G	8.89	8.69	8.64	2.86%	↓↓	'1'	'1'
	B-G-H	8.69	8.64	8.64	0.578%	→	'1'	'0'
	G-H-I	8.64	8.64	8.64	0%		'0'	'0'
Radial A-F	A-B-C	8.89	8.69	8.67	2.514%	↓↓	'1'	'1'
	B-C-D	8.69	8.67	8.67	0.231%	→	'1'	'0'
	C-D-E	8.67	8.67	8.77	1.148%		'0'	'0'
	D-E-F	8.67	8.77	8.76	1.03%		'0'	'1'

Table C.183: Radial topology / Phase to phase (0 Ω) fault / F_4.

Circuit	3-points window	k_{s_1}	k_{s_2}	k_{s_3}	$\Delta k_{s_{13}}\%$	FS search	$k_{s_1} > k_{s_2}$	$k_{s_2} > k_{s_3}$
Radial A-I	A-B-G	1.053	1.01	1	5.19%	↓↓	'1'	'1'
	B-G-H	1.01	1	1	1%	→	'1'	'0'
	G-H-I	1	1	1	0%		'0'	'0'
Radial A-F	A-B-C	1.053	1.01	1.006	4.59%	↓↓	'1'	'1'
	B-C-D	1.01	1.006	1.007	0.29%	→	'1'	'0'
	C-D-E	1.006	1.007	1.028	2.17%		'0'	'0'
	D-E-F	1.007	1.028	1.029	2.15%		'0'	'0'

Table C.184: Radial topology / Phase to phase (60 Ω) fault / F_4.

Circuit	3-points window	k_{s_1}	k_{s_2}	k_{s_3}	$\Delta k_{s_{13}}\%$	FS search	$k_{s_1} > k_{s_2}$	$k_{s_2} > k_{s_3}$
Radial A-I	A-B-G	7.735	7.556	7.512	2.94%	↓↓	'1'	'1'
	B-G-H	7.556	7.512	7.512	0.59%	→	'1'	'0'
	G-H-I	7.512	7.512	7.512	0%		'0'	'0'
Radial A-F	A-B-C	7.735	7.556	7.538	2.59%	↓↓	'1'	'1'
	B-C-D	7.556	7.538	7.542	0.2%	→	'1'	'0'
	C-D-E	7.538	7.542	7.626	1.16%		'0'	'0'
	D-E-F	7.542	7.626	7.626	1.05%		'0'	'0'

Table C.185: Radial topology / Phase to ground (0 Ω) fault / F_5.

Circuit	3-points window	k_{s_1}	k_{s_2}	k_{s_3}	$\Delta k_{s_{13}}\%$	FS search	$k_{s_1} > k_{s_2}$	$k_{s_2} > k_{s_3}$
Radial A-I	A-B-G	3.791	3.688	3.662	3.45%		'1'	'1'
	B-G-H	3.688	3.662	2.872	23.95%		'1'	'1'
	G-H-I	3.662	2.872	2.872	25.2%	→	'1'	'0'
Radial A-F	A-B-C	3.791	3.688	3.677	3.045%		'1'	'1'
	B-C-D	3.688	3.677	3.679	0.25%		'1'	'0'
	C-D-E	3.677	3.679	3.725	1.29%		0'	'0'
	D-E-F	3.679	3.725	3.724	1.21%		'0'	'1'

Table C.186: Radial topology / Phase to ground (20 Ω) fault / F_5.

Circuit	3-points window	k_{s_1}	k_{s_2}	k_{s_3}	$\Delta k_{s_{13}}\%$	FS search	$k_{s_1} > k_{s_2}$	$k_{s_2} > k_{s_3}$
Radial A-I	A-B-G	9.32	9.1	9.05	2.948%		'1'	'1'
	B-G-H	9.1	9.05	7.61	17.35%		'1'	'1'
	G-H-I	9.05	7.61	7.61	17.8%	→	'1'	'0'
Radial A-F	A-B-C	9.32	9.1	9.08	2.618%		'1'	'1'
	B-C-D	9.1	9.08	9.08	0.22%		'1'	'0'
	C-D-E	9.08	9.08	9.19	1.2%		'0'	'0'
	D-E-F	9.08	9.19	9.18	1.092%		'0'	'1'

Table C.187: Radial topology / Phase to phase (0 Ω) fault / F_5.

Circuit	3-points window	k_{s_1}	k_{s_2}	k_{s_3}	$\Delta k_{s_{13}}\%$	FS search	$k_{s_1} > k_{s_2}$	$k_{s_2} > k_{s_3}$
Radial A-I	A-B-G	1.488	1.434	1.421	4.63%		'1'	'1'
	B-G-H	1.434	1.421	1	33.78%		'1'	'1'
	G-H-I	1.421	1	1	36.91%	→	'1'	'0'
Radial A-F	A-B-C	1.488	1.434	1.429	4.07%		'1'	'1'
	B-C-D	1.434	1.429	1.43	0.28%		'1'	'0'
	C-D-E	1.429	1.43	1.456	1.877%		'0'	'0'
	D-E-F	1.43	1.456	1.456	1.796%		'0'	'0'

Table C.188: Radial topology / Phase to phase (60 Ω) fault / F_5.

Circuit	3-points window	k_{s_1}	k_{s_2}	k_{s_3}	$\Delta k_{s_{13}}\%$	FS search	$k_{s_1} > k_{s_2}$	$k_{s_2} > k_{s_3}$
Radial A-I	A-B-G	8.081	7.895	7.848	2.93%		'1'	'1'
	B-G-H	7.895	7.848	6.374	20.63%		'1'	'1'
	G-H-I	7.848	6.374	6.374	21.47%	→	'1'	'0'
Radial A-F	A-B-C	8.081	7.895	7.876	2.58%		'1'	'1'
	B-C-D	7.895	7.876	7.879	0.19%		'1'	'0'
	C-D-E	7.876	7.879	7.968	1.16%		'0'	'0'
	D-E-F	7.879	7.968	7.968	1.13%		'0'	'0'

Table C.189: Radial topology / Phase to ground (0 Ω) fault / F_6.

Circuit	3-points window	k_{s_1}	k_{s_2}	k_{s_3}	$\Delta k_{s_{13}}\%$	FS search	$k_{s_1} > k_{s_2}$	$k_{s_2} > k_{s_3}$
Radial A-I	A-B-G	3.808	3.705	3.68	3.448%		'1'	'1'
	B-G-H	3.705	3.68	2.886	23.93%		'1'	'1'
	G-H-I	3.68	2.886	2.869	25.78%	→	'1'	'1'
Radial A-F	A-B-C	3.808	3.705	3.695	3.042%		'1'	'1'
	B-C-D	3.705	3.695	3.696	0.25%		'1'	'0'
	C-D-E	3.695	3.696	3.743	1.293%		'0'	'0'
	D-E-F	3.696	3.743	3.741	1.21%		'0'	'1'

Table C.190: Radial topology / Phase to ground (20 Ω) fault / F_6.

Circuit	3-points window	k_{s_1}	k_{s_2}	k_{s_3}	$\Delta k_{s_{13}}\%$	FS search	$k_{s_1} > k_{s_2}$	$k_{s_2} > k_{s_3}$
Radial A-I	A-B-G	9.33	9.11	9.06	2.94%		'1'	'1'
	B-G-H	9.11	9.06	7.62	17.33%		'1'	'1'
	G-H-I	9.06	7.62	7.59	18.17%	→	'1'	'1'
Radial A-F	A-B-C	9.33	9.11	9.09	2.61%		'1'	'1'
	B-C-D	9.11	9.09	9.1	0.11%		'1'	'0'
	C-D-E	9.09	9.1	9.2	1.2%		'0'	'0'
	D-E-F	9.1	9.2	9.2	1.09%		'0'	'0'

Table C.191: Radial topology / Phase to phase (0 Ω) fault / F_6.

Circuit	3-points window	k_{s_1}	k_{s_2}	k_{s_3}	$\Delta k_{s_{13}}\%$	FS search	$k_{s_1} > k_{s_2}$	$k_{s_2} > k_{s_3}$
Radial A-I	A-B-G	1.499	1.445	1.432	4.59%		'1'	'1'
	B-G-H	1.445	1.432	1.009	33.66%		'1'	'1'
	G-H-I	1.432	1.009	1	37.67%	→	'1'	'1'
Radial A-F	A-B-C	1.499	1.445	1.44	4.04%		'1'	'1'
	B-C-D	1.445	1.44	1.441	0.28%		'1'	'0'
	C-D-E	1.44	1.441	1.467	1.86%		'0'	'0'
	D-E-F	1.441	1.467	1.467	1.78%		'0'	'0'

Table C.192: Radial topology / Phase to phase (60 Ω) fault / F_6.

Circuit	3-points window	k_{s_1}	k_{s_2}	k_{s_3}	$\Delta k_{s_{13}}\%$	FS search	$k_{s_1} > k_{s_2}$	$k_{s_2} > k_{s_3}$
Radial A-I	A-B-G	8.091	7.904	7.858	2.93%		'1'	'1'
	B-G-H	7.904	7.858	6.382	20.63%		'1'	'1'
	G-H-I	7.858	6.382	6.35	21.99%	→	'1'	'1'
Radial A-F	A-B-C	8.091	7.904	7.886	2.58%		'1'	'1'
	B-C-D	7.904	7.886	7.889	0.2%		'1'	'0'
	C-D-E	7.886	7.889	7.977	1.16%		'0'	'0'
	D-E-F	7.889	7.977	7.977	1.13%		'0'	'0'

Table C.193: PV inverters FRT responses / Radial topology / Phase to ground (0 Ω) fault.

PV inverter	Loading level	Network conditions	Fault location					
			F_1	F_2	F_3	F_4	F_5	F_6
PV_1	100%	$V_{3\phi}$ [pu]	0.686	0.888	0.92	0.73	0.887	0.888
		$V_{1\phi}$ [pu]	0.71	0.892	0.919	0.758	0.889	0.891
		V_2/V_1	0.214	0.045	0.026	0.168	0.047	0.046
PV_2	25%	$V_{3\phi}$ [pu]	0.684	0.888	0.92	0.73	0.887	0.888
		$V_{1\phi}$ [pu]	0.71	0.892	0.919	0.758	0.889	0.891
		V_2/V_1	0.214	0.045	0.026	0.168	0.047	0.046
PV_3	75%	$V_{3\phi}$ [pu]	0.598	0.866	0.918	0.643	0.863	0.865
		$V_{1\phi}$ [pu]	0.567	0.844	0.889	0.636	0.839	0.842
		V_2/V_1	0.415	0.079	0.045	0.316	0.081	0.08
PV_4	100%	$V_{3\phi}$ [pu]	0.522	0.841	0.9	0.522	0.833	0.836
		$V_{1\phi}$ [pu]	0.53	0.821	0.878	0.53	0.811	0.814
		V_2/V_1	0.476	0.098	0.055	0.476	0.104	0.102
PV_5	100%	$V_{3\phi}$ [pu]	0.522	0.841	0.9	0.522	0.833	0.836
		$V_{1\phi}$ [pu]	0.53	0.821	0.878	0.53	0.811	0.814
		V_2/V_1	0.476	0.098	0.055	0.476	0.104	0.102
PV_6	100%	$V_{3\phi}$ [pu]	0.515	0.833	0.893	0.515	0.515	0.519
		$V_{1\phi}$ [pu]	0.511	0.804	0.862	0.511	0.511	0.517
		V_2/V_1	0.471	0.098	0.055	0.471	0.471	0.459
PV_7	100%	$V_{3\phi}$ [pu]	0.515	0.833	0.893	0.515	0.515	0.519
		$V_{1\phi}$ [pu]	0.511	0.804	0.862	0.511	0.511	0.517
		V_2/V_1	0.471	0.098	0.055	0.471	0.471	0.459
PV_8	50%	$V_{3\phi}$ [pu]	0.559	0.817	0.883	0.559	0.559	0.559
		$V_{1\phi}$ [pu]	0.549	0.824	0.885	0.549	0.55	0.55

Continued on next page

Table C.193 – *Continued from previous page*

PV inverter	Loading level	Network conditions	Fault location					
			F_1	F_2	F_3	F_4	F_5	F_6
		V_2/V_1	0.473	0.105	0.059	0.473	0.473	0.474
PV_9	100%	$V_{3\phi}$ [pu]	0.521	0.84	0.898	0.527	0.837	0.839
		$V_{1\phi}$ [pu]	0.514	0.805	0.864	0.522	0.8	0.803
		V_2/V_1	0.47	0.097	0.054	0.45	0.1	0.098
PV_{10}	25%	$V_{3\phi}$ [pu]	0.519	0.836	0.894	0.525	0.833	0.835
		$V_{1\phi}$ [pu]	0.514	0.805	0.864	0.522	0.8	0.803
		V_2/V_1	0.47	0.097	0.054	0.45	0.1	0.098
PV_{11}	25%	$V_{3\phi}$ [pu]	0.573	0.968	0.997	0.58	0.97	0.972
		$V_{1\phi}$ [pu]	0.559	0.895	0.948	0.569	0.9	0.902
		V_2/V_1	0.451	0.108	0.06	0.432	0.103	0.101
PV_{12}	50%	$V_{3\phi}$ [pu]	0.576	0.972	1.002	0.582	0.975	0.976
		$V_{1\phi}$ [pu]	0.559	0.895	0.948	0.569	0.9	0.902
		V_2/V_1	0.451	0.108	0.06	0.432	0.103	0.101
PV_{13}	50%	$V_{3\phi}$ [pu]	0.566	0.566	0.568	0.572	0.817	0.82
		$V_{1\phi}$ [pu]	0.553	0.554	0.562	0.562	0.822	0.825
		V_2/V_1	0.463	0.464	0.456	0.444	0.106	0.104
PV_{14}	50%	$V_{3\phi}$ [pu]	0.558	0.558	0.558	0.565	0.821	0.823
		$V_{1\phi}$ [pu]	0.57	0.57	0.571	0.578	0.839	0.842
		V_2/V_1	0.491	0.492	0.492	0.47	0.11	0.108

Table C.194: PV inverters FRT responses / Radial topology / Phase to ground (20 Ω) fault.

PV inverter	Loading level	Network conditions	Fault location					
			F_1	F_2	F_3	F_4	F_5	F_6
PV_1	100%	$V_{3\phi}$ [pu]	0.85	0.904	0.926	0.858	0.903	0.903
		$V_{1\phi}$ [pu]	0.835	0.908	0.927	0.846	0.907	0.908
		V_2/V_1	0.083	0.036	0.023	0.075	0.037	0.036
PV_2	25%	$V_{3\phi}$ [pu]	0.85	0.904	0.926	0.858	0.903	0.903
		$V_{1\phi}$ [pu]	0.835	0.908	0.927	0.846	0.907	0.908
		V_2/V_1	0.083	0.036	0.023	0.075	0.037	0.036
PV_3	75%	$V_{3\phi}$ [pu]	0.809	0.892	0.928	0.82	0.889	0.891
		$V_{1\phi}$ [pu]	0.748	0.871	0.902	0.766	0.869	0.871
		V_2/V_1	0.147	0.062	0.039	0.133	0.064	0.063
PV_4	100%	$V_{3\phi}$ [pu]	0.793	0.869	0.91	0.769	0.862	0.864
		$V_{1\phi}$ [pu]	0.746	0.863	0.894	0.725	0.857	0.858
		V_2/V_1	0.153	0.077	0.048	0.175	0.081	0.08
PV_5	25%	$V_{3\phi}$ [pu]	0.793	0.869	0.91	0.769	0.862	0.864
		$V_{1\phi}$ [pu]	0.746	0.863	0.894	0.725	0.857	0.858
		V_2/V_1	0.153	0.077	0.048	0.175	0.081	0.08
PV_6	100%	$V_{3\phi}$ [pu]	0.788	0.862	0.904	0.764	0.579	0.582
		$V_{1\phi}$ [pu]	0.736	0.846	0.877	0.715	0.548	0.554
		V_2/V_1	0.152	0.076	0.048	0.174	0.338	0.331
PV_7	50%	$V_{3\phi}$ [pu]	0.788	0.862	0.904	0.764	0.579	0.582
		$V_{1\phi}$ [pu]	0.736	0.846	0.877	0.715	0.548	0.554
		V_2/V_1	0.152	0.076	0.048	0.174	0.338	0.331
PV_8	50%	$V_{3\phi}$ [pu]	0.782	0.848	0.894	0.755	0.629	0.628
		$V_{1\phi}$ [pu]	0.742	0.864	0.901	0.717	0.589	0.589

Continued on next page

Table C.194 – *Continued from previous page*

PV inverter	Loading level	Network conditions	Fault location					
			F_1	F_2	F_3	F_4	F_5	F_6
		V_2/V_1	0.161	0.081	0.051	0.184	0.339	0.341
PV_9	100%	$V_{3\phi}$ [pu]	0.794	0.868	0.908	0.775	0.865	0.867
		$V_{1\phi}$ [pu]	0.748	0.847	0.879	0.735	0.844	0.845
		V_2/V_1	0.151	0.076	0.047	0.167	0.078	0.076
PV_{10}	25%	$V_{3\phi}$ [pu]	0.864	0.79	0.904	0.771	0.861	0.849
		$V_{1\phi}$ [pu]	0.748	0.847	0.879	0.735	0.844	0.868
		V_2/V_1	0.151	0.076	0.047	0.167	0.078	0.081
PV_{11}	25%	$V_{3\phi}$ [pu]	0.955	0.98	1.003	0.945	0.982	0.983
		$V_{1\phi}$ [pu]	0.81	0.938	0.969	0.796	0.94	0.942
		V_2/V_1	0.155	0.084	0.053	0.171	0.08	0.079
PV_{12}	50%	$V_{3\phi}$ [pu]	0.955	0.98	1.008	0.95	0.987	0.988
		$V_{1\phi}$ [pu]	0.81	0.938	0.969	0.796	0.94	0.942
		V_2/V_1	0.155	0.084	0.053	0.171	0.08	0.079
PV_{13}	50%	$V_{3\phi}$ [pu]	0.786	0.633	0.606	0.764	0.847	0.849
		$V_{1\phi}$ [pu]	0.749	0.601	0.59	0.731	0.867	0.868
		V_2/V_1	0.159	0.334	0.377	0.175	0.082	0.081
PV_{14}	50%	$V_{3\phi}$ [pu]	0.785	0.627	0.596	0.763	0.852	0.854
		$V_{1\phi}$ [pu]	0.751	0.587	0.572	0.732	0.879	0.881
		V_2/V_1	0.166	0.351	0.405	0.183	0.086	0.084

Table C.195: PV inverters FRT responses / Radial topology / Phase to phase (0 Ω) fault.

PV inverter	Loading level	Network conditions	Fault location					
			F_1	F_2	F_3	F_4	F_5	F_6
PV_1	100%	$V_{3\phi}$ [pu]	0.421	0.804	0.874	0.495	0.8	0.803
		$V_{1\phi}$ [pu]	0.44	0.832	0.887	0.533	0.829	0.832
		V_2/V_1	0.278	0.047	0.027	0.207	0.049	0.048
PV_2	25%	$V_{3\phi}$ [pu]	0.421	0.804	0.874	0.495	0.8	0.803
		$V_{1\phi}$ [pu]	0.44	0.832	0.887	0.533	0.829	0.832
		V_2/V_1	0.278	0.047	0.027	0.207	0.049	0.048
PV_3	75%	$V_{3\phi}$ [pu]	0.223	0.739	0.84	0.326	0.733	0.738
		$V_{1\phi}$ [pu]	0.061	0.751	0.835	0.268	0.746	0.75
		V_2/V_1	0.832	0.085	0.047	0.463	0.088	0.086
PV_4	100%	$V_{3\phi}$ [pu]	0.218	0.682	0.802	0.218	0.665	0.671
		$V_{1\phi}$ [pu]	0.095	0.71	0.816	0.095	0.696	0.701
		V_2/V_1	0.827	0.109	0.057	0.828	0.117	0.114
PV_5	100%	$V_{3\phi}$ [pu]	0.218	0.682	0.802	0.218	0.665	0.671
		$V_{1\phi}$ [pu]	0.095	0.71	0.816	0.095	0.696	0.701
		V_2/V_1	0.827	0.109	0.057	0.828	0.117	0.114
PV_6	100%	$V_{3\phi}$ [pu]	0.193	0.681	0.797	0.193	0.193	0.197
		$V_{1\phi}$ [pu]	0.018	0.7	0.802	0.018	0.018	0.023
		V_2/V_1	1.002	0.109	0.057	1.003	1.002	0.949
PV_7	100%	$V_{3\phi}$ [pu]	0.193	0.681	0.797	0.193	0.193	0.197
		$V_{1\phi}$ [pu]	0.018	0.7	0.802	0.118	0.018	0.023
		V_2/V_1	1.002	0.109	0.057	1.003	1.002	0.949
PV_8	50%	$V_{3\phi}$ [pu]	0.211	0.662	0.787	0.211	0.211	0.211
		$V_{1\phi}$ [pu]	0.012	0.703	0.817	0.012	0.012	0.012

Continued on next page

Table C.195 – *Continued from previous page*

PV inverter	Loading level	Network conditions	Fault location					
			F_1	F_2	F_3	F_4	F_5	F_6
		V_2/V_1	1	0.117	0.062	1.001	1.001	1.001
PV_9	100%	$V_{3\phi}$ [pu]	0.212	0.687	0.809	0.221	0.682	0.687
		$V_{1\phi}$ [pu]	0.144	0.708	0.812	0.147	0.704	0.708
		V_2/V_1	0.802	0.109	0.057	0.748	0.112	0.109
PV_{10}	25%	$V_{3\phi}$ [pu]	0.211	0.684	0.805	0.22	0.679	0.683
		$V_{1\phi}$ [pu]	0.144	0.708	0.812	0.147	0.704	0.708
		V_2/V_1	0.802	0.109	0.057	0.748	0.112	0.109
PV_{11}	25%	$V_{3\phi}$ [pu]	0.312	0.815	0.955	0.335	0.898	0.903
		$V_{1\phi}$ [pu]	0.202	0.77	0.9	0.175	0.815	0.82
		V_2/V_1	0.782	0.122	0.064	0.726	0.116	0.113
PV_{12}	50%	$V_{3\phi}$ [pu]	0.314	0.818	0.96	0.337	0.902	0.907
		$V_{1\phi}$ [pu]	0.202	0.77	0.9	0.175	0.815	0.82
		V_2/V_1	0.782	0.122	0.064	0.726	0.116	0.113
PV_{13}	50%	$V_{3\phi}$ [pu]	0.207	0.208	0.21	0.214	0.66	0.666
		$V_{1\phi}$ [pu]	0.014	0.014	0.019	0.031	0.704	0.709
		V_2/V_1	1	1.001	0.967	0.917	0.118	0.116
PV_{14}	50%	$V_{3\phi}$ [pu]	0.219	0.22	0.22	0.227	0.655	0.661
		$V_{1\phi}$ [pu]	0.004	0.004	0.003	0.003	0.707	0.712
		V_2/V_1	0.999	1	1	0.916	0.124	0.121

Table C.196: PV inverters FRT responses / Radial topology / Phase to phase (60 Ω) fault.

PV inverter	Loading level	Network conditions	Fault location					
			F_1	F_2	F_3	F_4	F_5	F_6
PV_1	100%	$V_{3\phi}$ [pu]	0.908	0.912	0.919	0.908	0.911	0.912
		$V_{1\phi}$ [pu]	0.912	0.916	0.922	0.913	0.916	0.916
		V_2/V_1	0.023	0.018	0.014	0.022	0.018	0.018
PV_2	25%	$V_{3\phi}$ [pu]	0.908	0.912	0.919	0.908	0.911	0.912
		$V_{1\phi}$ [pu]	0.912	0.916	0.922	0.913	0.916	0.916
		V_2/V_1	0.023	0.018	0.014	0.022	0.018	0.018
PV_3	75%	$V_{3\phi}$ [pu]	0.898	0.905	0.917	0.899	0.903	0.904
		$V_{1\phi}$ [pu]	0.879	0.884	0.894	0.88	0.883	0.884
		V_2/V_1	0.039	0.03	0.024	0.038	0.031	0.03
PV_4	100%	$V_{3\phi}$ [pu]	0.893	0.881	0.896	0.871	0.877	0.877
		$V_{1\phi}$ [pu]	0.883	0.874	0.887	0.864	0.871	0.871
		V_2/V_1	0.04	0.037	0.03	0.049	0.039	0.039
PV_5	100%	$V_{3\phi}$ [pu]	0.893	0.881	0.896	0.871	0.877	0.877
		$V_{1\phi}$ [pu]	0.883	0.874	0.887	0.864	0.871	0.871
		V_2/V_1	0.04	0.037	0.03	0.049	0.039	0.039
PV_6	100%	$V_{3\phi}$ [pu]	0.886	0.874	0.889	0.864	0.686	0.686
		$V_{1\phi}$ [pu]	0.866	0.858	0.87	0.848	0.693	0.694
		V_2/V_1	0.04	0.037	0.03	0.048	0.144	0.143
PV_7	100%	$V_{3\phi}$ [pu]	0.886	0.874	0.889	0.864	0.686	0.686
		$V_{1\phi}$ [pu]	0.866	0.858	0.87	0.848	0.693	0.694
		V_2/V_1	0.04	0.037	0.03	0.048	0.144	0.143
PV_8	50%	$V_{3\phi}$ [pu]	0.874	0.861	0.877	0.85	0.666	0.661
		$V_{1\phi}$ [pu]	0.888	0.878	0.891	0.868	0.707	0.702

Continued on next page

Table C.196 – *Continued from previous page*

PV inverter	Loading level	Network conditions	Fault location					
			F_1	F_2	F_3	F_4	F_5	F_6
		V_2/V_1	0.043	0.04	0.032	0.052	0.154	0.156
PV_9	100%	$V_{3\phi}$ [pu]	0.892	0.881	0.894	0.874	0.879	0.88
		$V_{1\phi}$ [pu]	0.87	0.863	0.875	0.855	0.862	0.862
		V_2/V_1	0.04	0.037	0.03	0.46	0.037	0.037
PV_{10}	25%	$V_{3\phi}$ [pu]	0.888	0.876	0.89	0.869	0.875	0.875
		$V_{1\phi}$ [pu]	0.87	0.863	0.875	0.855	0.862	0.862
		V_2/V_1	0.04	0.037	0.03	0.046	0.037	0.037
PV_{11}	25%	$V_{3\phi}$ [pu]	1.002	0.987	0.997	0.991	0.992	0.992
		$V_{1\phi}$ [pu]	0.961	0.949	0.962	0.953	0.956	0. 956
		V_2/V_1	0.04	0.041	0.033	0.048	0.038	0.038
PV_{12}	50%	$V_{3\phi}$ [pu]	1.006	0.992	1.001	0.996	0.997	0.997
		$V_{1\phi}$ [pu]	0.961	0.949	0.962	0.953	0.956	0.956
		V_2/V_1	0.04	0.041	0.033	0.048	0.038	0.038
PV_{13}	50%	$V_{3\phi}$ [pu]	0.877	0.661	0.541	0.855	0.862	0.863
		$V_{1\phi}$ [pu]	0.891	0.702	0.58	0.874	0.88	0.881
		V_2/V_1	0.042	0.154	0.237	0.049	0.04	0.039
PV_{14}	50%	$V_{3\phi}$ [pu]	0.883	0.655	0.525	0.861	0.868	0.868
		$V_{1\phi}$ [pu]	0.91	0.711	0.576	0.892	0.897	0.898
		V_2/V_1	0.44	0.162	0.255	0.051	0.041	0.041

Tables C.197 to C.217 enclose all 3-points windows and associated data for the same type of faults at locations F_1 to F_6 respectively.

Table C.197: Radial topology / Phase to ground (0 Ω) fault / F_1.

Circuit	3-points window	k_{s_1}	k_{s_2}	k_{s_3}	$\Delta k_{s_{13}}\%$	FS search	$k_{s_1} > k_{s_2}$	$k_{s_2} > k_{s_3}$
Radial A-I	A-B-G	4.5	2.2	2	86.21%		'1'	'1'
	B-G-H	2.2	2	2	10%	→	'1'	'0'
	G-H-I	2	2	2	0%		'0'	'0'
Radial A-F	A-B-C	4.5	2.2	2	86.21%	↓↓	'1'	'1'
	B-C-D	2.2	2	2	9.68%	→	'1'	'0'
	C-D-E	2	2	2	0%		'0'	'0'
	D-E-F	2	2	2	0%		'0'	'0'

Table C.198: Radial topology / Phase to ground (20 Ω) fault / F_1.

Circuit	3-points window	k_{s_1}	k_{s_2}	k_{s_3}	$\Delta k_{s_{13}}\%$	FS search	$k_{s_1} > k_{s_2}$	$k_{s_2} > k_{s_3}$
Radial A-I	A-B-G	11.7	6.4	6	70.95%		'1'	'1'
	B-G-H	6.4	6	5.9	8.2%	↓	'1'	'1'
	G-H-I	6	5.9	6	0%	→	'1'	'0'
Radial A-F	A-B-C	11.7	6.4	6	72.5%	↓↓	'1'	'1'
	B-C-D	6.4	5.9	5.9	8.24%	→	'1'	'0'
	C-D-E	5.9	5.9	5.9	0%		'0'	'0'
	D-E-F	5.9	5.9	6	1.69%		'0'	'0'

Table C.199: Radial topology / Phase to phase (0 Ω) fault / F_1.

Circuit	3-points window	k_{s_1}	k_{s_2}	k_{s_3}	$\Delta k_{s_{13}}\%$	FS search	$k_{s_1} > k_{s_2}$	$k_{s_2} > k_{s_3}$
Radial A-I	A-B-G	3.5	1.2	1	131.58%		'1'	'1'
	B-G-H	1.2	1	1	19.01%	→	'1'	'0'
	G-H-I	1		1	0%		'0'	'0'
Radial A-F	A-B-C	4	1.2	1	145.09%	↓↓	'1'	1'
	B-C-D	1.2	1	0.9	29.03%	↓	'1'	'1'
	C-D-E	1	0.9	1	0%	→	'1'	'0'
	D-E-F	0.9	1	1	10.34%		'0'	'0'

Table C.200: Radial topology / Phase to phase (60 Ω) fault / F_1.

Circuit	3-points window	k_{s_1}	k_{s_2}	k_{s_3}	$\Delta k_{s_{13}}\%$	FS search	$k_{s_1} > k_{s_2}$	$k_{s_2} > k_{s_3}$
Radial A-I	A-B-G	43.1	24.32	22.63	68.2%		'1'	'1'
	B-G-H	24.32	22.63	22.54	7.68%	↓	'1'	'1'
	G-H-I	22.63	22.54	22.61	0.09%	→	'1'	'0'
Radial A-F	A-B-C	43.1	24.32	22.59	68.36%	↓↓	'1'	1'
	B-C-D	24.32	22.59	22.7	6.98%	→	'1'	'0'
	C-D-E	22.59	22.7	22.6	0.04%		'0'	'1'
	D-E-F	22.7	22.6	22.69	0.04%		'1'	'0'

Table C.201: Radial topology / Phase to ground (0 Ω) fault / F_2.

Circuit	3-points window	k_{s_1}	k_{s_2}	k_{s_3}	$\Delta k_{s_{13}}\%$	FS search	$k_{s_1} > k_{s_2}$	$k_{s_2} > k_{s_3}$
Radial A-I	A-B-G	21.4	11.9	9.2	86.12%		'1'	'1'
	B-G-H	11.9	9.2	9.2	27%		'1'	'0'
	G-H-I	9.2	9.2	9.2	0%		'0'	'0'
Radial A-F	A-B-C	21.4	11.9	9.2	86.12%		'1'	'1'
	B-C-D	11.9	9.2	8.5	34.46%		'1'	'1'
	C-D-E	9.2	8.5	2	109.64%		'1'	'1'
	D-E-F	8.5	2	2	156%	→	'1'	'0'

Table C.202: Radial topology / Phase to ground (20 Ω) fault / F_2.

Circuit	3-points window	k_{s_1}	k_{s_2}	k_{s_3}	$\Delta k_{s_{13}}\%$	FS search	$k_{s_1} > k_{s_2}$	$k_{s_2} > k_{s_3}$
Radial A-I	A-B-G	27.2	15.3	11.8	85.1%		'1'	'1'
	B-G-H	15.3	11.8	11.8	27%		'1'	'0'
	G-H-I	11.8	11.8	11.8	0%		'0'	'0'
Radial A-F	A-B-C	27.2	15.3	11.8	85.08%		'1'	'1'
	B-C-D	15.3	11.8	11	33.86%		'1'	'1'
	C-D-E	11.8	11	2.8	105.47%		'1'	'1'
	D-E-F	11	2.8	2.8	148.19%	→	'1'	'0'

Table C.203: Radial topology / Phase to phase (0 Ω) fault / F_2.

Circuit	3-points window	k_{s_1}	k_{s_2}	k_{s_3}	$\Delta k_{s_{13}}\%$	FS search	$k_{s_1} > k_{s_2}$	$k_{s_2} > k_{s_3}$
Radial A-I	A-B-G	21	11	8.2	97.5%		'1'	'1'
	B-G-H	11	8.2	8.2	30.66%		'1'	'0'
	G-H-I	8.2	8.2	8.2	0%		'0'	'0'
Radial A-F	A-B-C	21	11	8.2	97.5%		'1'	'1'
	B-C-D	11	8.2	7.5	39.33%		'1'	'1'
	C-D-E	8.2	7.5	1	129.34%		'1'	'1'
	D-E-F	7.5	1	1	205.26%	→	'1'	'0'

Table C.204: Radial topology / Phase to phase (60 Ω) fault / F_2.

Circuit	3-points window	k_{s_1}	k_{s_2}	k_{s_3}	$\Delta k_{s_{13}}\%$	FS search	$k_{s_1} > k_{s_2}$	$k_{s_2} > k_{s_3}$
Radial A-I	A-B-G	55.51	31.37	24.3	84.21%		'1'	'1'
	B-G-H	31.37	24.3	24.2	26.93%		'1'	'1'
	G-H-I	24.3	24.2	24.28	0.08%		'1'	'0'
Radial A-F	A-B-C	55.51	31.37	24.26	84.35%		'1'	'1'
	B-C-D	31.37	24.3	22.57	33.76%		'1'	'1'
	C-D-E	24.3	22.57	6.11	102.85%		'1'	'1'
	D-E-F	22.57	6.11	6.12	141.81%	→	'1'	'0'

Table C.205: Radial topology / Phase to ground (0 Ω) fault / F_3.

Circuit	3-points window	k_{s_1}	k_{s_2}	k_{s_3}	$\Delta k_{s_{13}}\%$	FS search	$k_{s_1} > k_{s_2}$	$k_{s_2} > k_{s_3}$
Radial A-I	A-B-G	37.4	21.2	16.5	83.49%		'1'	'1'
	B-G-H	21.2	16.5	16.4	27%		'1'	'1'
	G-H-I	16.5	16.4	16.5	0%		'1'	'0'
Radial A-F	A-B-C	37.4	21.2	16.4	84%		'1'	'1'
	B-C-D	21.2	16.4	15.3	33.46%		'1'	'1'
	C-D-E	16.4	15.3	2.03	128.189%		'1'	'1'
	D-E-F	15.3	2.03	2.001	206.388%	→	'1'	'1'

Table C.206: Radial topology / Phase to ground (20 Ω) fault / F_3.

Circuit	3-points window	k_{s_1}	k_{s_2}	k_{s_3}	$\Delta k_{s_{13}}\%$	FS search	$k_{s_1} > k_{s_2}$	$k_{s_2} > k_{s_3}$
Radial A-I	A-B-G	42.7	24.3	18.9	83.12%		'1'	'1'
	B-G-H	24.3	18.9	18.8	26.61%		'1'	'1'
	G-H-I	18.9	18.8	18.9	0%		'1'	'0'
Radial A-F	A-B-C	42.7	24.3	18.9	83.12%		'1'	'1'
	B-C-D	24.3	18.9	17.6	33.06%		'1'	'1'
	C-D-E	18.9	17.6	2.5	126.15%		'1'	'1'
	D-E-F	17.6	2.5	2.4	202.67%	→	'1'	'1'

Table C.207: Radial topology / Phase to phase (0 Ω) fault / F_3.

Circuit	3-points window	k_{s_1}	k_{s_2}	k_{s_3}	$\Delta k_{s_{13}}\%$	FS search	$k_{s_1} > k_{s_2}$	$k_{s_2} > k_{s_3}$
Radial A-I	A-B-G	36.3	20.2	15.6	86.13%		'1'	'1'
	B-G-H	20.2	15.6	15.6	26.85%		'1'	'0'
	G-H-I	15.6	15.6	15.5	0.642%		'0'	'1'
Radial A-F	A-B-C	36.3	20.2	15.6	83.33%		'1'	'1'
	B-C-D	20.2	15.6	14.3	35.33%		'1'	'1'
	C-D-E	15.6	14.3	1.035	141.74%		'1'	'1'
	D-E-F	14.3	1.035	1	244.26%	→	'1'	'1'

Table C.208: Radial topology / Phase to phase (60 Ω) fault / F_3.

Circuit	3-points window	k_{s_1}	k_{s_2}	k_{s_3}	$\Delta k_{s_{13}}\%$	FS search	$k_{s_1} > k_{s_2}$	$k_{s_2} > k_{s_3}$
Radial A-I	A-B-G	68.83	39.02	30.3	83.67%		'1'	'1'
	B-G-H	39.02	30.3	30.17	26.69%		'1'	'1'
	G-H-I	30.3	30.17	30.27	0.1%		'1'	'0'
Radial A-F	A-B-C	68.83	39.02	30.25	83.81%		'1'	'1'
	B-C-D	39.02	30.25	28.28	33.03%		'1'	'1'
	C-D-E	30.25	28.28	3.93	126.42%		'1'	'1'
	D-E-F	28.28	3.93	3.87	202.97%	→	'1'	'1'

Table C.209: Radial topology / Phase to ground (0 Ω) fault / F_4.

Circuit	3-points window	k_{s_1}	k_{s_2}	k_{s_3}	$\Delta k_{s_{13}}\%$	FS search	$k_{s_1} > k_{s_2}$	$k_{s_2} > k_{s_3}$
Radial A-I	A-B-G	5.8	2.9	2	106.54%	↓↓	'1'	'1'
	B-G-H	2.9	2	2	39%	→	'1'	'0'
	G-H-I	2	2	2	0%		'0'	'0'
Radial A-F	A-B-C	5.8	2.9	2.1	102.78%		'1'	'1'
	B-C-D	2.9	2.1	2.1	33.8%	→	'1'	'0'
	C-D-E	2.1	2.1	2.1	0%		'0'	'0'
	D-E-F	2.1	2.1	2.1	0%		'0'	'0'

Table C.210: Radial topology / Phase to ground (20 Ω) fault / F_4.

Circuit	3-points window	k_{s_1}	k_{s_2}	k_{s_3}	$\Delta k_{s_{13}}\%$	FS search	$k_{s_1} > k_{s_2}$	$k_{s_2} > k_{s_3}$
Radial A-I	A-B-G	12.9	7.1	5.2	91.67%	↓↓	'1'	'1'
	B-G-H	7.1	5.2	5.2	32.57%	→	'1'	'0'
	G-H-I	5.2	5.2	5.2	0%		'0'	'0'
Radial A-F	A-B-C	12.9	7.1	5.4	88.58%		'1'	'1'
	B-C-D	7.1	5.4	5.4	28.49%	→	'1'	'0'
	C-D-E	5.4	5.4	5.4	0%		'0'	'0'
	D-E-F	5.4	5.4	5.4	0%		'0'	'0'

Table C.211: Radial topology / Phase to phase (0 Ω) fault / F_4.

Circuit	3-points window	k_{s_1}	k_{s_2}	k_{s_3}	$\Delta k_{s_{13}}\%$	FS search	$k_{s_1} > k_{s_2}$	$k_{s_2} > k_{s_3}$
Radial A-I	A-B-G	4.8	1.9	1	148.05%	↓↓	'1'	'1'
	B-G-H	1.9	1	1	69.23%	→	'1'	'0'
	G-H-I	1	1	1	0%		'0'	'0'
Radial A-F	A-B-C	4.8	1.9	1	148.05%		'1'	'1'
	B-C-D	1.9	1	1	69.23%	→	'1'	'0'
	C-D-E	1	1	1	0%		'0'	'0'
	D-E-F	1	1	1	0%		'0'	'0'

Table C.212: Radial topology / Phase to phase (60 Ω) fault / F_4.

Circuit	3-points window	k_{s_1}	k_{s_2}	k_{s_3}	$\Delta k_{s_{13}}\%$	FS search	$k_{s_1} > k_{s_2}$	$k_{s_2} > k_{s_3}$
Radial A-I	A-B-G	44.16	24.93	18.66	87.18%	↓↓	'1'	'1'
	B-G-H	24.93	18.66	18.58	30.64%	→	'1'	'1'
	G-H-I	18.66	18.58	18.64	0.11%		'1'	'0'
Radial A-F	A-B-C	44.16	24.93	19.24	84.64%		'1'	'1'
	B-C-D	24.93	19.24	19.27	26.77%	→	'1'	'0'
	C-D-E	19.24	19.27	19.25	0.05%		'0'	'1'
	D-E-F	19.27	19.25	19.32	0.26%		'1'	'0'

Table C.213: Radial topology / Phase to ground (0 Ω) fault / F_5.

Circuit	3-points window	k_{s_1}	k_{s_2}	k_{s_3}	$\Delta k_{s_{13}}\%$	FS search	$k_{s_1} > k_{s_2}$	$k_{s_2} > k_{s_3}$
Radial A-I	A-B-G	20.9	11.6	8.7	88.83%		'1'	'1'
	B-G-H	11.6	8.7	2	129%		'1'	'1'
	G-H-I	8.7	2	2	158%	→	'1'	'0'
Radial A-F	A-B-C	20.9	11.6	8.9	86.96%		'1'	'1'
	B-C-D	11.6	8.9	8.9	27.55%		'1'	'0'
	C-D-E	8.9	8.9	9	1.119%		'0'	'0'
	D-E-F	8.9	9	9	1.12%		'0'	'0'

Table C.214: Radial topology / Phase to ground (20 Ω) fault / F_5.

Circuit	3-points window	k_{s_1}	k_{s_2}	k_{s_3}	$\Delta k_{s_{13}}\%$	FS search	$k_{s_1} > k_{s_2}$	$k_{s_2} > k_{s_3}$
Radial A-I	A-B-G	26.5	14.9	11.2	87.26%		'1'	'1'
	B-G-H	14.9	11.2	2.8	125.6%		'1'	'1'
	G-H-I	11.2	2.8	2.8	150%	→	'1'	'0'
Radial A-F	A-B-C	26.5	14.9	11.5	85.07%		'1'	'1'
	B-C-D	14.9	11.5	11.5	26.91%		'1'	'0'
	C-D-E	11.5	11.5	11.5	0%		'0'	'0'
	D-E-F	11.7	11.7	11.7	0%		'0'	'0'

Table C.215: Radial topology / Phase to phase (0 Ω) fault / F_5.

Circuit	3-points window	k_{s_1}	k_{s_2}	k_{s_3}	$\Delta k_{s_{13}}\%$	FS search	$k_{s_1} > k_{s_2}$	$k_{s_2} > k_{s_3}$
Radial A-I	A-B-G	19.9	10.6	7.7	95.81%		'1'	'1'
	B-G-H	10.6	7.7	1	149.22%		'1'	'1'
	G-H-I	7.7	1	1	207.216%	→	'1'	'0'
Radial A-F	A-B-C	19.9	10.6	7.9	92.31%		'1'	'1'
	B-C-D	10.6	7.9	7.9	30.68%		'1'	'0'
	C-D-E	7.9	7.9	8	1.26%		'0'	'0'
	D-E-F	7.9	8	8	1.25%		'0'	'0'

Table C.216: Radial topology / Phase to phase (60 Ω) fault / F_5.

Circuit	3-points window	k_{s_1}	k_{s_2}	k_{s_3}	$\Delta k_{s_{13}}\%$	FS search	$k_{s_1} > k_{s_2}$	$k_{s_2} > k_{s_3}$
Radial A-I	A-B-G	54.79	30.96	23.22	86.91%		'1'	'1'
	B-G-H	30.96	23.22	6.21	122.95%		'1'	'1'
	G-H-I	23.22	6.21	6.24	142.81%	→	'1'	'0'
Radial A-F	A-B-C	54.79	30.96	23.93	84.41%		'1'	'1'
	B-C-D	30.96	23.93	23.99	26.51%		'1'	'0'
	C-D-E	23.93	23.99	23.95	0.08%		'0'	'1'
	D-E-F	23.99	23.95	24.04	0.21%		'1'	'0'

Table C.217: Radial topology / Phase to ground (0 Ω) fault / F_6.

Circuit	3-points window	k_{s_1}	k_{s_2}	k_{s_3}	$\Delta k_{s_{13}}\%$	FS search	$k_{s_1} > k_{s_2}$	$k_{s_2} > k_{s_3}$
Radial A-I	A-B-G	21.3	11.9	8.8	89.29%		'1'	'1'
	B-G-H	11.9	8.8	2.1	129%		'1'	'1'
	G-H-I	8.8	2.1	2	158%	→	'1'	'1'
Radial A-F	A-B-C	21.3	11.9	9.1	86.52%		'1'	'1'
	B-C-D	11.9	9.1	9.1	27.91%		'1'	'0'
	C-D-E	9.1	9.1	9.1	0%		'0'	'0'
	D-E-F	9.1	9.1	9.2	1.09%		'0'	'0'

Table C.218: Radial topology / Phase to ground (20 Ω) fault / F_6.

Circuit	3-points window	k_{s_1}	k_{s_2}	k_{s_3}	$\Delta k_{s_{13}}\%$	FS search	$k_{s_1} > k_{s_2}$	$k_{s_2} > k_{s_3}$
Radial A-I	A-B-G	26.9	15.1	11.3	87.8%		'1'	'1'
	B-G-H	15.1	11.3	2.9	124.915%		'1'	'1'
	G-H-I	11.3	2.9	2.8	150%	→	'1'	'1'
Radial A-F	A-B-C	26.9	15.1	11.7	84.92%		'1'	'1'
	B-C-D	15.1	11.7	11.7	26.91%		'1'	'0'
	C-D-E	11.5	11.5	11.5	0%		'0'	'0'
	D-E-F	11.7	11.7	11.7	0%		'0'	'0'

Table C.219: Radial topology / Phase to phase (0 Ω) fault / F_6.

Circuit	3-points window	k_{s_1}	k_{s_2}	k_{s_3}	$\Delta k_{s_{13}}\%$	FS search	$k_{s_1} > k_{s_2}$	$k_{s_2} > k_{s_3}$
Radial A-I	A-B-G	20.4	10.9	7.9	95.66%		'1'	'1'
	B-G-H	10.9	7.9	1.1	147.74%		'1'	'1'
	G-H-I	7.9	1.1	1	207%	→	'1'	'1'
Radial A-F	A-B-C	20.4	10.9	8.1	92.31%		'1'	'1'
	B-C-D	10.9	8.1	8.1	31%		'1'	'0'
	C-D-E	8.1	8.1	8.2	1.22%		'0'	'0'
	D-E-F	8.1	8.2	8.2	1.22%		'0'	'0'

Table C.220: Radial topology / Phase to phase (60 Ω) fault / F_6.

Circuit	3-points window	k_{s_1}	k_{s_2}	k_{s_3}	$\Delta k_{s_{13}}\%$	FS search	$k_{s_1} > k_{s_2}$	$k_{s_2} > k_{s_3}$
Radial A-I	A-B-G	55.14	31.16	23.37	86.91%		'1'	'1'
	B-G-H	31.16	23.37	6.25	122.95%		'1'	'1'
	G-H-I	23.37	6.25	6.13	144.67%	→	'1'	'1'
Radial A-F	A-B-C	55.14	31.16	24.08	84.42%		'1'	'1'
	B-C-D	31.16	24.08	24.15	26.49%		'1'	'0'
	C-D-E	24.08	24.15	24.1	0.08%		'0'	'1'
	D-E-F	24.15	24.1	24.2	0.21%		'1'	'0'